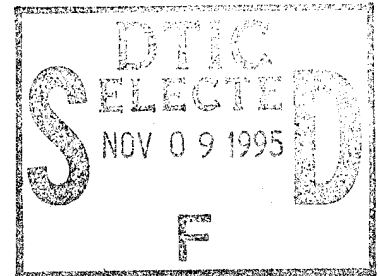


D44/831

NASA Contractor Report 4118

Static and Dynamic Large Deflection Flexural Response of Graphite-Epoxy Beams

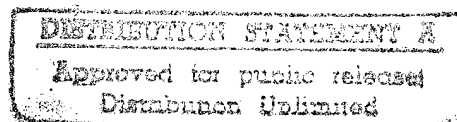


Mark D. Sensmeier, O. Hayden Griffin, Jr.,
and Eric R. Johnson

GRANT NAG1-343
MARCH 1988

19951024 095

DEPARTMENT OF DEFENSE
PLASTICS TECHNICAL EVALUATION CENTER
ARMADCON, BOSTON



NASA

S DTIC QUALITY INSPECTED 8

POSTED 03/17/81

NASA Contractor Report 4118

Static and Dynamic Large Deflection Flexural Response of Graphite-Epoxy Beams

Mark D. Sensmeier, O. Hayden Griffin, Jr.,
and Eric R. Johnson
Virginia Polytechnic Institute and State University
Blacksburg, Virginia

Prepared for
Langley Research Center
under Grant NAG1-343



National Aeronautics
and Space Administration

Scientific and Technical
Information Division

1988

Accession For	
NTIS GPO/NI	<input checked="" type="checkbox"/>
DTIC TAB	<input type="checkbox"/>
Unannounced	<input type="checkbox"/>
Justification	
By DTIC-AI memo	
Distri Date 11-2-95	
Availability Codes	
Dist	Avail and/or Special
A-1	

**Static and Dynamic Large Deflection Flexural Response
of Graphite-Epoxy Beams**

by

Mark David Sensmeier

O. H. Griffin, Chairman

Engineering Science & Mechanics

(ABSTRACT)

In support of crashworthiness studies of composite airframes, the present study was undertaken to understand the large deflection flexural response and failure of graphite-epoxy laminated beams. The beam specimens were subjected to eccentric axial impact loads and to static eccentric axial loads, in order to assess the damage caused by impact.

A geometrically and materially nonlinear analysis of the response and failure of the static test specimens is presented. The analysis employed an incremental, noniterative finite element model based on the Kantrovich method and a corotational solution technique. Width-wise effects are included by assuming specific forms of the displacements across the width, with length-wise variation introduced as a degree of freedom. This one-dimensional, 22 degree of freedom finite element accurately predicted the load-deflection and strain-deflection responses of the static test specimens.

Inclusion of nonlinear material behavior was found to be important in correctly predicting load-deflection response of uniaxial materials, while inclusion of width-wise effects was determined to be more important for laminates with off-axis plies due to the existence of coupling between bending and twisting curvatures (D_{16} and D_{26}). Once material nonlinearity begins to occur in flexure, even symmetric laminates exhibit bending-stretching coupling due to different material response in tension and compression.

Acknowledgements

This study was supported by the NASA-Virginia Tech Composites Program under NASA Grant NAG-1-343. Thanks are due to Karen Jackson for her assistance with the experimental portion of this work performed at NASA Langley Research Center, and George Palko, III, for his effort with the mechanical apparatus. Thanks to Jack Beuth for performing the Iosipescu shear tests.

Table of Contents

1.0 Introduction	1
2.0 Experimental Procedure	6
2.1 Beam Specimens	8
2.2 Static Test Fixture	10
2.3 Dynamic Test Fixture	13
2.4 Data Acquisition	19
2.4.1 Static Tests	19
2.4.2 Dynamic Tests	19
2.5 Test Procedures	21
2.5.1 Static Tests	21
2.5.2 Dynamic Tests	21
3.0 Experimental Results	23
3.1 Static Tests	23
3.1.1 $[0]_{30}$ Laminate	23
3.1.2 $[(30/0/-30)_s]_s$ Laminate	24

3.1.3	[(45/-45/0/90) ₄] _s Laminate	24
3.1.4	[0] ₁₈ Laminate	28
3.1.5	[(15/0/-15) ₃] _s Laminate	28
3.1.6	[(30/0/-30) ₃] _s Laminate	28
3.1.7	[(45/0/-45) ₃] _s Laminate	31
3.1.8	[(45/-45/0/90) ₂] _s Laminate	31
3.1.9	[(45/-45) ₂ /(0) ₈ /(-45/45) ₂] _t Laminate	35
3.1.10	Observations	35
3.2	Dynamic Tests	37
3.2.1	Group One (Laminates A1 through A5)	37
3.2.2	Group Two (Laminates B1 through B3)	49
3.2.3	Group Three (Laminates C1 through C6)	51
3.2.4	Quarter-point surface strain response	54
3.2.5	Transverse Strain Response	54
3.2.5.1	Thick Laminates	55
3.2.5.2	Thin Laminates	58
4.0	Impact Alleviation Tests	65
4.1	Test Description	67
4.2	Dynamic Results	68
4.3	Results	70
4.3.1	Thick Laminates	70
4.3.1.1	[0] ₃₀ Laminate	70
4.3.1.2	[(30/0/-30) ₅] _s Laminate	71
4.3.1.3	[(45/-45/0/90) ₄] _s Laminate	76
4.3.2	Thin Laminates	76
4.3.2.1	[0] ₁₈ Laminate	76
4.3.2.2	[(15/0/-15) ₃] _s Laminate	79

4.3.2.3	[(30/0/-30) ₃]s Laminate	82
4.3.2.4	[(45/0/-45) ₃]s Laminate	82
4.3.2.5	[(45/-45/0/90) ₂]s Laminate	87
4.3.2.6	[(45/-45) ₂ /(0) ₈ /(-45/45) ₂]t Laminate	92
4.4	Observations	92
5.0	Material Characterization Tests	97
5.1	Test Methods	98
5.1.1	Tension	98
5.1.2	Compression	98
5.1.3	Inplane Shear	99
5.2	Data Reduction	102
5.3	Results	102
5.3.1	Longitudinal Response	102
5.3.1.1	Tension	102
5.3.1.2	Compression	104
5.3.1.3	Combined	104
5.3.2	Transverse Response	110
5.3.2.1	Tension	110
5.3.2.2	Compression	110
5.3.2.3	Combined	110
5.3.3	Inplane Shear	114
5.4	Summary of Material Characterization	114
6.0	Analytical Development	117
6.1	Assumptions	118
6.2	Finite Element Formulation	119
6.2.1	Strain-Displacement Equations	119

6.2.2	Constitutive Equations	122
6.2.3	Variational Energy Formulation	123
6.2.4	Formulation of Finite Element Equations	124
6.3	Nonlinearity	128
6.3.1	Geometric Nonlinearity	128
6.3.1.1	Stiffness Transformation	129
6.3.1.2	Corotational Procedure	132
6.3.2	Material Nonlinearity	133
6.4	Model Verification	134
7.0	Numerical Results	139
7.1	Model	139
7.1.1	Material Model	139
7.1.2	Mesh	140
7.1.3	Boundary Conditions and Applied Loads	140
7.1.4	Mesh Refinement	143
7.2	Correlation of Numerical and Experimental Results	145
7.2.1	Thick Laminates	145
7.2.2	Thin Laminates	148
7.2.3	Observations	154
7.3	Material Nonlinearity and Width-Wise Effects	158
7.3.1	$[0]_{30}$ Laminate	159
7.3.2	$[(30/0/-30)_s]_s$ Laminate	159
7.3.3	Observations	163
7.4	Width-Wise Reponse of Laminates	165
7.4.1.1	Effect of Off-Axis Ply Angles	166
7.4.1.2	Effect of Stacking Sequence	167
7.4.1.3	Effect of Beam Width	170

7.4.1.4 Effect of Material Nonlinearity	170
7.4.2 Cross Sectional Warping	170
7.5 Failure Analysis	175
7.5.1 Obtaining Finite Element Results	175
7.5.2 Failure Criteria and Strengths	176
7.5.3 Results	178
7.5.4 Observations	180
 8.0 Conclusions and Recommendations	 182
8.1 Conclusions	183
8.2 Recommendations	185
 References	 187
 Appendix A. Dynamic End Displacement-Time for Group One Laminates	 189
 Appendix B. Dynamic Data for Group Two and Group Three Laminates	 192
 Appendix C. Quarter-Point Dynamic Strain Data	 205
 Appendix D. Transverse Dynamic Strain Data	 213
 Appendix E. Finite Element Equations	 218
 Appendix F. Stress-Strain Curve Approximation Polynomials	 226
F.1 Longitudinal Tension	227
F.2 Longitudinal Compression	228
F.3 Transverse Tension	228

F.4	Transverse Compression	229
F.5	Inplane Shear	230
F.6	Poisson's Ratio	231

List of Illustrations

Figure 1. Basic load configuration	7
Figure 2. Specimen being statically tested in load frame	12
Figure 3. Schematic of drop tower	14
Figure 4. Schematic of upper hinge	15
Figure 5. Photograph of drop tower	16
Figure 6. Photograph of specimen installed in drop tower	17
Figure 7. Schematic of drop tower used by Derian and Hyer (1986)	18
Figure 8. Static load and strain response for $[0]_{30}$ Laminate	25
Figure 9. Static load and strain response for $[(30/0/-30)_s]_s$ Laminate	26
Figure 10. Static load and strain response for $[(45/-45/0/90)_4]_s$ Laminate	27
Figure 11. Static load and strain response for $[0]_{18}$ Laminate	29
Figure 12. Static load and strain response for $[(15/0/-15)_3]_s$ Laminate	30
Figure 13. Static load and strain response for $[(30/0/-30)_3]_s$ Laminate	32
Figure 14. Static load and strain response for $[(45/0/-45)_3]_s$ Laminate	33
Figure 15. Static load and strain response for $[(45/-45/0/90)_2]_s$ Laminate	34
Figure 16. Static load and strain response for $[(45/-45)_2/(0)_8/(-45/45)_2]_t$ Laminate	36
Figure 17. Dynamic load responses for laminate A1	39
Figure 18. Dynamic strain responses for laminate A1	40
Figure 19. Dynamic displacement responses for laminate A1	41
Figure 20. Dynamic load responses for laminate A2	42
Figure 21. Dynamic strain responses for laminate A2	43

Figure 22. Dynamic load responses for laminate A3	44
Figure 23. Dynamic strain responses for laminate A3	45
Figure 24. Dynamic load responses for laminate A4	46
Figure 25. Dynamic strain responses for laminate A4	47
Figure 26. Dynamic load responses for laminate A5	48
Figure 27. Dynamic load responses for [(30/0/-30) ₅]s laminates	52
Figure 28. Dynamic strain responses for [(30/0/-30) ₅]s laminates	53
Figure 29. Dynamic midplane strains and curvatures for [(30/0/-30) ₅]s laminate	56
Figure 30. Dynamic midplane strains and curvatures for [(45/-45/0/90) ₄]s laminate	57
Figure 31. Dynamic midplane strains and curvatures for [0] ₁₈ laminate	59
Figure 32. Dynamic midplane strains and curvatures for [(15/0/-15) ₃]s laminate	60
Figure 33. Dynamic midplane strains and curvatures for [(30/0/-30) ₃]s laminate	61
Figure 34. Dynamic midplane strains and curvatures for [(45/0/-45) ₃]s laminate	62
Figure 35. Dynamic midplane strains and curvatures for [(45/-45/0/90) ₂]s laminate	63
Figure 36. Dynamic midplane strains and curvatures for [(45/-45) ₂ /(0) ₈ /(-45/45) ₂]t laminate	64
Figure 37. End load vs end displacement for impacted and virgin [0] ₃₀ beams	72
Figure 38. Surface strain magnitudes for impacted and virgin [0] ₃₀ beams	73
Figure 39. End load vs end displacement for impacted and virgin [(30/0/-30) ₅]s beams ..	74
Figure 40. Surface strain magnitudes for impacted and virgin [(30/0/-30) ₅]s beams	75
Figure 41. End load vs end displacement for impacted and virgin [(45/-45/0/90) ₄]s beams ..	77
Figure 42. Surface strain magnitudes for impacted and virgin [(45/-45/0/90) ₄]s beams ..	78
Figure 43. End load vs end displacement for impacted and virgin [0] ₁₈ beams	80
Figure 44. Surface strain magnitudes for impacted and virgin [0] ₁₈ beams	81
Figure 45. End load vs end displacement for impacted and virgin [(15/0/-15) ₃]s beams ..	83
Figure 46. Surface strain magnitudes for impacted and virgin [(15/0/-15) ₃]s beams	84
Figure 47. End load vs end displacement for impacted and virgin [(30/0/-30) ₃]s beams ..	85
Figure 48. Surface strain magnitudes for impacted and virgin [(30/0/-30) ₃]s beams	86
Figure 49. End load vs end displacement for impacted and virgin [(45/0/-45) ₃]s beams ..	88

Figure 50. Surface strain magnitudes for impacted and virgin [(45/0/-45) ₃] _s beams	89
Figure 51. End load vs end displacement for impacted and virgin [(45/-45/0/90) ₂] _s beams	90
Figure 52. Surface strain magnitudes for impacted and virgin [(45/-45/0/90) ₂] _s beams	91
Figure 53. End load vs end displacement for impacted and virgin [(45/-45) ₂ /(0) ₈ /(-45/45) ₂] beams	93
Figure 54. Surface strain magnitudes for impacted and virgin [(45/-45) ₂ /(0) ₈ /(-45/45) ₂] beams	94
Figure 55. Gurdal compression test fixture	100
Figure 56. Iosipescu specimen geometry and dimensions	101
Figure 57. Longitudinal tension stress-strain response	105
Figure 58. Poisson response in longitudinal tension	106
Figure 59. Longitudinal compression stress-strain response	107
Figure 60. Poisson response in longitudinal compression	108
Figure 61. Longitudinal stress-strain response	109
Figure 62. Transverse tension stress-strain response	111
Figure 63. Transverse compression stress-strain response	112
Figure 64. Transverse stress-strain response	113
Figure 65. Inplane shear stress-strain response	115
Figure 66. Definition of beam coordinate system	120
Figure 67. Typical beam element	127
Figure 68. Global and local coordinates of element	130
Figure 69. Clamped-clamped beam test case	136
Figure 70. Simply-supported Inextensional Beam Test Case	137
Figure 71. Inextensional Cantilever Beam Test Case	138
Figure 72. Geometry and dimensions of hinge support	141
Figure 73. Finite element mesh and boundary conditions used in analysis	142
Figure 74. Solution versus number of elements	144
Figure 75. Predicted and measured response of [0] ₃₀ beam	146
Figure 76. Predicted and measured response of [(30/0/-30) ₅] _s beam	147

Figure 77. Predicted and measured response of $[(45/-45/0/90)_4]_s$ beam	149
Figure 78. Predicted and measured response of $[0]_{18}$ beam	150
Figure 79. Predicted and measured response of $[(15/0/-15)_3]_s$ beam	151
Figure 80. Predicted and measured response of $[(30/0/-30)_3]_s$ beam	152
Figure 81. Predicted and measured response of 0.75-inch $[(30/0/-30)_3]_s$ beam	153
Figure 82. Predicted and measured response of $[(45/0/-45)_3]_s$ beam	155
Figure 83. Predicted and measured response of $[(45/-45/0/90)_2]_s$ beam	156
Figure 84. Predicted and measured response of $[(45/-45)_2/(0)_8/(-45/45)_2]$ beam	157
Figure 85. Load-displacement predictions for $[0]_{30}$ beam using different analyses	160
Figure 86. Surface strain predictions for $[0]_{30}$ beam using different analyses	161
Figure 87. Load-displacement predictions for $[(30/0/-30)_5]_s$ beam using different analyses	162
Figure 88. Surface strain predictions for $[(30/0/-30)_5]_s$ beam using different analyses	164
Figure 89. Effect of off-axis ply angle on width-wise curvature of $[(\theta/0/-\theta)_3]_s$ beams	168
Figure 90. Effect of stacking sequence on width-wise curvature	169
Figure 91. Effect of beam width on width-wise curvature	171
Figure 92. Effect of material nonlinearity on width-wise curvature	172
Figure 93. Cross sectional warping in $[0]_{30}$ and $[(30/0/-30)_5]_s$ beams	174
Figure 94. Predicted tensile fiber failure criteria values at experimental failure loads	179
Figure 95. End displacement versus time for laminates A2 and A3	190
Figure 96. End displacement versus time for laminates A4 and A5	191
Figure 97. Load and strain versus time for laminate B1	193
Figure 98. Load and strain versus time for laminate B3	194
Figure 99. Load and strain versus time for laminate C1	195
Figure 100. Load and strain versus time for laminate C2	196
Figure 101. Load and strain versus time for laminate C3	197
Figure 102. Load and strain versus time for laminate C4	198
Figure 103. Load and strain versus time for laminate C5	199
Figure 104. Load and strain versus time for laminate C6	200

Figure 105. End displacement versus time for laminates B1 and B3	201
Figure 106. End displacement versus time for laminates C1 and C2	202
Figure 107. End displacement versus time for laminates C3 and C4	203
Figure 108. End displacement versus time for laminates C5 and C6	204
Figure 109. Quarter point strains versus time for laminate B1	206
Figure 110. Quarter point strains versus time for laminate B3	207
Figure 111. Quarter point strains versus time for laminate C1	208
Figure 112. Quarter point strains versus time for laminate C2	209
Figure 113. Quarter point strains versus time for laminate C4	210
Figure 114. Quarter point strains versus time for laminate C5	211
Figure 115. Quarter point strains versus time for laminate C6	212
Figure 116. Transverse strains versus time for laminates B2 and B3	214
Figure 117. Transverse strains versus time for laminates C1 and C2	215
Figure 118. Transverse strains versus time for laminates C3 and C4	216
Figure 119. Transverse strains versus time for laminates C5 and C6	217

List of Tables

Table 1. Laminate Definitions and Impactor Masses	9
Table 2. Dimensions of Beam Specimens	11
Table 3. Dynamic peak loads for group one laminates	50
Table 4. Peak dynamic and static loads from experiments	66
Table 5. Peak Loads and Strains During Impact Alleviation Tests	69
Table 6. Summary of failure stresses	103
Table 7. Summary of material characterization tests	116

Nomenclature

A	Laminate extension stiffness matrix
B	Laminate coupling stiffness matrix
b	Beam half-width
D	Laminate bending stiffness matrix
E_{1c}	Compressive fiber-direction modulus
E_{1t}	Tensile fiber-direction modulus
E_{2c}	Compressive transverse modulus
E_{2t}	Tensile transverse modulus
E_e	Laminate strain energy
E_p	Strain energy due to initial axial force in element
E_E	Energy of applied loads
F^i	Element force vectors
$F(\sigma), F(\epsilon)$	Failure functions
G_{12}	Inplane shear modulus
g	Quadratic term in Kantrovich expansion for w
h	Total laminate thickness
i, j	Index variables

K	Global finite element stiffness matrix
k	Element stiffness matrix in global coordinate system
\bar{k}	Element stiffness matrix in element local coordinate system
L	Length of finite element
M_x, M_y, M_{xy}	Moment resultants
N_x, N_y, N_{xy}	Inplane force resultants
P	Initial axial tensile force acting on element
Q	Global force vector
\bar{Q}	Lamina plane stress stiffness matrix
q	Element force vector in global coordinate system
\bar{q}	Element force vector in element local coordinate system
S	Inplane shear strength
T	Corotational transformation matrix
t	Corotational transformation submatrix
U	Constant term in Kantrovich expansion for u°
u	Displacement in x-direction
u°	Displacement in x-direction of laminate midplane
V	Constant term in Kantrovich expansion for v°
v	Displacement in y-direction
v°	Displacement in y-direction of laminate midplane
W	Constant term in Kantrovich expansion for w
w	Displacement in z-direction
x, y, z	Global orthogonal coordinate axes
$\bar{x}, \bar{y}, \bar{z}$	Element local orthogonal coordinate axes
X_c	Compressive fiber-direction strength
X_t	Tensile fiber-direction strength
Y_c	Compressive transverse strength
Y_t	Tensile transverse strength

α	Quadratic term in Kantrovich expansion for u^o
β	Beam width
γ_{12}^u	Inplane engineering shear strain at failure
Δ	Element displacement vector
δ	Increment
$\varepsilon_1, \varepsilon_2, \gamma_{12}$	Engineering strains in principal material coordinate system
$\varepsilon_{1t}^u, \varepsilon_{2t}^u$	Tensile failure strains
$\varepsilon_{1c}^u, \varepsilon_{2c}^u$	Compressive failure strains
$\varepsilon_x, \varepsilon_y, \gamma_{xy}$	Engineering strains in beam coordinate system
$\varepsilon_x^o, \varepsilon_y^o, \gamma_{xy}^o$	Midplane engineering strains in beam coordinate system
$\varepsilon_{xt}, \varepsilon_{yt}$	Surface strains on tensile side of beam
$\varepsilon_{xc}, \varepsilon_{yc}$	Surface strains on compressive side of beam
η	Linear term in Kantrovich expansion for u^o
Θ	Linear term in Kantrovich expansion for w
θ	Ply angle
$\kappa_x, \kappa_y, \kappa_{xy}$	Laminate curvatures
ν_{12}, ν_{21}	Major and minor Poisson's ratios
Σ	Summation
$\sigma_1, \sigma_2, \sigma_{12}$	Principal stresses
Φ	Corotational transformation angle
φ	Hermite cubic interpolation functions
ψ	Linear interpolation functions
ω	Linear term in Kantrovich expansion for v^o

1.0 Introduction

It is forecast that the next generation transport aircraft will utilize advanced composite materials in the primary structure in addition to their current utilization in secondary structural components. Crashworthiness of the composite primary structural design is an important safety issue. Crashworthiness is the capability of a structure to absorb impact energy and thereby protect the passengers or cargo from dangerous deceleration levels encountered in a crash situation. Derian and Hyer (1986) provide a detailed discussion of the aspects of crashworthiness, specifically regarding the use of composite materials versus metals. The reader is referred to that study for further information and literature concerning crashworthiness.

The current study is an extension of the work performed by Derian and Hyer (1986). In this previous study, a drop tower was designed and used to induce compressive axial impact loading on rectangular cross-section composite beams. Static and dynamic tests were performed using that load configuration, and it was found that for practical laminates, there was no difference between the static and dynamic failure modes. Several conclusions from that study were investigated further in the current study. They are:

1. Some spurious noise was present in the dynamic data. Particularly noteworthy was the data in the initial end displacement response. It was apparent from this data that the beam was actually moving upward shortly after impact. However, further analysis of high-speed motion pictures revealed that this was not the case. It was felt that unwanted upward motion of an optical transducer wedge was the cause of this noise.
2. Peak loads were encountered in the dynamic tests that were several times higher than the static failure loads of the beams.
3. For both the static and dynamic tests, the compressive side surface strains at the center of the beam were always greater in magnitude than the tensile side surface strains. This is not predicted by standard beam theory and was not expected.
4. Neither phenomenological (strain tensor polynomial) nor mechanistic (maximum fiber strain) failure criteria were successful in predicting failure based on experimental strain data.
5. An existing finite element code successfully predicted the load and displacement response statically and dynamically. However, this program only allowed linear elastic properties which could be different in tension and compression. It also did not predict surface strains, so the aforementioned difference in strain magnitudes could not be predicted. Furthermore, the input properties used in the finite element runs were obtained empirically from the flexure tests themselves, not from independent material characterization.

The current study investigated further these issues. The overall goals of this study were to:

1. Revise the drop tower designed by Derian and Hyer (1986) and conduct further impact tests to determine the effects of these revisions. Specifically, it was desired to see if these changes removed spurious noise observed in the data from Derian and Hyer.

2. Conduct static and dynamic tests with a new material batch to determine if the results obtained in the previous study were peculiar to a specific material batch. Specific interest is in the difference in strain magnitudes between the tensile and compressive sides of the beam, as was observed by Derian and Hyer.
3. Investigate the extent and nature of the damage, if any, induced by the high load spikes encountered early in the impact tests.
4. Develop a finite element program to predict the load-displacement and strain-displacement response. Specific interest is in predicting and determining the cause of the observed difference in strain magnitudes. Independent uniaxial material characterization was needed to provide a material model for this analysis.
5. Analytically predict failure of the beams from the finite element results.

The drop tower designed and utilized by Derian and Hyer (1986) was revised to attempt to remove some of the spurious noise in the dynamic data. A number of beams were fabricated from a new material batch and tested in the revised fixture, along with some specimens remaining from the Derian and Hyer study. Furthermore, a series of static tests was performed on the new beams to investigate further the issue of difference in tensile side and compressive side strain magnitudes. The procedure for the aforementioned tests is described in Chapter 2, and the results are presented in Chapter 3.

A series of tests was performed in which beams were impacted, but not allowed to deflect to failure. These beams were then tested statically and the results compared to results obtained from the static tests of virgin beams to assess the damage induced by the initial load spikes. The results from these tests are presented in Chapter 4.

A full set of material characterization tests were performed on the material system from which the new beams were fabricated. Specifically, fiber-direction tension and compression, trans-

verse tension and compression, and inplane shear tests were conducted. The results of these tests are shown in Chapter 5.

The problem of predicting the load and strain response of composite beams undergoing large deflections is not a trivial one. Very little work has been done on this problem. However, there is an extensive body of literature involving large deflections of isotropic bodies. The reader is referred to the excellent literature survey performed by Gadala, et al (1984). This paper presents a number of popular formulation methods used for nonlinear problems (both geometric and material). Early work was done by Herrmann (1956) on large deflections of a plate (in the von Karman sense- i.e. up to ten times the plate thickness) and the effects of these large deflections on flexural motions of plates. Herrmann (1956) solved the set of nonlinear equilibrium equations for various problems of flexural vibrational motion of plates found that it was important to account for the large deflections in order to predict such motions.

Yang, Norris, and Stavsky (1966) provided early work on nonlinear deformations in heterogeneous plates. Their theory was a generalization of a theory developed by Mindlin (1951). Mindlin's theory included the effects of rotary inertia and shear deformation on deflection of homogeneous, isotropic plates. Reddy (1980) developed a penalty plate-bending element based on the Yang, Norris, and Stavsky (1966) theory, and successfully used the element to analyze a number of plate problems.

However, all the theories mentioned above were restricted to unimodular linear elastic analysis. Jones and Morgan (1980) solved the equilibrium equations for cross-ply laminates exhibiting different moduli in tension and compression. They solved these equations with an iterative technique to keep track of the changing neutral surface. Reddy (1980) considered a general bimodulus laminated plate using finite elements. However, the analyses by Jones and Morgan (1980) and Reddy (1980) both were limited to small deflections. Turvey (1982) used a dynamic relaxation finite element method to study the nonlinear (in the von Karman sense) flexure of bimodulus composite strips.

The aforementioned studies deal either with small deformations or moderately large deformations in the von Karman sense. However, the problem considered in this study involves deflections several orders of magnitude greater than the thicknesses of the beams. Thus, the theories discussed above were not wholly applicable to this problem, although they provided a great deal of information on nonlinear finite element techniques. Yang (1972) presented an incremental, corotational procedure for very large deformation analysis of isotropic, homogeneous beams. This procedure involves solving the equilibrium equations incrementally, updating the geometry after each increment. In the current study, Yang's (1972) procedure was extended to incorporate a generally anisotropic beam with nonlinear stress-strain properties. Some effort was made to include the effects of width-wise deformations of the beams. The development of this finite element model is detailed in Chapter 6. The results obtained from this model are presented in Chapter 7. Also, the width-wise response of the composite beam element was investigated. Additionally, several failure criteria were applied to the analytical results in an attempt to predict laminate failure. These issues are also discussed in Chapter 7.

Finally, Chapter 8 includes conclusions derived from the study and some recommendations for future work in this area.

2.0 Experimental Procedure

The basic beam loading configuration used in this study is shown schematically in Figure 1. The detail dimensions for the loading situation are also shown in this figure. This is the same loading used by Derian and Hyer (1986). The beam is loaded in a beam-column fashion with a small eccentricity to promote bending. The downward load was applied at the top of the beam which was free to move vertically. The bottom end of the beam did not move. Both ends of the beam were hinged to allow free rotation. Static tests were conducted on a standard screw-driven load frame, while the dynamic tests were conducted on a drop tower designed specifically for this testing.

It should be noted that the magnitudes of the bending strains in this load configuration are several orders of magnitude greater than the strains due to the axial compressive load. Thus, the beam is, effectively, in a state of pure bending.

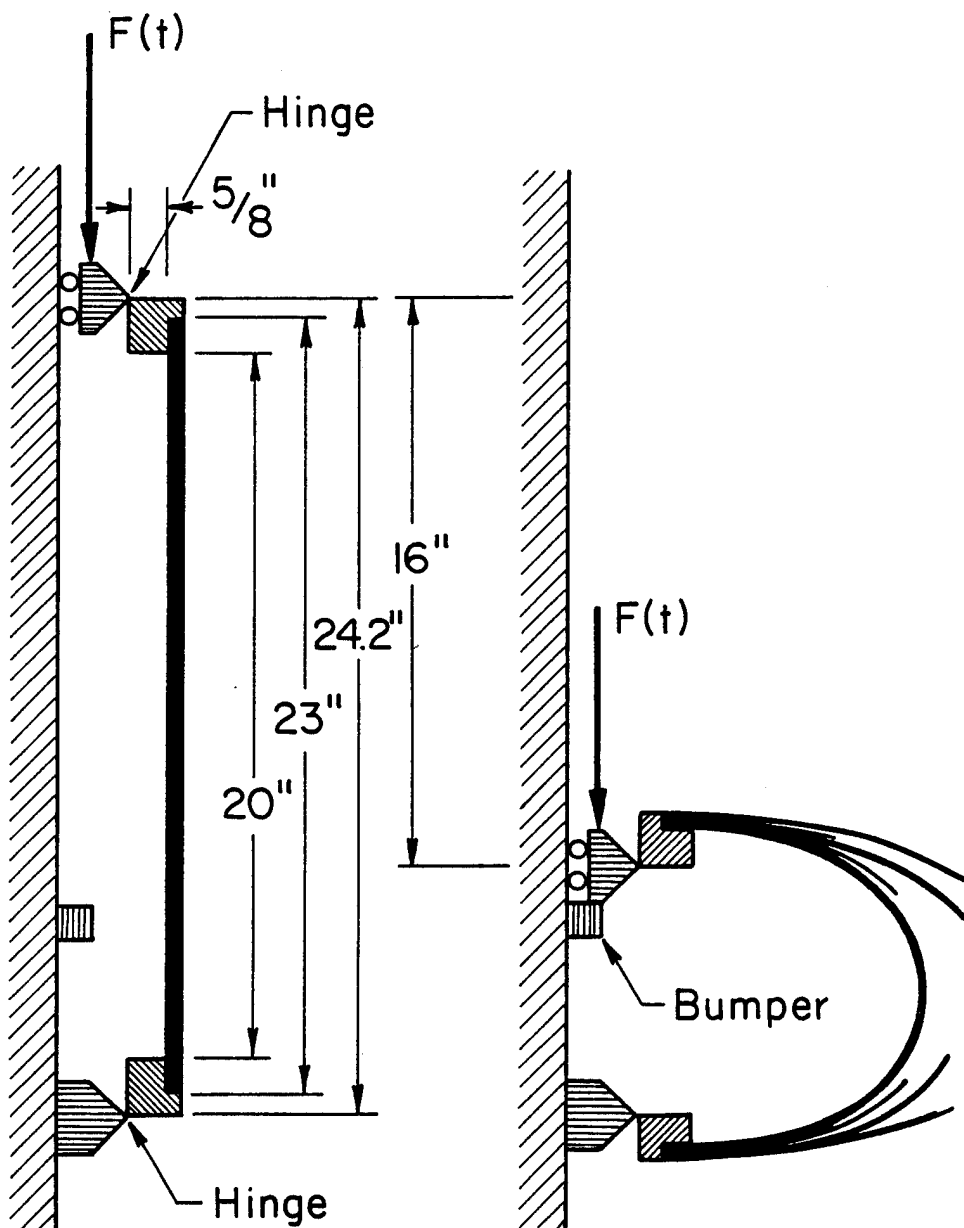


Figure 1. Basic load configuration

2.1 Beam Specimens

The material used in this study was AS4/3502 graphite/epoxy. The layups for the laminates tested are shown in Table 1 on page 9. The laminates were fabricated by the National Aeronautics and Space Administration's Langley Research Center using pre-preg tape. A 16 by 24 inch (40.6 by 61.0 cm) panel was made for each laminate. From each panel, six 2 by 23 inch (5.08 by 58.4 cm) beams were cut. These beams were C-scanned to detect manufacturing defects. Each beam was assigned a number, e.g. P3-1. The 'P' signifies that the beam was from this new material batch rather than a specimen used by Derian and Hyer (1986). The number after the 'P' refers to the panel, or laminate, from which the beam was cut. The number after the dash refers to the specific beam cut from that panel. For example, specimen P3-1 is the number 1 beam cut from the $[(30/0/-30)_5]_s$ panel.

There were three basic groups of laminates considered in this study. First, some specimens remaining from the study by Derian and Hyer (1986) were tested. These were laminates A1 through A5. For further details on these beams, see that reference. Second, some replicates of layups used by Derian and Hyer were made from the new material batch. These were laminates B1 through B3. The purpose of these first two groups was to assess the effects of the changes in the dynamic fixture and to assess the effects of the two different material batches, respectively.

The third group, laminates C1 through C6, were thinner versions of laminates Derian and Hyer investigated and are typical of a stringer layup. Derian and Hyer studied a family of $[(\theta/0/-\theta)_5]_s$ laminates, with θ increasing from 0° to 90° in steps of 15° , to study the effect of the various off-axis ply angles. Laminates C1 through C4 were from a family of $[(\theta/0/-\theta)_3]_s$ laminates with θ increasing from 0° to 45° in steps of 15° . Laminate C5 is a quasi-isotropic layup one-half as thick as the quasi-isotropic laminate considered by Derian and Hyer (1986).

Table 1. Laminate Definitions and Impactor Masses

Laminate number	Panel number	Layup	Number of plies	Impactor weight (lb)
A1 ¹	1	[0] ₃₀	30	47.85
A2 ¹	2	[(15/0/-15) ₅]s	30	39.0
A3 ¹	4	[(45/0/-45) ₅]s	30	25.0
A4 ¹	5	[(60/0/-60) ₅]s	30	25.0
A5 ¹	11	[(45/-45/0/90) ₄]s	32	25.0
B1	P5	[0] ₃₀	30	47.85
B2	P3	[(30/0/-30) ₅]s	30	25.0
B3	P4	[(45/-45/0/90) ₄]s	32	25.0
C1	P1	[0] ₁₈	18	15.4
C2	P6	[(15/0/-15) ₃]s	18	13.2
C3	P7	[(30/0/-30) ₃]s	18	11.0
C4	P8	[(45/0/-45) ₃]s	18	11.0
C5	P9	[(45/-45/0/90) ₂]s	16	11.0
C6	P10	[(45/-45) ₂ /(0) ₈ /(-45/45) ₂]t	16	11.0

¹Laminates remaining from study by Derian and Hyer (1986)

Laminate C6, $[(45/-45)_2/(0)_8/(-45/45)_2]_t$, is typical of stringer layups now being studied for application to composite fuselage structures.

For the remainder of this report, the laminates are referred to by different laminate numbers depending upon the group of which the laminate is a member. Table 1 on page 9 includes the panel number from which the beams were cut as well as the laminate numbers for the present study. For example, the beam referred to above as P3-1 will henceforth be referred to as B2-1.

The width and length of each beam was measured to determine if the dimensions were as specified. Also, the thickness of each beam at its top, center, and bottom was measured using a micrometer. These measurements were then averaged for each laminate type, and the results are listed in Table 2 on page 11.

2.2 Static Test Fixture

The static tests were performed on a standard screw-driven Instron load frame. The hinges used in the dynamic tests were bolted to flat plates and mounted to the heads of the Instron load frame. Figure 2 is a photograph of a specimen being tested in the static fixture. The static test configuration allowed the beams to deflect only about 13 inches (33.0 cm) before the hinges contacted the support plates and the hinged-end conditions were violated. However, this distance was sufficient to load most of the laminates to failure.

Table 2. Dimensions of Beam Specimens

Laminate	Width (in)	Length (in)	Average thickness (in)		
			Top	Middle	Bottom
B1	2.00	23.00	0.1577	0.1697	0.1632
B2	2.00	23.00	0.1635	0.1710	0.1690
B3	2.00	23.00	0.1784	0.1805	0.1748
C1	2.00	23.00	0.0944	0.0992	0.0972
C2	2.00	23.00	0.0989	0.1018	0.1018
C3	2.00	23.00	0.1023	0.1028	0.1025
C4	2.00	23.00	0.1035	0.1038	0.1029
C5	2.00	23.00	0.0912	0.0918	0.0915
C6	2.00	23.00	0.0877	0.0879	0.0885

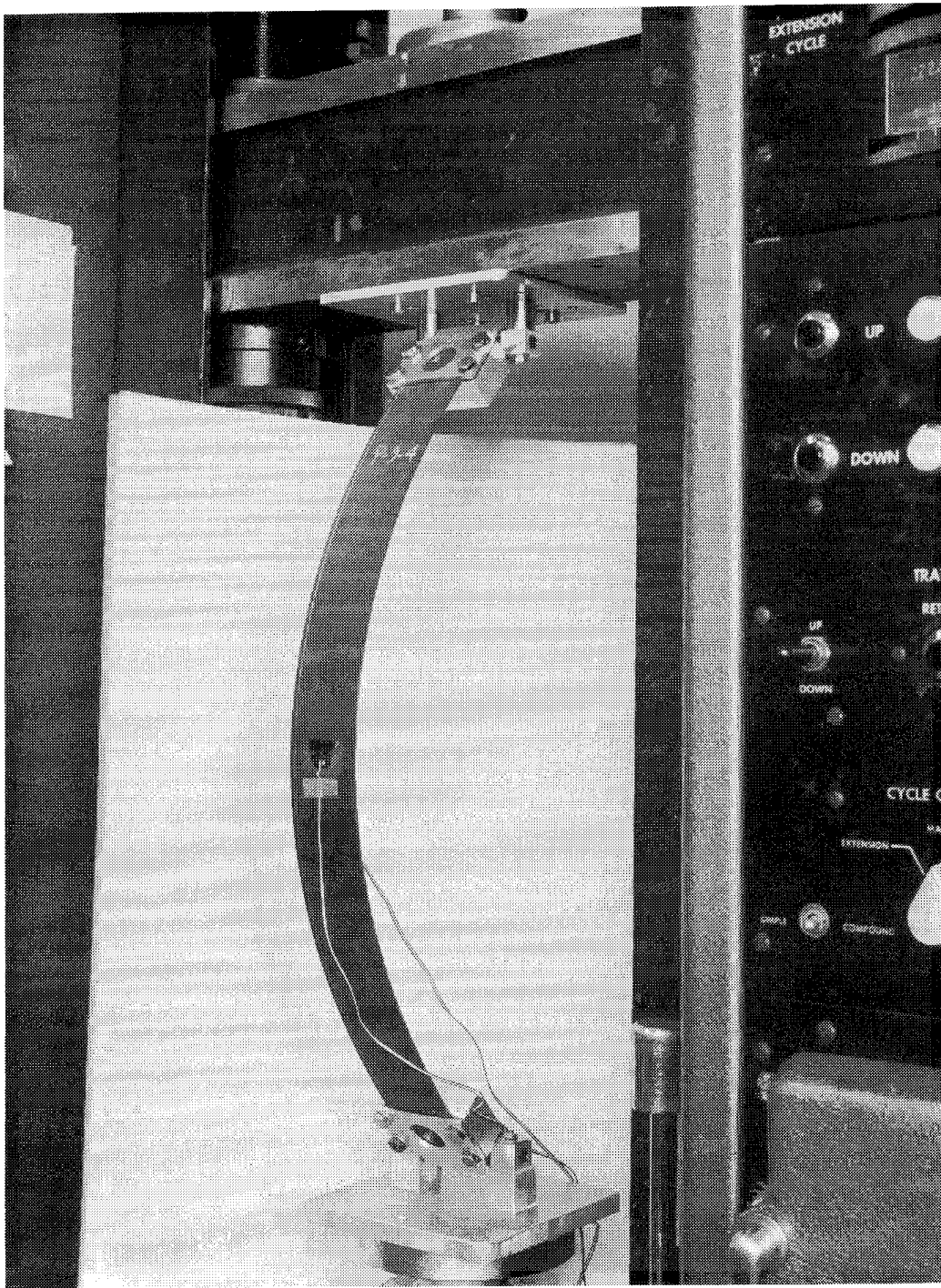


Figure 2. Specimen being statically tested in load frame

2.3 *Dynamic Test Fixture*

A schematic of the drop tower used for the dynamic tests is shown in Figure 3. Four vertical steel rods ten feet long and one inch in diameter were fastened to channels fixed to the floor and a structural support beam of the testing building. The slider which supports the upper hinged-end of the beam specimen slid down the innermost two rods on low-friction linear bearings. Figure 4 shows a schematic of the upper hinge. The mass car slid down the outermost two rods on similar bearings and provided the impact force. The lower hinge was fastened to a load platform. This platform was supported on the lower channel by four vertical load transducers. The outputs from the transducers were added to obtain the vertical end load. Photographs of the drop tower and of an installed specimen are shown in Figure 5 and Figure 6, respectively.

The main difference between the current drop tower and that designed by Derian and Hyer (1986) was the addition of the two outer steel rods. On the fixture used by Derian and Hyer, the mass car and slider both rode on what are currently the two inner steel rods. (The wedge counter weight was also added to the tower.) Another difference between the two fixtures was the positioning of the four piezoelectric load transducers. In the Derian and Hyer fixture, two transducers were placed in each of the two hinge supports. However, in the revised fixture, all four are placed between the load platform and bottom channel. Further, the tower was moved to a different building and supported more rigidly than it had been previously. The drop tower arrangement used by Derian and Hyer is shown schematically in Figure 7.

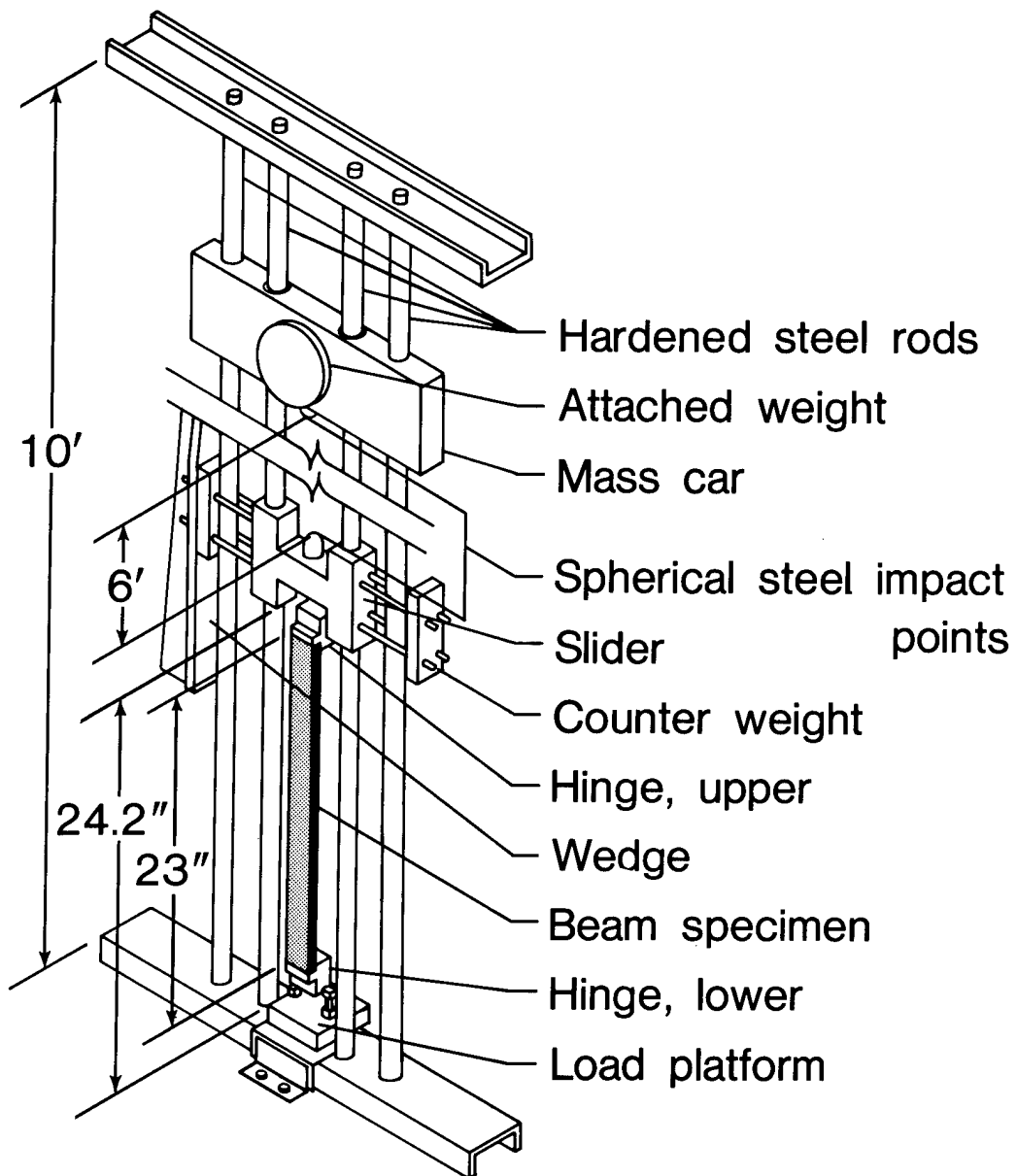


Figure 3. Schematic of drop tower

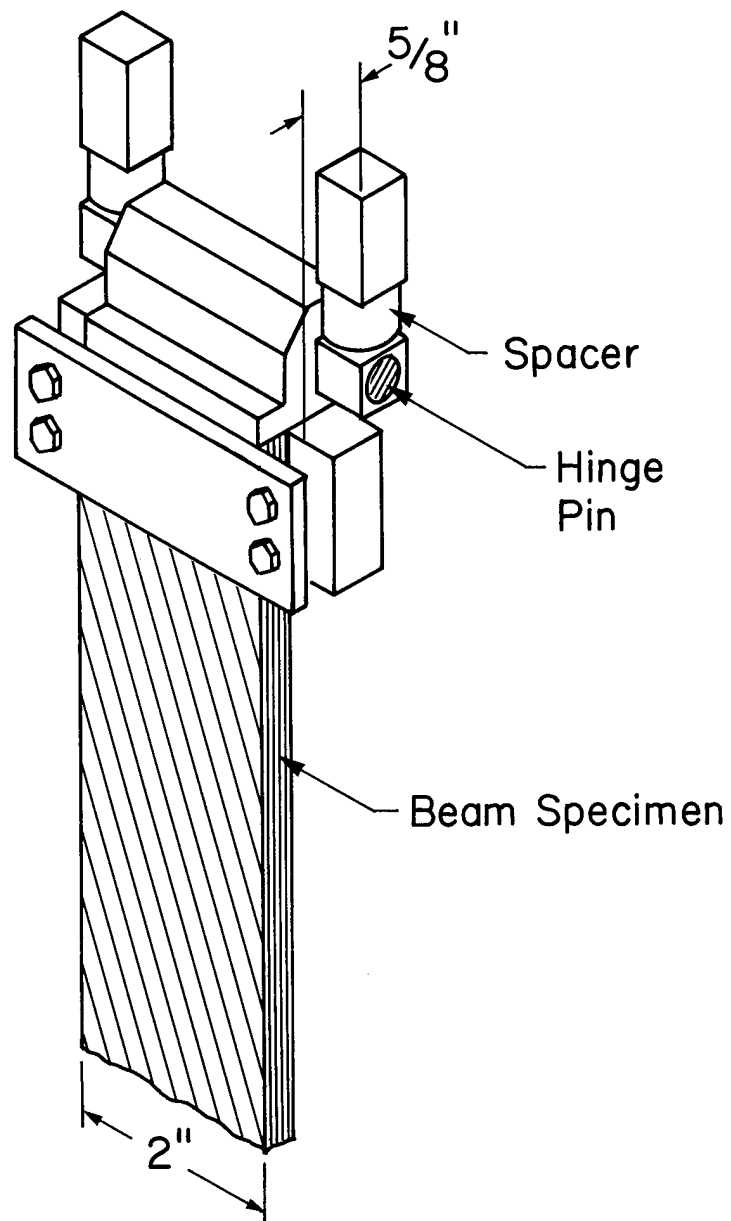


Figure 4. Schematic of upper hinge

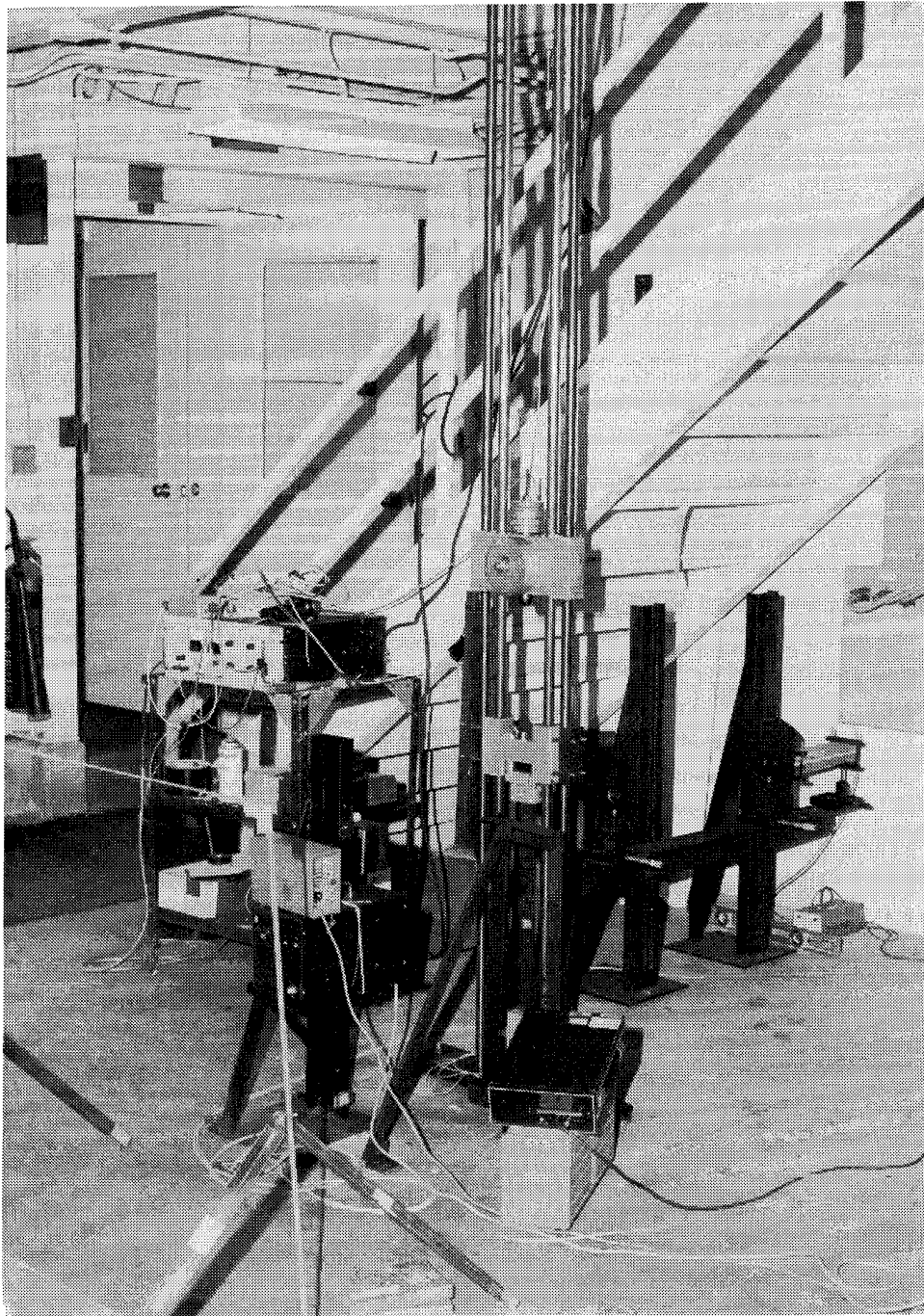


Figure 5. Photograph of drop tower

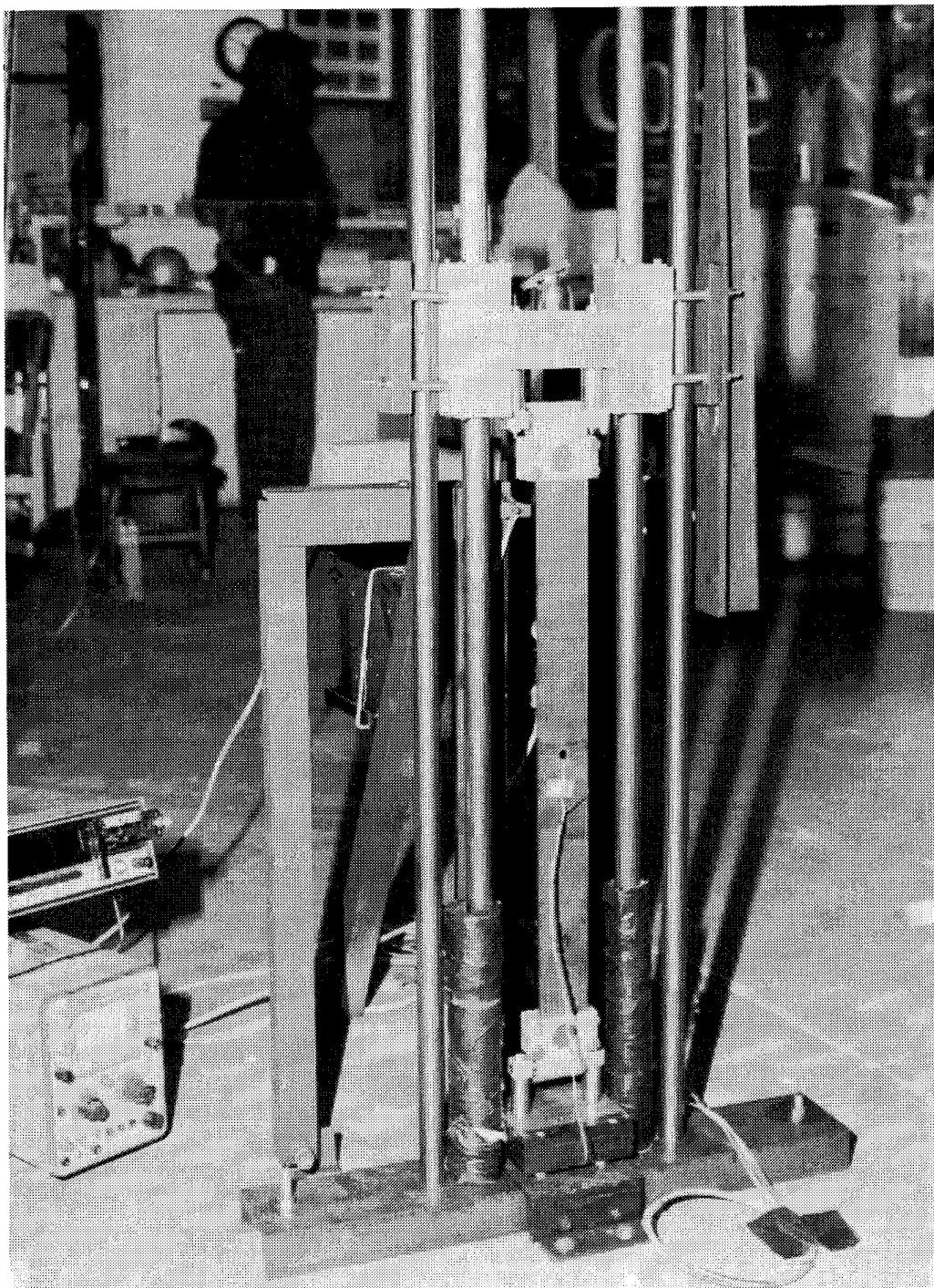


Figure 6. Photograph of specimen installed in drop tower

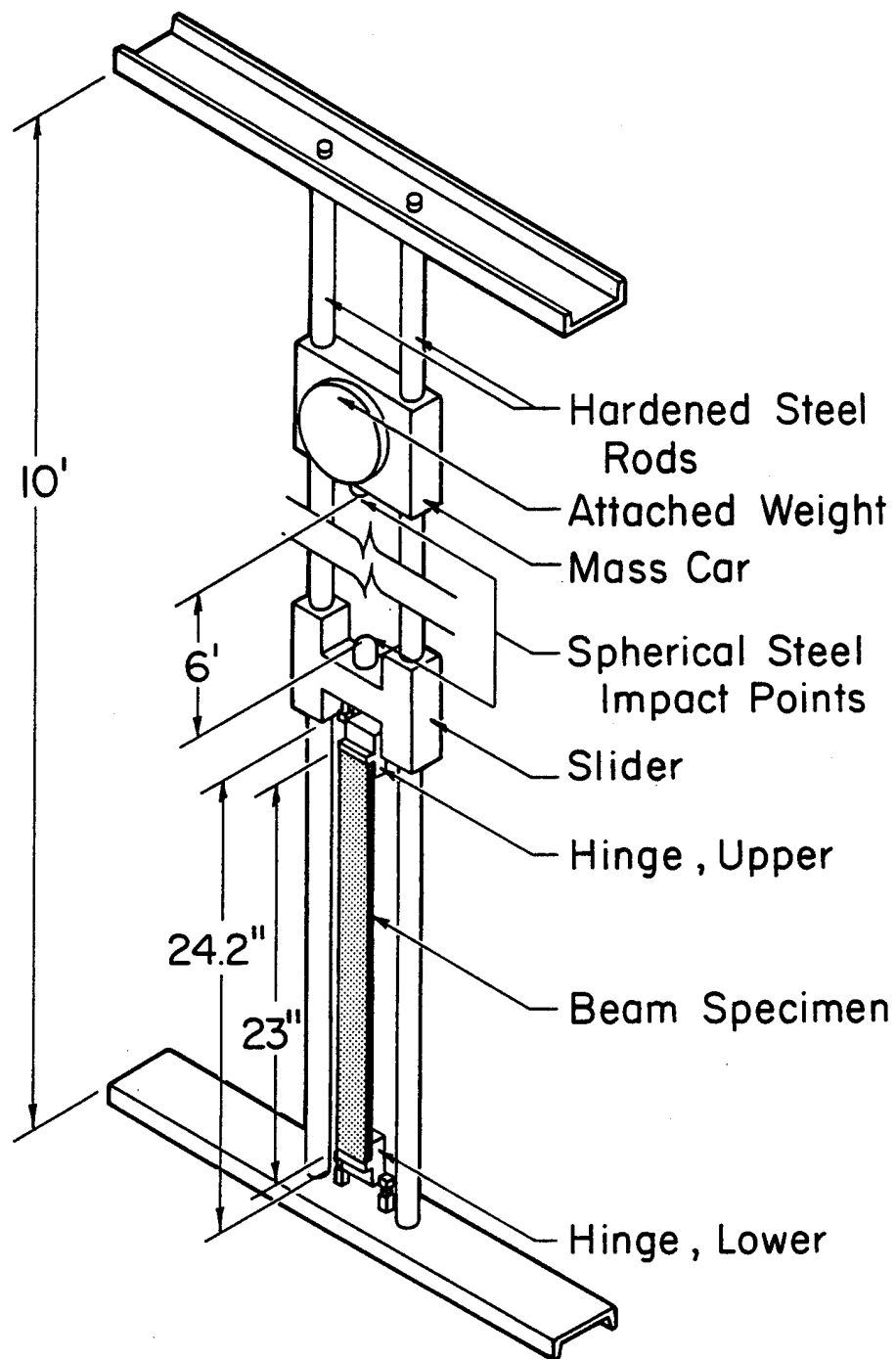


Figure 7. Schematic of drop tower used by Derian and Hyer (1986)

2.4 Data Acquisition

The data acquisition methods for the static and dynamic tests were essentially identical to those used by Derian and Hyer (1986). See pages 18-21 of that reference for a more detailed description of the acquisition systems used. A brief summary of these procedures is given in this section.

2.4.1 Static Tests

The static tests were performed at the National Aeronautics and Space Administration's Langley Research Center. Four data sets were recorded for all the static tests. These were end load, end displacement, and axial surface strains on both sides at the center of the beam. The crosshead speed was set at two inches (5.08 cm) per minute, the maximum allowed by this particular machine. This rate was used to measure end displacement. The end load-end displacement curve was plotted on the Instron chart recorder. The strains were recorded on an X-Y plotter, then manually digitized.

2.4.2 Dynamic Tests

The dynamic tests were performed at NASA Langley Research Center's Impact Dynamics Research Facility. Four data channels were used for most of the specimens tested. These were end load, end displacement, and axial surface strains on both sides at the center of each specimen. One beam of each laminate type also had axial strain gages on both sides at both of the beam quarter-points (total of six strains). One beam of each laminate type had, in ad-

dition to the center longitudinal gages, one transverse strain gage at the center of each side of the beam to investigate Poisson effects and anticlastic curvature (total of four strains).

The dynamic load was measured using the four piezoelectric force transducers below the bottom hinge support block. This signal and the signals from the strain gages were conditioned by amplifiers designed and built at NASA Langley Research Center. The end displacement was measured using a laser optical displacement transducer. An 18 (45.7 cm) inch long tapered bar was fastened to the slider and rode outside the outermost vertical rods. The bar tapered from a two inch (5.08 cm) width at the bottom to a one inch (2.54 cm) width at the top

Derian and Hyer (1986) described this system: "A laser beam, which was diffracted into a horizontal line of light, shined on the front of the bar. Directly behind the tapered bar, a one-inch long array of 1024 light sensitive diodes was mounted horizontally. When the specimen was in the fully upright undeflected position, the bottom of the tapered bar fully shadowed the diode array. As the top of the specimen deflected downward, more and more of the diodes became exposed to the light. When the specimen traveled its full 18 [sic] in. of axial displacement, the entire array was exposed to the laser light. An electronic circuit counted the number of diodes exposed to the laser light. The counter generated an analog signal proportional to the number of the activated diodes. With proper calibration, the optical transducer provided a signal proportional to the vertical end displacement of the beam."

All the dynamic signals were filtered at 1-KHz to remove spurious noise. These signals were converted into FM signals and recorded on magnetic tape. These tapes were then digitized at 4000 samples per second.

2.5 Test Procedures

2.5.1 Static Tests

One specimen for each laminate considered was tested statically to failure or until hinge contact. Derian and Hyer (1986) showed that it was not necessary to repeatedly load to higher end displacements then unload. Except for major failure events, no noticeable energy was lost during loading, so these tests were performed under monotonic loading. The end displacement was continuously increased until the specimen failed or until the hinge contacted, whichever came first.

2.5.2 Dynamic Tests

Three specimens of each laminate considered were tested dynamically to failure. For all the laminates from the new material batch (designated by B or C), specimens with two, four, or six strain gages were used. The six foot drop height used by Derian and Hyer (1986) was also used for these tests. The impactor masses were calculated by determining the amount of work required to deflect the laminates 16 inches (40.6 cm) in the static tests. Twenty percent was added to each of these energies to account for any energy lost in friction. From this energy value, the impactor mass was computed. Table 1 on page 9 presents the impactor mass used for each laminate.

The same test procedure used by Derian and Hyer (1986) was used for the current study. This procedure was: "Before any tests were attempted, calibration signals, corresponding to known levels of physical quantities, were recorded on each channel to facilitate digitization.

With the impactor mass in place, the specimen was clamped into the hinges and the instrumentation was connected to the recorders. Next, all the transducers were balanced and zeroed. A 10 sec. countdown procedure was used wherein at 5 sec. the FM tape recorder was activated and at 1 sec. the movie camera was started. Finally, at time zero, the mass was released and the dynamic load, strain, and displacement histories were recorded."

3.0 Experimental Results

3.1 Static Tests

The load-displacement and surface strain-displacement results for the static tests are presented in this section. As previously mentioned, the data is presented up to the point of failure or the point of hinge contact, whichever occurred first.

3.1.1 $[0]_{30}$ Laminate

The end load-end displacement and surface strain-end displacement relations for the $[0]_{30}$ beam are shown in Figure 8. This laminate suffered one catastrophic failure event resulting in total loss of load-carrying capacity. As was observed by Derian and Hyer (1986), the magnitude of the compressive side surface strain was higher than that of the tensile side surface strain. The percent difference between these values increases until failure. At one inch (2.54 cm), this difference was about nine percent. Just prior to failure, the difference was about 13 percent. The percent difference is defined as:

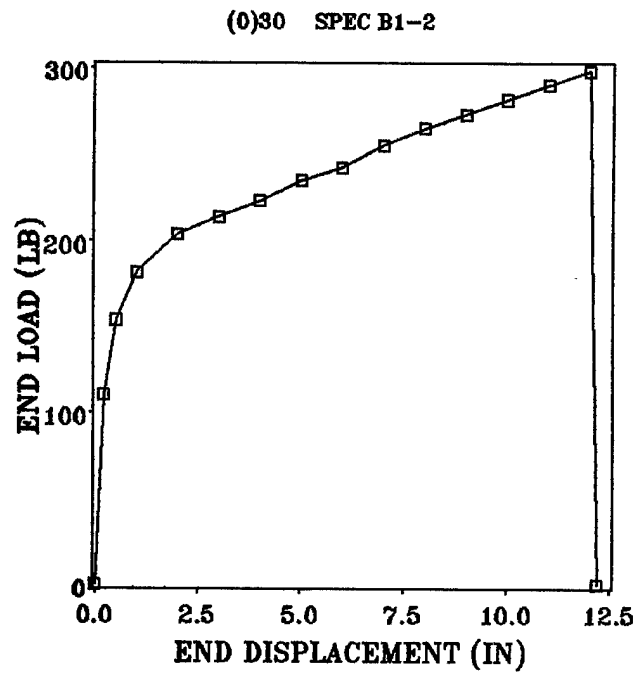
$$\text{Percent difference} = \frac{|\epsilon_c| - \epsilon_t}{\epsilon_t} \times 100 \quad (3.1)$$

3.1.2 [(30/0/-30)₅]s Laminate

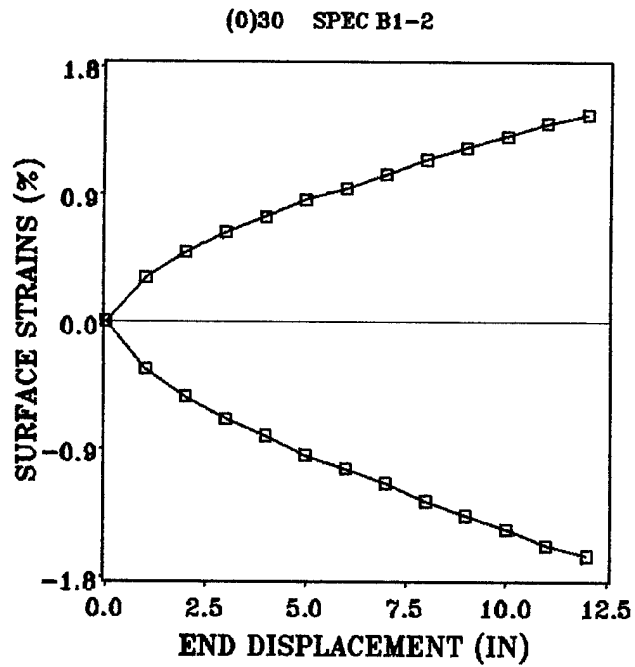
The end load-end displacement and surface strain-end displacement relations for the [(30/0/-30)₅]s are shown in Figure 9. This laminate suffered three major failure events resulting in almost total loss of load carrying capacity. In addition to these events, numerous audible damage events occurred during the test. The difference between the surface strain magnitudes on the tensile and compressive sides of the beam were very large. This was also observed by Derian and Hyer (1986). At 0.5 inches (1.27 cm) of end displacement, the percent difference between these strain magnitudes was about 11 percent. This difference increased to about 30 percent just prior to the first major failure event.

3.1.3 [(45/-45/0/90)₄]s Laminate

The end load-end displacement and surface strain-end displacement relations for the [(45/-45/0/90)₄]s are shown in Figure 10. This laminate suffered one major failure event resulting in a loss of almost 90 percent of load carrying capacity. Numerous audible damage events occurred during the test. The difference between the surface strain magnitudes on the tensile and compressive sides of the beam were large, as was also observed by Derian and Hyer (1986). At one inch (2.54 cm) of end displacement, the difference between these strain magnitudes was about 5.4 percent. This difference increased to about 21 percent just prior to failure.

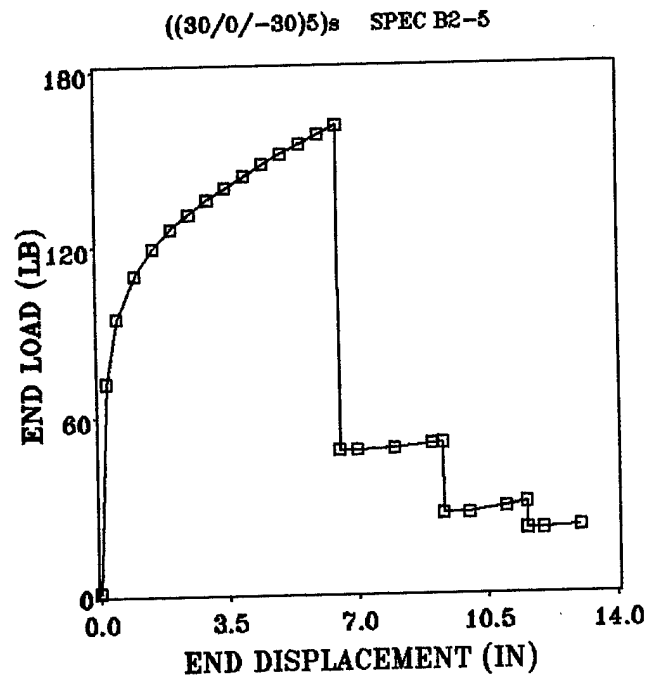


(a) End load versus end displacement

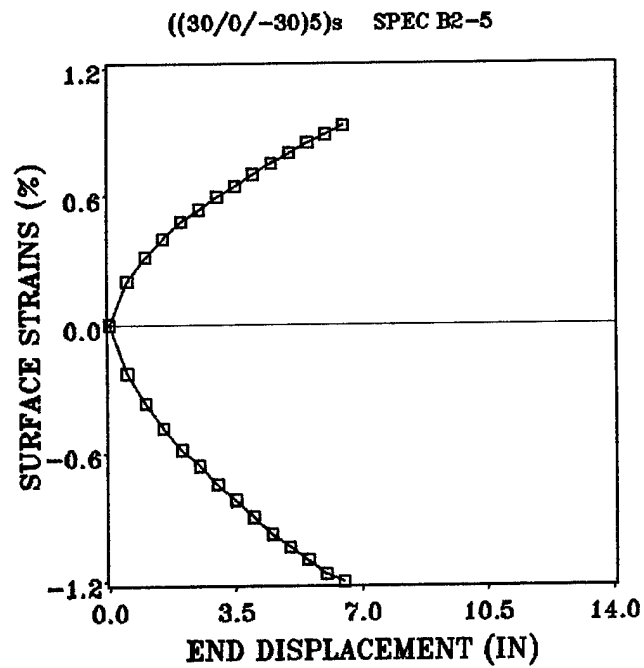


(b) Surface strains versus end displacement

Figure 8. Static load and strain response for $[0]_{30}$ Laminate

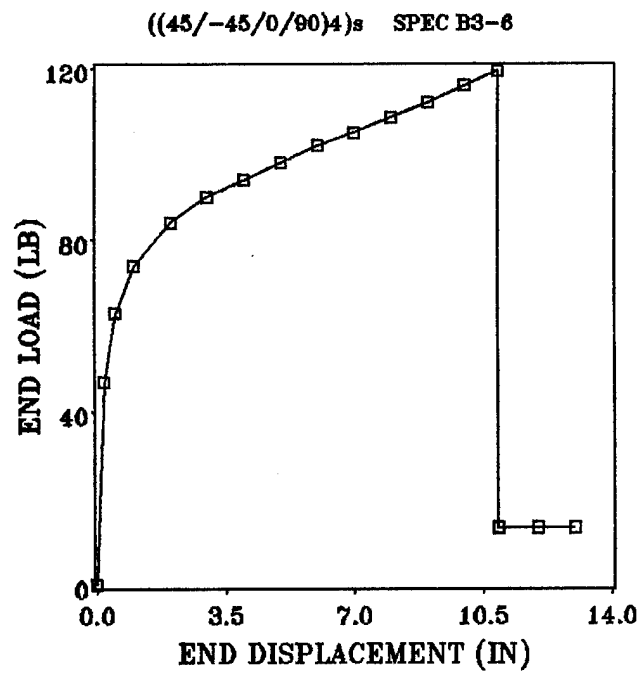


(a) End load versus end displacement

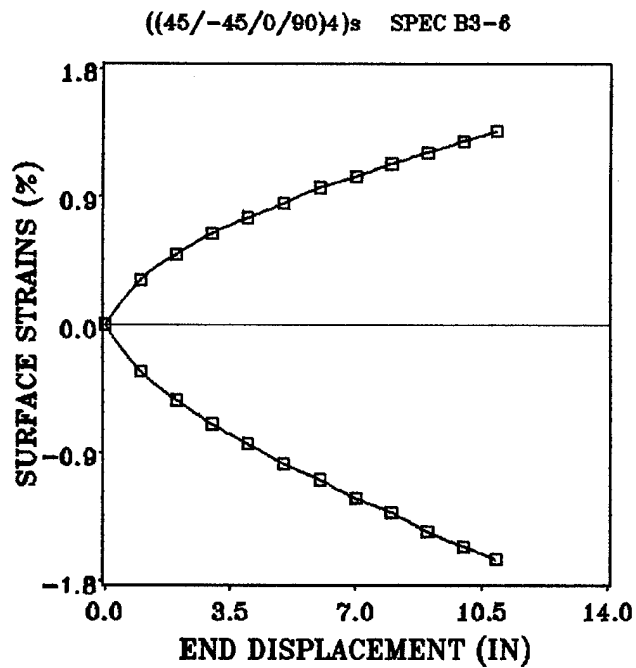


(b) Surface strains versus end displacement

Figure 9. Static load and strain response for [(30/0/-30)₅]_s Laminate



(a) End load versus end displacement



(b) Surface strains versus end displacement

Figure 10. Static load and strain response for [(45/-45/0/90)₄]_s Laminate

3.1.4 $[0]_{18}$ Laminate

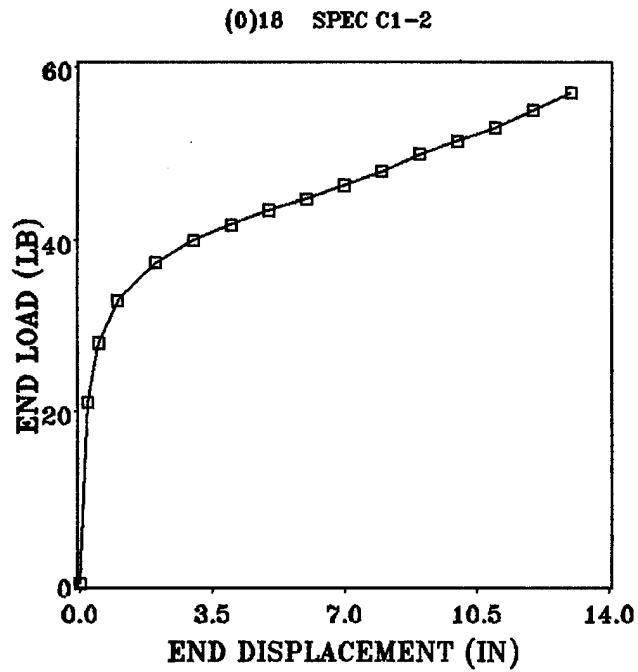
The end load-end displacement and surface strain-end displacement relations for the $[0]_{18}$ laminate are shown in Figure 11. Hinge contact occurred in this test prior to any failure causing loss of load-carrying capacity. Visual inspection of the beam did not reveal any noticeable damage prior to hinge contact. The difference between the surface strain magnitudes for the $[0]_{18}$ beam was smaller than in the thicker beams [30-32 plies]. At 0.5 inches of end displacement, the difference was only about six percent. This difference remained approximately constant throughout the remainder of the test.

3.1.5 $[(15/0/-15)_3]_s$ Laminate

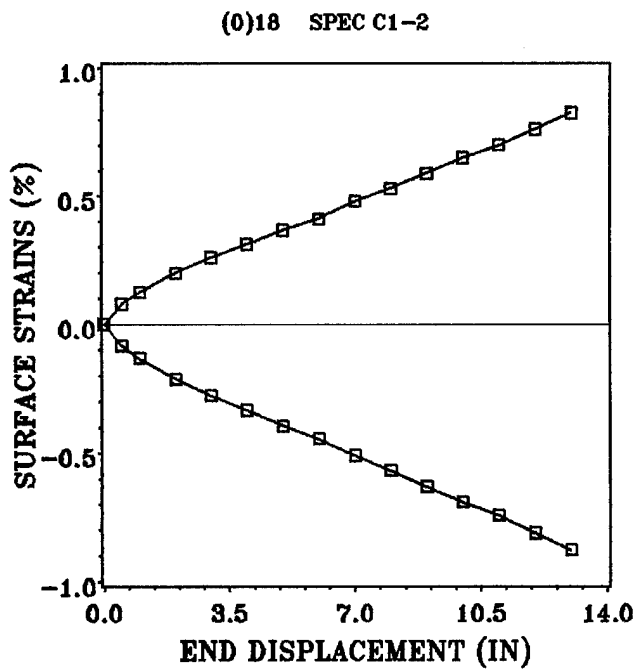
The end load-end displacement and surface strain-end displacement results for the $[(15/0/-15)_3]_s$ are shown in Figure 12. There were two noticeable failures in this laminate prior to hinge contact. However, the total loss in load was only about 11 percent. The strain magnitude difference in this laminate exhibited characteristics different from the other beams tested. The difference was about 11 percent at 0.5 inches (1.27 cm) of end displacement, decreasing gradually to about five percent just prior to the initial failure event.

3.1.6 $[(30/0/-30)_3]_s$ Laminate

The end load-end displacement and surface strain-end displacement relations for the $[(30/0/-30)_3]_s$ are shown in Figure 13. The upper hinge contacted the support plate prior to any failure that resulted in load-carrying loss in the laminate. There were several audible damage events during loading that did not cause a noticeable loss in load-carrying capacity.

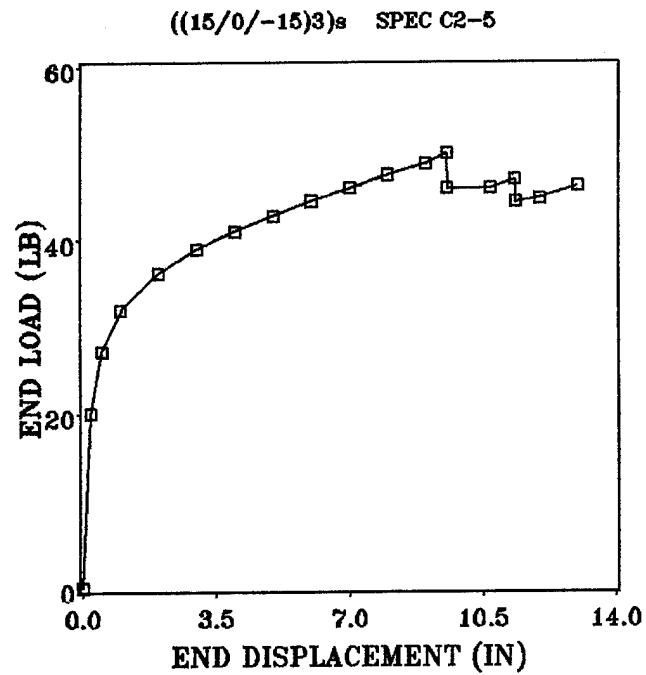


(a) End load versus end displacement

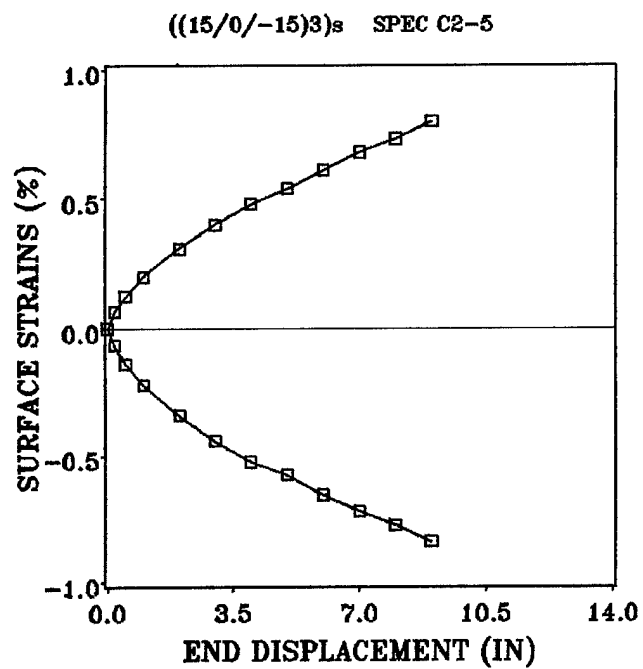


(b) Surface strains versus end displacement

Figure 11. Static load and strain response for [0]₁₈ Laminate



(a) End load versus end displacement



(b) Surface strains versus end displacement

Figure 12. Static load and strain response for [(15/0/-15)₃]_s Laminate

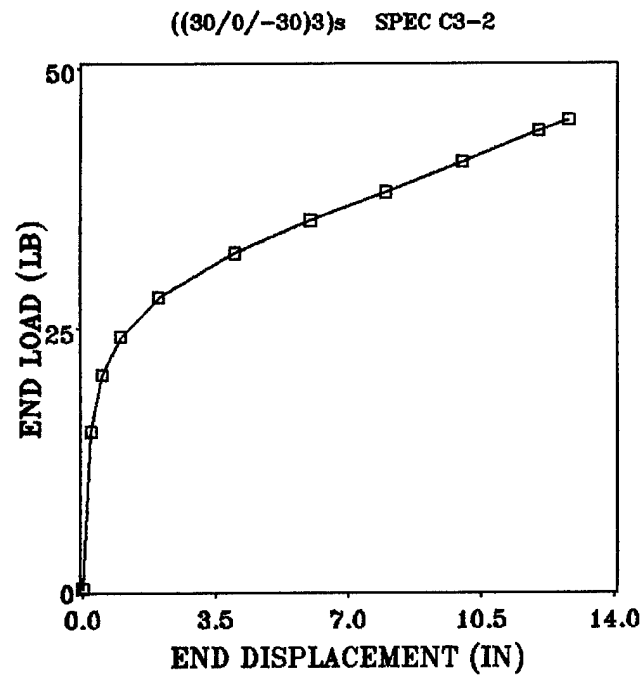
The surface strain magnitude difference is approximately 14 percent at 0.5 inches (1.27 cm) of end displacement, increases to about 23 percent at four inches (10.2 cm) of end displacement, and then steadily decreases to about 10 percent just prior to hinge contact.

3.1.7 [(45/0/-45)₃]s Laminate

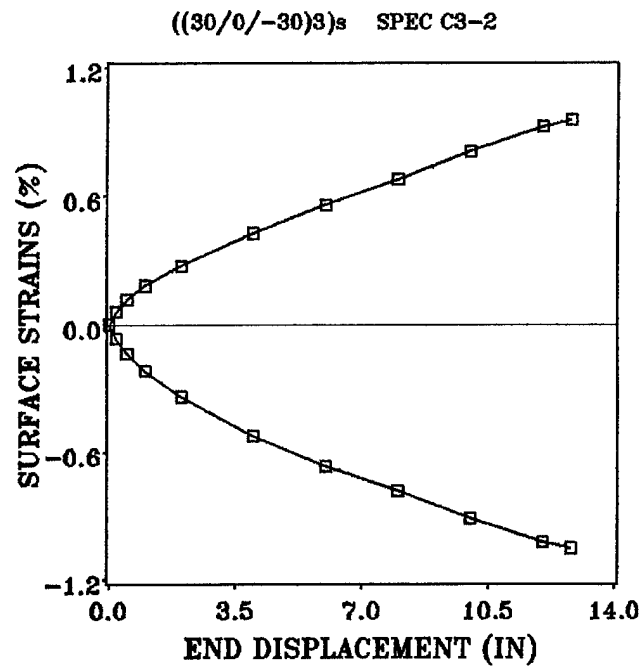
The end load-end displacement and surface strain-end displacement relations for the [(45/0/-45)₃]s are shown in Figure 14. The upper hinge contacted the support plate prior to any failure that resulted in load-carrying loss in the laminate. There were several audible damage events during loading that did not cause a noticeable loss in load-carrying capacity. The surface strain magnitude difference is approximately 17 percent at 0.5 inches (1.27 cm) of end displacement, and increases to about 30 percent just prior to hinge contact.

3.1.8 [(45/-45/0/90)₂]s Laminate

The end load-end displacement and surface strain-end displacement relations for the [(45/-45/0/90)₂]s are shown in Figure 15. The upper hinge contacted the support plate prior to any failure that resulted in load-carrying loss in the laminate. There were no audible damage events during loading. The surface strain magnitude difference is approximately 10 percent at 0.5 inches (1.27 cm) of end displacement, and increases to about 27 percent just prior to hinge contact.

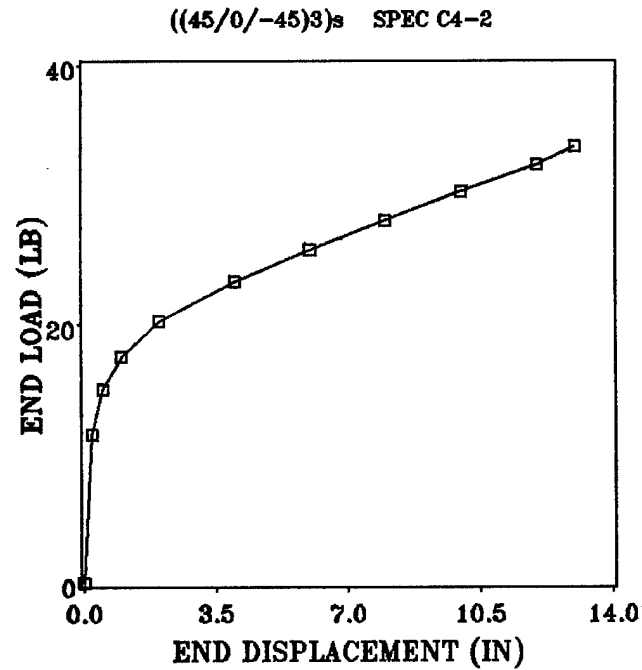


(a) End load versus end displacement

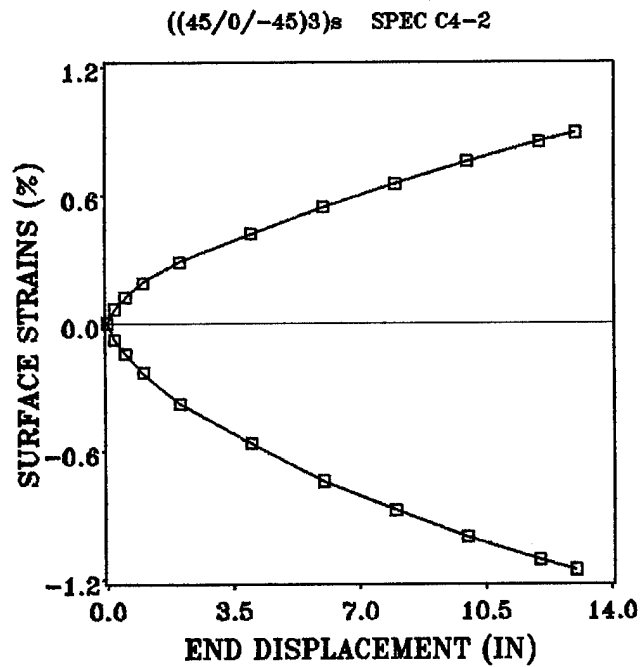


(b) Surface strains versus end displacement

Figure 13. Static load and strain response for [(30/0/-30)₃]_s Laminate

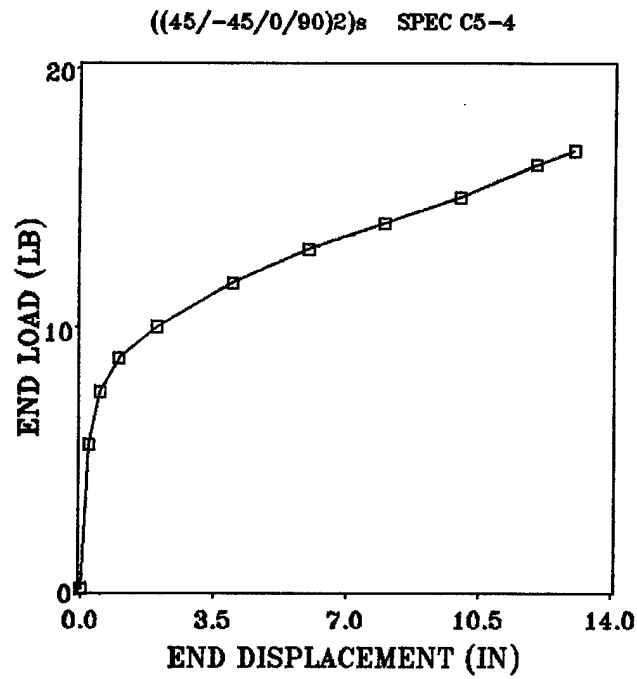


(a) End load versus end displacement

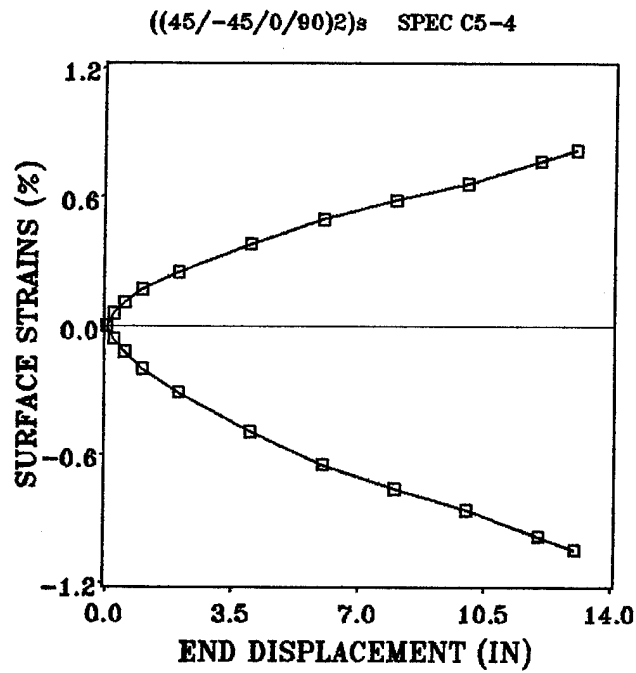


(b) Surface strains versus end displacement

Figure 14. Static load and strain response for [(45/0/-45)₃]_s Laminate



(a) End load versus end displacement



(b) Surface strains versus end displacement

Figure 15. Static load and strain response for [(45/-45/0/90)₂]_s Laminate

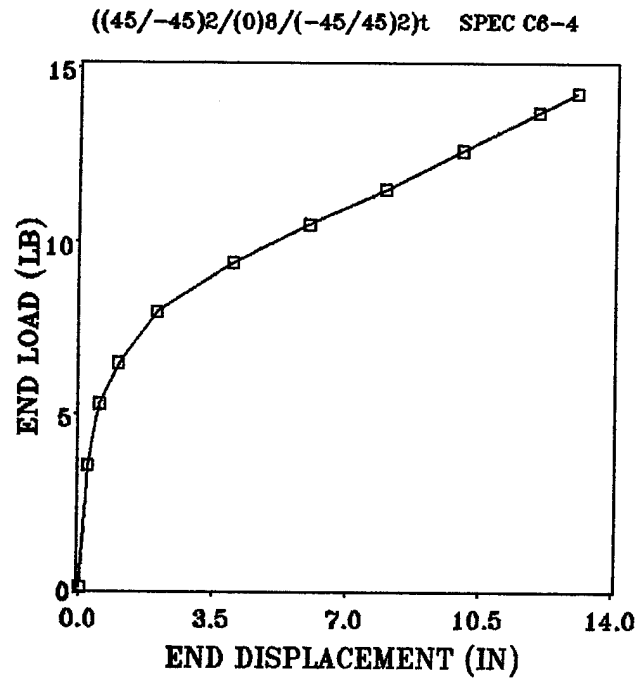
3.1.9 $[(45/-45)_2/(0)_8/(-45/45)_2]_t$ Laminate

The end load-end displacement and surface strain-end displacement relations for the $[(45/-45)_2/(0)_8/(-45/45)_2]_t$ beam are shown in Figure 16. The upper hinge contacted the support plate prior to any failure that resulted in load-carrying loss in the laminate. There were no audible damage events during loading. The surface strain magnitude difference is approximately five percent at 0.5 inches (1.27 cm) of end displacement, increases to about 29 percent at four inches (10.2 cm) of end displacement, then decreases to about 15 percent just prior to hinge contact.

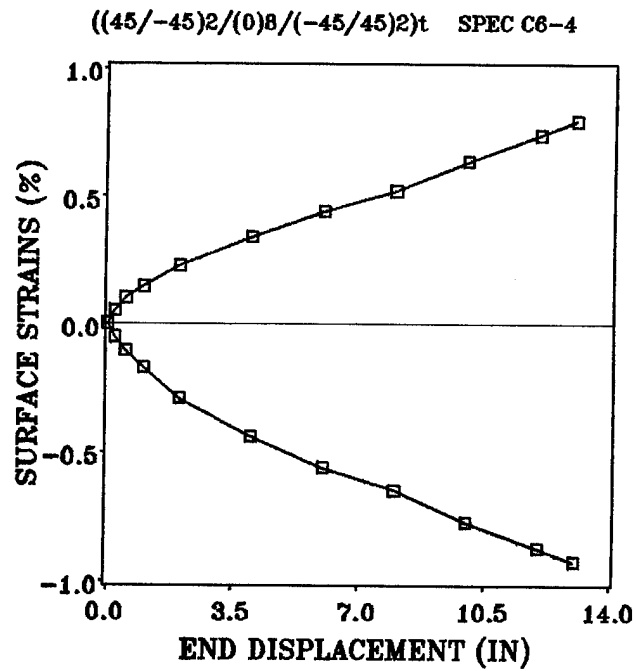
3.1.10 Observations

From these static tests, some observations were made. These are:

1. The difference between the surface strain magnitudes on the tensile and compressive sides of the beams is a real phenomenon. This difference is apparent not only in the tests performed by Derian and Hyer (1986) but also in the current set of tests. Since this difference occurs also for the new material batch, it is not batch-dependent.
2. The strain magnitude difference increases monotonically with end displacement for the thick laminates. However, for some thin laminates, the difference increased up to an end displacement of about four inches (10.2 cm), then decreased slightly during the remainder of the test. The reason for this behavior can not be determined from the test data. It is possible that some type of nonlinear effect, particularly suppression of anticlastic curvature, may be causing this strain response. This issue will be discussed in some detail in Chapter 7.



(a) End load versus end displacement



(b) Surface strains versus end displacement

Figure 16. Static load and strain response for $[(45/-45)_2/(0)_8/(-45/45)_2]_t$ Laminate

3.2 *Dynamic Tests*

The three groups of laminates considered in this study were:

1. Specimens remaining from the study by Derian and Hyer (1986) (laminates A1 through A5)
2. Replicate specimens of layups identical to some laminates studied by Derian and Hyer (1986) (laminates B1 through B3)
3. New, thin layups (laminates C1 through C6) The results from each of these groups are presented in this section.

A number of plots are taken from the study by Derian and Hyer (1986). These plots and the data from that study are referred to as previous results, while the results from the current study are referred to as current results.

3.2.1 **Group One (Laminates A1 through A5)**

The purpose of testing the laminates in Group One was to assess the effects of the changes made in the drop tower test fixture. Since the laminates in Group One remained from the previous study, it was expected that any differences between the current results and the previous results would be a result of fixture modification.

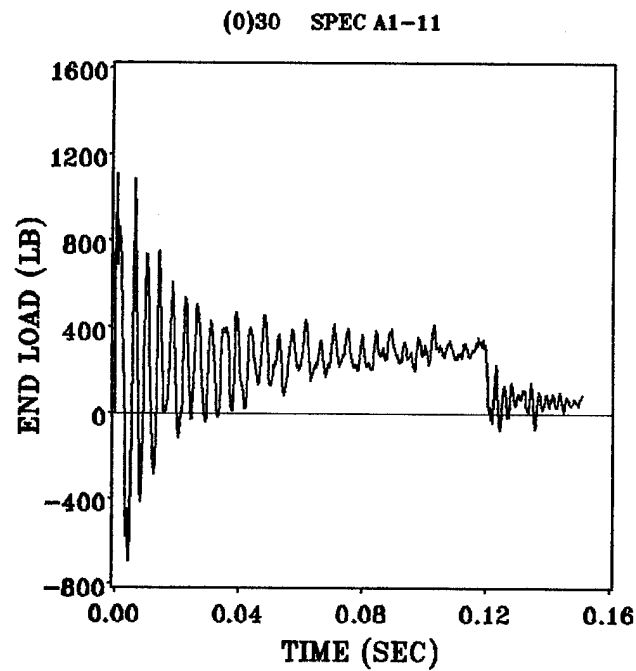
The end load-time and surface strain-time relations for the $[0]_{30}$ laminates from the current and previous study (but all from previous material batch) are shown in Figure 17 and Figure 18, respectively. The end displacement-time relation for the previous and current re-

sults is shown in Figure 19. The legends on the figures from the previous study refer to specimen numbers used by Derian and Hyer. The peak load from the current study was approximately 80 percent of the peak load from the previous study. The natures of the remaining load responses were quite similar, though. The strain responses from the current and previous studies were also quite similar. The end displacement-time responses were almost identical. The noise early in the time history was evident in both the current and previous results. Derian and Hyer (1986) discussed this phenomenon, and concluded that it was probably erroneous data caused by upward motion of the displacement transducer wedge and not actually upward motion of the test specimen. Thus, test fixture changes did not remove this effect. The end displacement-time relations for the remaining laminates in Group One are not shown here, but are presented in Appendix A. The same characteristics are evident in all of these relations.

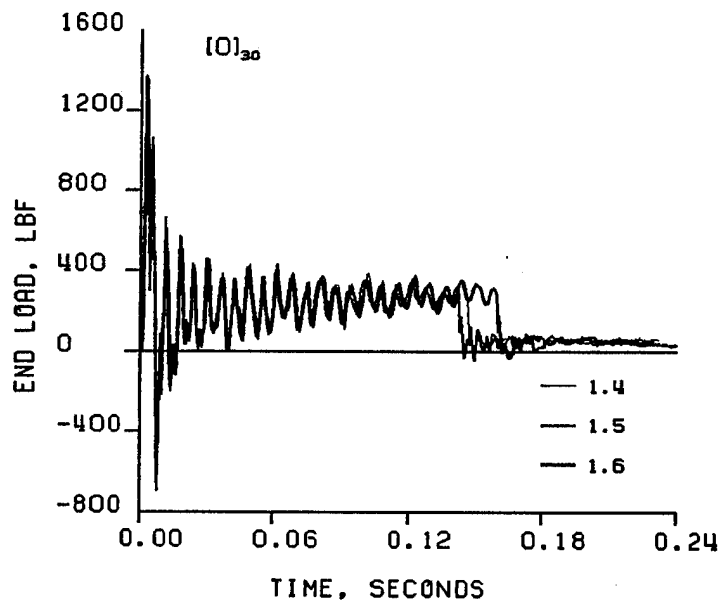
The end load-time and surface strain-time relations for laminates A2 through A4 are shown in Figure 20 through Figure 25. The end load-time relations for laminate A5 are shown in Figure 26. There is no strain-time data for this laminate due to strain gage failure. The peak loads from the current study are consistently lower than the peak loads from the previous study. The surface strain responses are generally quite similar between the previous and current results.

From the dynamic tests conducted with specimens from Group One, some observations were made. These are:

1. The peak loads in the current study were all about 65 to 85 percent of those encountered in the tests conducted by Derian and Hyer (1986). The average peak loads from the previous study are compared to peak loads from the current study in Table 3 on page 50. It is believed that the reductions in peak loads are due to the manner in which load was measured in the two tests. In the current study, load was measured by four piezoelectric load transducers mounted between the base of the drop tower and a lead block. This

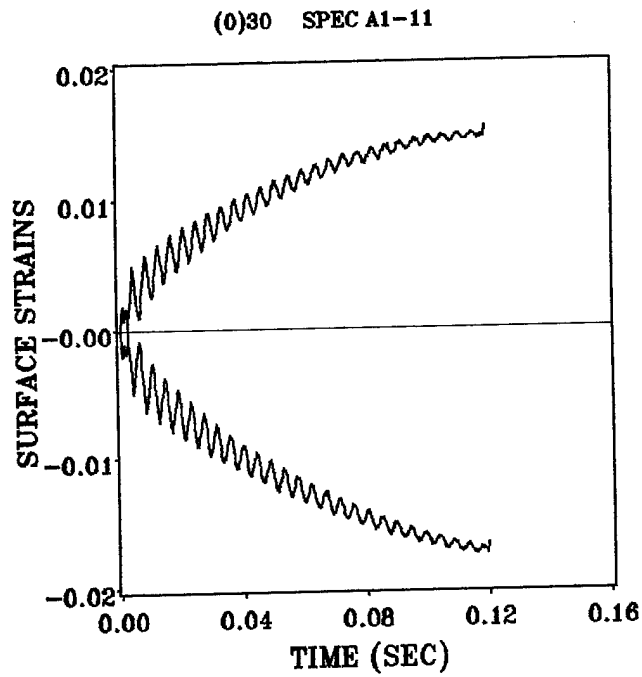


(a) Tested in revised drop tower

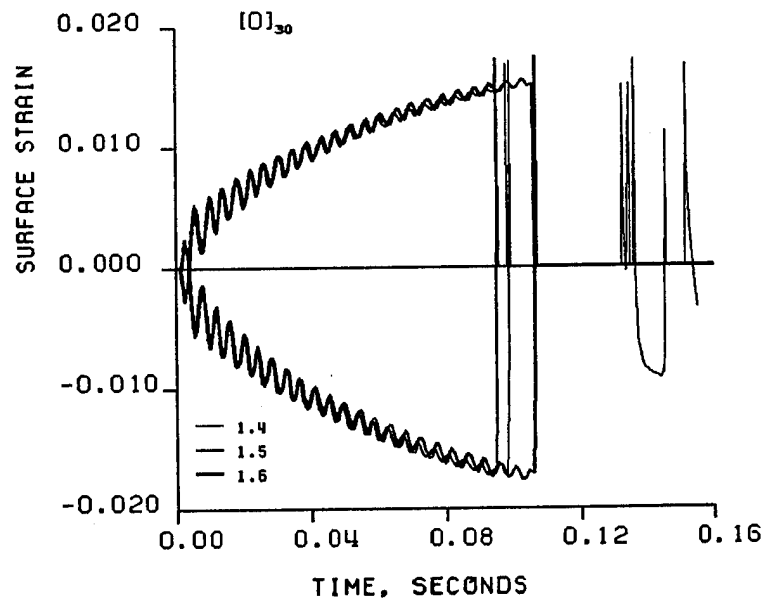


(b) Tested in original drop tower (Derian and Hyer, 1986)

Figure 17. Dynamic load responses for laminate A1



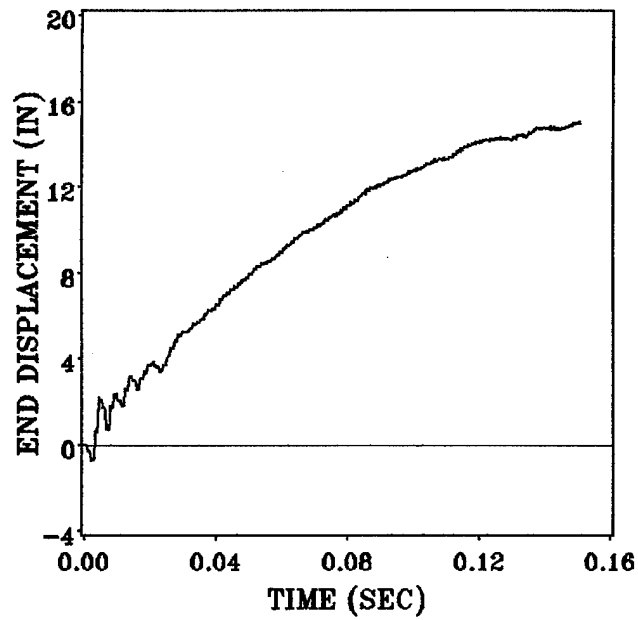
(a) Tested in revised drop tower



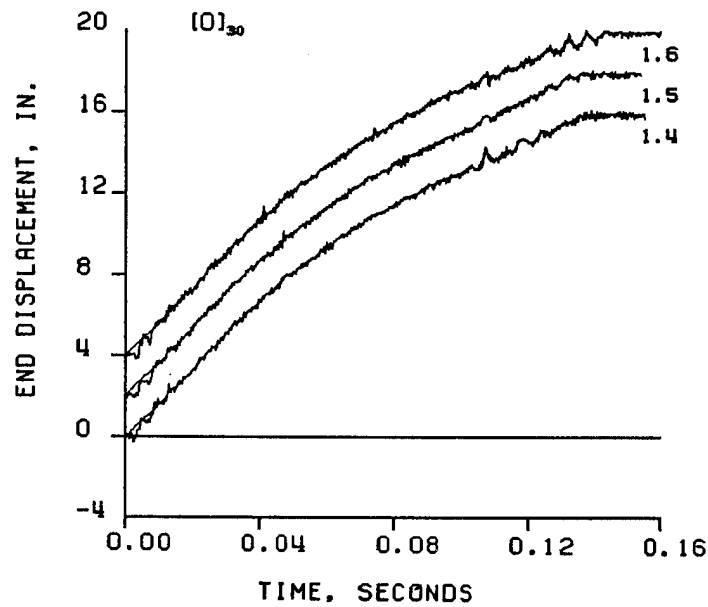
(b) Tested in original drop tower (Derian and Hyer, 1986)

Figure 18. Dynamic strain responses for laminate A1

(0)30 SPEC A1-11

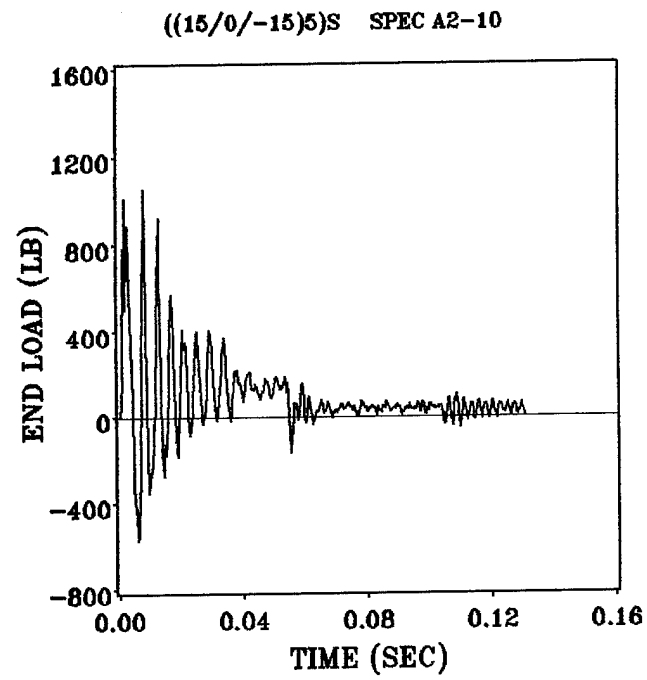


(a) Tested in revised drop tower

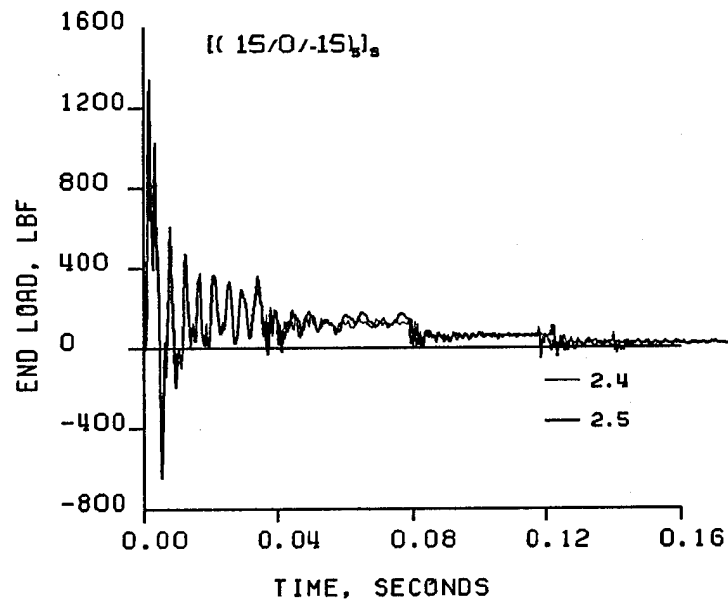


(b) Tested in original drop tower (Derian and Hyer, 1986)

Figure 19. Dynamic displacement responses for laminate A1

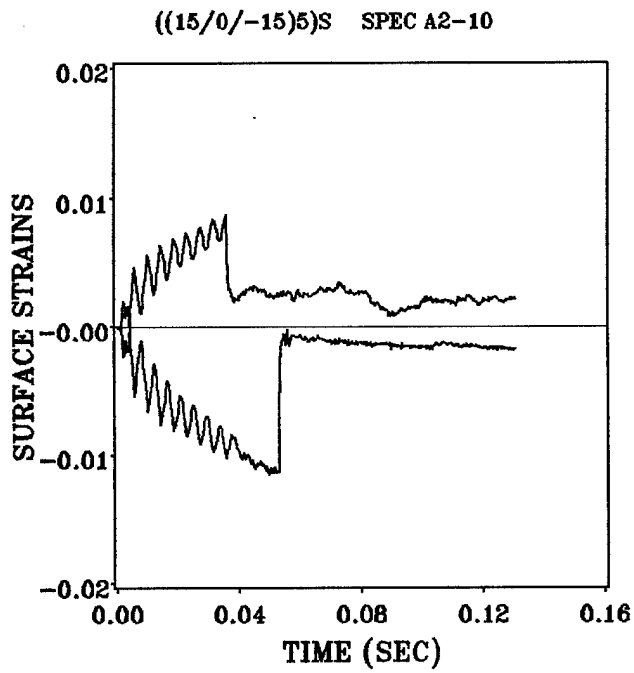


(a) Tested in revised drop tower

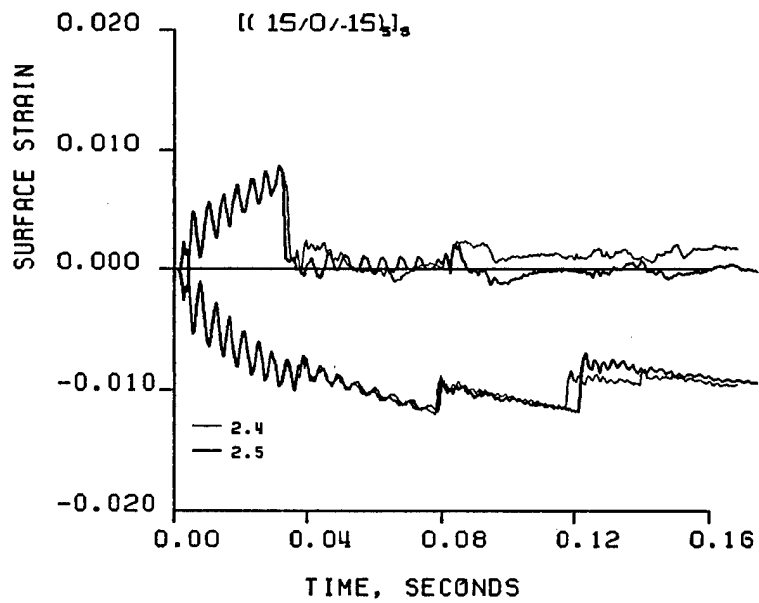


(b) Tested in original drop tower (Derian and Hyer, 1986)

Figure 20. Dynamic load responses for laminate A2

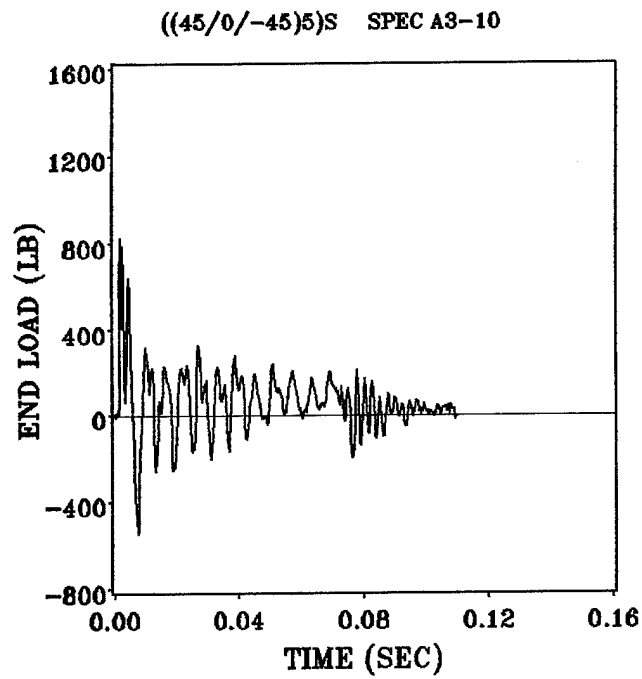


(a) Tested in revised drop tower

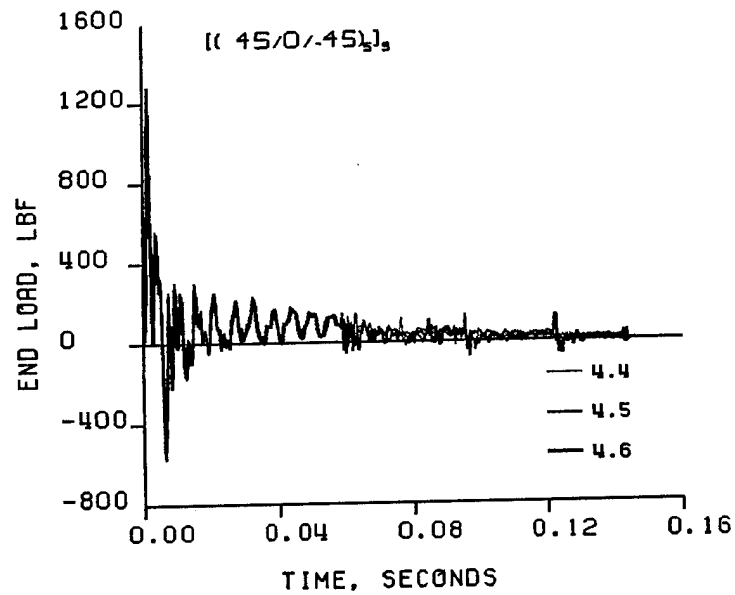


(b) Tested in original drop tower (Derian and Hyer, 1986)

Figure 21. Dynamic strain responses for laminate A2

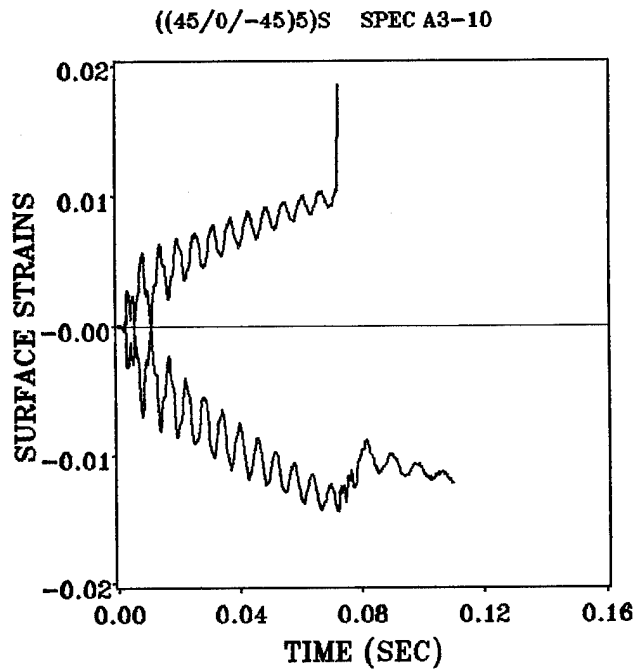


(a) Tested in revised drop tower

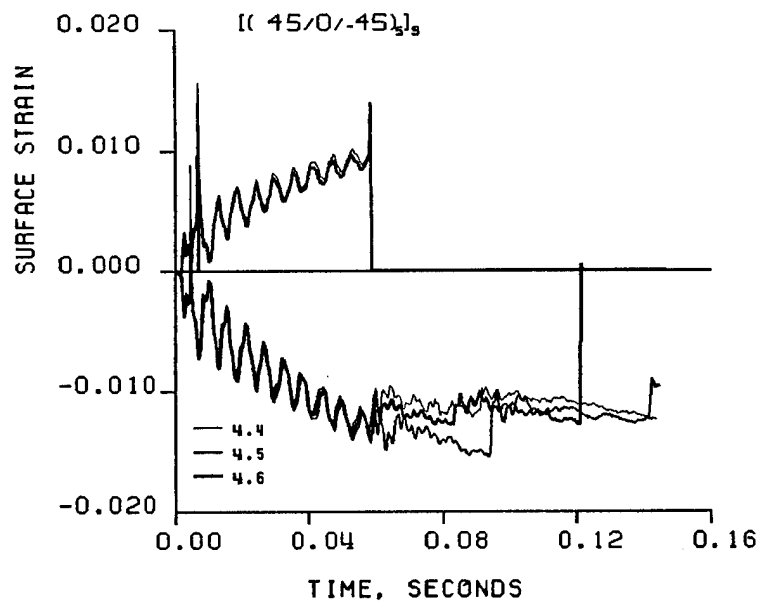


(b) Tested in original drop tower (Derian and Hyer, 1986)

Figure 22. Dynamic load responses for laminate A3

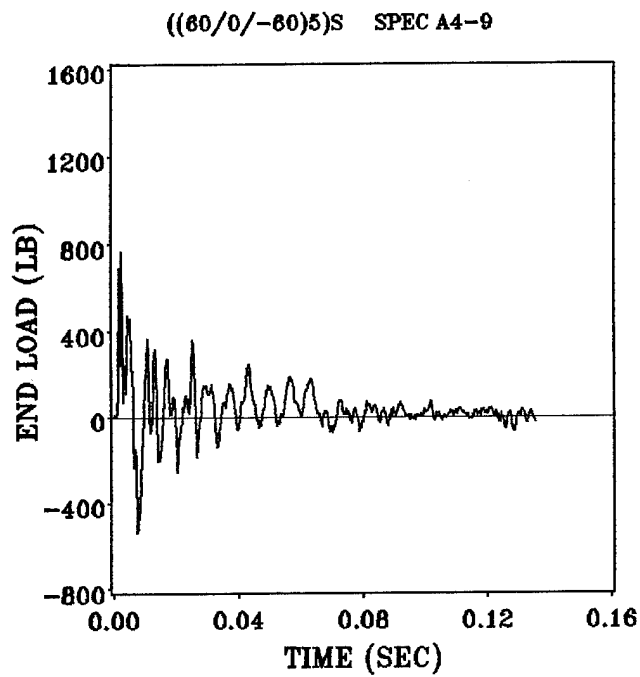


(a) Tested in revised drop tower

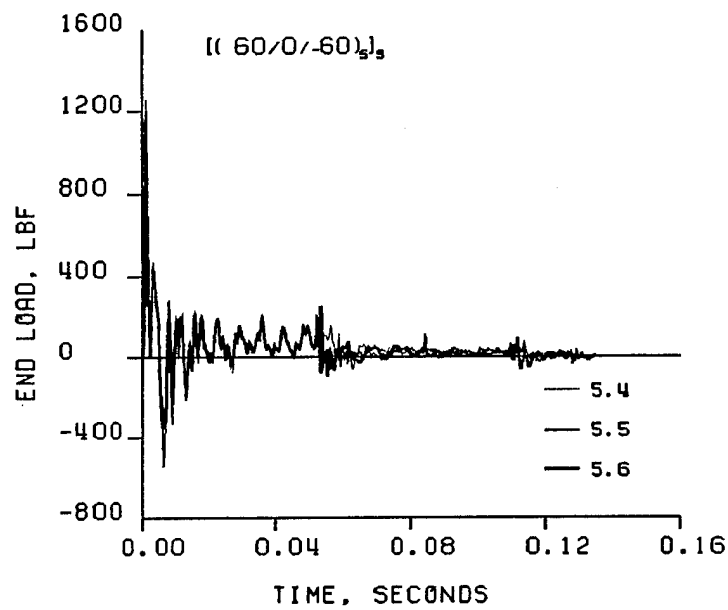


(b) Tested in original drop tower (Derian and Hyer, 1986)

Figure 23. Dynamic strain responses for laminate A3

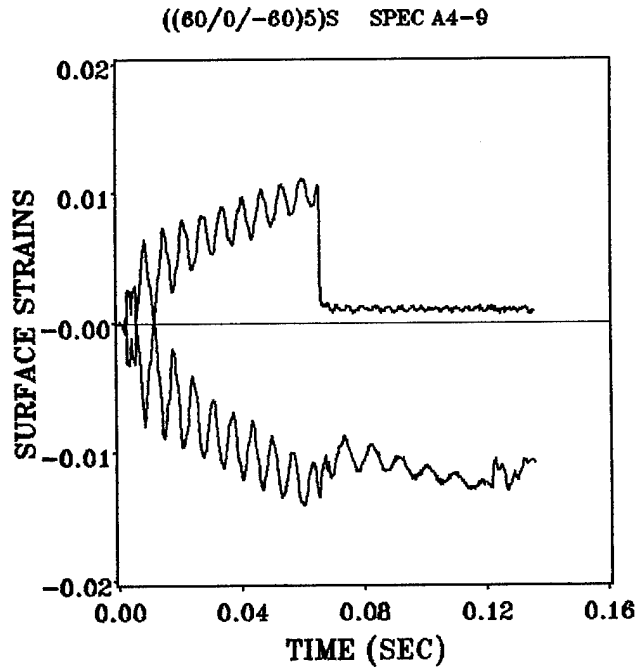


(a) Tested in revised drop tower

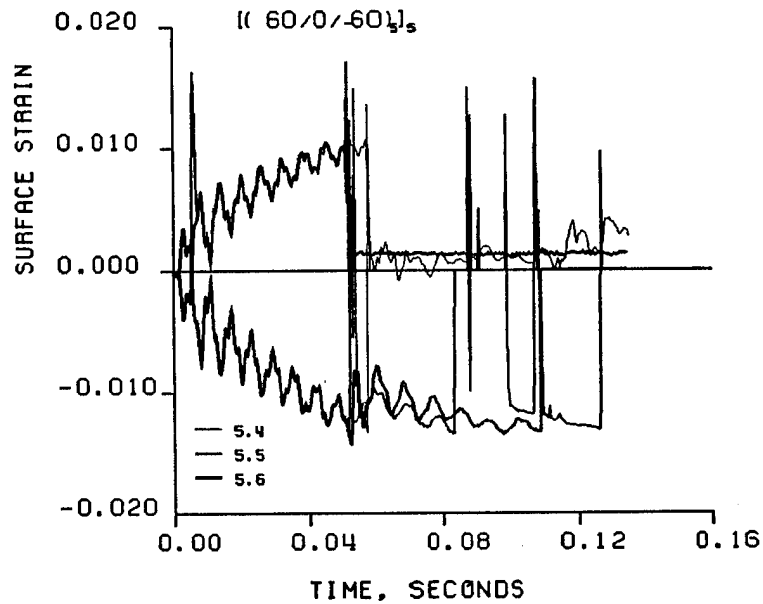


(b) Tested in original drop tower (Derian and Hyer, 1986)

Figure 24. Dynamic load responses for laminate A4

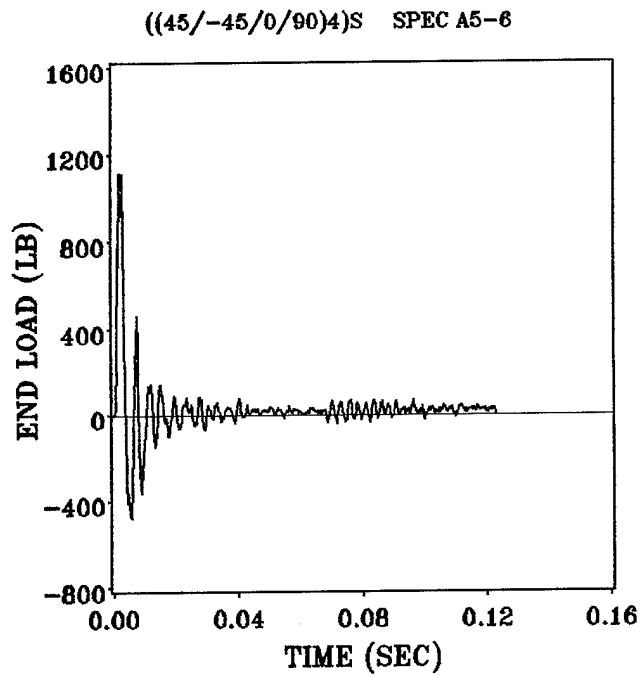


(a) Tested in revised drop tower

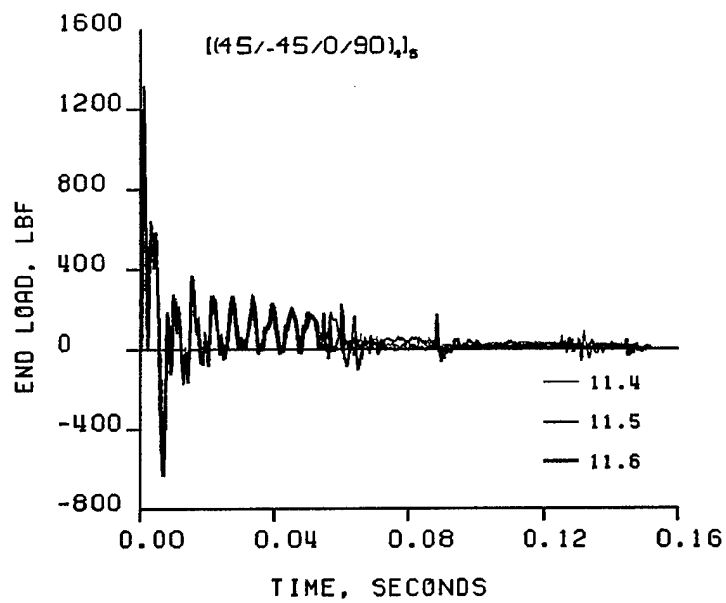


(b) Tested in original drop tower (Derian and Hyer, 1986)

Figure 25. Dynamic strain responses for laminate A4



(a) Tested in revised drop tower



(b) Tested in original drop tower (Derian and Hyer, 1986)

Figure 26. Dynamic load responses for laminate A5

differed from the previous study, in which the load transducers were mounted in the hinge attachments. In the revised tower, it is likely that some of the energy was absorbed by small vibrations in the tower before it could be translated into the load transducers. Furthermore, in the previous study the end load reported was the average of the loads at the top and bottom hinge supports. Since the load in the current study was measured at the bottom of the tower, some of the impactor energy may have been absorbed by axial inertia of the beams, resulting in lower measured load spikes at the base.

2. Generally, the surface strain responses are quite similar between the previous and current studies.
3. The revisions made to the drop tower did not alleviate the spurious noise early in the end displacement-time response. It is recommended that the attachment of the optical transducer wedge to the slider be made more secure to prevent upward motion of the wedge upon impact.
4. The high-frequency vibrations in all the responses from the previous study also existed in the results from the current study. Thus, these vibrations are probably due to some wave motions induced into the beam, not simply structural vibrational motion of the test fixture itself.

3.2.2 Group Two (Laminates B1 through B3)

The purpose of testing the laminates in Group Two was to assess the effects of the different material batches used in the previous and current studies. The results of these tests showed that any differences between the previous and current studies were of the same nature as the differences due to the changes made in the drop tower (as discussed in the previous section).

Table 3. Dynamic peak loads for group one laminates

Laminate	Peak loads (lb)		Ratio of revised to original
	Revised drop tower	Original drop tower ¹	
A1	1107	1290	0.86
A2	1057	1280	0.83
A3	828	1250	0.66
A4	770	975	0.79
A5	1115	1260	0.88

¹Derian and Hyer (1986)

As an example, the end load-time and surface strain-time responses for the $[(30/0/-30)_5]_s$ laminates from the previous and current material batches are shown in Figure 27 and Figure 28. The average peak load for the current specimens is about 30 percent lower than that from the previous results. The surface strain-time responses are quite similar. These observations are identical to those of the previous section. Thus, the differences between the two material batches is not noticeable from these results.

The load-time and strain-time results from the remaining laminates in this group are presented in Appendix B.

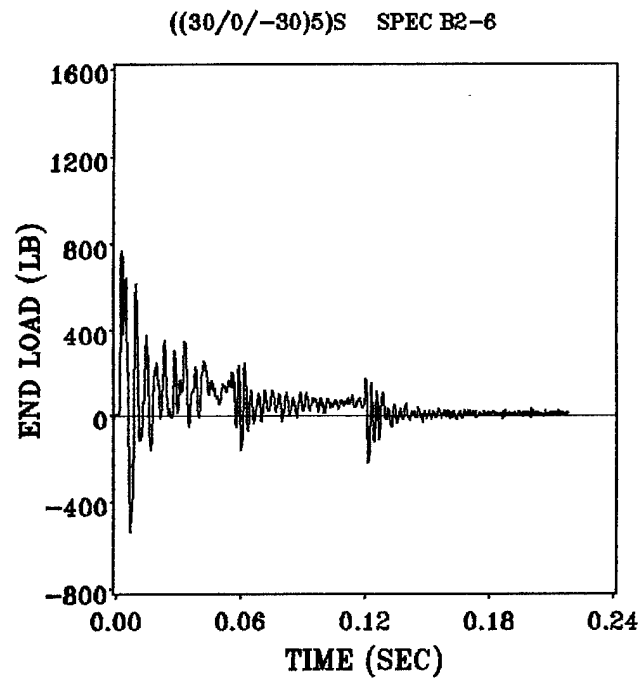
3.2.3 Group Three (Laminates C1 through C6)

The laminates in Group Three were tested primarily to collect further data on the dynamic response of laminated beams under axial impact. The nature of the load-time and surface strain-time response of these thin beams was identical to that exhibited by all of the remaining laminates. The only unique characteristic of some of the thinner beams was that laminates C4, C5, and C6 deflected the full range without suffering any major failures.

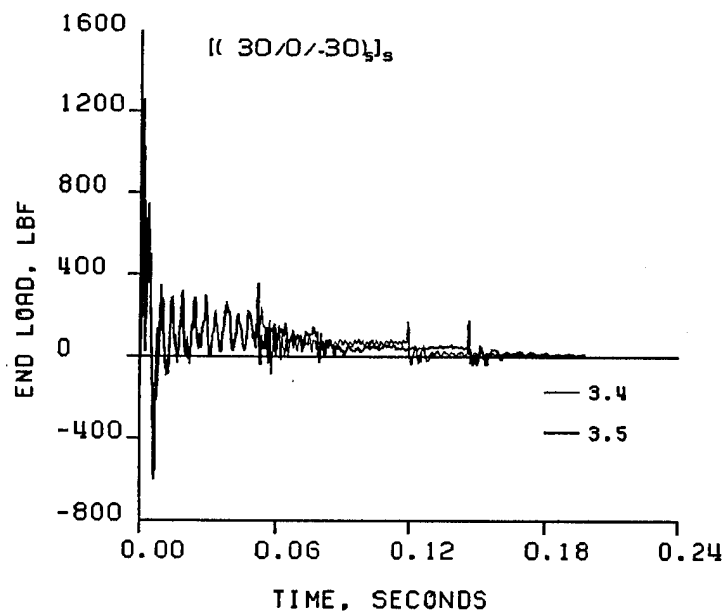
Since the results from these tests were as expected and the data was not used for any specific purpose in this study, the load-time and surface strain-time responses of these laminates are shown in Appendix B.

3.2.4 Quarter-point surface strain response

One specimen of each of the laminate types preceded by a B or C had installed upon it a total of six strain gages. Two of the gages were back to back longitudinal gages at the center of

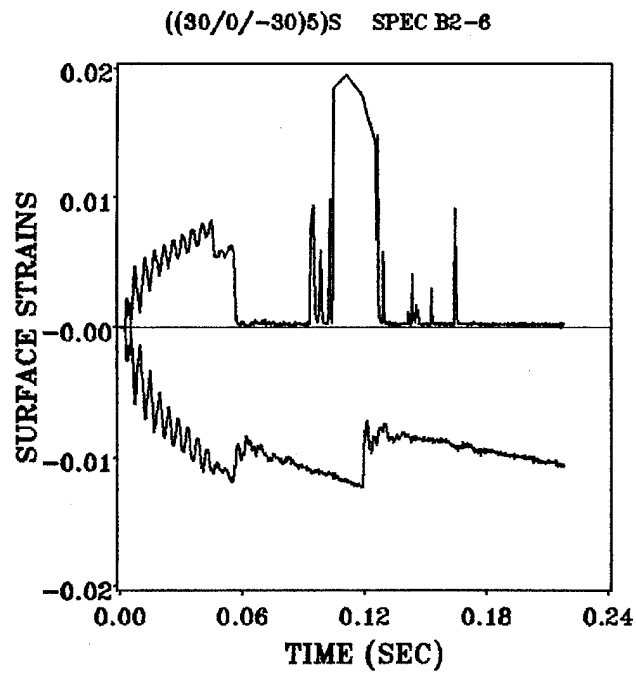


(a) Laminate B2 tested in revised drop tower

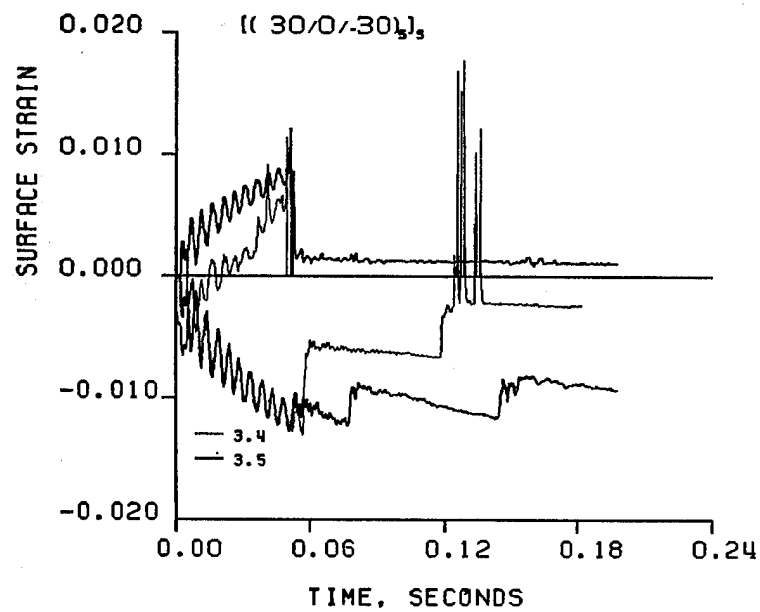


(b) Laminate 3 tested in original drop tower (Derian and Hyer, 1986)

Figure 27. Dynamic load responses for [(30/0/-30)₅]s laminates



(a) Laminate B2 tested in revised drop tower



(b) Laminate 3 tested in original drop tower (Derian and Hyer, 1986)

Figure 28. Dynamic strain responses for [(30/0/-30)₅]_S laminates

the beam. These strain results were presented earlier in this Chapter. The remaining four gages were longitudinal gages mounted back-to-back at each of the two quarter-points of the beam. It was noted earlier that all the beams tested exhibited an initial period of third-mode bending response. The strains at the two center strain gages were found to begin with values of opposite sign to their eventual tensile/compressive natures. However, it was expected that even in third-mode bending, the strains on the tensile side of the beam would be positive while the strains on the compressive side of the beam would be negative. This was found to be the case on all the beams which were equipped with quarter-point strain gages. The raw surface strain-time responses for the quarter-point strain gages are shown in Appendix C.

3.2.5 Transverse Strain Response

On one specimen of each of the laminates denoted by B or C, back-to-back strain gages were mounted in the center of the beam in a transverse manner. That is, these gages measured the surface strains in the width-wise direction of the beam. The purpose of these gages was to assess the dynamic response of the beam anticlastic curvature and laminate Poisson effect. The raw surface strain-time data for the transverse gages are shown in Appendix D. There is no transverse strain data presented for the $[0]_{30}$ laminate. A longitudinal transverse split occurred very early in the test for the $[0]_{30}$ specimen, causing the strain gages to fail. These data for the other layups were used to calculate midplane strains and curvatures for the results presented in this section.

Based on the Kirchhoff-Love hypothesis (Ashton and Whitney, 1970), midplane strains are defined as:

$$\epsilon_x^o = \frac{\epsilon_{xt} + \epsilon_{xc}}{2} \quad (3.2)$$

$$\varepsilon_y^o = \frac{\varepsilon_{yt} + \varepsilon_{yc}}{2} \quad (3.3)$$

where the t and c signify surface strains on the tensile and compressive surfaces of the beam, respectively. The curvatures are defined from the same hypothesis as:

$$\kappa_x = \frac{\varepsilon_{xt} - \varepsilon_{xc}}{h} \quad (3.4)$$

$$\kappa_y = \frac{\varepsilon_{yt} - \varepsilon_{yc}}{h} \quad (3.5)$$

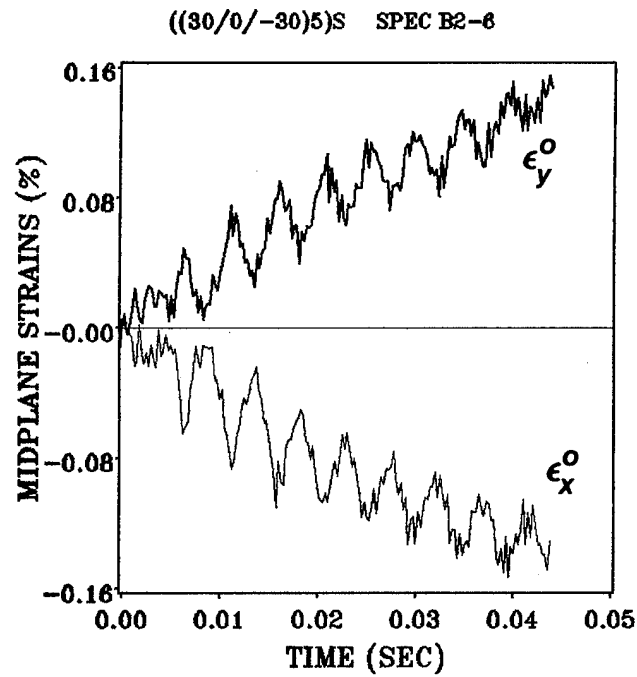
where h is the laminate thickness.

3.2.5.1 Thick Laminates

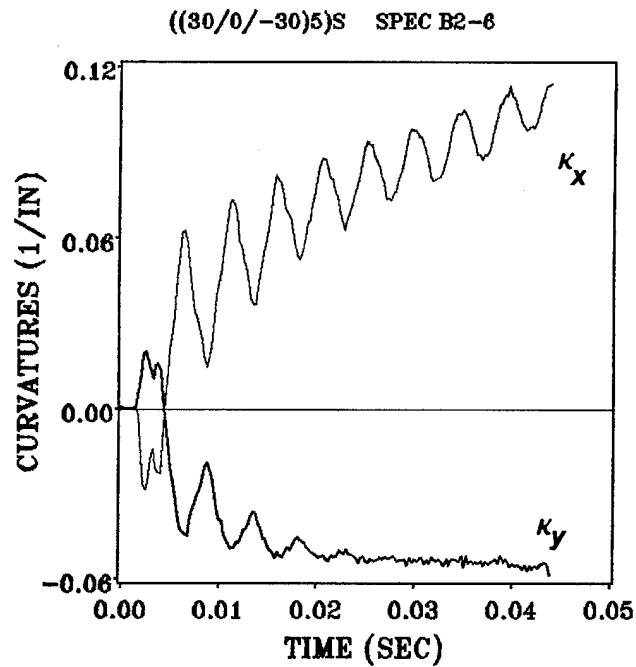
The dynamic midplane strains and curvatures versus time for the $[(30/0/-30)_5]_s$ and $[(45/-45/0/90)_4]_s$ laminates are shown in Figure 29 and Figure 30, respectively. From these figures, it can be seen that the trend of the transverse midplane strain, ε_y^o increased with that of the longitudinal midplane strain, ε_x^o for the thick beams. Also, the transverse curvature, κ_y , initially increases with longitudinal curvature, κ_x . However, the ratio of κ_y to κ_x decreases as κ_x increases. The transverse curvature tends to level off as longitudinal curvature increases.

3.2.5.2 Thin Laminates

The midplane strains and curvatures versus time for the thin laminates (C1 through C6) are shown in Figure 31 through Figure 36. For thin laminates, as was observed in the thick laminates, the transverse midplane strain increases with the longitudinal midplane strain. However, the transverse curvature responses for the thin laminates is quite different from that

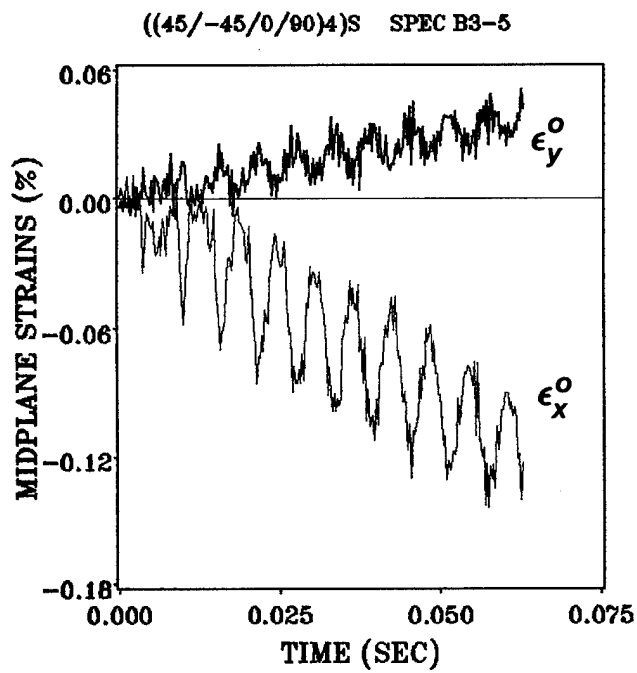


(a) Midplane strains versus time

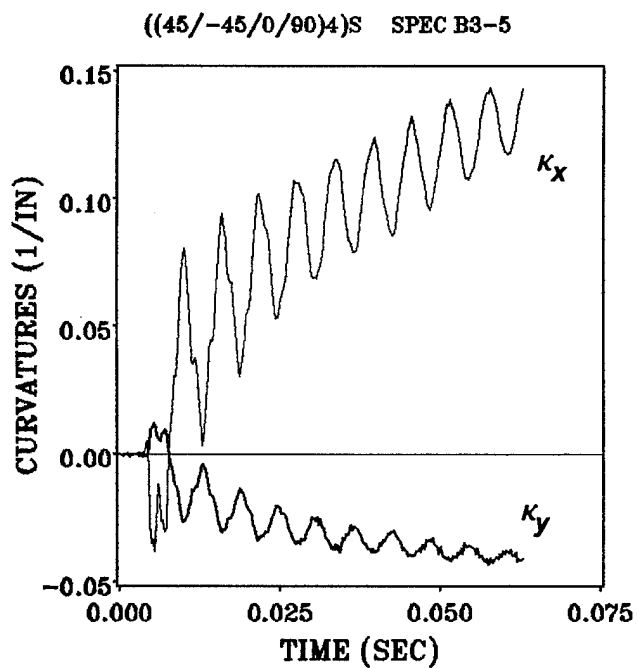


(b) Curvatures versus time

Figure 29. Dynamic midplane strains and curvatures for [(30/0/-30)₅]_s laminate



(a) Midplane strains versus time

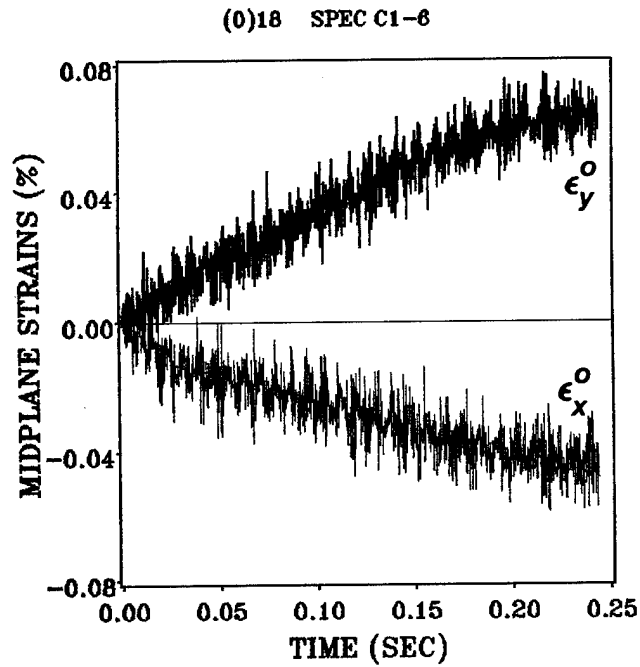


(b) Curvatures versus time

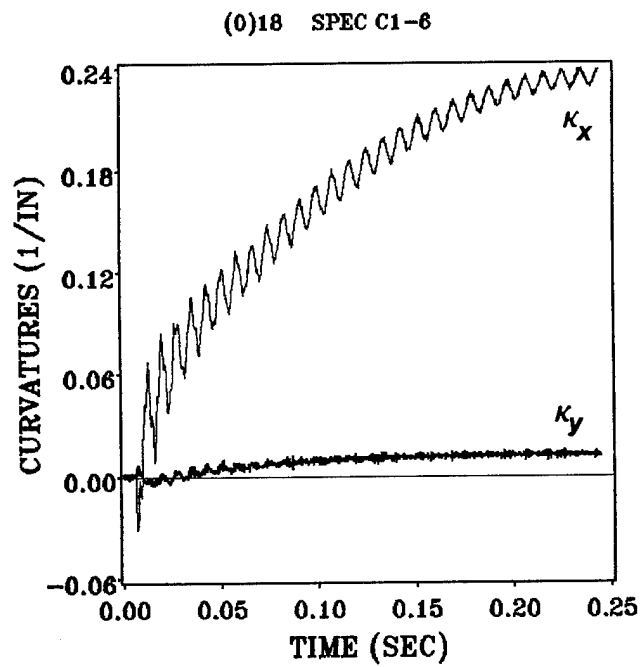
Figure 30. Dynamic midplane strains and curvatures for [(45/-45/0/90)₄]s laminate

exhibited by the thick laminates. In the thin laminates, the transverse curvature also increases in magnitude with the longitudinal curvature initially. However, the transverse curvature quickly reaches a maximum negative value, then begins to approach zero. For some of the laminates, the transverse curvature actually becomes positive.

The phenomenon exhibited by the transverse curvature response indicates that the transverse, or anticlastic, curvature becomes suppressed and eventually reverses for some laminates. Since only one specimen from each laminate was equipped with transverse strain gages, no transverse data for static tests was obtained. Thus, it is not known whether the observed suppression is a nonlinear large deformation effect present in both static and dynamic loading cases or whether it is strictly a dynamic effect. It is possible that if this suppression of transverse curvature exists in static loading that it could explain the decrease in the difference between surface strain magnitudes that was observed for the thin beams in the static tests discussed earlier.

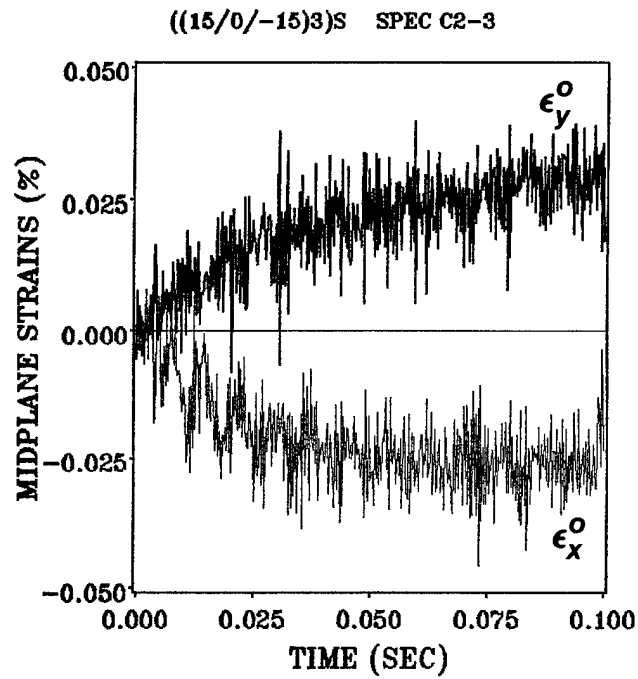


(a) Midplane strains versus time

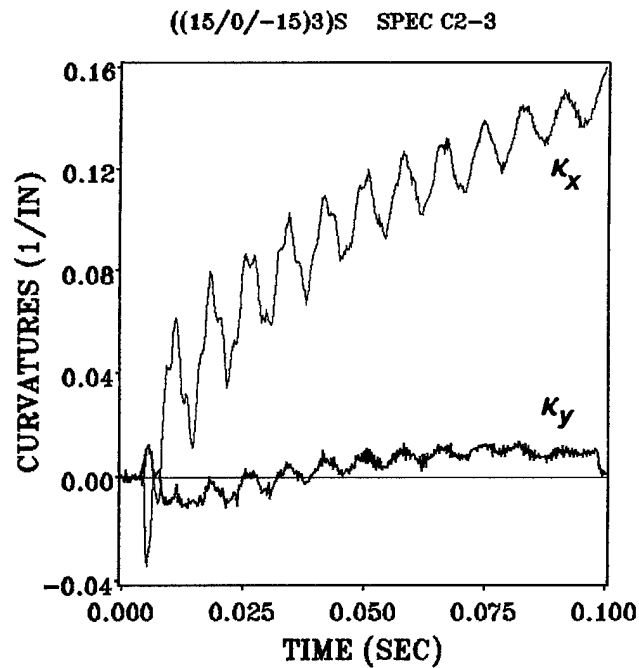


(b) Curvatures versus time

Figure 31. Dynamic midplane strains and curvatures for $[0]_{18}$ laminate

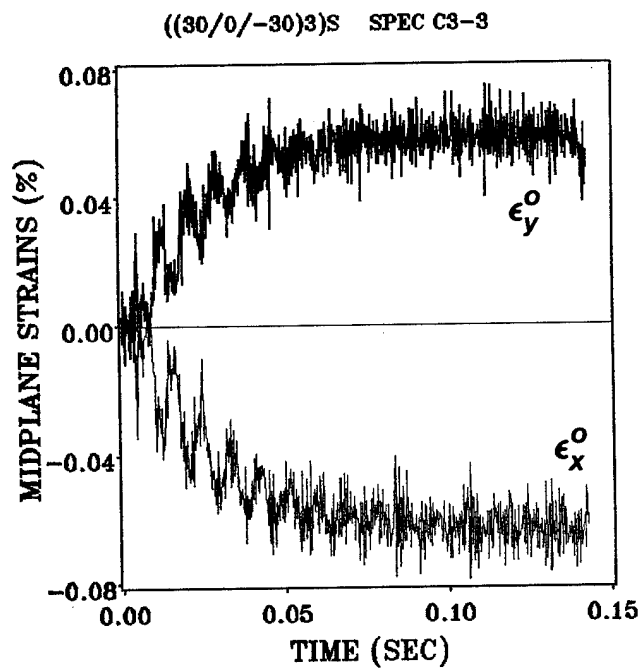


(a) Midplane strains versus time

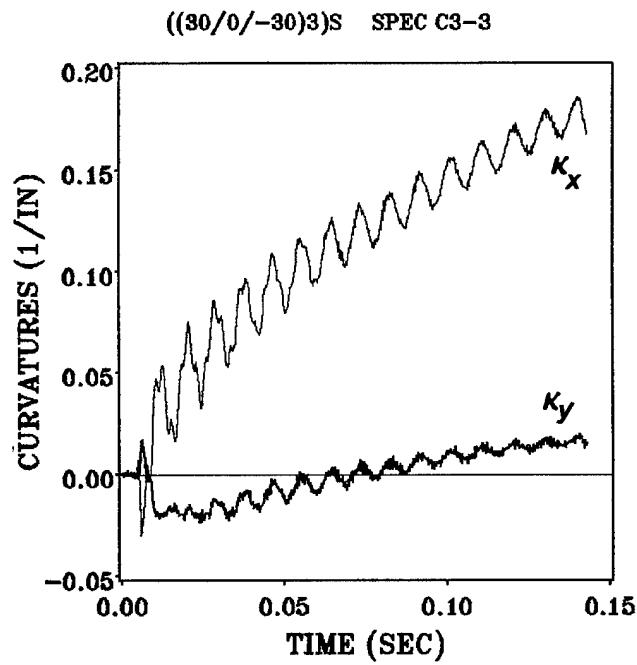


(b) Curvatures versus time

Figure 32. Dynamic midplane strains and curvatures for [(15/0/-15)₃]s laminate

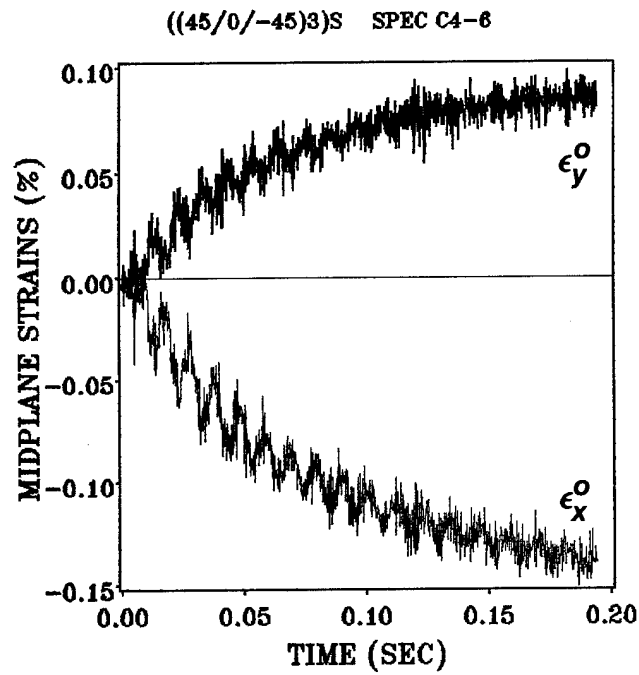


(a) Midplane strains versus time

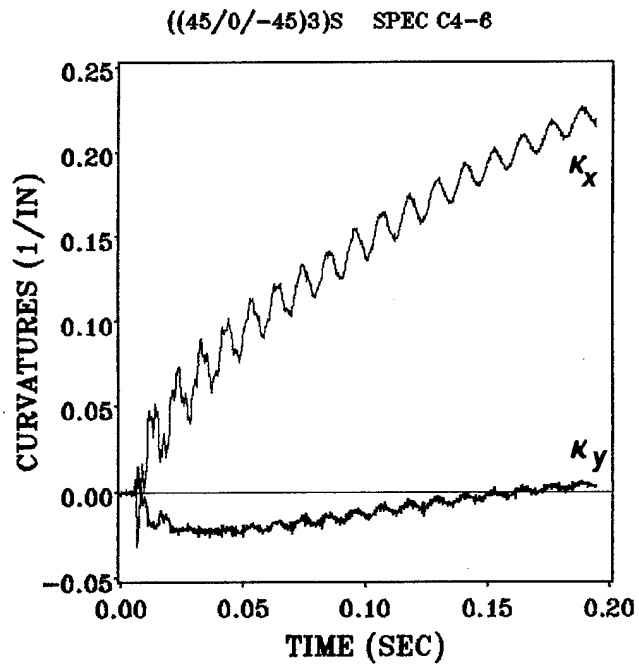


(b) Curvatures versus time

Figure 33. Dynamic midplane strains and curvatures for [(30/0/-30)₃]s laminate

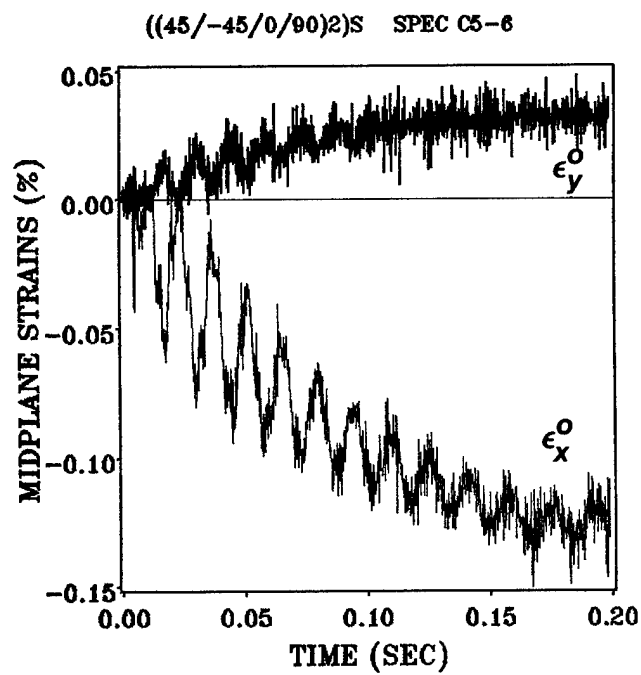


(a) Midplane strains versus time

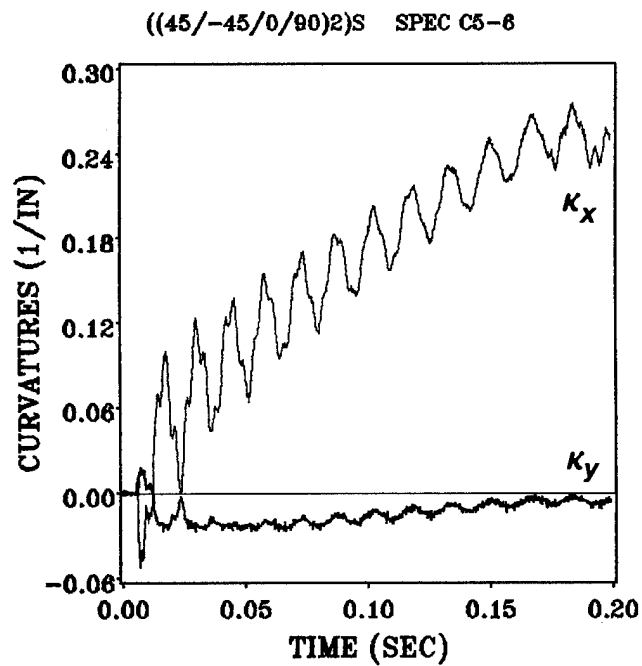


(b) Curvatures versus time

Figure 34. Dynamic midplane strains and curvatures for [(45/0/-45)₃]s laminate



(a) Midplane strains versus time



(b) Curvatures versus time

Figure 35. Dynamic midplane strains and curvatures for [(45/-45/0/90)₂]s laminate

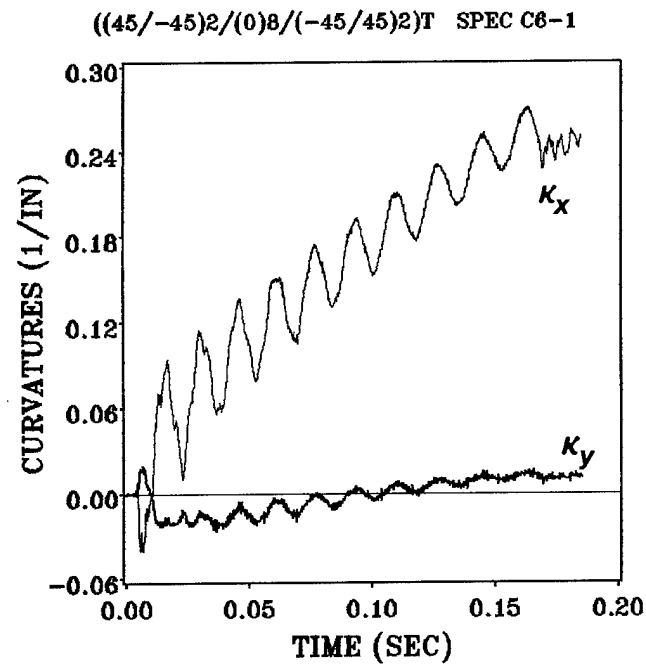
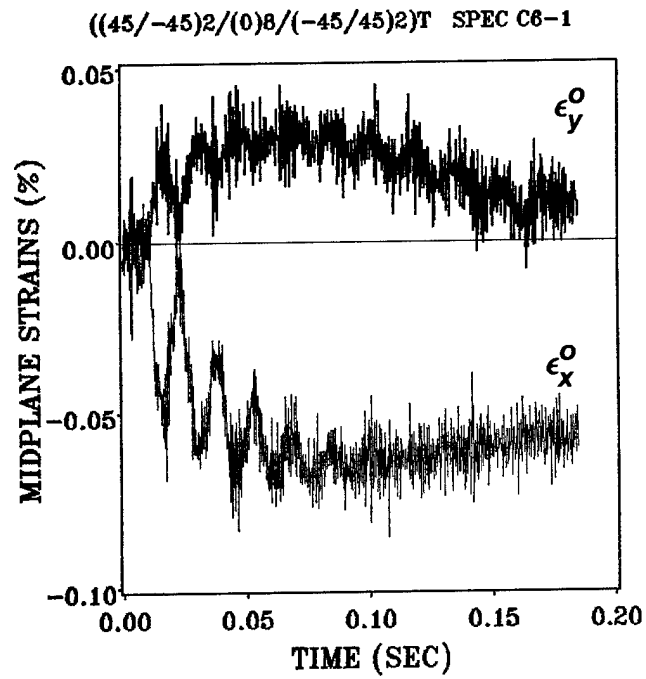


Figure 36. Dynamic midplane strains and curvatures for [(45/-45)₂/(0)₈/(-45/45)₂]t laminate

4.0 Impact Alleviation Tests

The presence of high load spikes in the dynamic data discussed in Chapter 1 raised questions about the possibility of early damage. These load spikes were all much larger than the static failure loads of the respective beams. The peak dynamic load, static failure load (or maximum static load for beams which did not fail), and the ratio between the dynamic and static maximum loads, for each laminate tested both statically and dynamically, are presented in Table 4 on page 66. The peak loads shown are averages of the replicate dynamic tests for each laminate. To determine if these peak loads initiated damage in the beams, a series of impact alleviation tests was performed. In these tests, the dynamic deflection of the beams was stopped shortly after impact, and the beams were then loaded statically to failure. The static response was compared to static response of virgin beams cut from the same panel to determine if any damage had been induced. The results of these tests and their implications to crashworthy designs will be discussed in this Chapter.

Table 4. Peak dynamic and static loads from experiments

Laminate number ¹	Peak dynamic load (lb)	Maximum static load (lb)	Dynamic to static peak load ratio
B1	1220.7	298.0	4.1
B2	819.6	161.2	5.1
B3	793.9	119.5	6.6
C1	612.7	57.0	10.7
C2	550.4	50.0	11.0
C3	431.4	52.0	8.3
C4	415.7	33.7	12.3
C5	444.2	16.9	26.3
C6	401.5	14.3	28.1

¹See Table 1 on page 9 for descriptions of laminates.

4.1 Test Description

The experimental apparatus used for these tests was the same fixture used for the dynamic tests discussed in Chapter 2. A length of aircraft hose was placed on each of the outside vertical rods. These hoses served as impact alleviators by stopping the motion of the mass cart. The hoses were cut to such a length that the maximum deflection of the beam specimens was less than two inches (5.08 cm). This distance was adequate to permit the high load spike to occur and also to allow the beams to exhibit the third-mode bending response and then begin the regular bending shape. However, the deflection was stopped well short of any major failure events in any of the beams. Thus, this test should be a good indicator of any damage induced by the very high initial peak load.

After a beam was impacted as described above, it was removed from the fixture and tested statically to failure. The static tests were performed in a manner identical to the static tests described in Chapter 2. However, these tests were performed on a different universal loading machine that was not available at the time of the other static tests. The setup for this machine allowed about 18 inches (45.7 cm) of deflection before hinge contact. The load was measured using the four-load-cell arrangement used in the dynamic tests. The end displacement and longitudinal strains on both the tensile and compressive surfaces were also recorded during these tests.

The impact alleviation test procedure can be summarized as follows:

1. Using the impact alleviation system, impact a beam in the dynamic fixture.
2. Carefully remove the beam from the dynamic fixture and install it in the static load frame.

3. Test the beam in static flexure until failure occurs, or until hinges contact if the beam does not fail.
4. Compare the static response of these beams to the static response of the virgin beams as discussed in Chapter 2.

It was desired to C-scan the beams after impact and before static testing. However, due to time constraints this was not done.

4.2 *Dynamic Results*

One specimen of each of the nine laminates was selected for the impact alleviation tests. Each specimen was impacted using the impact alleviation procedure described in Section 4.1. For each beam, the load and strain responses were obtained using the same data acquisition system described in Chapter 2. The peak compressive load along with peak tensile and compressive strains for both the tensile and compressive sides of the beams are listed in Table 5 on page 69. Due to a malfunction of the data acquisition system, the data for specimen B3-1 was lost. Note that the tensile side of the beam is defined as the side which undergoes tensile strains after the third mode bending response has disappeared. The compressive side is the side which undergoes compressive strains after this third mode has disappeared.

Table 5. Peak Loads and Strains During Impact Alleviation Tests

	Peak	Peak surface strains			
Specimen	compressive	tensile side		compressive side	
number	load (lb)	+ (%)	- (%)	- (%)	+ (%)
B1-3	1426	0.63	-0.23	-0.64	0.20
B2-1	1291	0.53	-0.31	-0.80	0.27
B3-1	NO DATA				
C1-3	688	0.40	-0.23	-0.46	0.23
C2-6	713	0.40	-0.27	-0.48	0.23
C3-5	639	0.37	-0.29	-0.50	0.24
C4-3	615	0.38	-0.34	-0.51	0.28
C5-2	529	0.40	-0.34	-0.51	0.28
C6-5	492	0.40	-0.40	-0.48	0.34

See Table 1 on page 9 for descriptions of laminates.

4.3 Results

4.3.1 Thick Laminates

4.3.1.1 $[0]_{30}$ Laminate

The static load-displacement response of the impacted and virgin beams are shown together in Figure 37. From this figure, it can be seen that the impacted beam had a reduced stiffness. This beam also failed at about eighty percent of the failure load of the virgin beam. This failure occurred at about 10.8 inches (27.4 cm) of end displacement, while the virgin beam did not fail until over 12 inches (30.5 cm) of end displacement. The end work required to deflect the impacted beam to failure was approximately 25 percent less than the work required to load the virgin beam to failure. Thus, the $[0]_{30}$ beam suffered significant damage from the initial impact. This damage, however, was not apparent to visual inspection of the beam prior to static testing.

The tensile side and compressive side surface strain magnitudes for both the impacted and virgin beams are plotted versus curvature in Figure 38. The curvature is defined from the Kirchhoff- Love assumption. That is,

$$\kappa_x = \frac{(\epsilon_{xt} - \epsilon_{xc})}{h} \quad (4.1)$$

From this figure, it can be seen that the damage caused by the initial impact had a large effect on the strain response of the beam. The large difference between the tensile side and compressive side surface strain magnitudes that was observed on the virgin beam is virtually nonexistent on the impacted beam. Also, at a curvature of approximately 0.09 in^{-1} (0.0354

cm⁻¹), some type of failure event occurred which caused a discontinuity in the strain curves for the impacted beam.

Inspection of the beam after testing revealed a number of longitudinal matrix cracks through the entire thickness of the laminate. Some of these cracks propagated over more than half the length of the beam, and probably were responsible for the discontinuity in the strain response and probably the reduction in laminate stiffness and strength.

4.3.1.2 [(30/0/-30)_s]_s Laminate

The static load-displacement response of the impacted and virgin beams are shown together in Figure 39. From this figure, it can be seen that the impacted beam had a reduced stiffness. As did the [0]₃₀ specimen, this impacted beam also failed at about eighty-five percent of the failure load of the virgin beam. This initial failure occurred at about 6.5 inches (16.5 cm) of end displacement, exactly the same end displacement at the failure of the virgin beam. The end work required to load the impacted beam to this initial failure was approximately 12 percent less than the work required to load the virgin beam to initial failure. The virgin beam has two subsequent failure events; however, the impacted beam had only one subsequent failure event. Thus, the [(30/0/-30)_s]_s suffered some damage from the initial impact, but was still able to deflect the same amount prior to initial failure.

The tensile side and compressive side surface strain magnitudes for both the impacted and virgin beams are plotted versus curvature in Figure 40. The curvature was computed from the experimental data using Equation (3.1). From this figure, it can be seen that the damage caused by the initial impact had little effect on the strain response of the beam. The large difference between the tensile side and compressive side surface strains observed on the virgin beam is virtually identical to that of the impacted beam.

(0)30

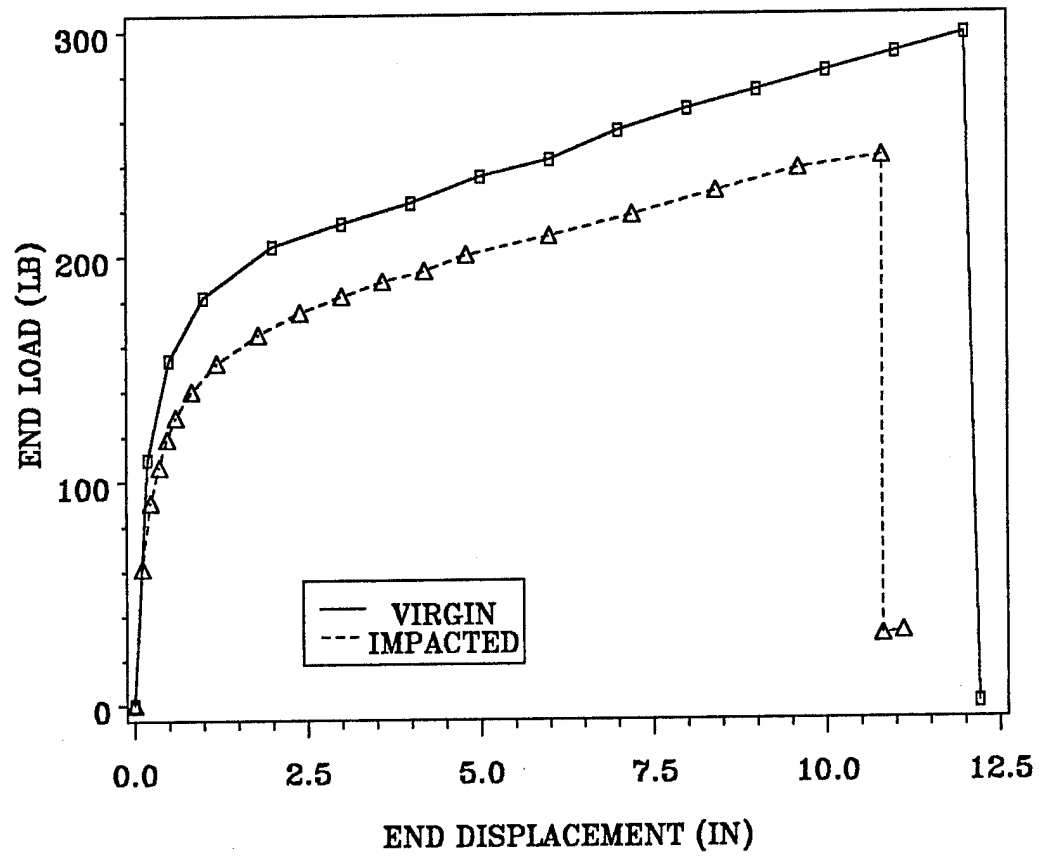


Figure 37. End load vs end displacement for impacted and virgin $[0]_{30}$ beams

(0)30

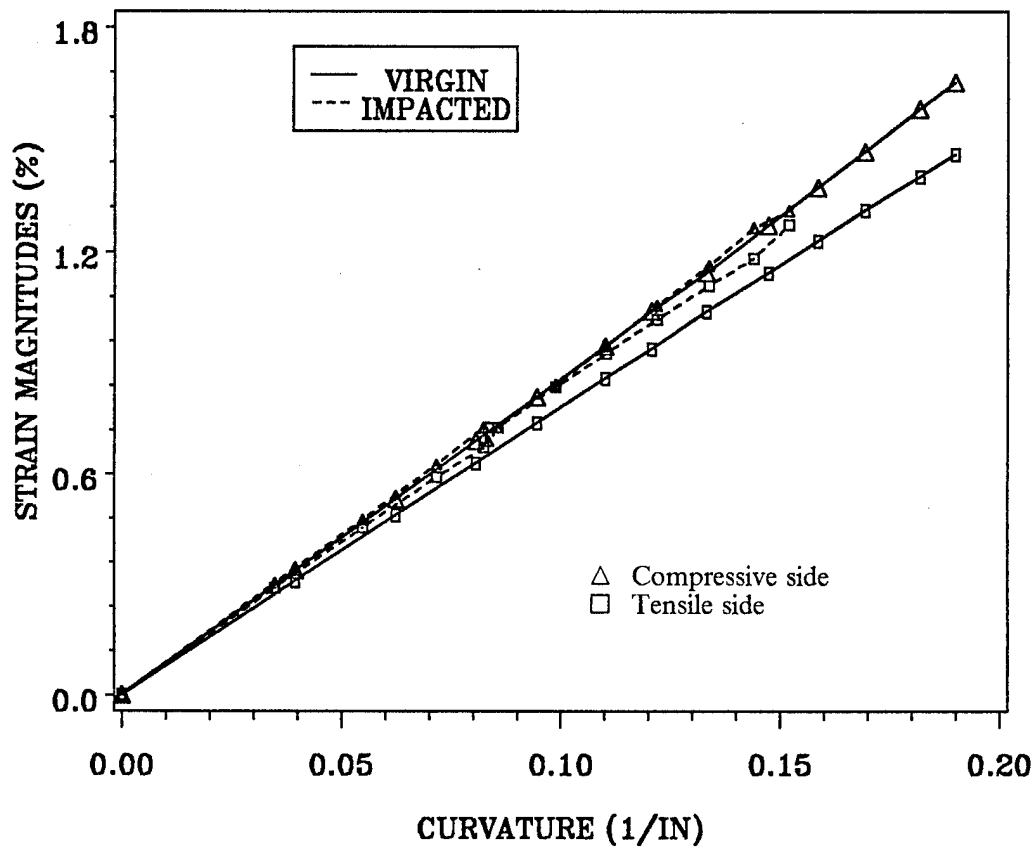


Figure 38. Surface strain magnitudes for impacted and virgin [0]₃₀ beams

$((30/0/-30)_5)_S$

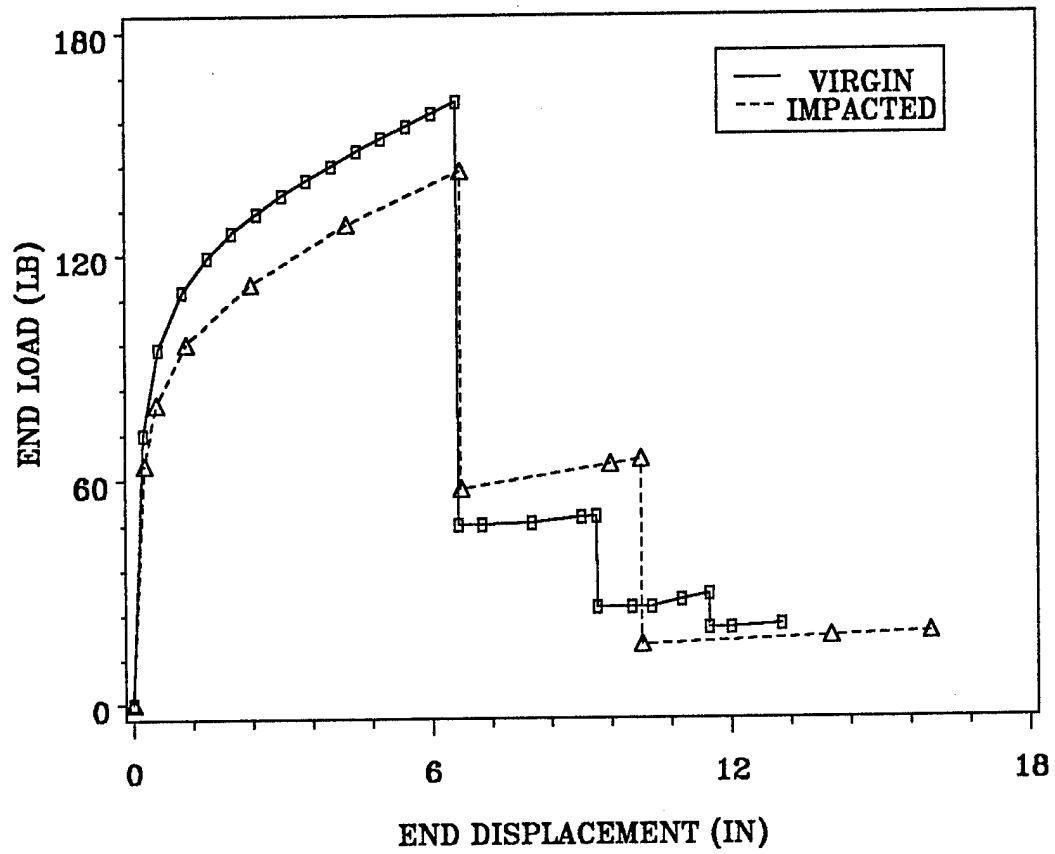


Figure 39. End load vs end displacement for impacted and virgin $[(30/0/-30)_5]_S$ beams

$((30/0/-30)_5)_S$

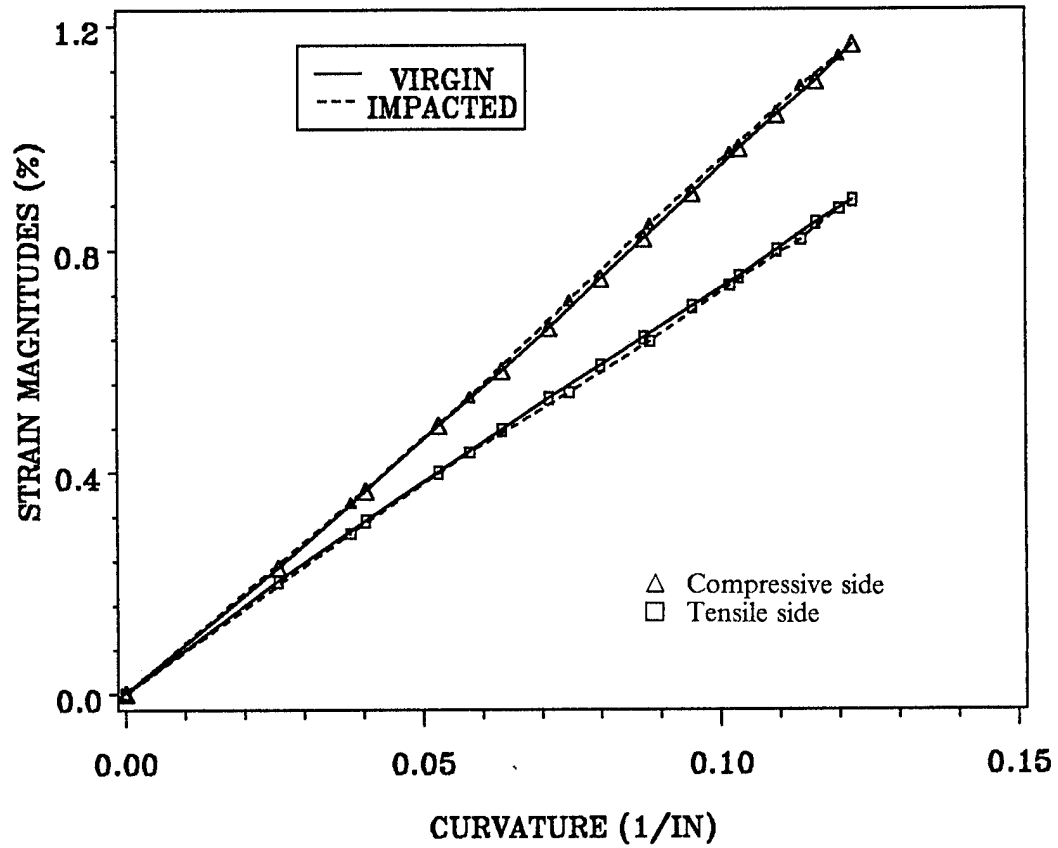


Figure 40. Surface strain magnitudes for impacted and virgin $[(30/0/-30)_5]_S$ beams

4.3.1.3 [(45/-45/0/90)₄]_s Laminate

The static load-displacement response of the impacted and virgin beams are shown together in Figure 41. From this figure, it can be seen that the impacted beam had a slightly reduced stiffness. This beam failed at over ninety percent of the failure load of the virgin beam. This failure occurred at about 10.5 inches (26.7 cm) of end displacement, about the same end displacement at the failure of the virgin beam. However, the work required to load the impacted beam to this failure event was approximately three percent more than the work required to load the virgin beam to initial failure. Thus, the [(45/-45/0/90)₄]_s suffered little damage from the initial impact, and was still able to deflect the same amount prior to initial failure.

The tensile side and compressive side surface strain magnitudes for both the impacted and virgin beams are plotted versus curvature in Figure 42. From this figure, it can be seen that the damage caused by the initial impact had no effect on the strain response of the beam. The large difference between the tensile side and compressive side surface strains that was observed on the virgin beam is virtually identical to that of the impacted beam.

4.3.2 Thin Laminates

4.3.2.1 [0]₁₈ Laminate

The static load-displacement response of the impacted and virgin beams are shown together in Figure 43. From this figure, it can be seen that the impacted beam actually had a slightly higher stiffness. No statement can be made about failure, since the beam did not fail within the end displacement range tested. The work required to load the impacted beam up to an end displacement of 14 inches was actually about seven percent higher than the work required

$((45/-45/0/90)_4)_S$

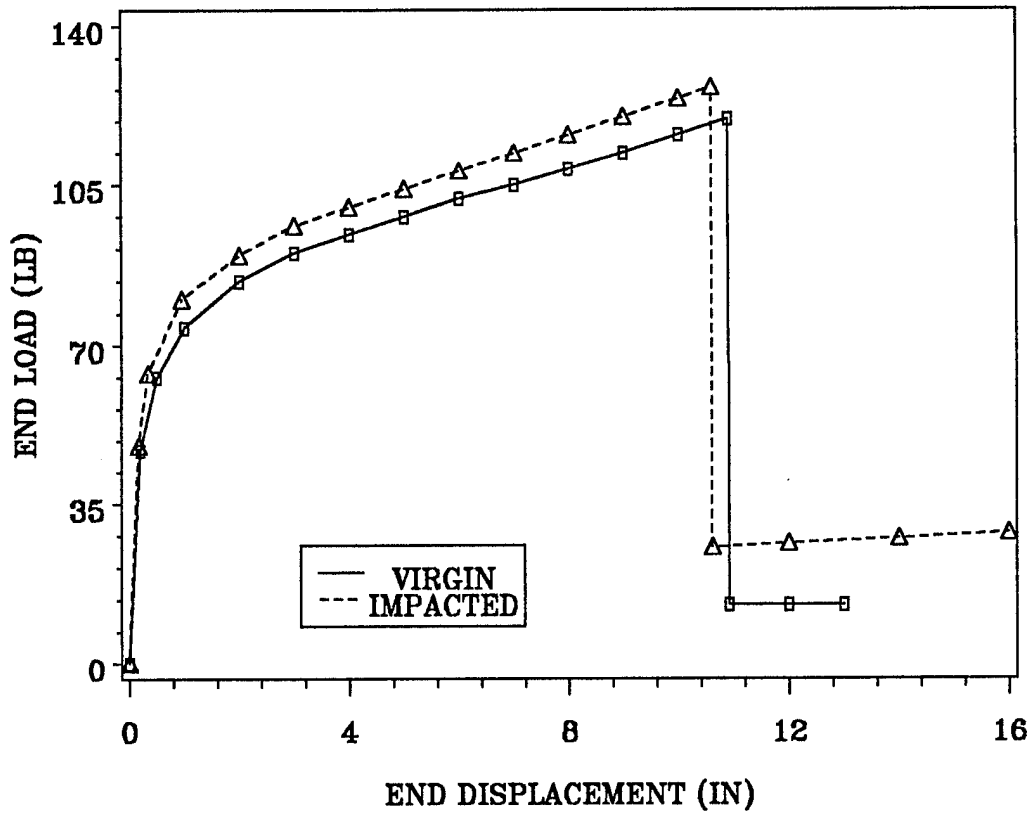


Figure 41. End load vs end displacement for impacted and virgin $[(45/-45/0/90)_4]_S$ beams

$((45/-45/0/90)_4)_S$

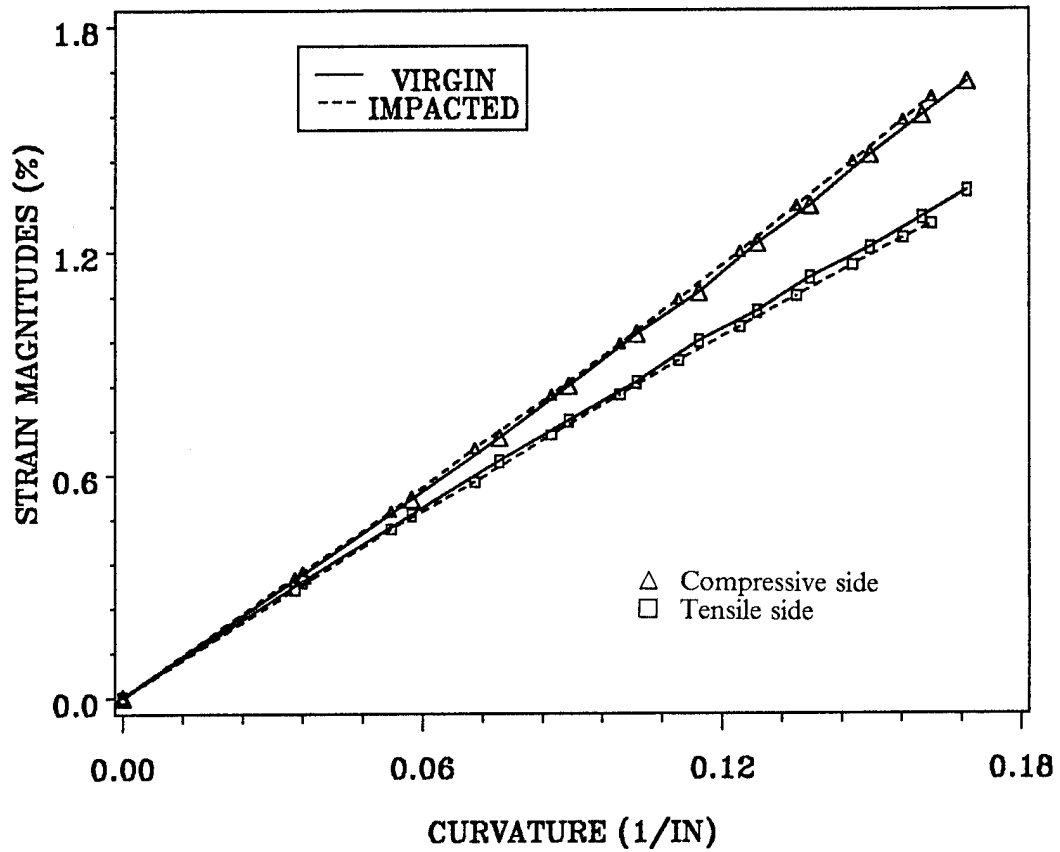


Figure 42. Surface strain magnitudes for impacted and virgin $[(45/-45/0/90)_4]_S$ beams

to load the virgin beam to the same displacement. Thus, the $[0]_{18}$ suffered no degradation from the initial impact, and in fact its stiffness was slightly higher than the stiffness of the virgin beam.

The tensile side and compressive side surface strain magnitudes for both the impacted and virgin beams are plotted versus curvature in Figure 44. Although it is difficult to ascertain from this figure, the initial impact caused anomaly in the strain response. The large difference between the tensile side and compressive side surface strains that was observed on the virgin beam also appears on the impacted beam. However, the difference in strain magnitudes gradually disappears, and at a curvature of approximately 0.15 in^{-1} (0.0591 cm^{-1}) it actually reverses. For the remainder of the static test, the tensile side surface strain is actually greater in magnitude than the compressive side strain. Similarly to the $[0]_{30}$ beam, a longitudinal split through all but a few plies was found in the $[0]_{18}$ after testing. This crack probably caused the discontinuity in the strain response and the change in the difference between the surface strain magnitudes on the tensile and compressive sides.

4.3.2.2 $[(15/0/-15)_3]_s$ Laminate

The static load-displacement response of the impacted and virgin beams are shown together in Figure 45. From this figure, it can be seen that the stiffness of the impacted beam was identical to the stiffness of the virgin beam. However, the impacted beam failed at slightly less load and displacement than the virgin beam. The end work required to deflect the impacted beam to the first noticeable failure event was approximately 12 percent less than the work required to load the virgin beam to its first failure event. Thus, the $[(15/0/-15)_3]_s$ suffered very slight degradation from the initial impact.

The tensile side and compressive side surface strain magnitudes for both the impacted and virgin beams are plotted versus curvature in Figure 46. From this figure, it can be seen that

(0)18

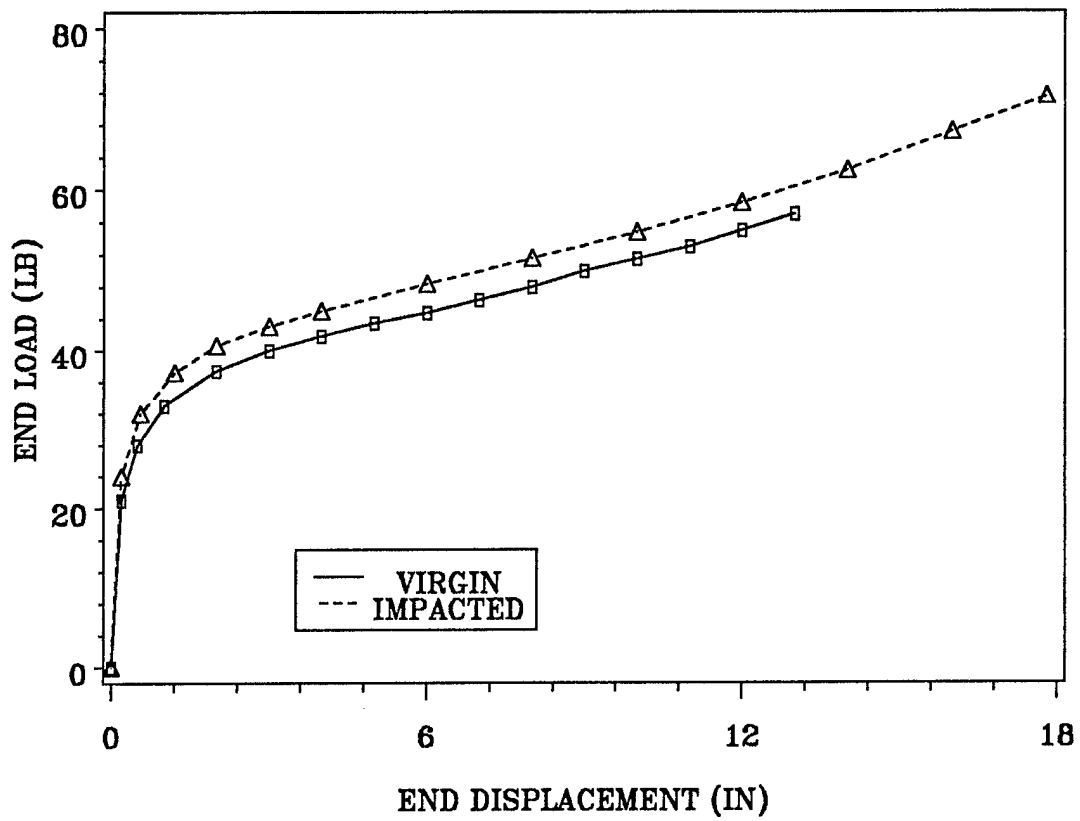


Figure 43. End load vs end displacement for impacted and virgin [0]₁₈ beams

(0)18

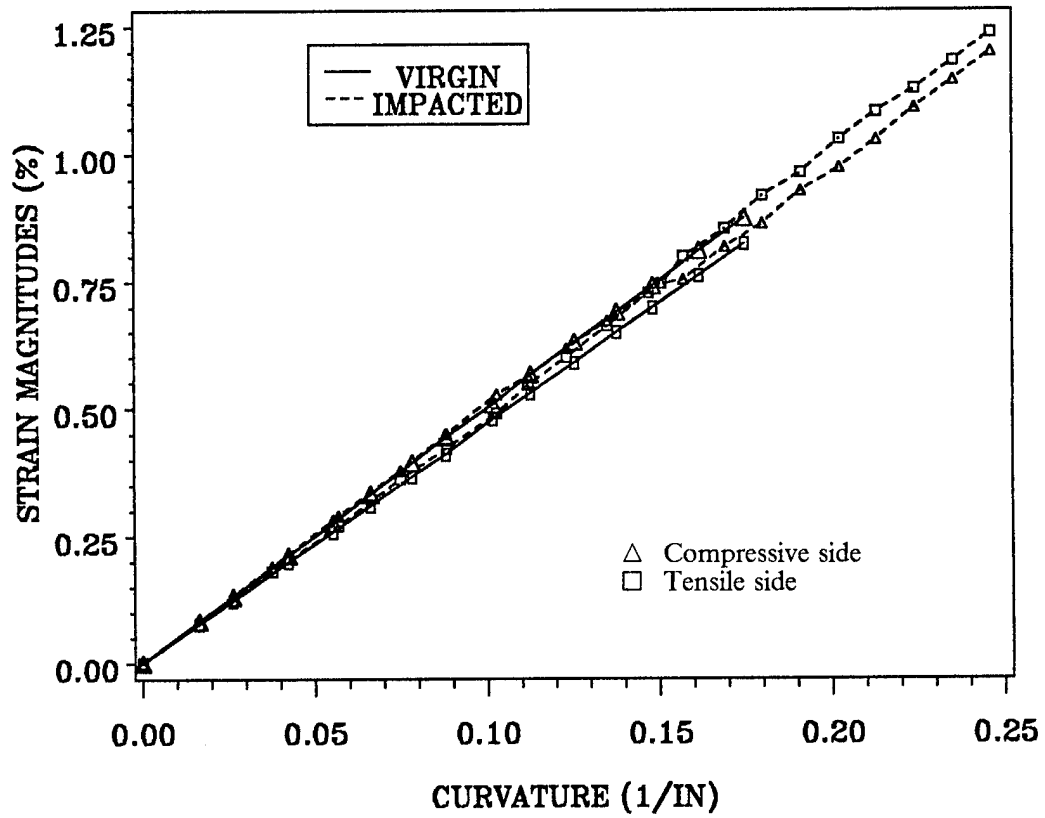


Figure 44. Surface strain magnitudes for impacted and virgin [0]₁₈ beams

the damage caused by the initial impact had no effect on the strain response of the beam. The large difference between the tensile side and compressive side surface strains that was observed on the virgin beam is virtually identical to that of the impacted beam.

4.3.2.3 [(30/0/-30)₃]s Laminate

The static load-displacement response of the impacted and virgin beams are shown together in Figure 47. From this figure, it can be seen that the stiffness of the impacted beam was slightly less than the stiffness of the virgin beam. Also, the impacted beam failed at slightly less load and displacement than the virgin beam. The end work required to load the impacted beam to failure was approximately 11 percent lower than the work required to load the virgin beam to failure.

The tensile side and compressive side surface strain magnitudes for both the impacted and virgin beams are plotted versus curvature in Figure 48. From this figure, it can be seen that the damage caused by the initial impact had little effect on the strain response of the beam. The large difference between the tensile side and compressive side surface strains on the virgin beam is approximately identical to that observed on the impacted beam.

4.3.2.4 [(45/0/-45)₃]s Laminate

The static load-displacement response of the impacted and virgin beams are shown together in Figure 49. From this figure, it can be seen that the stiffness of the impacted beam was very slightly less than the stiffness of the virgin beam. No statement can be made about failure, since the virgin beam had hinge contact before it failed. The end work required to deflect the impacted beam 13 inches was approximately two percent less than the work required to de-

$((15/0/-15)_3)_S$

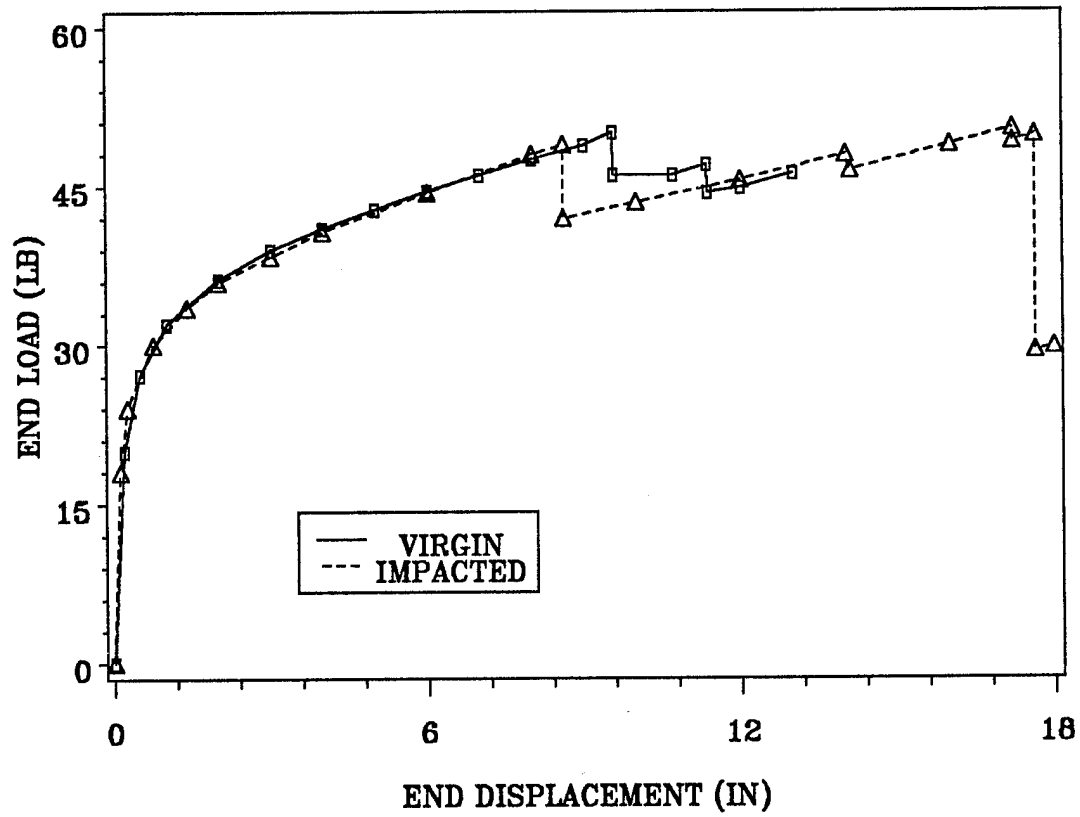


Figure 45. End load vs end displacement for impacted and virgin $((15/0/-15)_3)_S$ beams

$((15/0/-15)_3)_S$

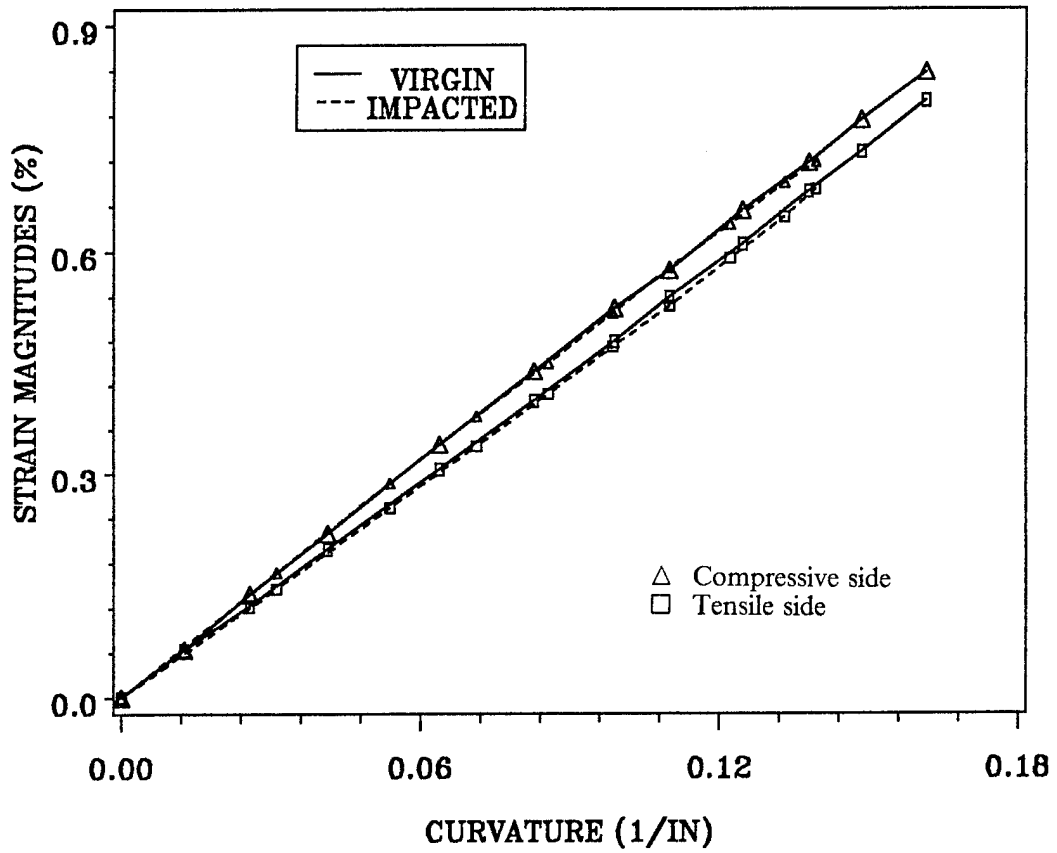


Figure 46. Surface strain magnitudes for impacted and virgin $((15/0/-15)_3)_S$ beams

$((30/0/-30)_3)_S$

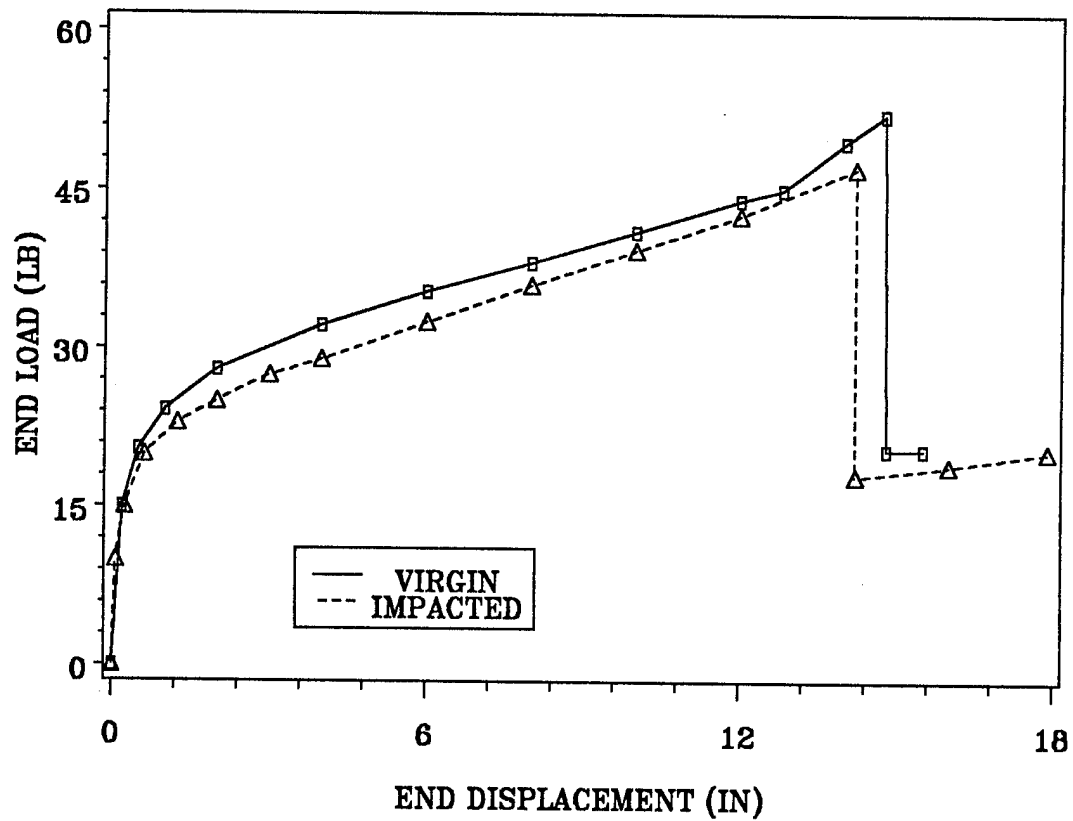


Figure 47. End load vs end displacement for impacted and virgin $[(30/0/-30)_3]_S$ beams

$((30/0/-30)_3)_S$

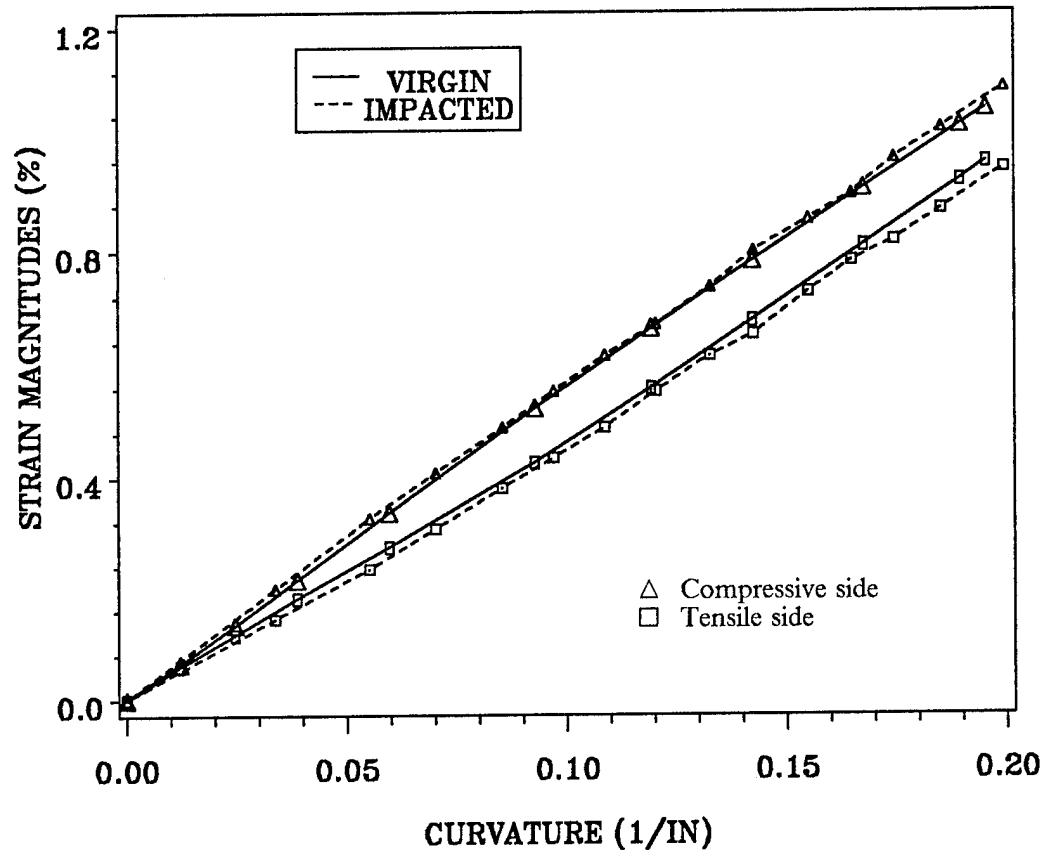


Figure 48. Surface strain magnitudes for impacted and virgin $[(30/0/-30)_3]_S$ beams

flect the virgin beam the same amount. Thus, the $[(45/0/-45)_3]_s$ suffered a very small amount of degradation in stiffness from the initial impact.

The tensile side and compressive side surface strain magnitudes for both the impacted and virgin beams are plotted versus curvature in Figure 50. From this figure, it can be seen that the damage caused by the initial impact had no effect on the strain response of the beam. The large difference between the tensile side and compressive side surface strains on the impacted beam is identical to that observed on the virgin beam.

4.3.2.5 $[(45/-45/0/90)_2]_s$ Laminate

The static load-displacement response of the impacted and virgin beams are shown together in Figure 51. From this figure, it can be seen that the stiffness of the impacted beam was actually greater than the stiffness of the virgin beam. The end work required to deflect the impacted beam 13 inches was approximately 17 percent greater than the work required to deflect the virgin beam the same amount. Thus, the $[(45/-45/0/90)_2]_s$ suffered no degradation in stiffness from the initial impact. No statement can be made about failure, since the virgin beam had hinge contact before it failed.

The tensile side and compressive side surface strain magnitudes for both the impacted and virgin beams are plotted versus curvature in Figure 52. From this figure, it can be seen that the initial impact actually decreased the amount of the difference in magnitudes between the tensile side and compressive side surface strains.

$((45/0/-45)_3)_S$

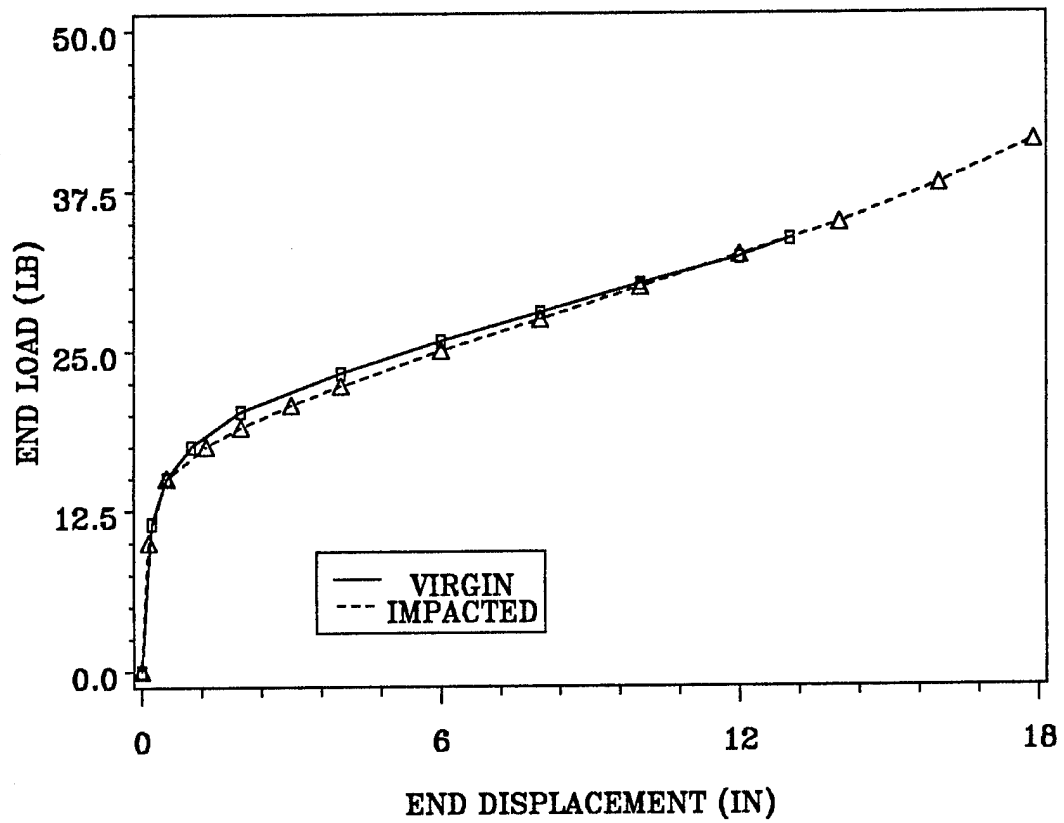


Figure 49. End load vs end displacement for impacted and virgin $[(45/0/-45)_3]_S$ beams

$((45/0/-45)_3)_S$

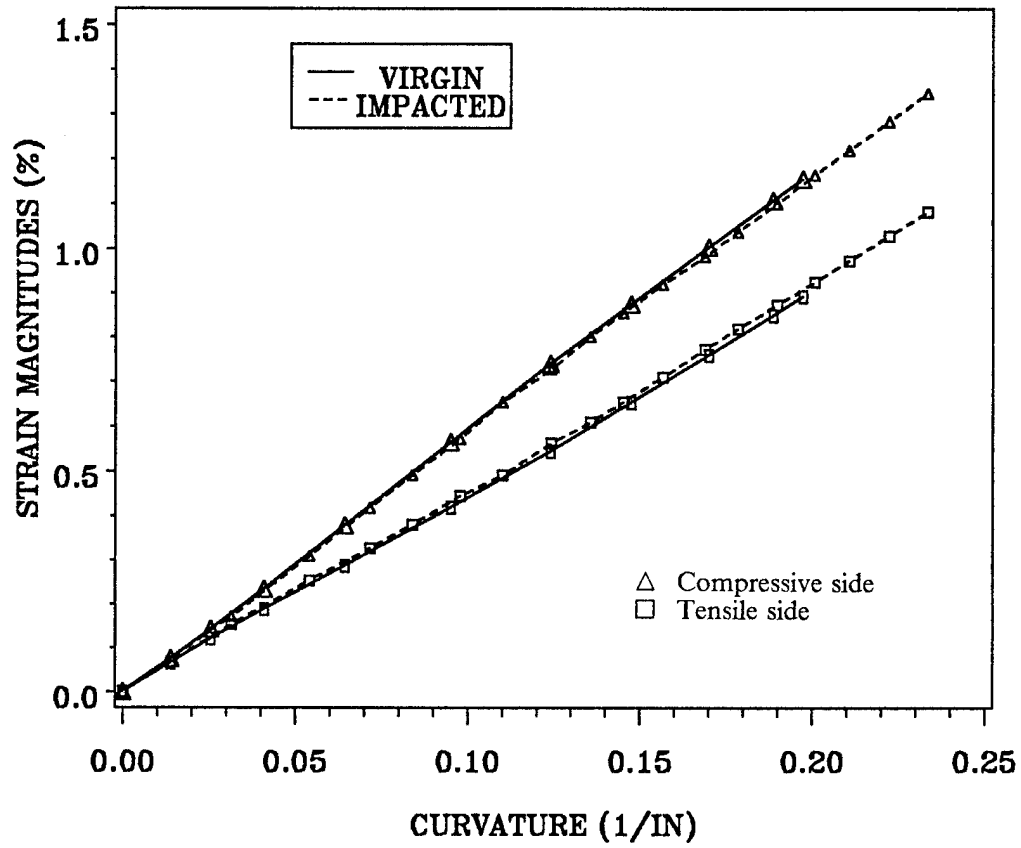


Figure 50. Surface strain magnitudes for impacted and virgin $[(45/0/-45)_3]_S$ beams

$((45/-45/0/90)_2)_S$

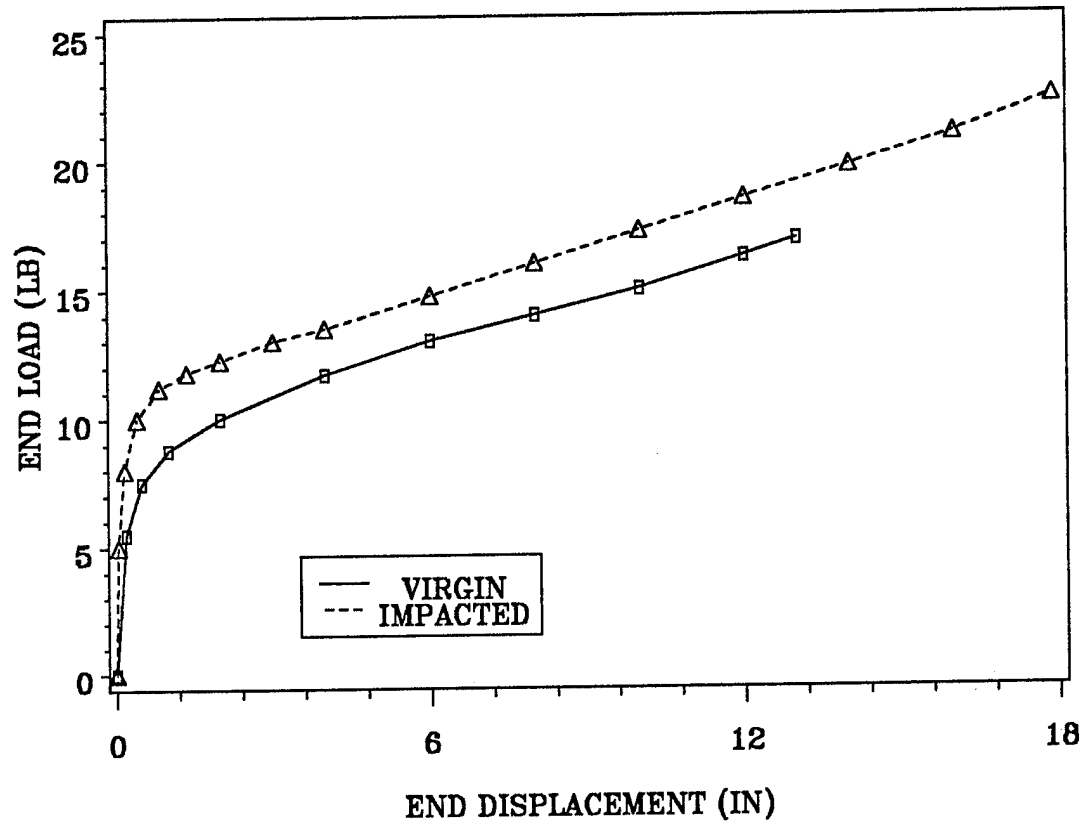


Figure 51. End load vs end displacement for impacted and virgin $[(45/-45/0/90)_2]_S$ beams

$((45/-45/0/90)_2)_S$

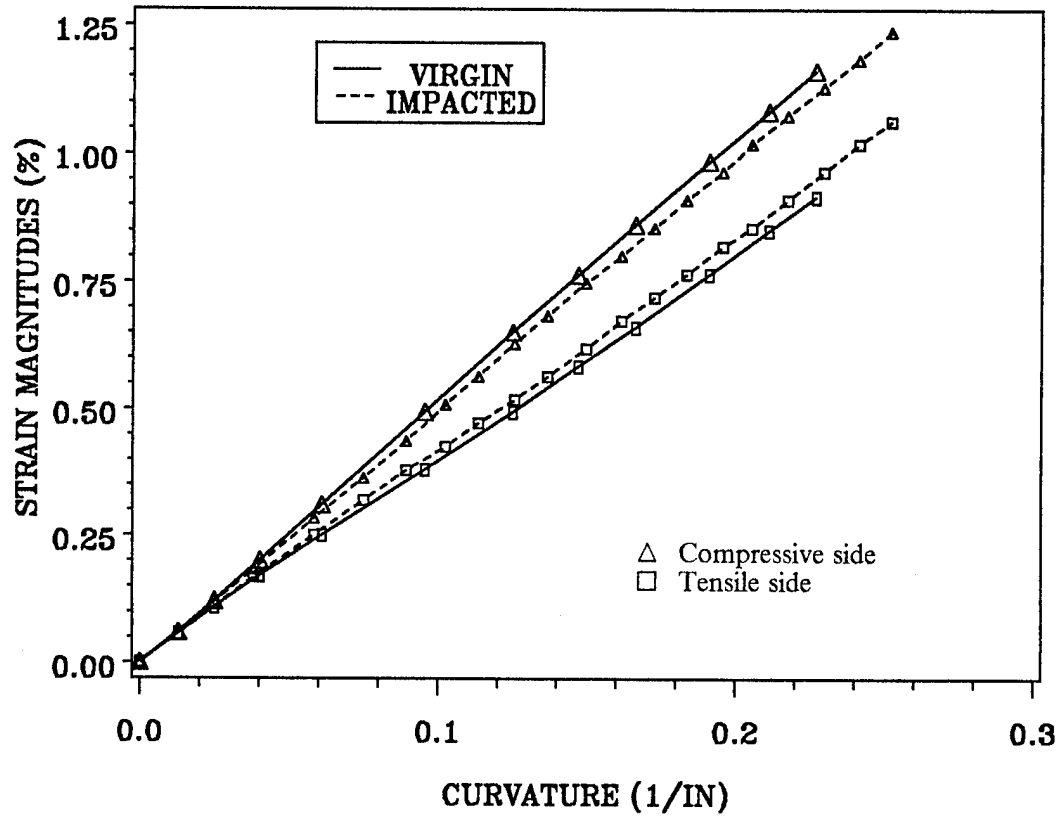


Figure 52. Surface strain magnitudes for impacted and virgin $[(45/-45/0/90)_2]_S$ beams

4.3.2.6 $[(45/-45)_2/(0)_8/(-45/45)_2]_t$ Laminate

The static load-displacement response of the impacted and virgin beams are shown together in Figure 53. From this figure it can be seen that the stiffness of the impacted beam was significantly greater than the stiffness of the virgin beam. Thus, the $[(45/-45)_2/(0)_8/(-45/45)_2]$ impacted beam appeared to be made stiffer by the initial impact. The end work required to deflect the impacted beam 13 inches was approximately 44 percent greater than the work required to deflect the virgin beam the same amount. No statement can be made about failure, since neither beam failed in the end displacement range tested.

The tensile side and compressive side surface strain magnitudes for both the impacted and virgin beams are plotted versus curvature in Figure 54. From this figure, it can be seen that the initial impact had no effect on the amount of the difference in magnitudes between the tensile side and compressive side surface strains.

4.4 Observations

From the results presented in this chapter, several observations were noted. These are:

1. The high initial load spike just after impact caused only slightly more degradation in energy-absorbing capacity in the thicker beams than in the thinner beams. For the $[0]_{30}$ beam, the degradation was caused by the extensive longitudinal splitting of the specimen. For the remaining thick-beam specimens the damage after impact was not so apparent. For the thick beams, the peak surface strains (as shown in Table 5 on page 69) were 40 to 60 percent higher than the peak surface strain magnitudes in the corresponding thin beams. This higher strain state likely caused more cracking, or damage, in the laminate.

$$[(45/-45)_2/(0)_8/(-45/45)_2]_t$$

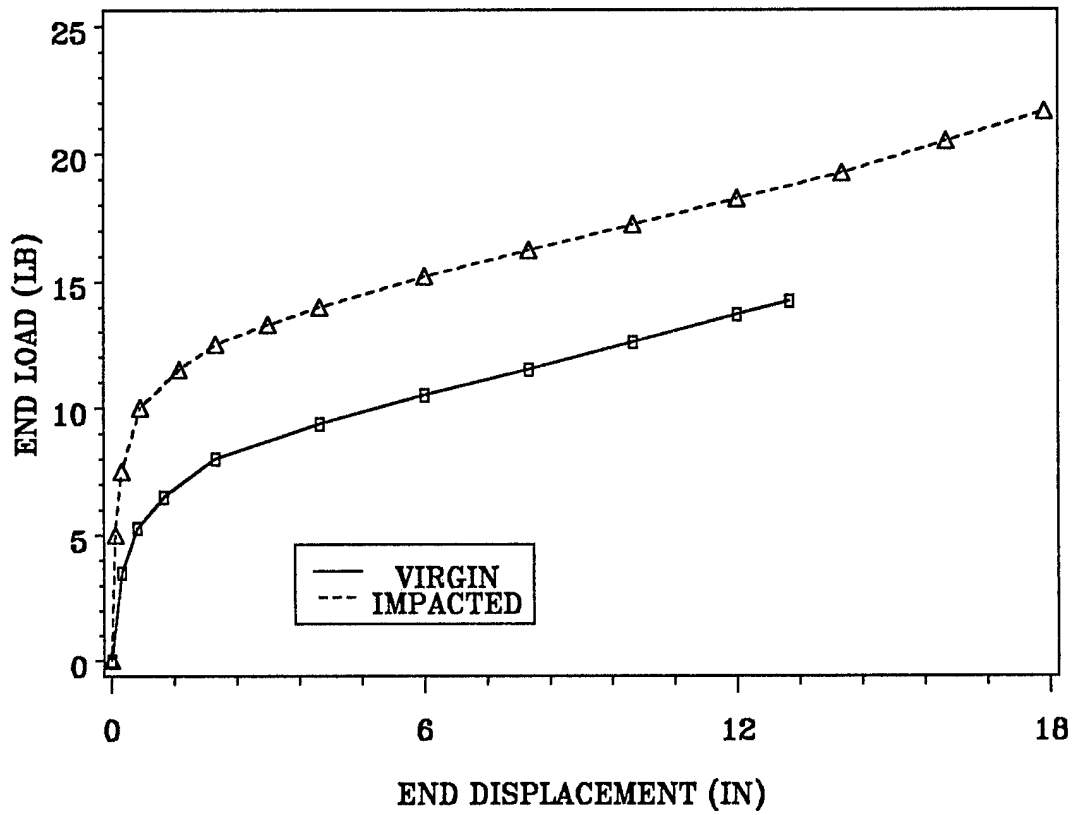


Figure 53. End load vs end displacement for impacted and virgin $[(45/-45)_2/(0)_8/(-45/45)_2]$ beams

$$[(45/-45)_2/(0)_8/(-45/45)_2]_t$$

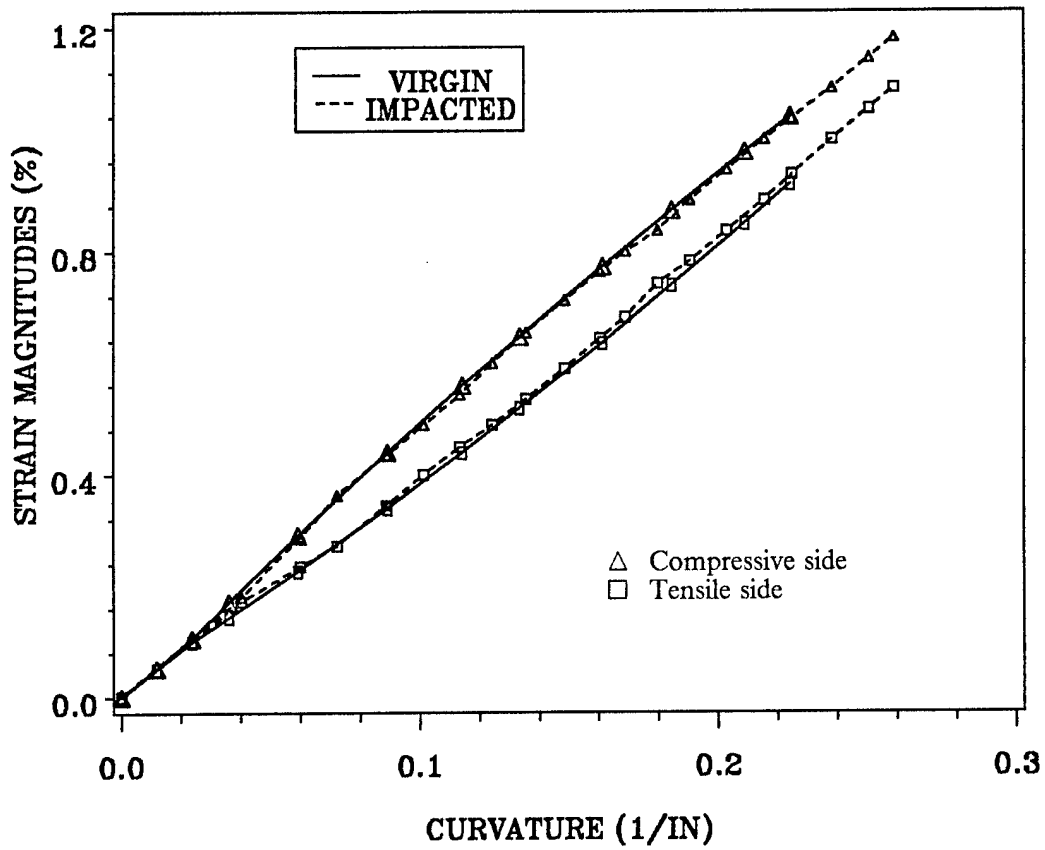


Figure 54. Surface strain magnitudes for impacted and virgin $[(45/-45)_2/(0)_8/(-45/45)_2]$ beams

This reduced the bending stiffness of the laminate and probably the flexural strength of the laminate.

The fact that the response of the thicker beams degrades more than the response of the thinner beams seems inconsistent with the fact that the ratios of dynamic peak load to maximum static load (as shown in Table 4 on page 66) are higher for the thin beams than for the thick beams. Thus, the peak strain levels are a better indicator of possible impact damage than the peak load levels.

2. The thick beams with a higher percentage of fibers directed in the longitudinal direction suffered more degradation energy-absorbing capacity. Specifically, the $[0]_{30}$ beam energy-absorbing capacity was reduced approximately 25 percent in terms of end work required to displace the beams to failure. The end work of the $[(30/0/-30)_5]_s$ beam was reduced about 12 percent, and the end work of the $[(45/-45/0/90)_4]_s$ beam was actually increased by about 3 percent.
3. The longitudinal strain magnitudes on the tensile and compressive sides of most of the specimens were virtually unaffected by the high initial load spike. The two unidirectional beams $[0]_{30}$ and $[0]_{18}$ were exceptions, since the impacted specimens exhibited smaller strain magnitude differences with respect to their virgin counterparts. This was due to the longitudinal splitting of these unidirectional beams.
4. The two compliant beam layups of $[(45/-45/0/90)_2]_s$ and $[(45/-45)_2/(0)_8/(-45/45)_2]$ actually showed an increase in stiffness of the impacted specimens relative to the virgin specimens. It is possible that some type of "pre-conditioning" mechanism was responsible for the increase in stiffness of these two beams. For example, Stinchcomb, et al (1985) found that fatiguing notched composite laminates removed some residual stresses and increased the tensile strength of the laminates. However, they also found that the stiffness of these laminates decreased. Thus, in light of the stiffness results from

Stinchcomb, et al (1985), and the fact that the static flexure tests in the current study were performed on two different test machines, no definitive statement can be made at this time regarding the apparent increase in stiffness of the impacted beam. It is recommended that further investigation of this phenomenon be performed.

5.0 Material Characterization Tests

It was noted in Chapter 2 that there was a difference between the magnitudes of the tensile and compressive surface strains on all of the beams tested in both the static and dynamic tests. Derian and Hyer (1986) suggested that nonlinear material behavior was a possible cause of this strain difference. Thus, it was desired to undertake a full characterization of the material used in the fabrication of the beams to determine if the material indeed exhibits nonlinear stress- strain behavior. If such behavior exists, then it could be incorporated into the analysis to better predict the response of the beams and the difference in strain magnitudes.

A full set of material characterization tests was performed using testing facilities at Virginia Tech. The response of the material in both the fiber and transverse material directions to both tension and compression was obtained. In addition to these tests, the inplane shear response was also analyzed. This chapter discusses the various test methods used for this characterization and presents the results.

5.1 Test Methods

5.1.1 Tension

The coupons for tensile testing were cut from a panel of AS4/3502 graphite/epoxy that was 18 plies thick (approximately 0.1 inches (0.254 cm) thick) and was laid up by NASA Langley Research Center's Fabrication Group. A diamond-blade saw was used to cut the panels. The coupons were 10 inches (25.40 cm) long with a gage length of 6.5 inches (16.51 cm). The width of the specimens was uniform along the length. For the specimens loaded in the fiber direction, the width was 0.5 inches (1.270 cm). The specimens loaded in the transverse direction were 1.0 inches (2.54 cm) wide. The specimens were not tabbed. One longitudinal and one transverse strain gage was mounted at the center of each coupon. The longitudinal gage measured axial strain, while the transverse gage measured strain due to the Poisson effect.

The tension tests were performed in a screw-driven United Testing Systems (UTS) tension/compression testing machine under displacement control. A strip of emery cloth was placed between the specimen and the standard Instron grips to increase friction and prevent slippage of specimen. The applied load was measured by UTS load cells. This load, along with the strains from the longitudinal- and transverse- mounted strain gages, was recorded using a computerized data acquisition system developed at Virginia Tech.

5.1.2 Compression

The coupons for compression testing were cut from the same panel as the tension coupons. The compression specimens were 1.5 inches (3.81 cm) long. Some of the specimens were 1.0

inches (2.54 cm) wide, and the rest were 0.75 inches (1.905 cm) wide. Each coupon had two axial strain gages mounted back-to-back at the center of the coupon. These two strain gage measurements were averaged to obtain the axial strain. This procedure removed any bending effects. These effects were found to be small, as the difference between the strains was less than three percent. There was also a transverse strain gage on one side of the coupon to measure Poisson ratio.

The compression tests were performed in the same universal test machine as the tension tests. A compression fixture designed by Dr. Zafer Gürdal of Virginia Tech was selected for these tests. This fixture will be described by Gürdal in a future publication. The Gürdal fixture is shown in Figure 55. The coupons are not gripped at the loaded ends by this fixture. This is an end-loading fixture with brooming of the specimen at the ends prevented by four quarter-cylindrical steel pieces that constrain transverse expansion at the ends. Along the sides of the specimen, four steel rods provide restraints against buckling. As in the tension tests, displacement-controlled loading was used, and load and strain data were recorded by the same computer-controlled data acquisition system.

5.1.3 Inplane Shear

An Iosipescu test (Iosipescu, 1967) was chosen to characterize the inplane shear response of this material. The coupons were cut from the same panel as were the tension and compression coupons. The geometry and dimensions of the Iosipescu specimens are shown in Figure 56. A rectangular rosette (0°, 45°, 90°) was mounted on each specimen.

The loading for the Iosipescu tests was applied using the same machine as the tension and compression tests. The load and strain gage data were again acquired by a computerized

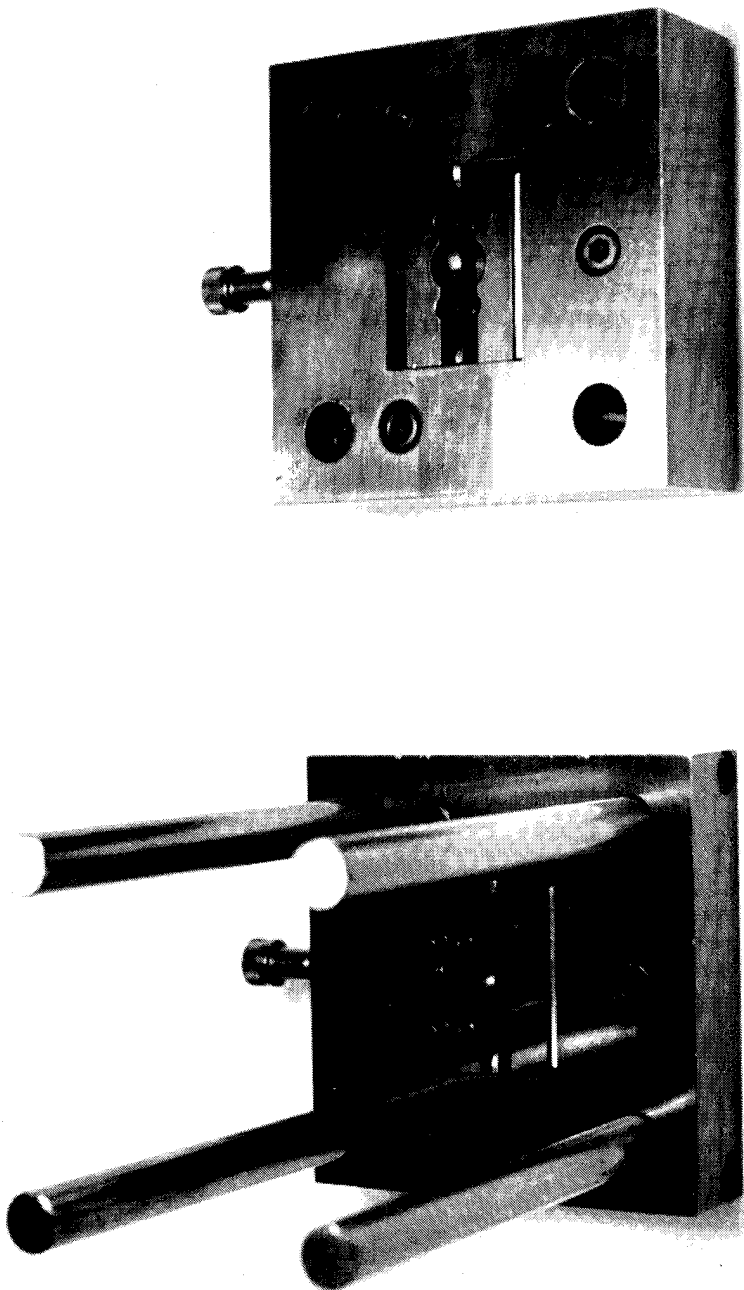


Figure 55. Gurdal compression test fixture

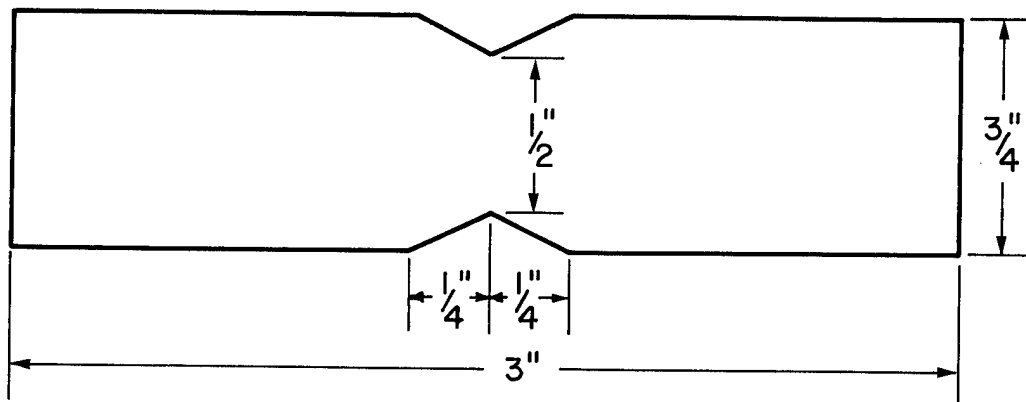


Figure 56. Iosipescu specimen geometry and dimensions

data acquisition system. The three normal strains were transformed to obtain the shear strain, and the shear stress was calculated from the applied load.

5.2 Data Reduction

As many as five replicates were used for each characterization test. The scatter in the response data was quite small. For each of the tests, the stress-strain curves for all the replicates were approximately coincident (within two percent). There was a fairly small variation in failure stresses. The minimum, maximum, and mean failure stresses for each test are presented in Table 6 on page 103. For the results shown in this Chapter, the average of the data from all the replicates within a given test were used. The material characterization curves are shown up to the highest recorded failure loads.

5.3 Results

5.3.1 Longitudinal Response

5.3.1.1 Tension

The tensile response of the material in the fiber direction (Figure 57) exhibited noticeable nonlinearity. The stress-strain curve has a small region of linear behavior beginning at the origin followed by a region in which the slope increases monotonically from its beginning

Table 6. Summary of failure stresses

Test	Minimum failure stress (ksi)	Maximum failure stress (ksi)	Mean failure stress (ksi)	Number of tests
Longitudinal tension	167.4	182.5	178.1	4
Longitudinal compression	-121.6	-139.0	-132.4	5
Transverse tension	7.42	7.51	7.46	2
Transverse compression	-30.4	-33.6	-32.3	3
Inplane shear	11.9	13.1	12.5	2

value. The Poisson response is presented in Figure 58. Initial values and the values at failure for the tensile fiber direction modulus, E_{1t} , are given in Table 7 on page 116. The Poisson's ratio was found to remain approximately constant at a value of 0.29.

5.3.1.2 Compression

The compression response of the material in the fiber direction (Figure 59) also exhibited noticeable nonlinearity. As in the tension tests, there was a small region of linear behavior near the origin. However, in contrast to the tension tests, monotonically decreasing slope followed the linear region. The compression Poisson response is shown in Figure 60. The transverse strain actually became negative near the origin. This was true even on specimens which were pre-loaded then unloaded prior to actual testing. This was believed to be a function of the test fixture, but no explanation could be found for this behavior, so this portion of the curve was ignored. The Poisson's ratio for the remainder of the curve was an approximately constant value of 0.30. The initial and final values of the compressive modulus, E_{1c} are presented in Table 7 on page 116.

5.3.1.3 Combined

A combined plot of the full longitudinal response, in both tension and compression, is shown in Figure 61. From this plot, the difference in the tensile and compressive response can easily be seen.

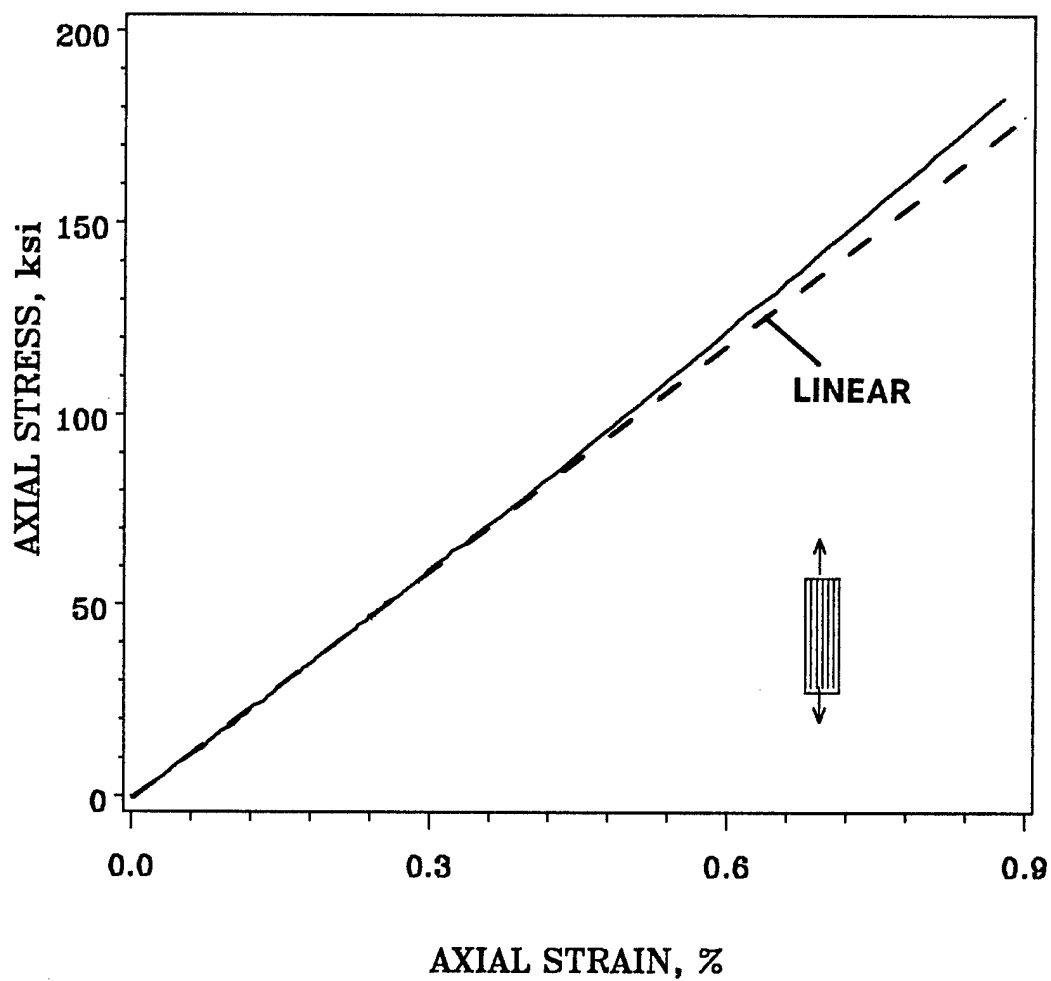


Figure 57. Longitudinal tension stress-strain response

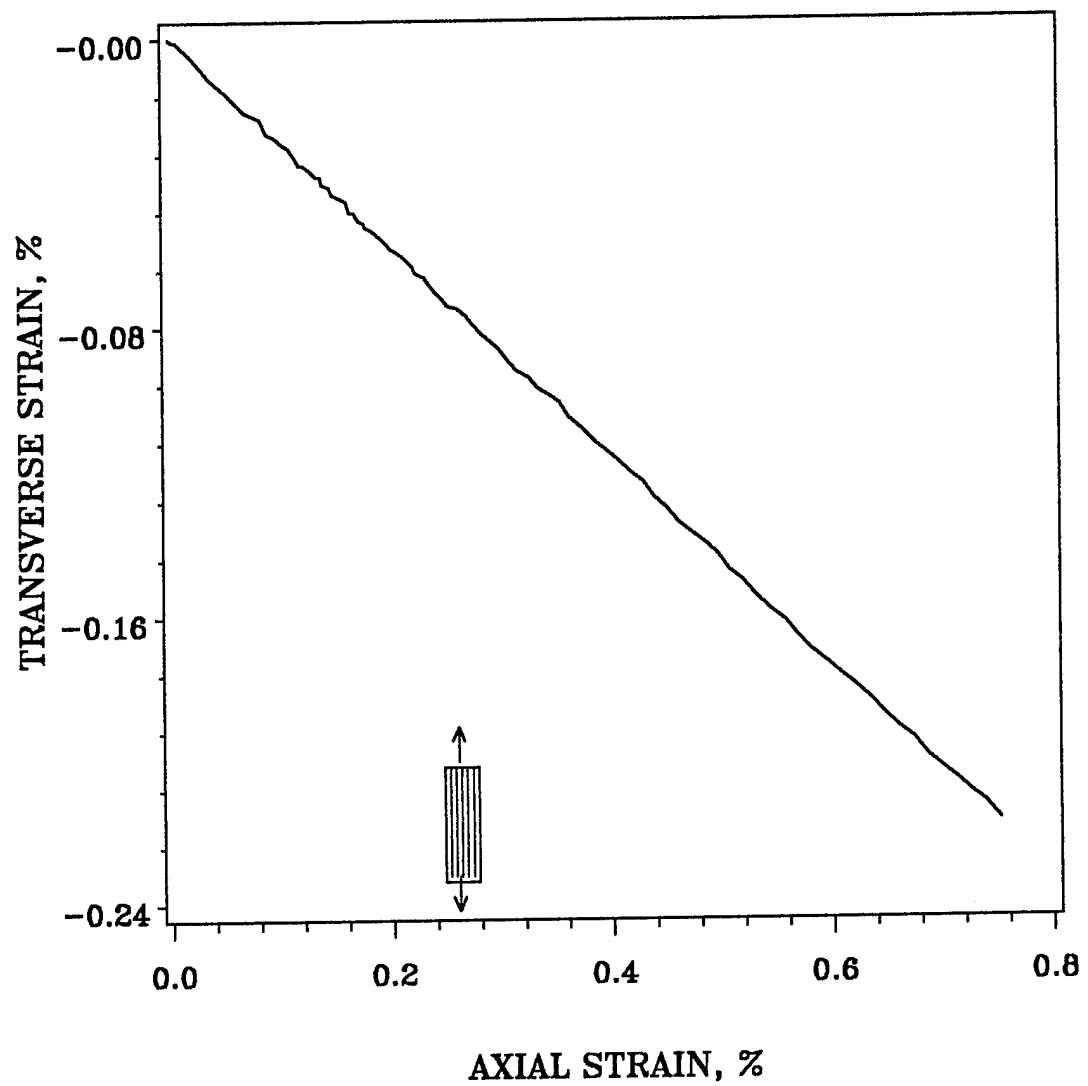


Figure 58. Poisson response in longitudinal tension

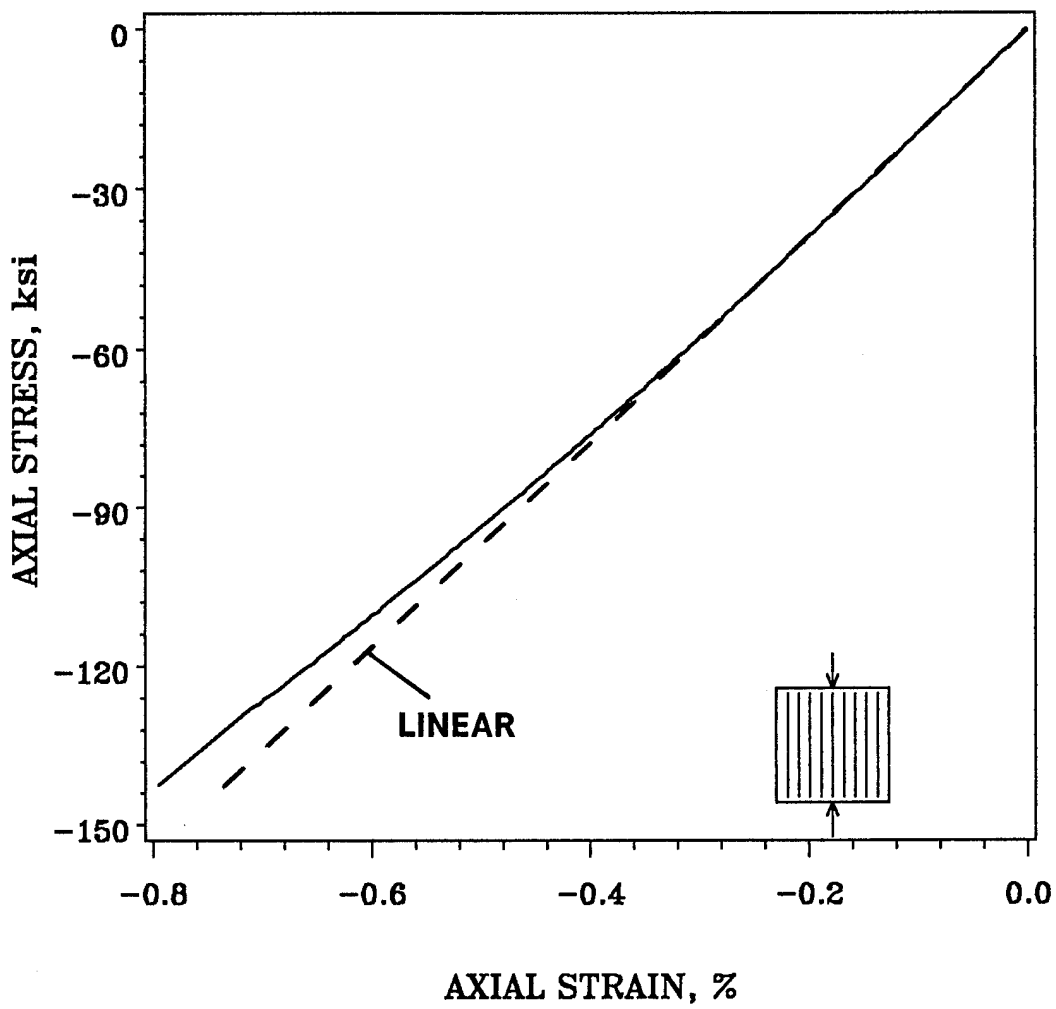


Figure 59. Longitudinal compression stress-strain response

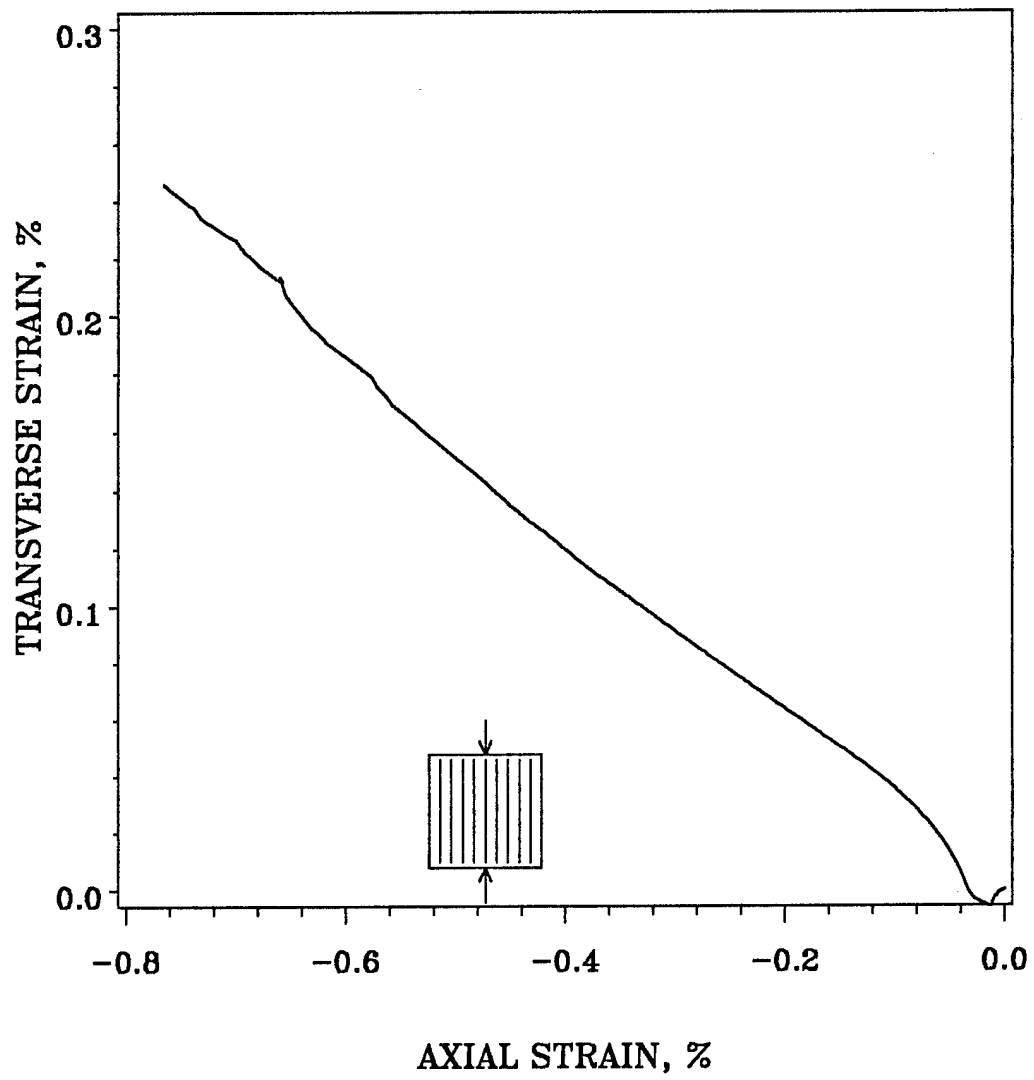


Figure 60. Poisson response in longitudinal compression

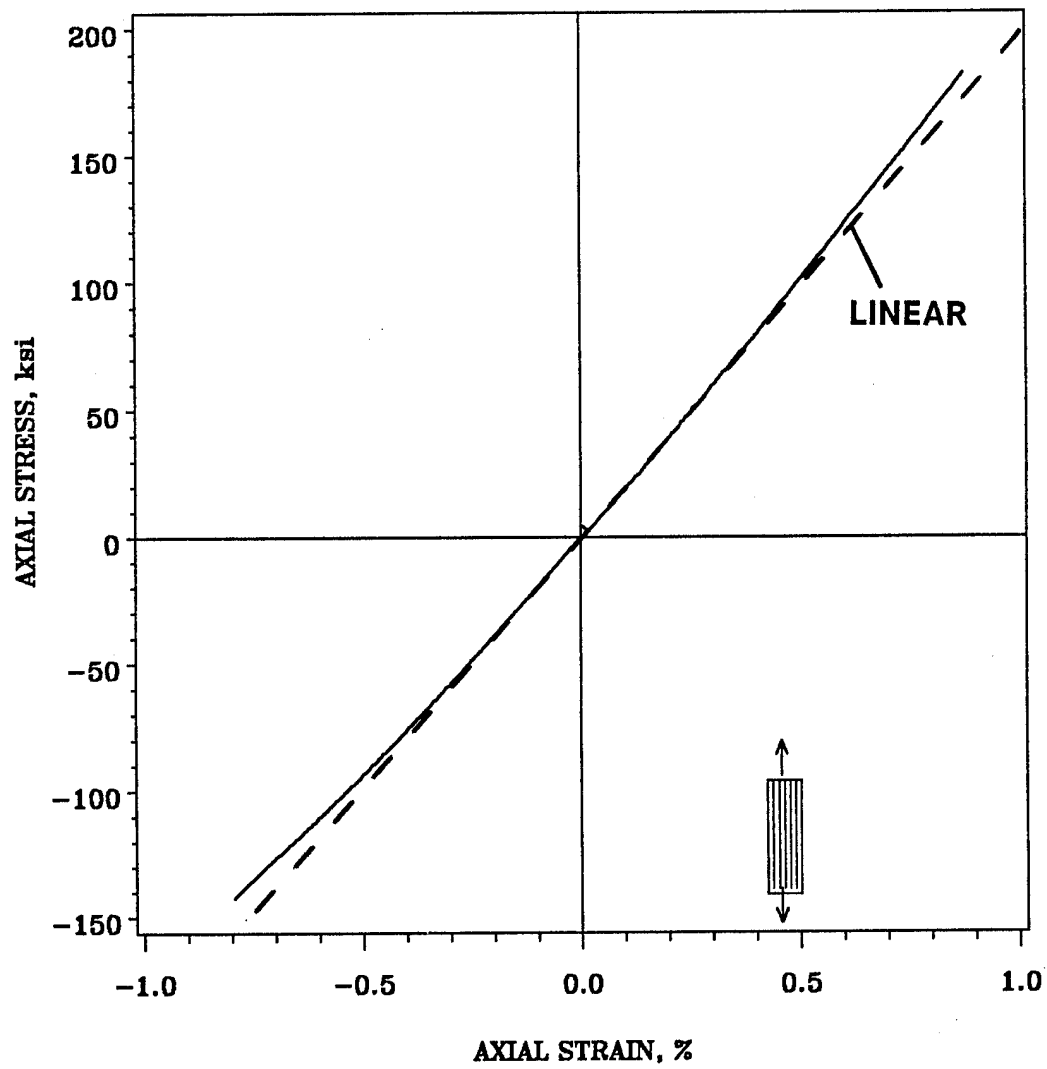


Figure 61. Longitudinal stress-strain response

5.3.2 Transverse Response

5.3.2.1 Tension

The tensile response of the material in the transverse direction differed from the response in other types of loading, and was essentially linear to failure, as shown in Figure 62. The initial and final values of the tensile transverse modulus, E_{2t} , are shown in Table 7 on page 116.

5.3.2.2 Compression

The compressive response of the material in the transverse direction exhibited substantial nonlinearity. As in the longitudinal compression tests, there was a small region of linear behavior followed by a continuous reduction in stiffness, as shown in Figure 63. The initial and final values of the compressive transverse modulus, E_{2c} , are presented in Table 7 on page 116.

5.3.2.3 Combined

The combined response in the transverse direction, including both tension and compression, is shown in Figure 64. The difference in transverse tensile and compressive response can easily be seen from this figure.

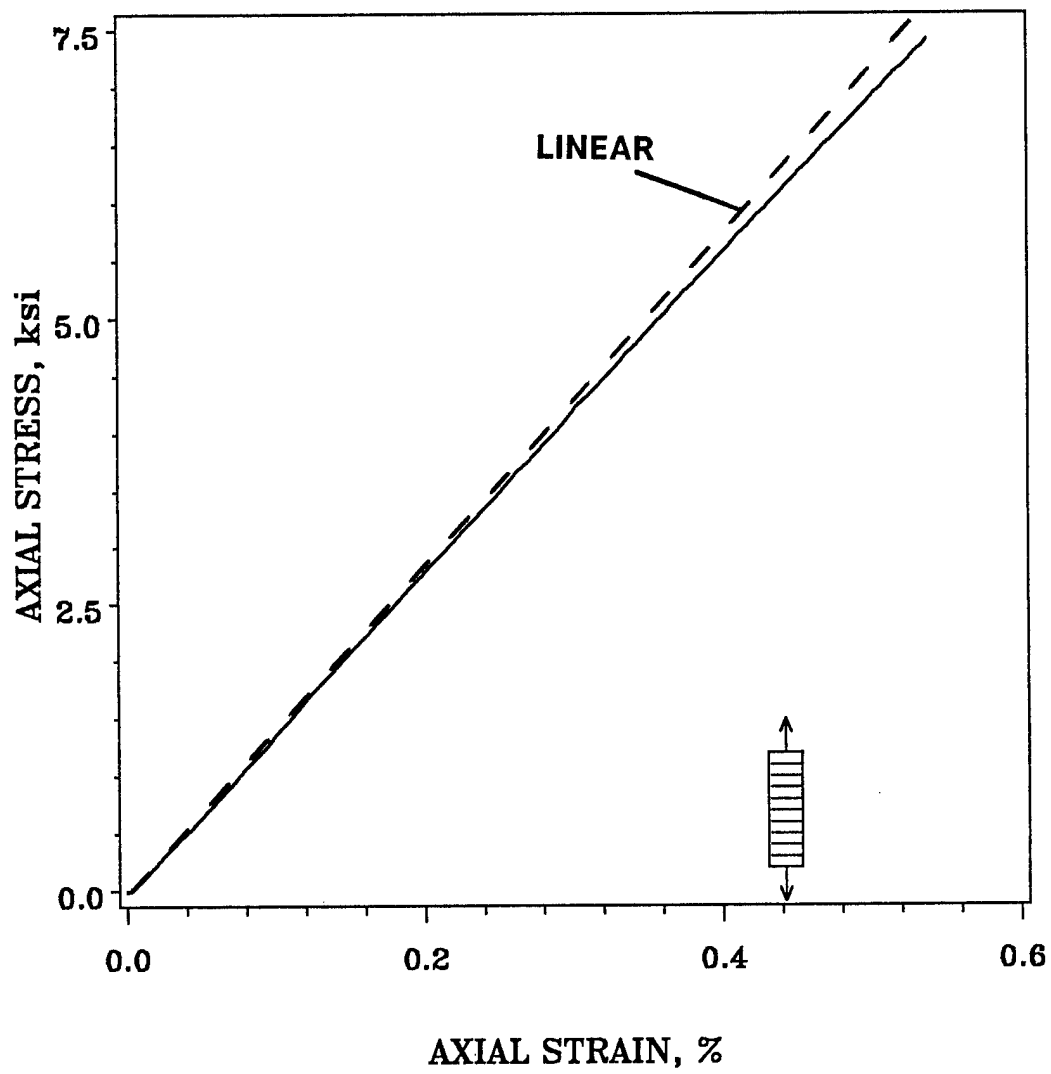


Figure 62. Transverse tension stress-strain response

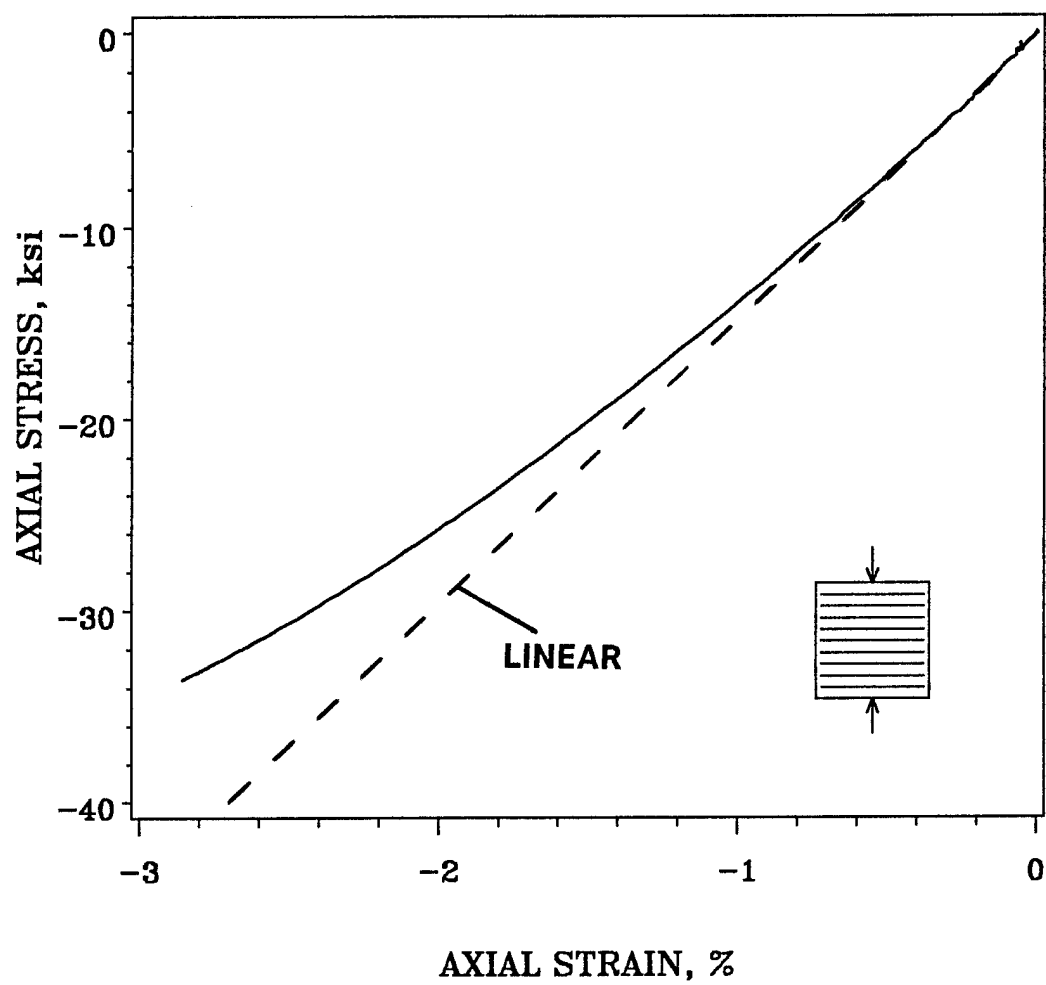


Figure 63. Transverse compression stress-strain response

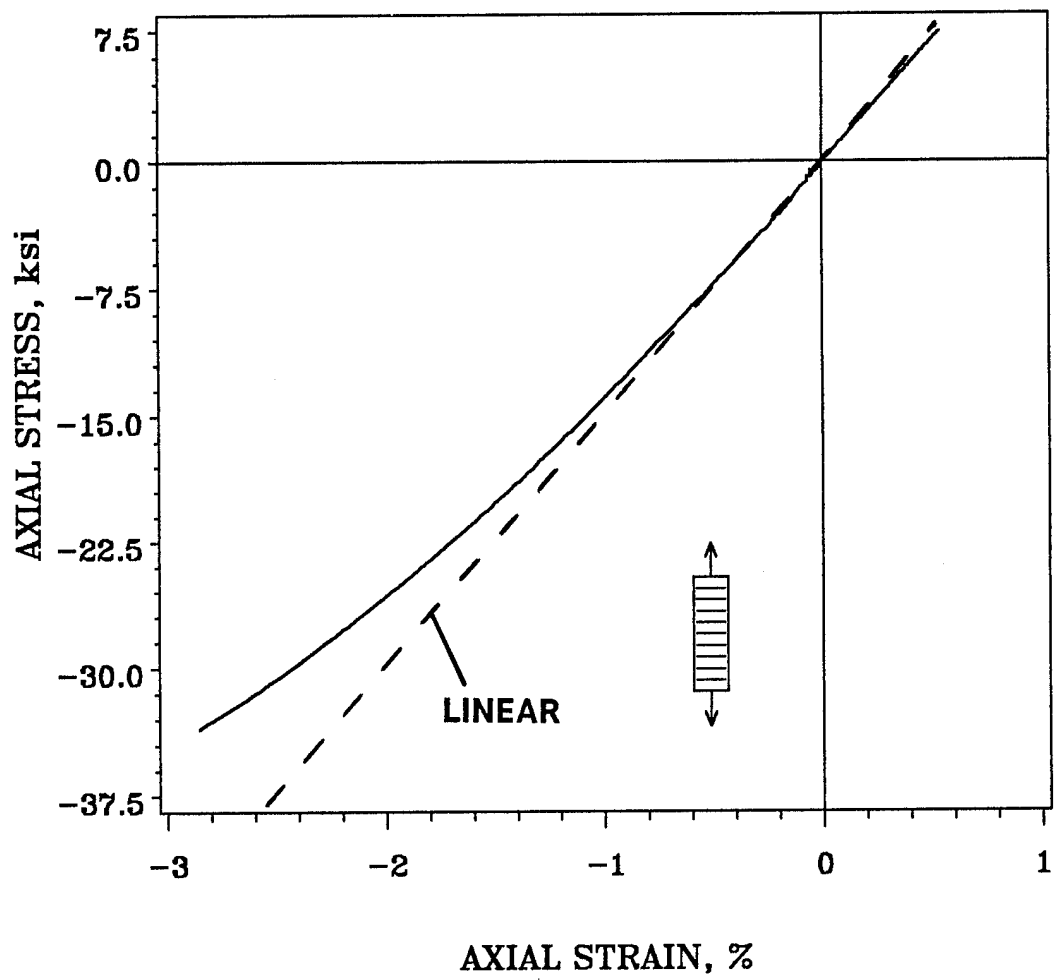


Figure 64. Transverse stress-strain response

5.3.3 Inplane Shear

The inplane shear response of the material showed a great deal of nonlinearity. The linear response region was much smaller than the linear regions in the four principal material tests discussed above. The shear stiffness continuously diminished to a value much smaller than the initial value. The shear stress-strain response is shown in Figure 65. The initial and final values of G_{12} are presented in Table 7 on page 116.

5.4 *Summary of Material Characterization*

The results of the material characterization tests are summarized in Table 7 on page 116. The initial and final values for moduli and the strains at which the final values are taken are listed in the table.

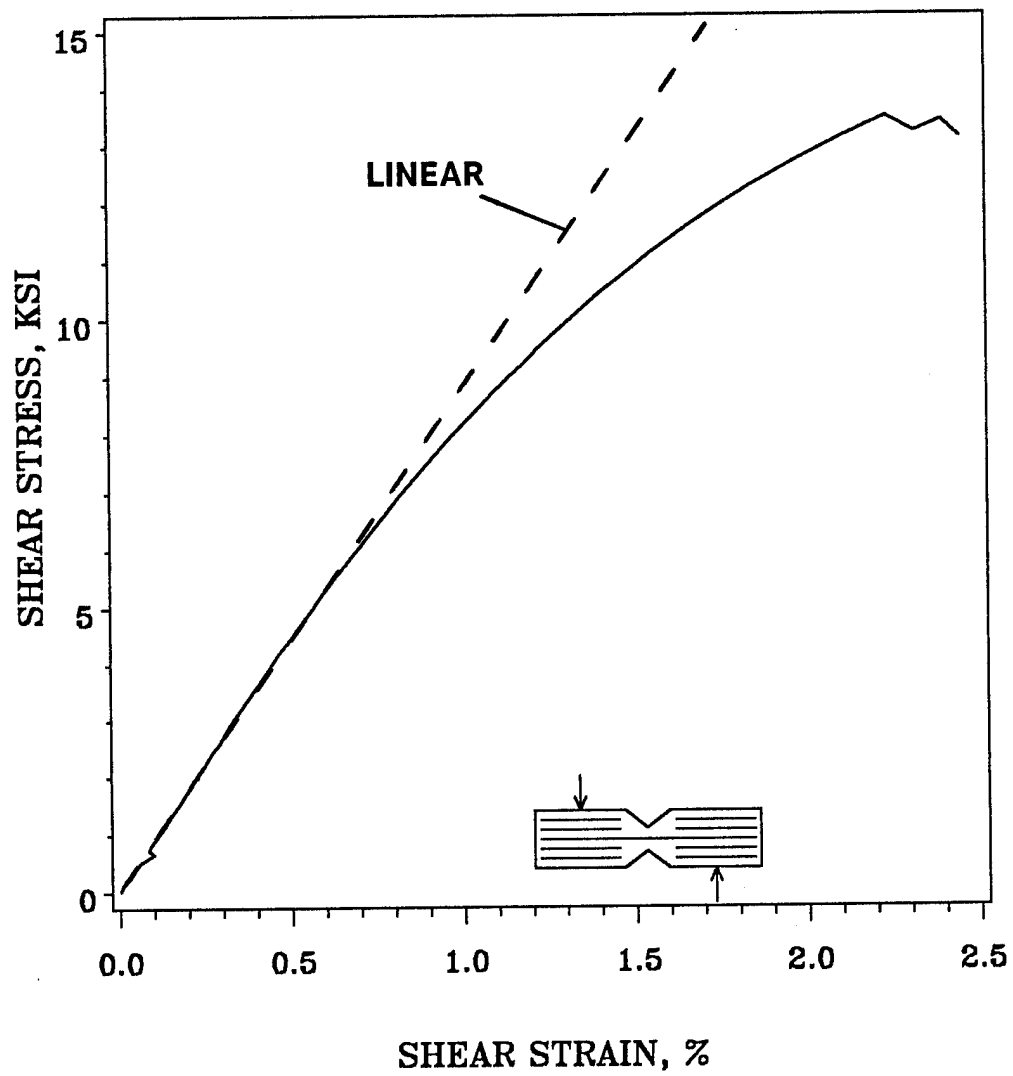


Figure 65. Inplane shear stress-strain response

Table 7. Summary of material characterization tests

Test	Initial modulus (Msi)	Final modulus (Msi)	Final strain (%)	% Change in modulus
Longitudinal tension	19.85	24.62	0.90	+ 24.0
Longitudinal compression	19.40	14.56	-0.70	-24.9
Transverse tension	1.43	1.21	0.55	-15.4
Transverse compression	1.48	0.76	-2.90	-48.6
Inplane shear	0.82	0.24	2.50	-70.7

6.0 Analytical Development

A finite element model was developed to predict the large deformation response of the beams.

The main goals of the analysis were:

1. To predict the static load-displacement response of the beams.
2. To predict the experimentally observed discrepancy between the magnitudes of the tensile side and compressive side strains.
3. To predict the load and displacement at failure.

Static analysis was performed in the present study, since a firm understanding of the static response is necessary before undertaking a dynamic analysis. Derian and Hyer (1986) used the existing finite element code, ACTION (Kamat, 1980, 1980a) to successfully predict the load-displacement response of the beams both statically and dynamically. However, this analysis used material property inputs which were derived empirically from the flexure experiments themselves. Furthermore, that analysis did not include prediction of the surface strain response. Thus, the goal of the current analysis was to predict both the displacement

and strain response using material property data obtained from a separate material characterization program.

6.1 Assumptions

A number of assumptions were made in development of the finite element model used in this analysis. They are:

1. A corotational procedure was used to account for the geometric nonlinearity encountered in the large deflection of the beams. This procedure will be discussed in detail later in this chapter. An advantage of this procedure is that small deflections can be assumed for a given load step. Thus, it is assumed that the deflections in a given element are on the order of the thickness of the beam within a load step.
2. Each element is modeled as a flat plate for each load step. That is, the basic assumptions of laminated plate theory (Ashton and Whitney, 1970) are valid.
3. Stress interaction is neglected. In other words, the stress-strain curves obtained from uniaxial material characterization tests are used to determine the stiffnesses of a given ply subjected to a multiaxial stress state.
4. To reduce the computational effort required for the analysis, the problem was simplified to a one-dimensional nature using the Kantrovich method (Fung, 1965). Preliminary analysis using cylindrical bending theory was largely unsuccessful, so a model which accounts for width-wise effects was developed. These effects are modeled by assuming forms for the incremental midplane displacements that are explicit in the y -coordinate and whose "coefficients" are unknown functions of the

x-coordinate. The following forms are used (see Figure 66 for definition of beam coordinate system):

$$\begin{aligned}u^0 &= U(x) + \eta(x)y + \alpha(x)y^2 \\v^0 &= V(x) + \omega(x)y \\w^0 &= W(x) + \Theta(x)y + g(x)y^2\end{aligned}\tag{6.1}$$

In addition to the beam deflections U , V , and W , the "coefficient" functions η , α , ω , Θ , and g are introduced into the model as degrees of freedom. This allows the inclusion of limited width-wise effects without the complexity of a two-dimensional model.

6.2 *Finite Element Formulation*

Beginning with the displacement assumptions listed above, a finite element model was developed using a variational energy formulation. The steps involved with this procedure are outlined in this section.

6.2.1 Strain-Displacement Equations

Using the Kirchhoff assumptions of thin plate theory the incremental displacements are

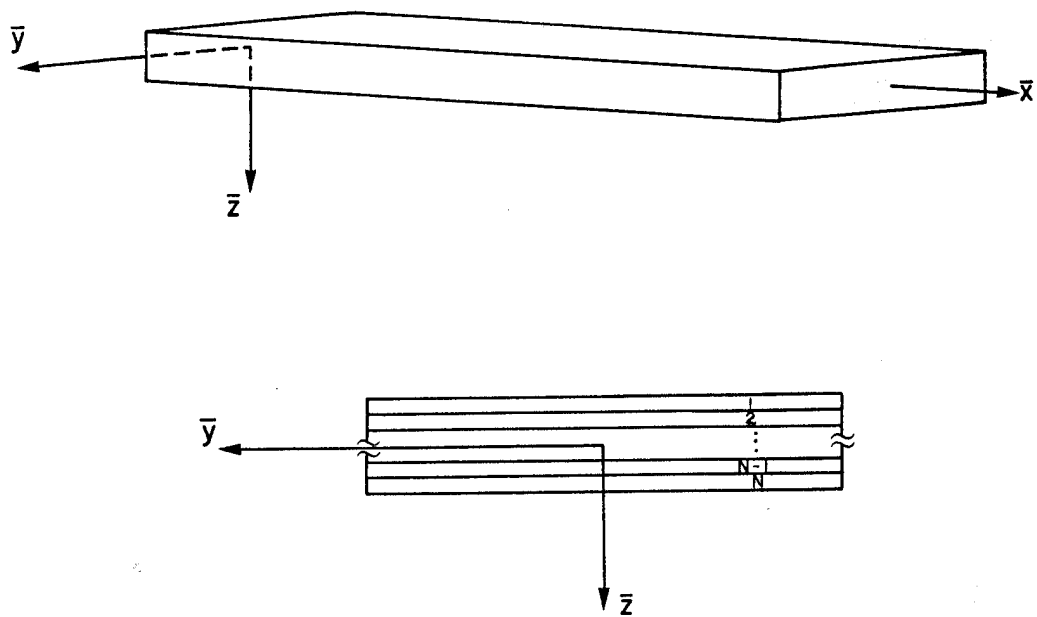


Figure 66. Definition of beam coordinate system

$$u = u^0 - zw_{,x}$$

$$v = v^0 - zw_{,y} \quad (6.2)$$

$$w = w^0$$

and the incremental strains are

$$\varepsilon_x = \varepsilon_x^0 + z\kappa_x$$

$$\varepsilon_y = \varepsilon_y^0 + z\kappa_y \quad (6.3)$$

$$\gamma_{xy} = \gamma_{xy}^0 + z\kappa_{xy}$$

where the incremental midplane strains and curvatures are given by the following expressions

$$\varepsilon_x^0 = u^0_{,x}$$

$$\varepsilon_y^0 = v^0_{,y} \quad (6.4)$$

$$\gamma_{xy}^0 = u^0_{,y} + v^0_{,x}$$

$$\kappa_x = -w_{,xx}$$

$$\kappa_y = -w_{,yy} \quad (6.5)$$

$$\kappa_{xy} = -2w_{,xy}$$

The kinematic assumptions presented in Equations (6.1) can then be substituted into Equations (6.4) and (6.5) to obtain the expressions for incremental midplane strains and

curvatures in terms of the functions $U, V, W, \alpha, \eta, \omega, \Theta$, and g . This yields the following equations

$$\begin{aligned}
 \varepsilon_x^0 &= U'(x) + \eta'(x)y + \alpha'(x)y^2 \\
 \varepsilon_y^0 &= \omega(x) \\
 \gamma_{xy}^0 &= \eta(x) + V'(x) + (2\alpha(x)y + \omega'(x))y \\
 \kappa_x &= -W''(x) - \Theta''(x)y - g''(x)y^2 \\
 \kappa_y &= -2g(x) \\
 \kappa_{xy} &= -2\Theta'(x) - 4g'(x)y
 \end{aligned} \tag{6.6}$$

where the primes denote derivatives with respect to x .

6.2.2 Constitutive Equations

Since all assumptions in this model are consistent with classical lamination theory, the incremental constitutive relations are of the familiar form (Jones, 1975):

$$\begin{Bmatrix} N \\ M \end{Bmatrix} = \begin{bmatrix} A & B \\ B & D \end{bmatrix} \begin{Bmatrix} \varepsilon^0 \\ \kappa \end{Bmatrix} \tag{6.8}$$

6.2.3 Variational Energy Formulation

The theorem of stationary potential energy can be expressed as:

$$\delta E_s + \delta E_p + \delta E_E = 0 \quad (6.9)$$

where E_s is the strain energy of the laminate, E_p is the strain energy in small bending due to an initial axial tensile force P acting in the local x -direction (Yang, 1972), and E_E is the energy of the applied loads. The expressions for the variations of these quantities in terms of the inplane forces and moments, the midplane strains and curvatures, and the applied loads are given by the following equations.

$$\delta E_s = \iint \{ N_x \delta \epsilon_x^0 + N_y \delta \epsilon_y^0 + N_{xy} \delta \gamma_{xy}^0 + M_x \delta \kappa_x + M_y \delta \kappa_y + M_{xy} \delta \kappa_{xy} \} dA \quad (6.10)$$

$$\delta E_p = \iint \{ P w_{,x} \delta w_{,x} \} dA \quad (6.11)$$

$$\delta E_E = \int \{ \bar{N}_x \delta u^0 + \bar{N}_y \delta v^0 + \bar{Q} \delta w + \bar{M}_x \delta w' \} dy \quad (6.12)$$

Note that the \bar{N} represents external applied loads. The value of the axial force P is determined from the "initial" geometry of the beam at the start of a given load step and from the known applied load. The expressions for midplane strains and curvatures (Equations (6.6) and (6.7)) and the constitutive relations (Equations (6.8)) can then be substituted into the variational expressions of Equations (6.10) through (6.12). Also, these expressions can be integrated in the width-wise direction since all the expressions are explicit in y . The algebra and integration is straightforward and will be omitted here.

6.2.4 Formulation of Finite Element Equations

The variational equations derived above can be used to formulate a finite element model of the problem. To do this, interpolation functions must be chosen to approximate the variables in the equations. Since only derivatives of the first order appear in these equations for the variables U, V, η, α , and ω , linear interpolation functions may be used.

$$U(x) = \sum_{j=1}^2 U_j \psi_j \quad (6.13)$$

$$V(x) = \sum_{j=1}^2 V_j \psi_j \quad (6.14)$$

$$\eta(x) = \sum_{j=1}^2 \eta_j \psi_j \quad (6.15)$$

$$\alpha(x) = \sum_{j=1}^2 \alpha_j \psi_j \quad (6.16)$$

$$\omega(x) = \sum_{j=1}^2 \omega_j \psi_j \quad (6.17)$$

The well-known linear interpolation functions, $\psi(x)$, are:

$$\psi_1(x) = 1 - \frac{\bar{x}}{L}$$

$$\psi_2(x) = \frac{\bar{x}}{L} \quad (6.18)$$

where \bar{x} is the local length coordinate of the element and L is the length of the element.

The linear interpolation used to approximate these functions allows for continuity of solutions at element nodes, but does not provide continuous first derivatives at the nodes. This is satisfactory, however, since essential boundary conditions at the ends

of an element for inplane displacements involve only the functions and not the derivatives.

The variational formulation requires, however, continuity of the transverse displacement and its derivative. Thus, a higher-order interpolation is required for this displacement. A Hermite cubic interpolation was chosen for W , Θ , and g .

$$W(x) = \sum_{j=1}^4 W_j \phi_j \quad (6.19)$$

$$\Theta(x) = \sum_{j=1}^4 \Theta_j \phi_j \quad (6.20)$$

$$g(x) = \sum_{j=1}^4 g_j \phi_j \quad (6.21)$$

The Hermite cubic interpolation functions, $\phi(x)$, are:

$$\begin{aligned} \phi_1(x) &= 1 - 3\left(\frac{\bar{x}}{L}\right)^2 + 2\left(\frac{\bar{x}}{L}\right)^3 \\ \phi_2(x) &= -\bar{x} + \frac{2\bar{x}^2}{L} - \frac{\bar{x}^3}{L^2} \\ \phi_3(x) &= 3\left(\frac{\bar{x}}{L}\right)^2 - 2\left(\frac{\bar{x}}{L}\right)^3 \\ \phi_4(x) &= -\bar{x}\left[\left(\frac{\bar{x}}{L}\right)^2 - \frac{\bar{x}}{L}\right] \end{aligned} \quad (6.22)$$

The Hermite cubic interpolation allows for continuous solutions as well as continuous first derivatives at the nodes.

If the approximated functions are substituted into the variational equations, a set of finite element equations is generated. There are eleven degrees of freedom at each node point. Eight of these are the displacement functions, U , V , W , η , α , ω , Θ , and g . The re-

maining three degrees of freedom are the negative first derivatives of W , Θ , and g . These degrees of freedom are introduced as a result of the Hermite cubic approximation. Thus, there are 22 degrees of freedom per element. The element stiffness matrix will be a 22 by 22 symmetric square matrix comprised of 64 submatrices. The finite element equations can be summarized in partitioned matrix form as:

$$\begin{array}{c}
 2 \\
 2 \\
 2 \\
 2 \\
 2 \\
 4 \\
 4 \\
 4
 \end{array}
 \begin{bmatrix}
 [k^{11}] & [k^{12}] & \cdot & \cdot & \cdot & \cdot & \cdot & [k^{18}] \\
 [k^{21}] & \cdot & & & & & & \cdot \\
 \cdot & & \cdot & & & & & \cdot \\
 \cdot & & & \cdot & & & & \cdot \\
 \cdot & & & & \cdot & & & \cdot \\
 \cdot & & & & & \cdot & & \cdot \\
 \cdot & & & & & & \cdot & \cdot \\
 [k^{81}] & \cdot & \cdot & \cdot & \cdot & \cdot & \cdot & [k^{88}]
 \end{bmatrix}
 \begin{Bmatrix}
 \{U\} \\
 \{\alpha\} \\
 \{\eta\} \\
 \{V\} \\
 \{\omega\} \\
 \{W\} \\
 \{g\} \\
 \{\Theta\}
 \end{Bmatrix}
 =
 \begin{Bmatrix}
 \{F^1\} \\
 \{F^2\} \\
 \cdot \\
 \cdot \\
 \cdot \\
 \cdot \\
 \cdot \\
 \{F^8\}
 \end{Bmatrix}
 \quad (6.23)$$

The numbers to the left of the equations refer to the size of the partitioned vector elements in the displacement vector. The expressions for the submatrices in terms of the laminate stiffnesses A , B , and D , the interpolation functions ψ and ϕ , are shown in Appendix E. The beam width also appears in these expressions as a result of integration in the y -direction.

A typical beam element with appropriate nodal degrees of freedom and forces is presented in Figure 67.

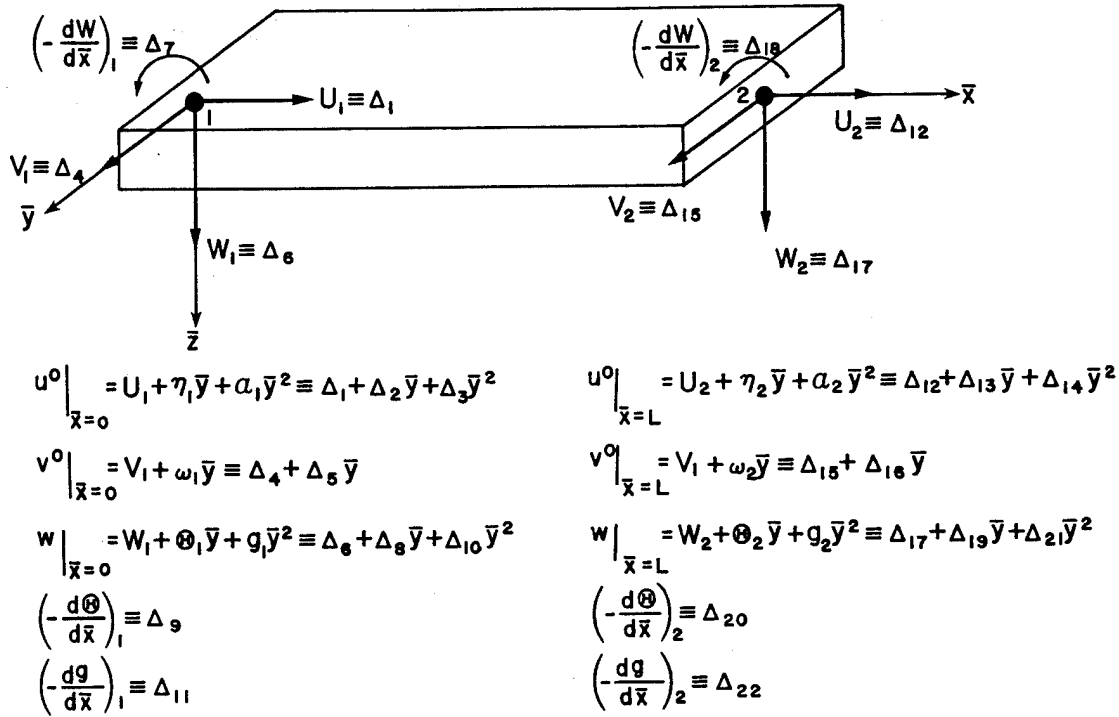


Figure 67. Typical beam element

6.3 Nonlinearity

The finite element model contains both geometric and material nonlinearity. The geometric nonlinearity is necessary due to the large global deflections of the beams. The material nonlinearity is incorporated to model the material response observed in the characterization tests. The following sections discuss these two nonlinearities and the manner in which they are incorporated into the model.

6.3.1 Geometric Nonlinearity

In finite element analysis there are generally two schemes which can be used to model nonlinear response. The first method, called Lagrangian, uses the full nonlinear equations that describe the response of a system. In other words, all displacements are referred to the initial coordinates. This method requires a nonlinear algorithm to solve the equations of motion. These equations can be quite cumbersome, and generally an iterative procedure is required to solve them. This can be computationally expensive. The second method is the Eulerian, or Updated Lagrangian, scheme. This procedure refers the displacements to a reference coordinate system which can change as the system moves.

A simplified derivative of an Updated Lagrangian method was chosen for this analysis. Specifically, the model utilizes a corotational procedure similar to that employed by Yang (1972). The prescribed load is applied in increments, or load steps, up to a desired level. The displacement in a given load step is referred to the coordinates at the end of the previous load step. In equation form, for the i -th load step,

$$[K]^{i-1} \{\delta\Delta\}^i = \{\delta Q\}^i \quad (6.24)$$

where $[K]^{i-1}$ is evaluated from the state at the end of load step $i-1$. This permits the use of small deflection theory in formulating the finite element model. The only restriction to this procedure is that the displacements in a given element within a load step must be within the limits of small deflection theory (less than the thickness of the beam).

6.3.1.1 Stiffness Transformation

As the beam deflects, the element local coordinate system rotates and translates with the element. Thus, the element stiffness matrix calculated at the beginning of a load step is referenced to the local coordinate system. It is then necessary to transform the stiffnesses into global stiffness terms to be assembled in the global stiffness matrix for the beam. This transformation is performed in the x - z plane, since the displacements in these directions are much greater than the corresponding displacements in the y -direction. This requires only one transformation angle. This angle is determined by drawing a straight line through the two nodes at the end of each element. As the beam deflects, both the coordinates of the node and the transformation angle change. Figure 68 shows this angle with respect to the global and local coordinate axes. The element local displacements and forces can be written in terms of the global displacements and forces via a transformation matrix, $[T]$. In the following discussion, $\{\bar{q}\}$, $\{\bar{\Delta}\}$, and $[\bar{K}]$ refer to forces, displacements, and stiffnesses, respectively, in the element local coordinate system.

The transformation relations are given by

$$\{\bar{q}\} = [T]\{q\} \quad (6.25)$$

$$\{\bar{\Delta}\} = [T]\{\Delta\} \quad (6.26)$$

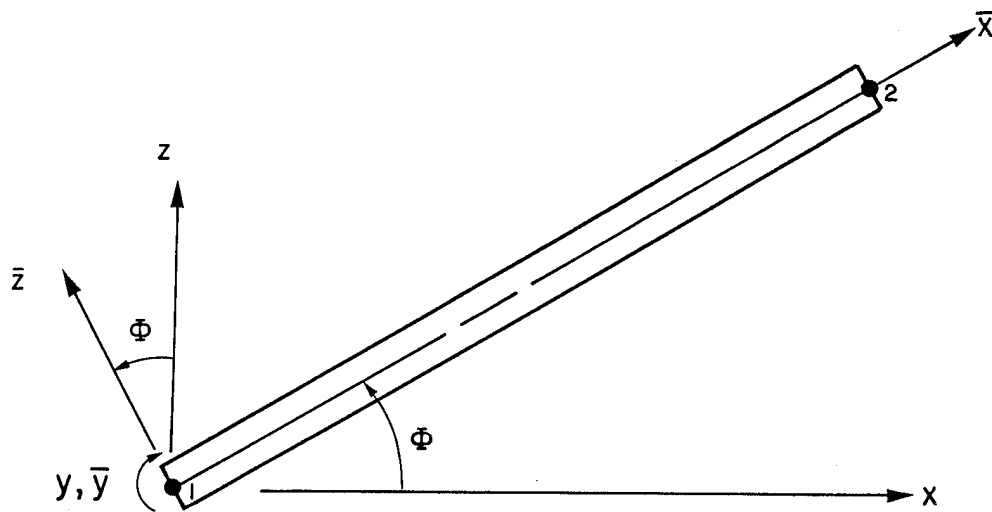


Figure 68. Global and local coordinates of element

The transformation matrix, in terms of the transformation angle, is

$$[T] = \begin{bmatrix} [t] & [0] \\ [0] & [t] \end{bmatrix} \quad (6.27)$$

where

$$[t] = \begin{bmatrix} \lambda & 0 & 0 & 0 & 0 & \mu & 0 & 0 & 0 & 0 & 0 \\ 0 & \lambda & 0 & 0 & 0 & 0 & 0 & \mu & 0 & 0 & 0 \\ 0 & 0 & \lambda & 0 & 0 & 0 & 0 & 0 & 0 & \mu & 0 \\ 0 & 0 & 0 & 1 & 0 & 0 & 0 & 0 & 0 & 0 & 0 \\ 0 & 0 & 0 & 0 & 1 & 0 & 0 & 0 & 0 & 0 & 0 \\ -\mu & 0 & 0 & 0 & 0 & \lambda & 0 & 0 & 0 & 0 & 0 \\ 0 & 0 & 0 & 0 & 0 & 0 & 1 & 0 & 0 & 0 & 0 \\ 0 & -\mu & 0 & 0 & 0 & 0 & 0 & \lambda & 0 & 0 & 0 \\ 0 & 0 & 0 & 0 & 0 & 0 & 0 & 0 & 1 & 0 & 0 \\ 0 & 0 & -\mu & 0 & 0 & 0 & 0 & 0 & 0 & \lambda & 0 \\ 0 & 0 & 0 & 0 & 0 & 0 & 0 & 0 & 0 & 0 & 1 \end{bmatrix} \quad (6.28)$$

where $\lambda = \cos \Phi$ and $\mu = \sin \Phi$.

The transformation proceeds as follows. Beginning with the finite element equations presented in the previous section (reorganized to group the displacements as shown in Figure 67)

$$[\bar{k}] \{\bar{\Delta}\} = \{\bar{q}\} \quad (6.29)$$

and substituting Equations (6.25) and (6.26), we have

$$[\bar{k}] [T] \{\Delta\} = [T] \{q\}. \quad (6.30)$$

Premultiplying both sides by the inverse of $[T]$, we obtain

$$[T]^{-1} [\bar{k}] [T] \{\Delta\} = \{q\} \quad (6.31)$$

So the global displacements and forces are related by an element stiffness matrix of the form

$$[k] = [T]^{-1} [\bar{k}] [T] = [T]^T [\bar{k}] [T] \quad (6.32)$$

since $[T]$ is orthogonal.

6.3.1.2 Corotational Procedure

After the first linear (material and geometric) step, the corotational procedure is summarized as follows:

1. Update the geometry by adding the incremental displacements from the previous load step to the total solution. This will yield the new locations of the nodes.
2. Calculate the new A, B, and D matrices for each element. Calculate element stiffness matrices in the element local coordinates using the new A, B, and D matrices.
3. Transform element stiffnesses to element global stiffness matrices by the procedure described above. The transformation angle is determined from the updated geometry as shown in Figure 68.
4. Assemble structural global stiffness matrix from transformed element stiffness matrices.

5. Apply load increment and appropriate boundary conditions, and solve for displacement increments.

$$[K]\{\delta\Delta\} = \{\delta Q\} \quad (6.33)$$

6. Calculate strain increments for each ply in each element.
7. Proceed to next load step.

6.3.2 Material Nonlinearity

The experimentally observed difference between the surface strain magnitudes on the compressive and tensile sides of the beams led Derian and Hyer (1986) to speculate that linear material behavior was perhaps not valid. From the material characterization tests discussed in Chapter 4, it was obvious that the material behavior was nonlinear. Therefore nonlinear stress-strain relations were included in the finite element model. The stress-strain curves were obtained from the material characterization tests discussed in Chapter 4. The experimental curves were approximated by polynomials, and these algebraic expressions were programmed into the model. These polynomial expressions are summarized in Appendix F. After the initial linear step, the basic procedure for implementation of the material nonlinearity is as follows:

1. At the beginning of each load step, determine the current strain state in each ply of each element.
2. From this ply strain state (i.e. knowing $\epsilon_1, \epsilon_2, \gamma_{12}$), determine the tangent modulus of the stress-strain curve for that strain level. This gives tangent values of E_1, E_2, ν_{12} , and G_{12} for each ply.

3. Knowing the ply stiffnesses, the tangent constitutive stiffness matrices A, B, and D can be found for each element.
4. These A, B, and D matrices can then be used to calculate the element stiffness matrices.

6.4 Model Verification

Three test cases were chosen to verify the finite element model. They were:

1. A beam clamped on both ends, subjected to a concentrated transverse load at its center (Mondkar and Powell, 1977).
2. An inextensional beam simply supported on both ends with one end fixed and the other end free to translate longitudinally, subjected to a concentrated transverse central load (Walker and Hall, 1968).
3. An inextensional cantilever beam, subjected to a concentrated transverse load at the free end (Walker and Hall, 1968).

These three test cases were chosen because they represent a varying range of large deflections. The clamped-clamped beam undergoes moderately large deflections, while the cantilever beam undergoes extreme large deflections. The references cited with each problem provide exact solutions with which the finite element model was compared.

All three reference solutions are based on classical beam theory. That is, there are no effects of width-wise deformations included in these analyses. Thus, width-wise degrees of freedom (i.e. α , η , V , ω , Θ and g) were eliminated from the finite element model in order to solve problems identical to the reference solutions. Since no known exact solutions exist with which to verify the width-wise aspect of the model, this was not done. However, the test cases that were performed were useful in verifying the capability of the model to predict large deformations. The width-wise effects were incorporated into the model through certain kinematic assumptions, so it was impossible to verify them other than to assess their effectiveness in modeling the experimental problem.

The finite element results and exact solution are compared in Figure 69 for the clamped-clamped beam case. The results from the simply supported beam are shown in Figure 70. The end-loaded cantilever results are shown in Figure 71. From these figures, it can be seen that the finite element model was successful in predicting large deformation response of beams. The accuracy of the finite element solution decreased as deflections became more extreme, but the results were still quite good even at the very large deflections encountered in the cantilever problem. Thus, the model was ready to apply to the eccentric axial compression experimental problem.

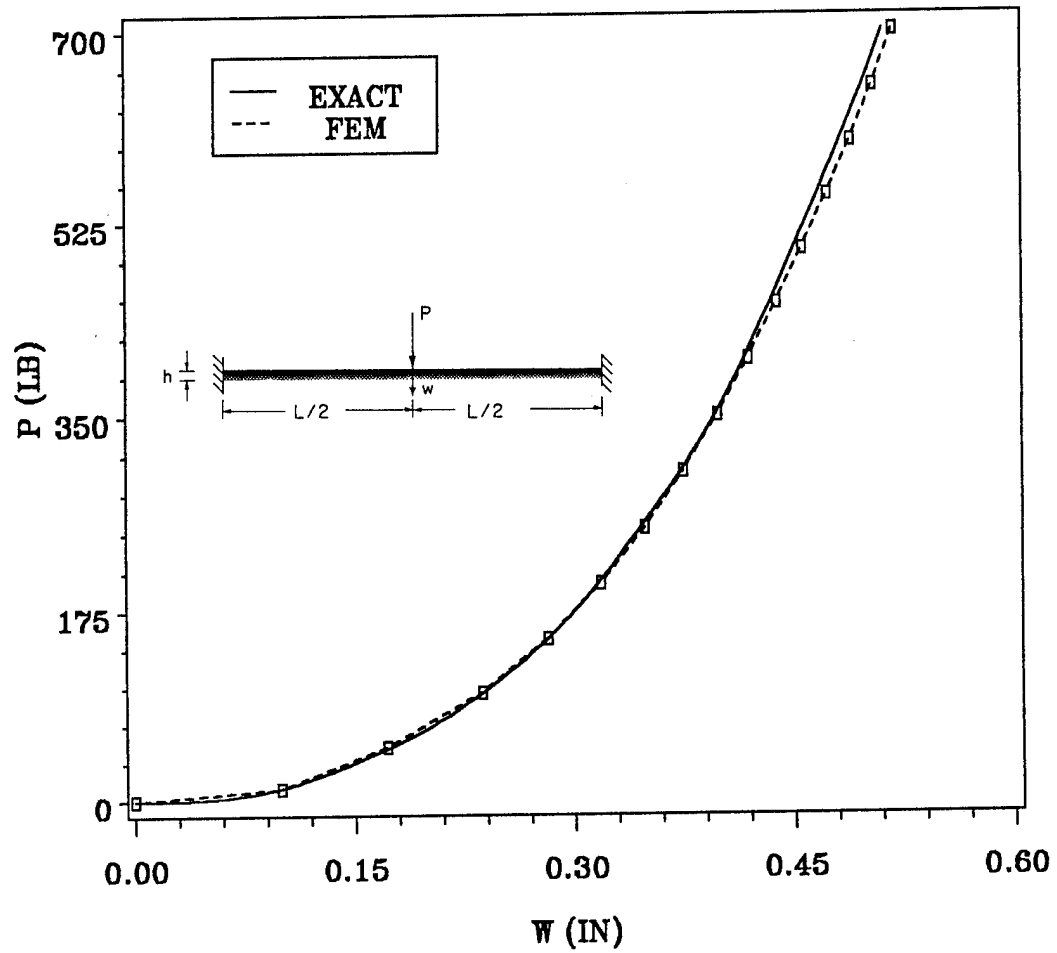


Figure 69. Clamped-clamped beam test case

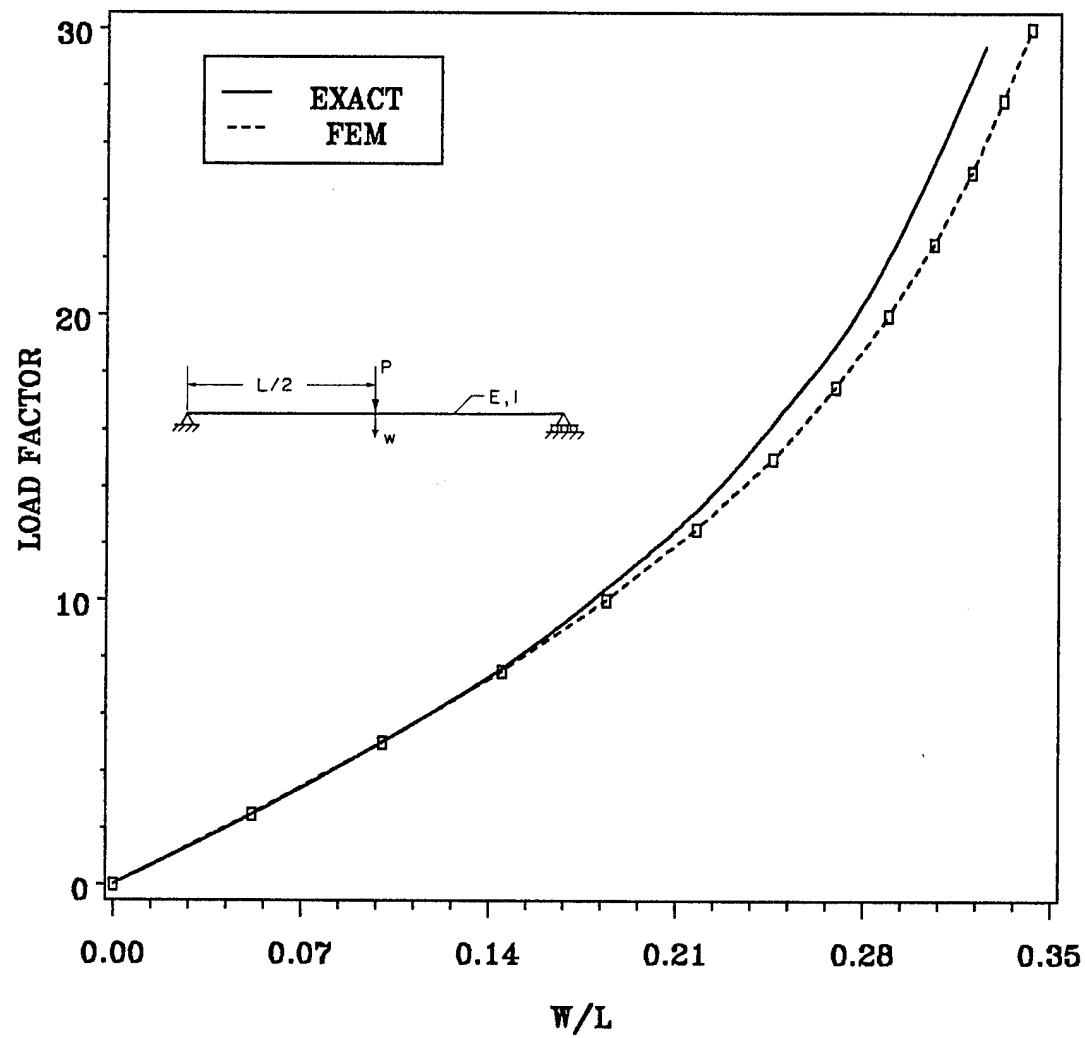


Figure 70. Simply-supported Inextensional Beam Test Case

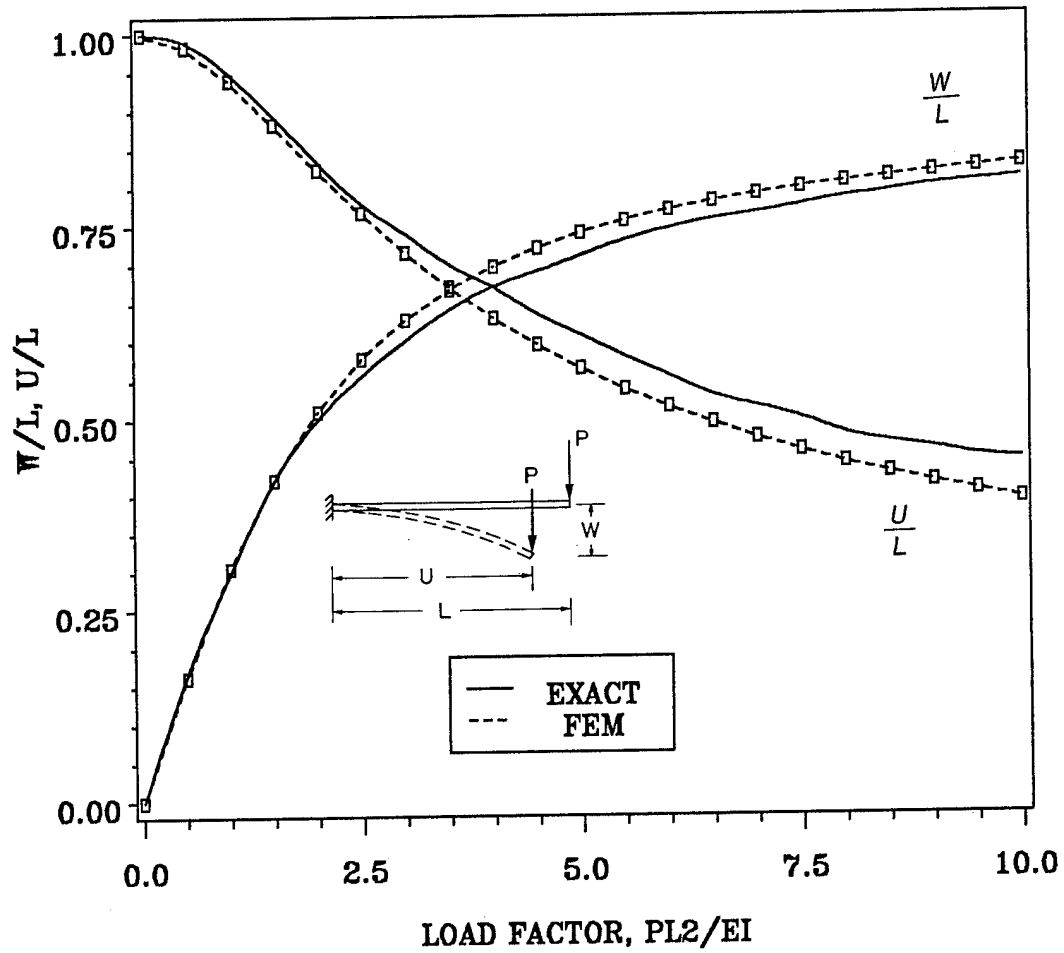


Figure 71. Inextensional Cantilever Beam Test Case

7.0 Numerical Results

Using the finite element model described in Chapter 6, a static analysis of the beam loading situation was performed. The finite element results were correlated with the experimental measurements discussed in Chapter 3.

7.1 *Model*

This section presents the material model used in the analysis, the finite element mesh, the applied boundary conditions and loads, and the mesh refinement.

7.1.1 Material Model

The material model used in the analysis was based on the material characterization tests discussed in Chapter 5. The nonlinear material model was implemented using the

procedure outlined in Chapter 6. The polynomials used to approximate the tangent moduli in the material principal directions are presented in Appendix F.

It should be noted that the nonlinear material model will yield a nonzero B matrix (laminar coupling stiffness), even for a symmetric layup.

7.1.2 Mesh

Forty elements were used to model the 20 inch (50.8 cm) unsupported portion of the beam between the hinges. Preliminary analysis on most of the laminates revealed that the deformation patterns were not symmetric with respect to the center of the beam. Thus, half-symmetry could not be used, and the entire length of the beam was modeled. The layup of each laminate was input as ply fiber angles, with the thickness of each ply equal to the measured thickness of the beam divided by the number of plies. Rigid link elements were incorporated into the model to represent the hinged beam supports. The hinge geometry is shown in Figure 72. The total eccentricity input in the model was 0.625 inches (1.59 cm) plus one-half of the thickness of the laminate. The latter term was necessary because the analysis is based on the midplane of the laminate. The total finite element mesh used for this analysis is shown in Figure 73.

7.1.3 Boundary Conditions and Applied Loads

The beam was simply supported in the experimental apparatus, with one end fixed and one end free to translate. Both ends were hinged, allowing rotation in the x-z plane. To accurately model these boundary conditions in the finite element model, the following boundary conditions were applied:

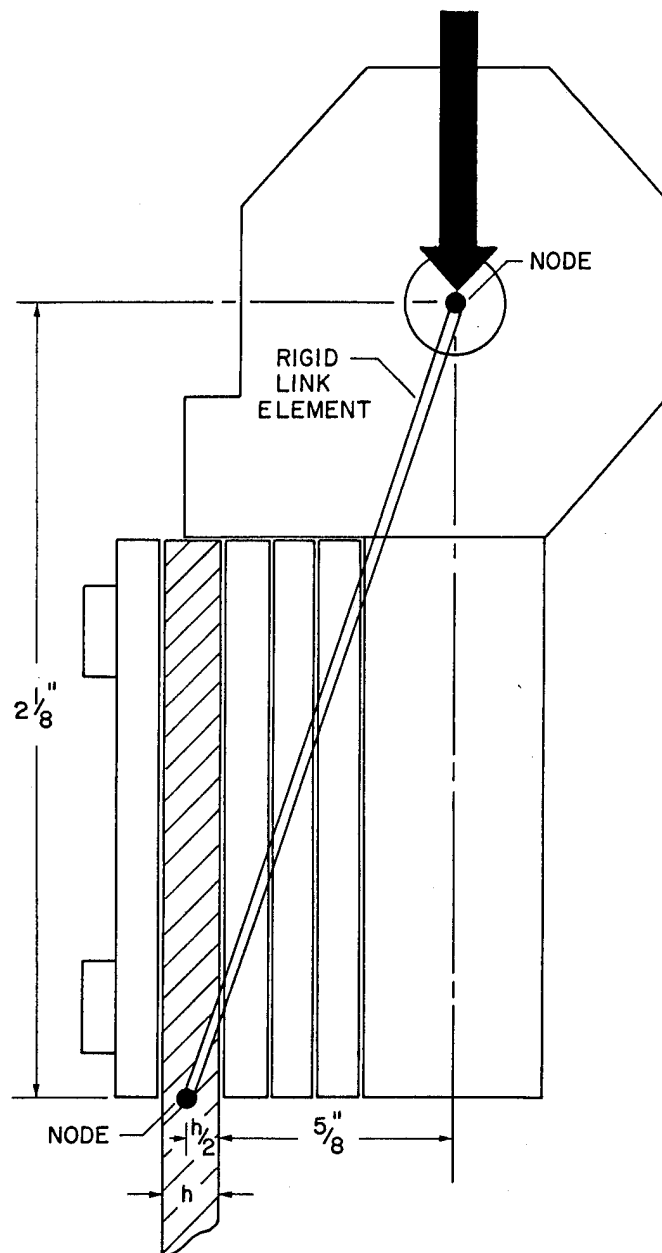


Figure 72. Geometry and dimensions of hinge support

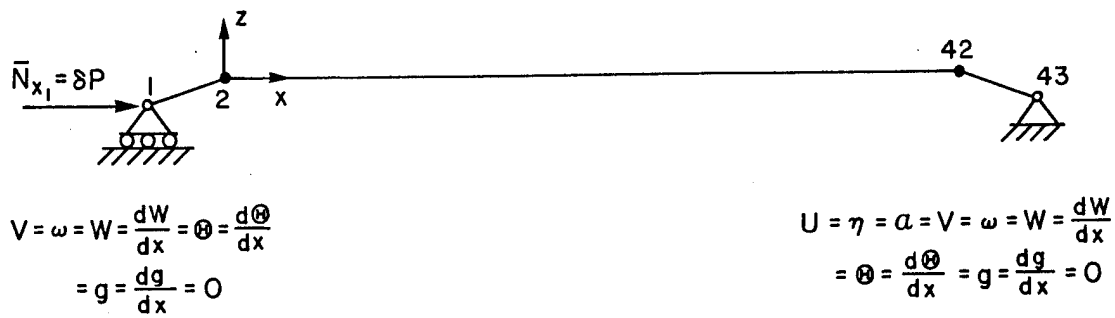


Figure 73. Finite element mesh and boundary conditions used in analysis

1. Node 43 at the right end ($x = 22.125$ in. (56.2 cm)) of the mesh represents the bottom hinge pivot. This node was prevented from all translation.
2. Node 1 at the left end ($x = -2.125$ in. (-5.40 cm)) of the mesh represents the top hinge pivot. This point was fixed to prevent transverse (w) deflection and sideways (v) deflection. However, no boundary condition was applied to limit the longitudinal deflection (u).
3. The hinges were assumed to rigidly clamp the ends of the beams. Thus, the end of the beam remained flat. To model this, all width-wise displacements were fixed to zero at nodes 1 and 43.
4. The x-direction end load was applied incrementally at the left end of the beam.

The boundary conditions and applied load are shown pictorially and explicitly in Figure 73.

7.1.4 Mesh Refinement

Figure 74 shows the predicted end displacement at an end load of 170 pounds for the $[(30/0/-30)_s]_s$ laminate as a function of the number of elements along the unsupported beam length. From this figure, it can be seen that using 20 elements would provide a good approximation to the solution. However, since the computer runs were relatively inexpensive (17 CPU seconds on an IBM 3090 mainframe computer for 40 elements), a 40 element mesh was chosen to gain better accuracy.

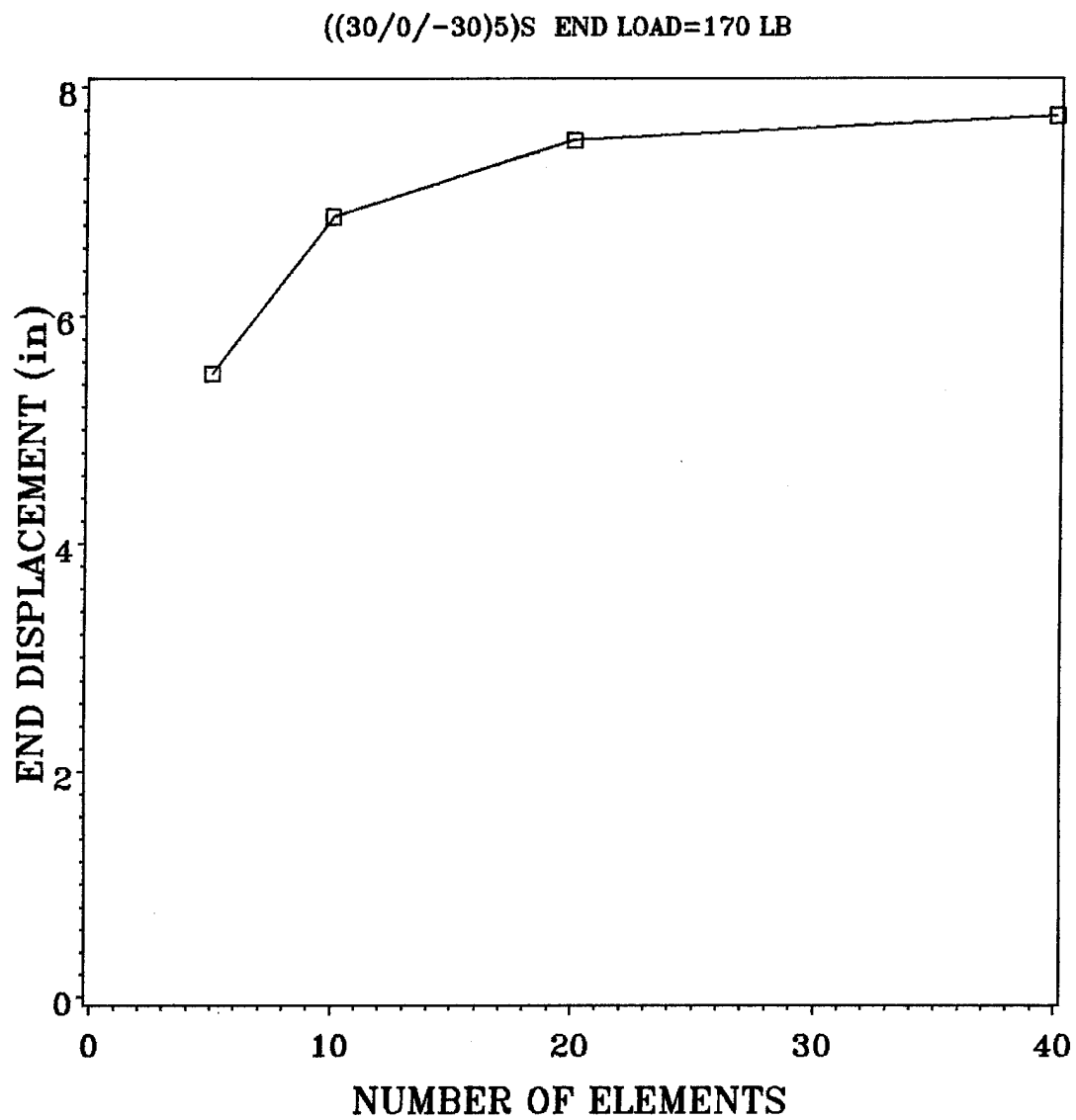


Figure 74. Solution versus number of elements

7.2 Correlation of Numerical and Experimental Results

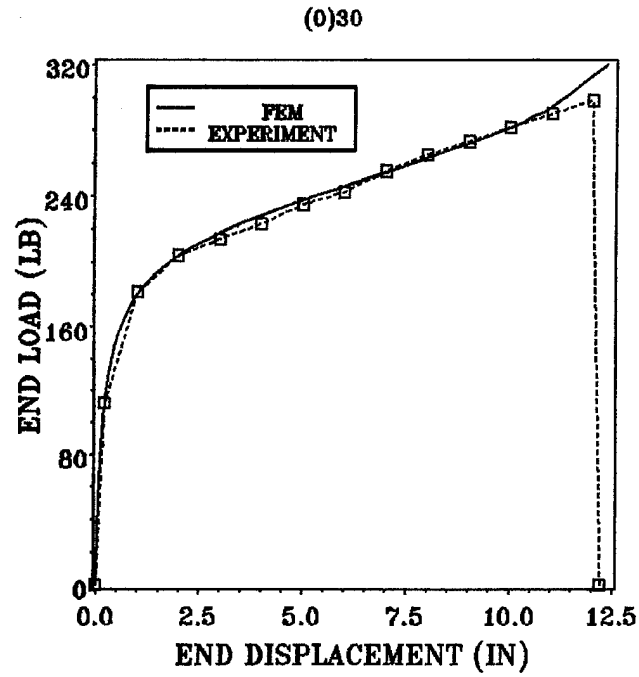
The finite element model was applied to the static loading case described in the previous section for each of the laminates tested statically. In addition, the $[(30/0/-30)_3]_s$ laminate was also modeled for a width of 0.75 inches (1.91 cm) to compare to a 0.75 inch (1.91 cm) beam that was tested statically. The results of the finite element cases are presented in this section along with the experimental results to demonstrate the correlation between the two.

7.2.1 Thick Laminates

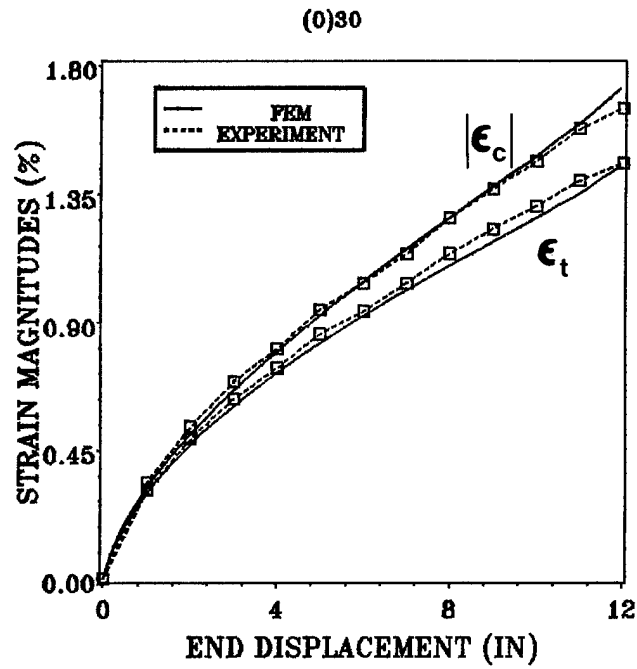
The finite element prediction and experimental end load-end displacement and surface strain magnitude-end displacement response for the $[0]_{30}$ laminate are shown in Figure 75. There is good agreement for both the load-displacement response and the surface strain response of the laminate.

The results for the $[(30/0/-30)_5]_s$ laminate are shown in Figure 76. Again, the model was successful in predicting the experimental response of the laminate to static loading. The model also predicted nearly the exact amount of difference between the surface strain magnitudes on the tensile and compressive sides of the beam. The cause of this strain magnitude difference will be discussed later in this Chapter.

The response of the $[(45/-45/0/90)_4]_s$ laminate is presented in Figure 77. The model is slightly stiffer than the experiment, but predicts the strain magnitude difference almost exactly. The reason for the higher stiffness of the model is not known. However, at a

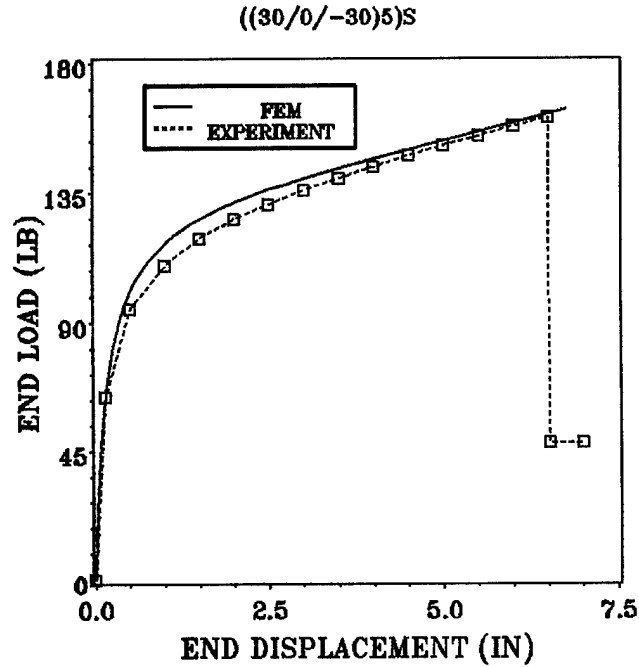


(a) End load versus end displacement

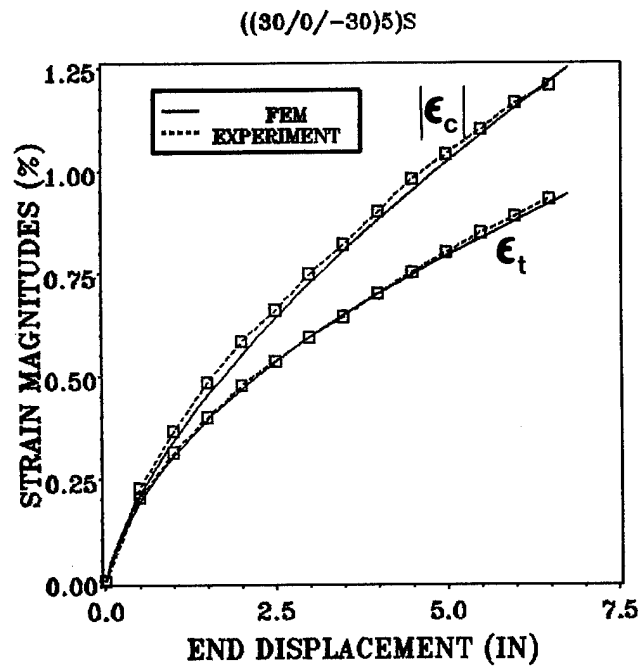


(b) Surface strain magnitudes versus end displacement

Figure 75. Predicted and measured response of $[0]_{30}$ beam



(a) End load versus end displacement



(b) Surface strain magnitudes versus end displacement

Figure 76. Predicted and measured response of $[(30/0/-30)_5]_S$ beam

given end displacement the model predicts a load about five percent higher than measured in the experiment.

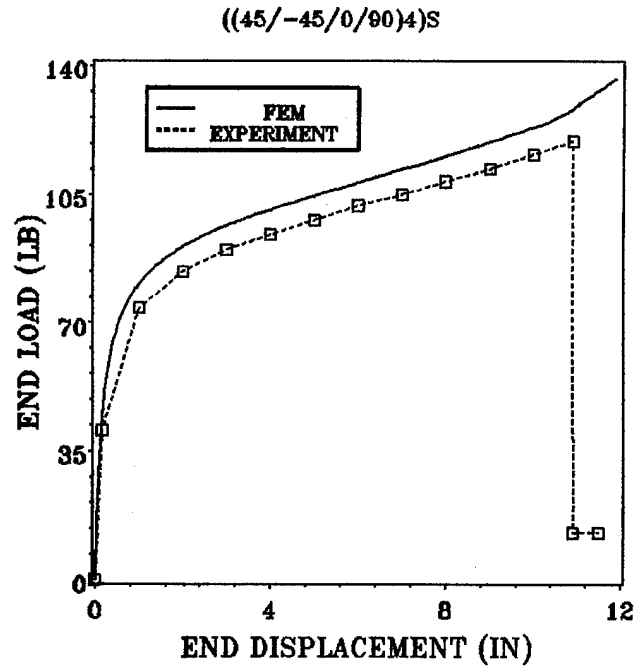
7.2.2 Thin Laminates

The response of the $[0]_{18}$ laminate is presented in Figure 78. The correlation between the predicted and measured load-displacement curves is quite good. However, the model overpredicts the strains by approximately 20 percent. The cause of this is not clear, but the success of the model at predicting the response of the other laminates leads to suspicion of the experimental data for this laminate.

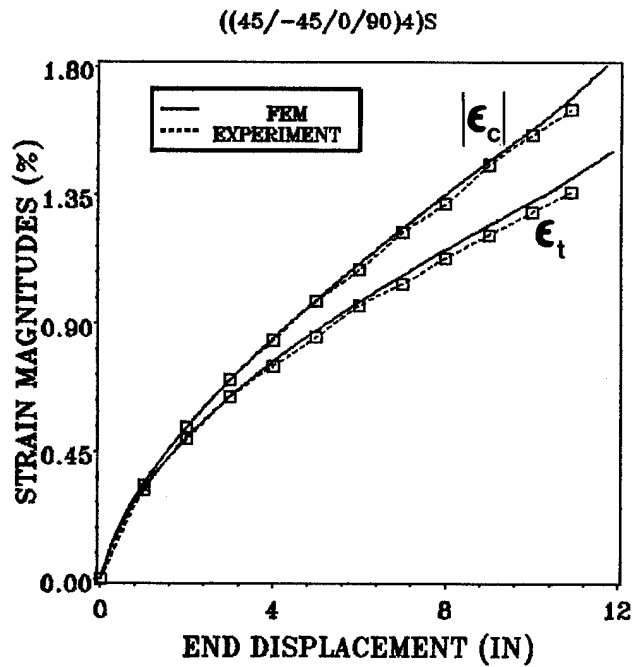
The response of the $[(15/0/-15)_3]_s$ laminate is shown in Figure 79. The model was too stiff in this case by about 20 percent. The model predicts surface strain magnitudes fairly well, but it slightly underpredicts the difference between the tensile and compressive sides.

The response for the $[(30/0/-30)_3]_s$ laminate is shown in two figures. The response of the two-inch (5.08 cm) wide beam is shown in Figure 80, while the response of the narrower 0.75-inch (1.91 cm) wide beam is shown in Figure 81. For the two-inch beam case, the model was slightly stiffer than the experiment. At end displacements greater than about 3.5 inches (8.89 cm), the model also overpredicted the difference between the surface strain magnitudes on the tensile and compressive sides of the beam. For the 0.75-inch (1.91 cm) wide case, the model did very well in predicting both load-displacement and strain magnitude response.

The response for the $[(45/0/-45)_3]_s$ laminate is shown in Figure 82. The response for the $[(45/-45/0/90)_2]_s$ laminate is shown in Figure 83, and the results for the $[(45/-45)_2/0_8/(-45/45)_2]$ laminate are shown in Figure 84. From these three figures,

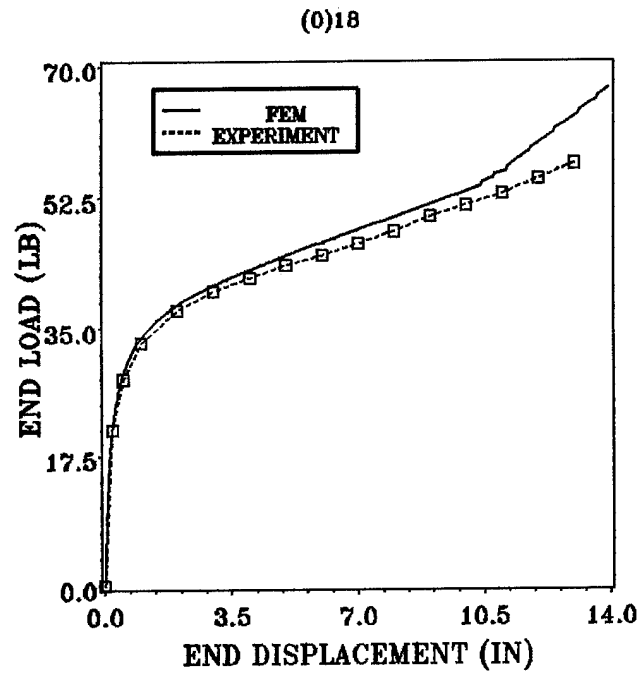


(a) End load versus end displacement

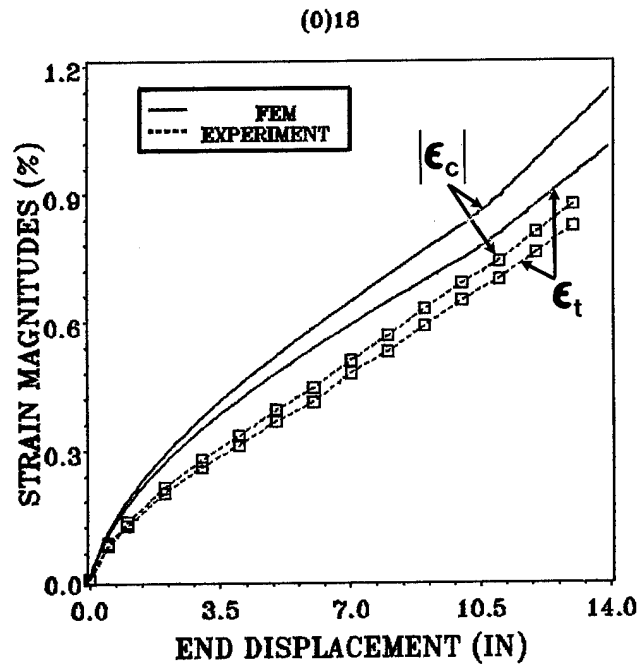


(b) Surface strain magnitudes versus end displacement

Figure 77. Predicted and measured response of $[(45/-45/0/90)_4]_S$ beam

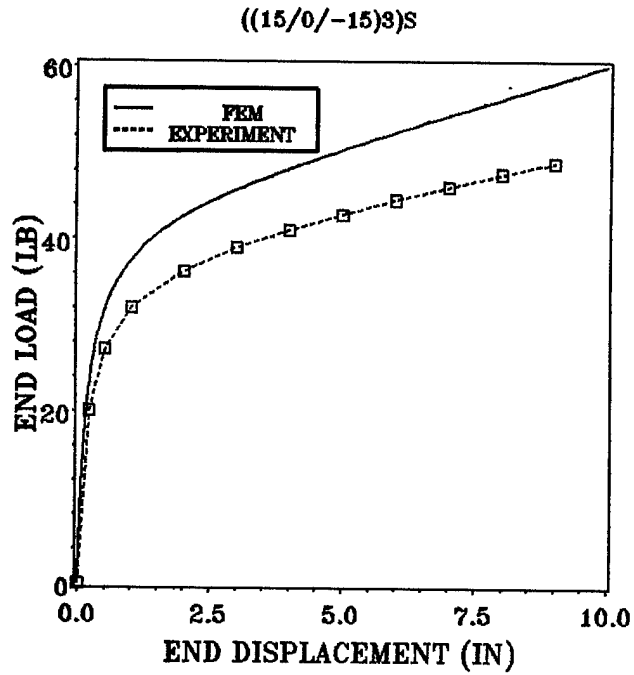


(a) End load versus end displacement

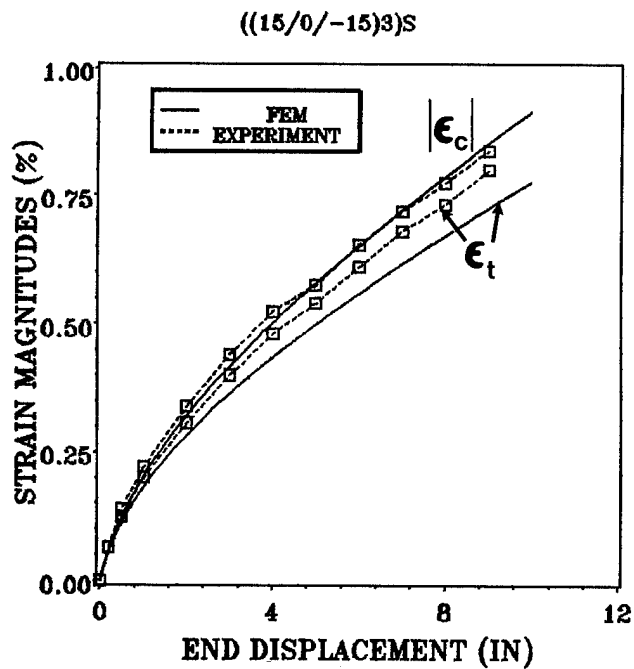


(b) Surface strain magnitudes versus end displacement

Figure 78. Predicted and measured response of [0]₁₈ beam

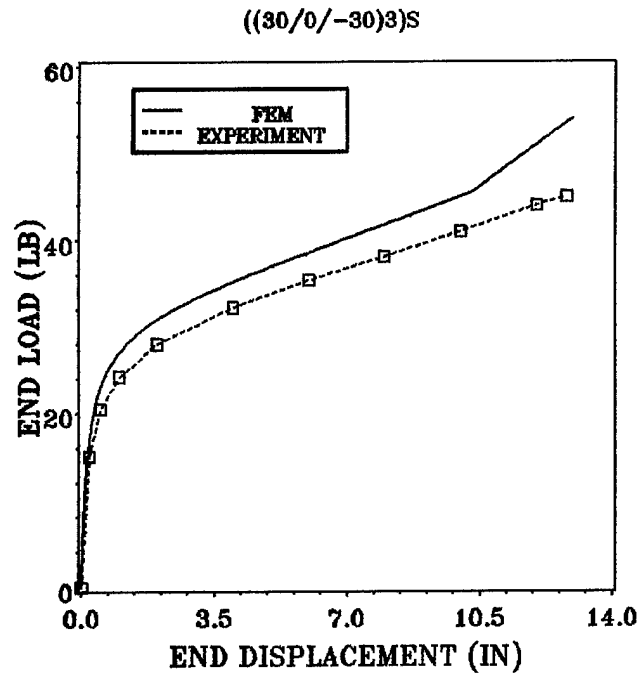


(a) End load versus end displacement

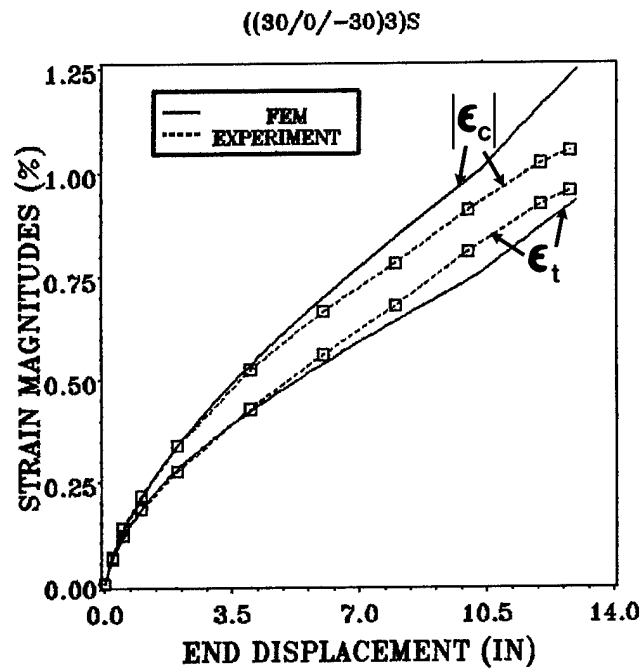


(b) Surface strain magnitudes versus end displacement

Figure 79. Predicted and measured response of [(15/0/-15)₃]S beam

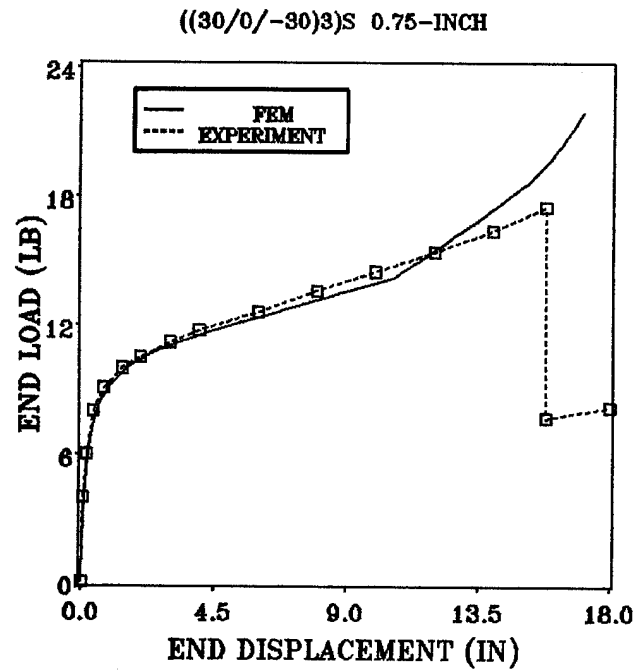


(a) End load versus end displacement

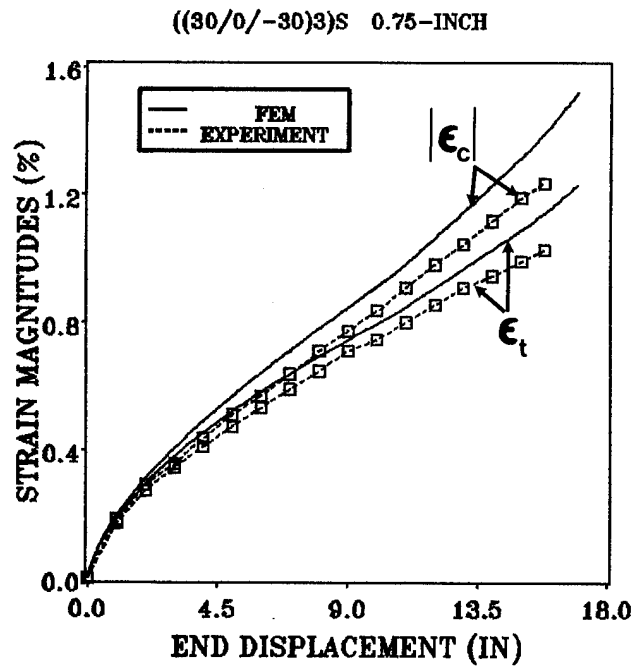


(b) Surface strain magnitudes versus end displacement

Figure 80. Predicted and measured response of [(30/0/-30)₃]s beam



(a) End load versus end displacement



(b) Surface strain magnitudes versus end displacement

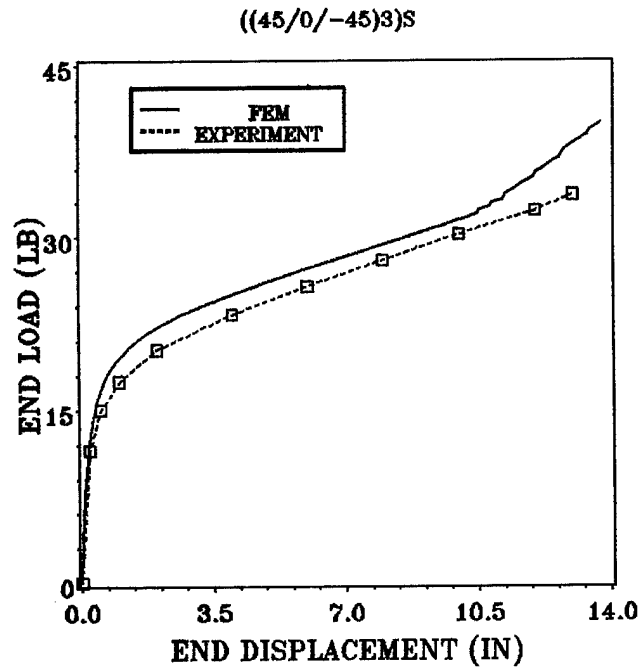
Figure 81. Predicted and measured response of 0.75-inch [(30/0/-30)₃]s beam

it can be seen that the model was quite successful in predicting the response of all three beams. The model was slightly too stiff for all three beams, but the maximum difference between predicted and measured load was at worst about 20 percent for the $[(45/-45/0/90)_2]_s$ laminate.

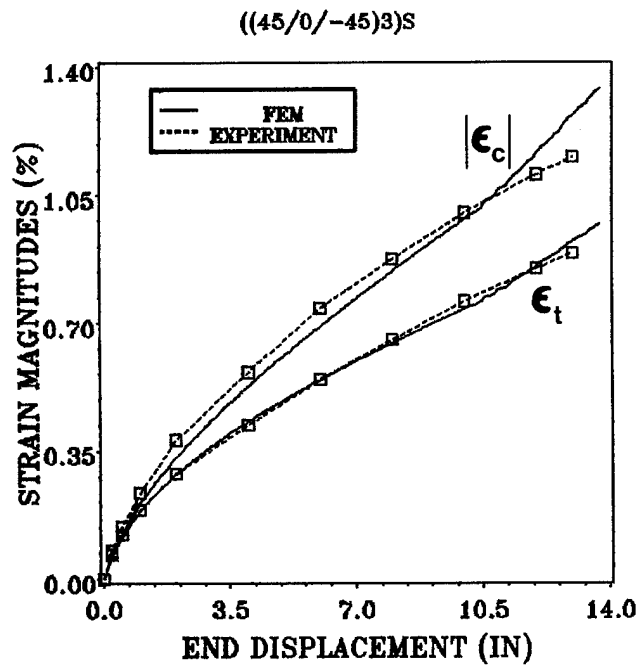
7.2.3 Observations

From the discussion and figures presented in this section, some observations were made. They are:

1. The model successfully predicted the load-displacement response for the majority of the laminates tested. The model was consistently stiffer than the experiments, but only by a small amount in most cases. Thus, the model is slightly conservative. This result is not unexpected, as the model does not include such softening effects as transverse shear deformation or damage accumulation. Furthermore, displacement models tend to be too stiff and generally provide an upper bound solution.
2. The model successfully predicted the experimentally-observed difference between the surface strain magnitudes on the tensile and compressive sides of the beams. The capability to predict this difference with analysis based upon a material model using stress-strain data obtained from uniaxial tests is a significant accomplishment.

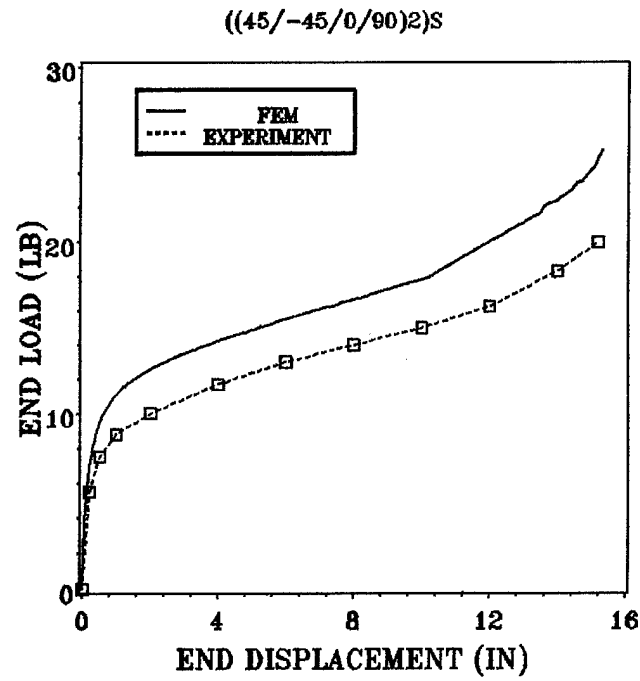


(a) End load versus end displacement

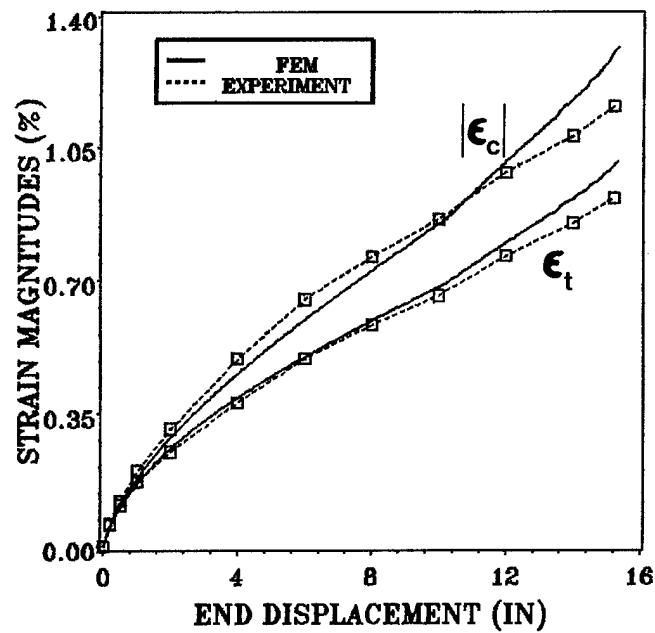


(b) Surface strain magnitudes versus end displacement

Figure 82. Predicted and measured response of [(45/0/-45)₃]s beam

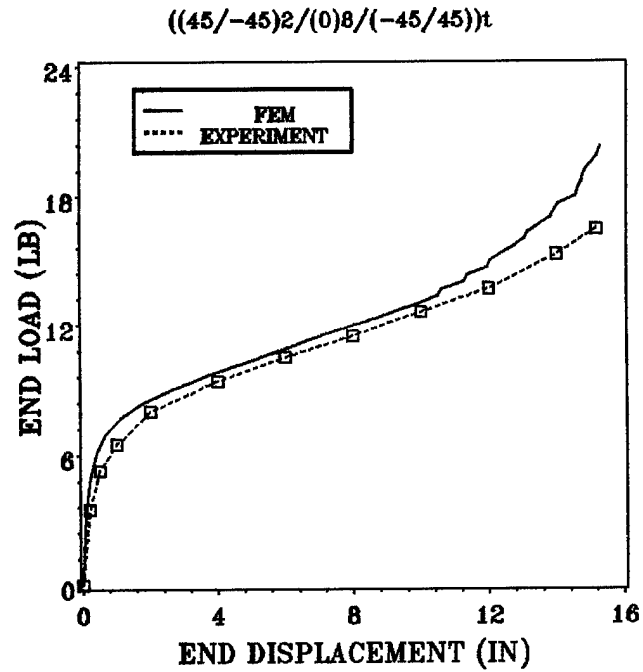


(a) end load versus end displacement
 $((45/-45/0/90)_2)_S$

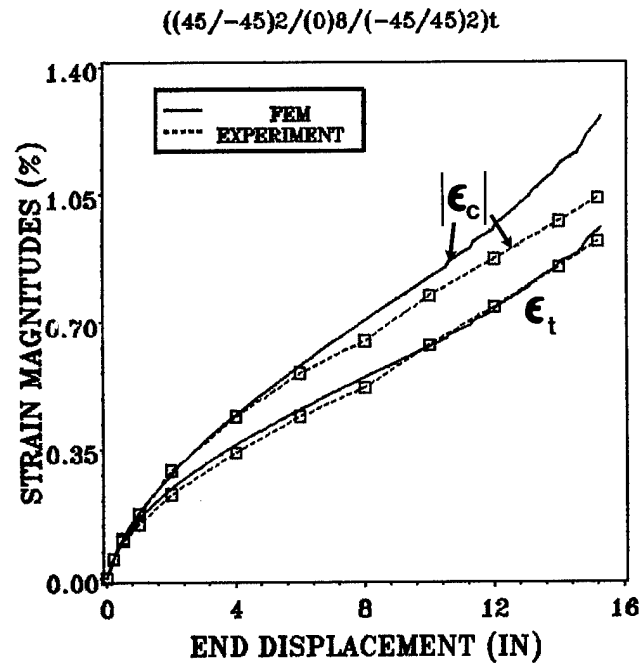


(b) Surface strain magnitudes versus end displacement

Figure 83. Predicted and measured response of $[(45/-45/0/90)_2]_S$ beam



(a) End load versus end displacement



(b) Surface strain magnitudes versus end displacement

Figure 84. Predicted and measured response of $[(45/-45)_2/(0)_8/(-45/45)_2]$ beam

7.3 *Material Nonlinearity and Width-Wise Effects*

Since, the model proved effective in predicting both displacement and strain response in most of the beams considered, it was desired to use it to determine the effects which, when incorporated into the model, resulted in correct prediction of the large differences in strain magnitudes between the tensile side and compressive side of the beams. To do this, a version of the model was used in which the width-wise degrees of freedom (i.e. α , η , ω , Θ , and g) were removed. In this discussion, this version will be referred to as Generalized Cylindrical Bending (GCB).

The $[0]_{30}$ and $[(30/0/-30)_s]_s$ laminates were chosen for this study because they represented the lowest and highest degrees of coupling between longitudinal and twist curvatures of all the laminates tested. This coupling is discussed in detail later in this Chapter. Both laminates also provided excellent numerical-experimental correlation using the full model.

Each laminate was modeled using both the GCB model and the width-wise model. In addition, cases were run using both the nonlinear material model and a linear material model (using initial moduli obtained from the material characterization tests). Thus, a total of four cases were run for each laminate. All four cases incorporated geometric nonlinearity to model the large deflections exhibited by the beams. These cases will be referred to as:

1. Generalized Cylindrical Bending, Linear Material Model
2. Generalized Cylindrical Bending, Nonlinear Material Model
3. Width-wise Effects, Linear Material Model

4. Width-wise Effects, Nonlinear Material Model

The results for each of the laminates are discussed here.

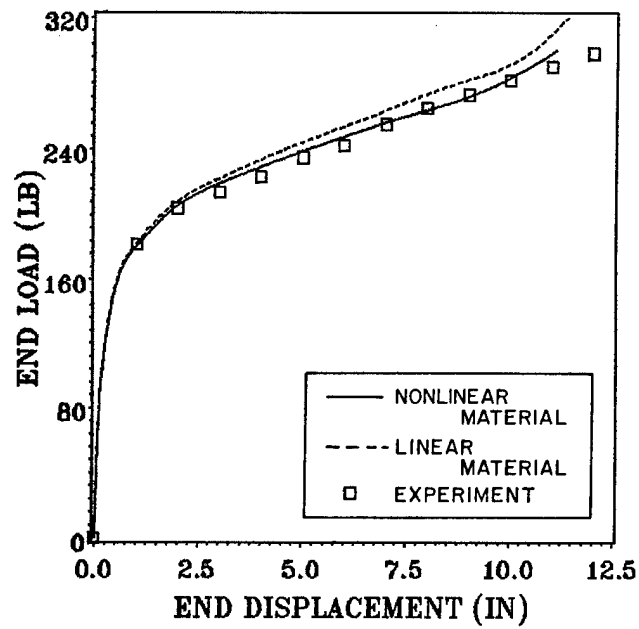
7.3.1 $[0]_{30}$ Laminate

The predicted end load-end displacement response for the $[0]_{30}$ laminate for all four cases is shown in Figure 85. All four cases correlate well with experiment. Case 4, the full model containing both nonlinear material and width-wise effects performs marginally better than the rest of the cases.

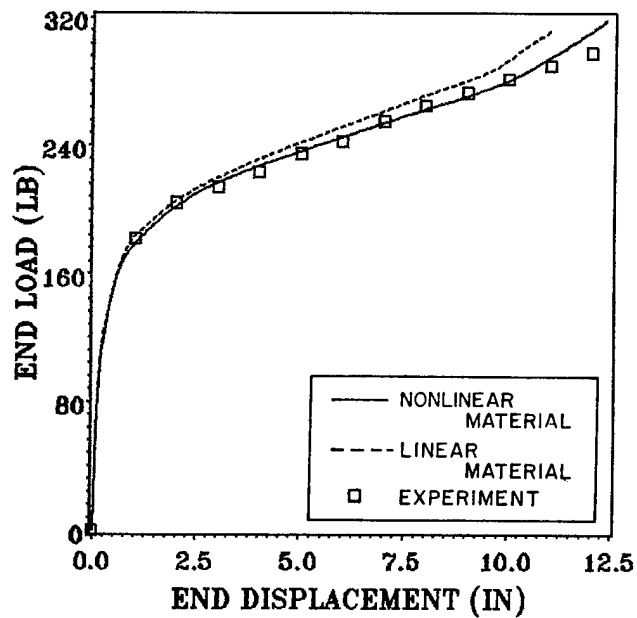
The predicted surface strain response for the $[0]_{30}$ laminate for all four cases is shown in Figure 86. The linear material analyses, Cases 1 and 3, underpredict the difference in strain magnitudes between the tensile and compressive sides. However, with the inclusion of the nonlinear material model, the strain difference is predicted well. The addition of width-wise effects contributes a relatively small amount of strain magnitude difference.

7.3.2 $[(30/0/-30)_5]_s$ Laminate

The predicted end load-end displacement response for the $[(30/0/-30)_5]_s$ laminate for all four cases is shown in Figure 87. The GCB model is far too stiff, and the effect of the material nonlinearity is very small. However, with the width-wise effects included, the load-displacement response correlates much more closely with experiment.

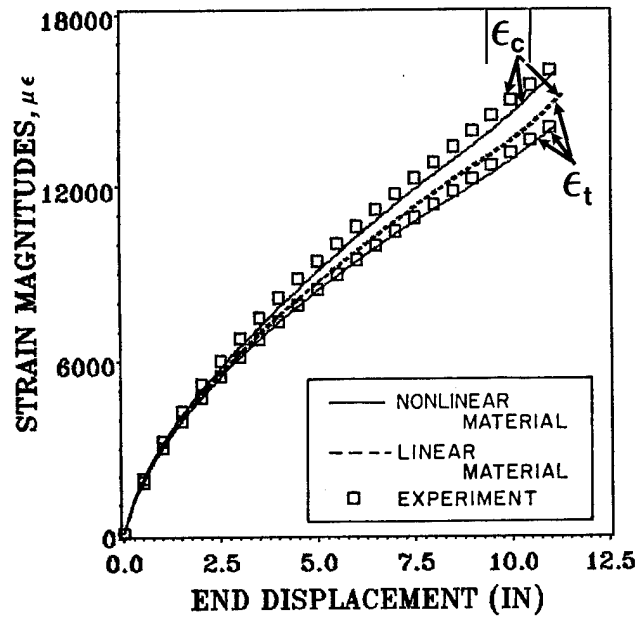


(a) Generalized cylindrical bending

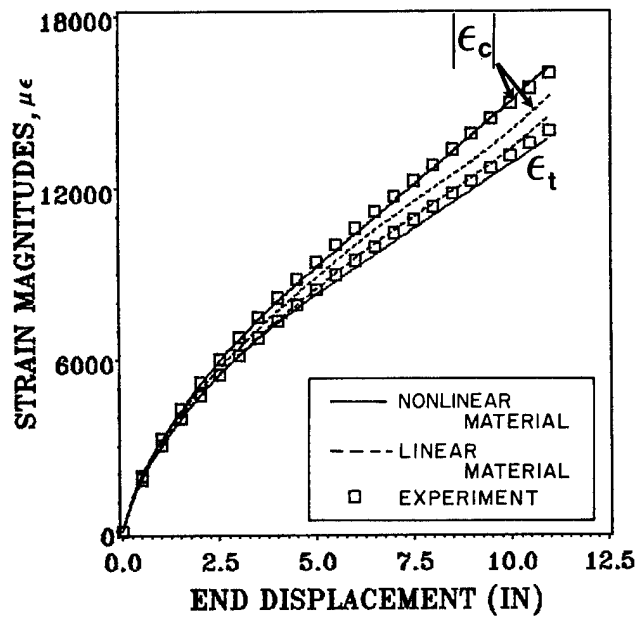


(b) Model with width-wise effects

Figure 85. Load-displacement predictions for $[0]_{30}$ beam using different analyses

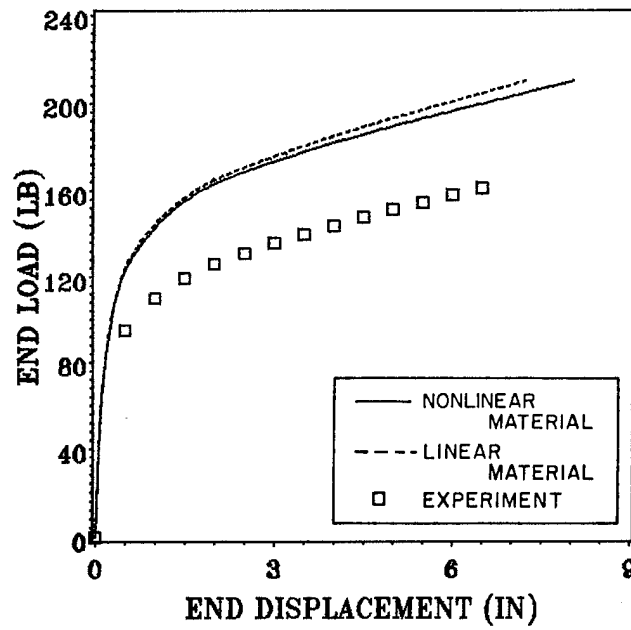


(a) Generalized cylindrical bending

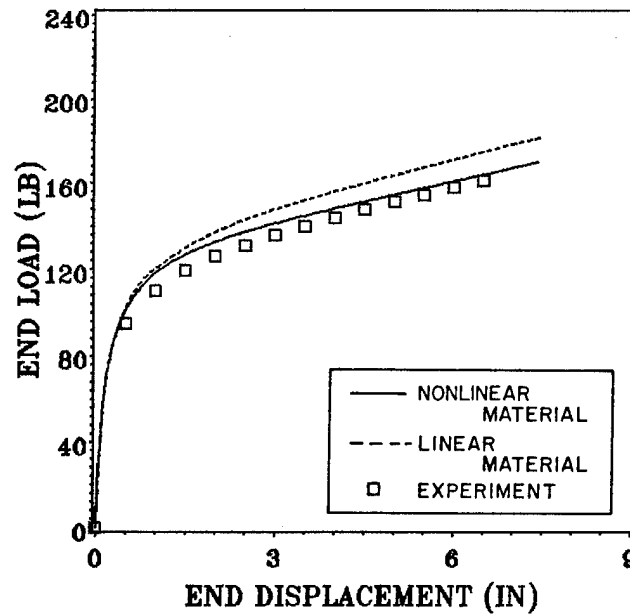


(b) Model with width-wise effects

Figure 86. Surface strain predictions for $[0]_{30}$ beam using different analyses



(a) Generalized cylindrical bending



(b) Model with width-wise effects

Figure 87. Load-displacement predictions for $[(30/0/-30)_s]_s$ beam using different analyses

The predicted surface strain response for the $[(30/0/-30)_5]_s$ laminate is shown in Figure 88. The GCB model, even with nonlinear material behavior, far underpredicts the strain magnitude difference observed experimentally. However, the width-wise model correlates quite well with experiment, even with the linear material behavior.

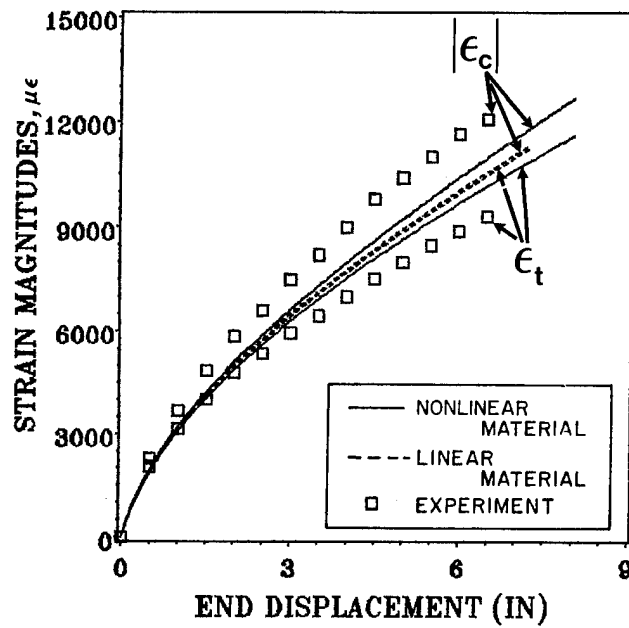
7.3.3 Observations

From the analyses discussed above, some observations can be made. These are:

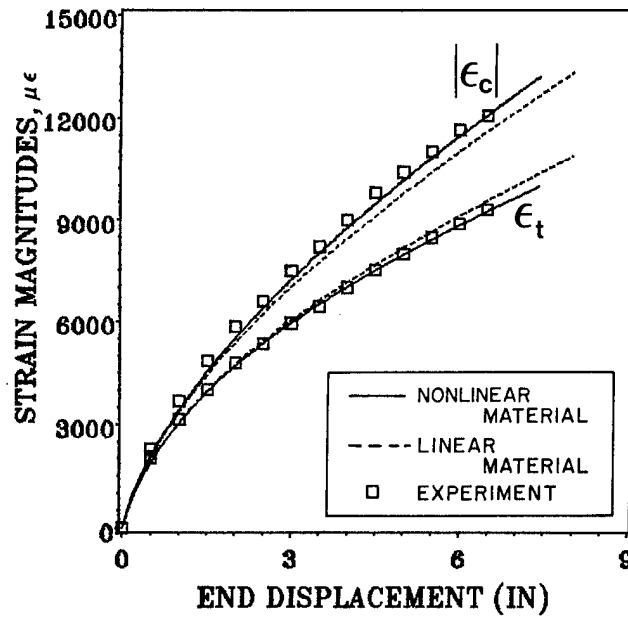
1. For the $[0]_{30}$ beam (no bend-twist coupling), the effect of material nonlinearity was greater than the width-wise effects on the strain response. However, neither the material model nor the width-wise effects had a pronounced effect on the load-displacement response. For the linear material case, the model predicted little or no difference between the surface strain magnitudes on the tensile and compressive sides of the beam. However, even without width-wise effects, the nonlinear material model predicted nearly correctly this difference in strain magnitudes.

At low strain levels (i.e. still in the linear range), the model predicted nearly identical strain magnitudes on the tensile and compressive sides of the $[0]_{30}$ beam. This is further evidence that material nonlinearity is responsible for the observed strain magnitude difference at higher strain levels for the unidirectional beam.

2. For the $[(30/0/-30)_5]_s$ beam (large amount of bend-twist coupling, as measured by the magnitude of D_{16}), the width-wise effects were extremely important in correlating the predicted response to the experimental response. The nonlinear material behavior improved the behavior of the model only a small amount. Even with the nonlinear material behavior included, the generalized cylindrical bending model predicted only a small difference between the surface strain magnitudes. However,



(a) Generalized cylindrical bending



(b) Model with width-wise effects

Figure 88. Surface strain predictions for $[(30/0/-30)_s]_s$ beam using different analyses

the width-wise model, even with linear material behavior, predicted nearly the correct difference.

7.4 Width-Wise Reponse of Laminates

In the previous sections, it was shown that the finite element model successfully predicted the experimental response of the laminates considered. It was also shown that including some width-wise degrees of freedom was extremely important to the performance of the model. The existence of these width-wise terms allows some very useful and interesting information to be obtained about the width-wise response of these laminates to static flexure. In this section, the width-wise response of a number of laminates will be presented. This discussion will include effects of shear-extension coupling terms, stacking sequence, beam width, and material nonlinearity on the width-wise response.

When a beam or plate undergoes flexural loading such that a longitudinal curvature is introduced, it will generally exhibit curvature of an opposite sense in the transverse (or width-wise) direction. This so-called "anticlastic" curvature was predicted for isotropic beams by Ashwell (1950). Hyer and Bhavani (1984) extended this analysis for balanced symmetric laminated composites. Their analysis incorporated the familiar Von Karman geometrically nonlinear strain-displacement relations for moderately large deflections. They demonstrated analytically and experimentally that for thin, wide plates, this anticlastic curvature was suppressed when longitudinal deflections became large. The beams considered in the current study had a much higher aspect ratio than the plates considered in the study by Hyer and Bhavani (1984). Thus, the suppression of anticlastic curvature should not be as pronounced in the beams considered here. However, there

was evidence in the flexure experiments discussed in Chapter 3 that some suppression of anticlastic curvature took place. But, since no static tests were performed with transverse strain gages to investigate this phenomenon, it was assumed for analytical purposes that no suppression of anticlastic curvature occurs.

The analysis by Hyer and Bhavani (1984) provided valuable information on anticlastic curvature in laminated composites. However, that analysis neglected twist curvatures (κ_{xy}). It was found in the current analysis that these twist curvatures can not only be present, but can have a significant effect on the predicted width-wise deformation pattern of some laminates. This section presents some of the current results to demonstrate the twisting effect.

The results in this section are based on the results predicted by the finite element analysis. From preliminary analysis, it was found that the width-wise degrees of freedom exhibited either symmetry or anti-symmetry about the center of the beam. Some of these degrees of freedom were zero at the beam center. Thus, these results are taken at the cross-section of the beam located at the first quarter-point ($x=5.0$ inches (12.7 cm)). The global translations and longitudinal rotation of the cross-section are removed to obtain an accurate representation of the true cross-sectional deformation. The figures presented here are the predicted deformed shapes of the laminate midplane (or y-axis) at the beam station considered.

7.4.1.1 Effect of Off-Axis Ply Angles

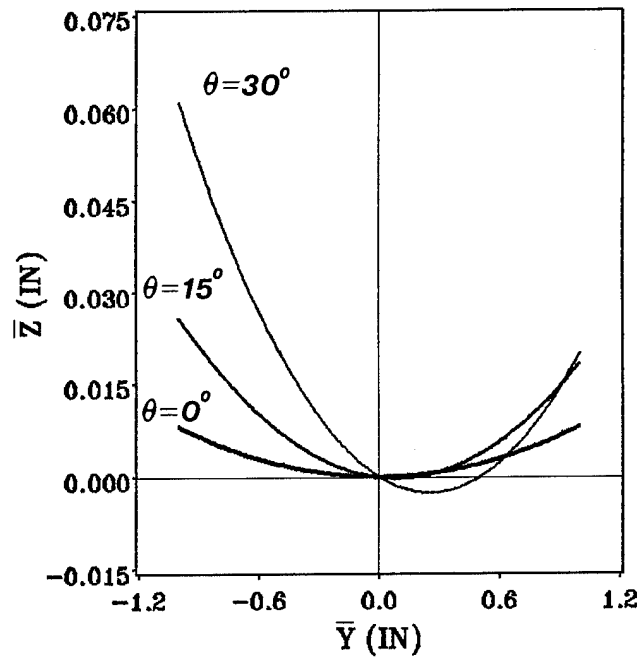
Figure 89 presents the deformed midplane shapes for a family of $[(\theta/0/-\theta)_3]_s$ laminates with θ varying from 0° to 90° by increments of 15° . It can be seen from this figure that the largest magnitude of anticlastic curvature appears for the case of $\theta = 30^\circ$. This is expected, since of the laminates considered, this laminate has the largest coupling

term, D_{12} , between longitudinal curvature and transverse curvature of the laminates considered.

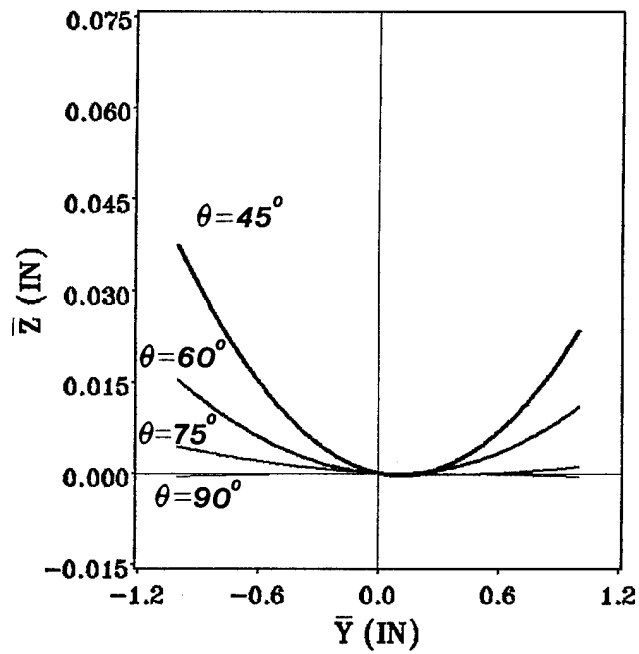
However, a more interesting trend can be seen from this figure than just the magnitude of anticlastic curvature. For some of the laminates, there is a very pronounced non-symmetry of anticlastic curvature. This nonsymmetry is most noticeable for the case of $\theta = 30^\circ$. The cause of this phenomenon is the presence of twisting curvature in the laminates. An individual off-axis ply will exhibit shear-extension coupling, represented by the familiar plane stress coefficient, \bar{Q}_{16} . For each θ ply in the laminates considered, there is a corresponding $-\theta$ ply. Thus, there is no A_{16} laminate shear-extension coupling. However, since the θ plies are each farther from the beam midplane than the corresponding $-\theta$ plies, their contribution to the bending stiffnesses are slightly greater. This leads to a nonzero value for D_{16} , the coupling term between longitudinal and twist curvatures. This causes twisting to occur for the case of pure bending considered here.

7.4.1.2 Effect of Stacking Sequence

The effect of varying stacking sequence is shown in Figure 90 for the case of $\theta = 30^\circ$. The figure presents deformed midplane shapes for laminates of $[(30/0/-30)_3]_s$, $[(-30/0/30)_3]_s$, and $[(30/-30/0)_3]_s$. From this figure, it can be seen that switching the locations of the 30° and -30° plies reverses the nonsymmetry of the midplane shape. This is expected, since the signs of the shear-extension coupling terms are opposite for the 30° and -30° plies. It can also be seen from the $[(30/-30/0)_3]_s$ laminate that putting the 30° and -30° plies closer together results in a smaller amount of nonsymmetry in anticlastic curvature.

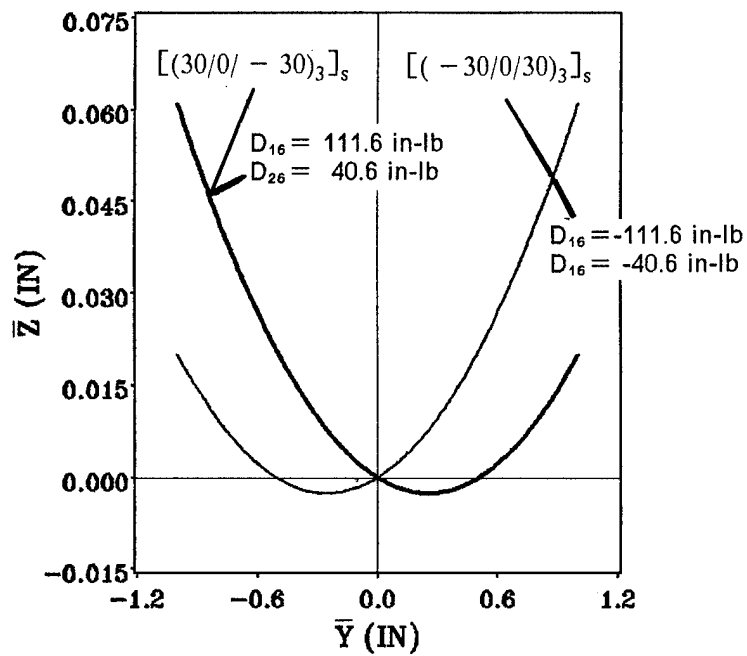


(a) $\theta = 0^\circ, 15^\circ, \text{ and } 30^\circ$

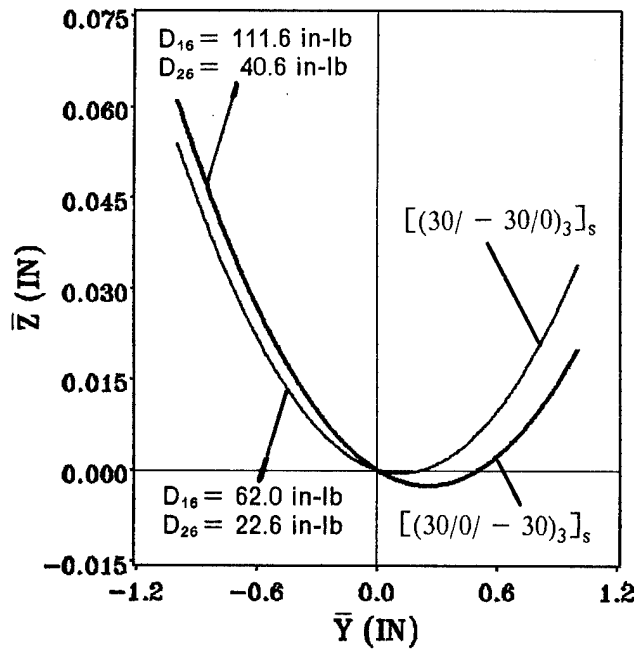


(b) $\theta = 45^\circ, 60^\circ, 75^\circ, \text{ and } 90^\circ$

Figure 89. Effect of off-axis ply angle on width-wise curvature of $[(\theta/0/-\theta)_s]$ s beams



(a) $[(30/0/-30)_3]_s$ and $[(-30/0/30)_3]_s$ laminates



(b) $[(30/0/-30)_3]_s$ and $[(30/-30/0)_3]_s$ laminates

Figure 90. Effect of stacking sequence on width-wise curvature

7.4.1.3 Effect of Beam Width

Figure 91 shows the predicted deformed midplane shapes for the $[(30/0/-30)_3]_s$ laminate for widths of two inches (5.08 cm) and 0.75 inches (1.91 cm). From this figure, it is seen that the nature of the anticlastic curvature is not changed by varying the width.

7.4.1.4 Effect of Material Nonlinearity

Figure 92 shows the deformed midplane shapes for the $[(30/0/-30)_3]_s$ laminate for both the linear material case and nonlinear material case. From this figure, it is obvious that the nonlinear material behavior has very little effect on the deformed shape of the cross-section. Thus, it is primarily the bending-twisting coupling and not the nonlinearity that causes the width-wise nonsymmetry due to bending.

7.4.2 Cross Sectional Warping

In addition to the anticlastic curvature discussed above, the presence of the width-wise degrees of freedom in the longitudinal displacement, u^o , means that cross-sectional warping is permitted. That is, plane sections do not remain plane during loading. However, the Kirchhoff-Love assumption requires that displacements be a linear function through the beam thickness. So vertical lines on a cross section remain straight even though the plane may warp.

It was desired to examine the types of warping predicted by the model. The $[0]_{30}$ and $[(30/0/-30)_5]_s$ laminates were again chosen for this study for the same reasons mentioned previously. The analysis was performed on both laminates by applying load until

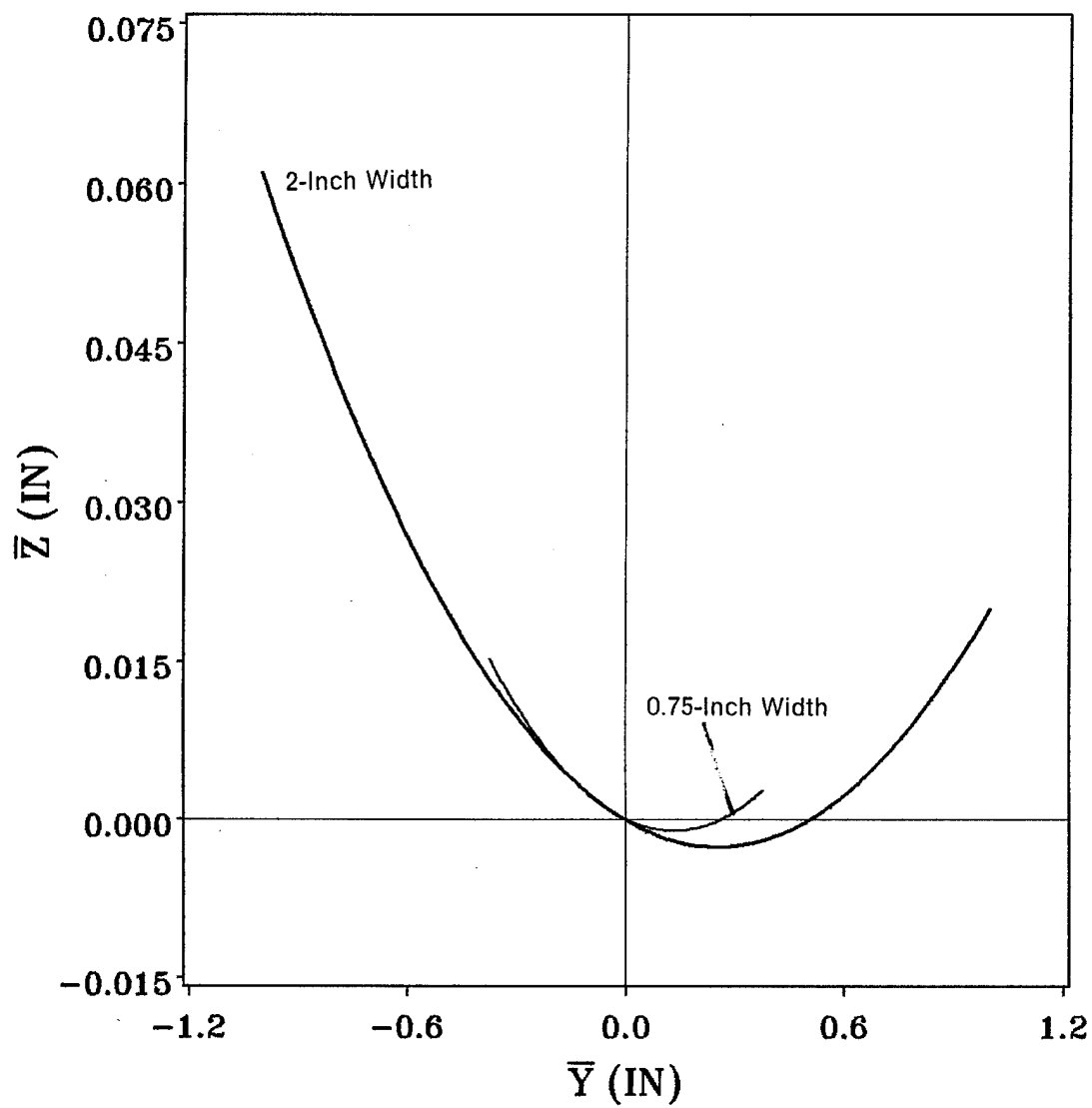


Figure 91. Effect of beam width on width-wise curvature

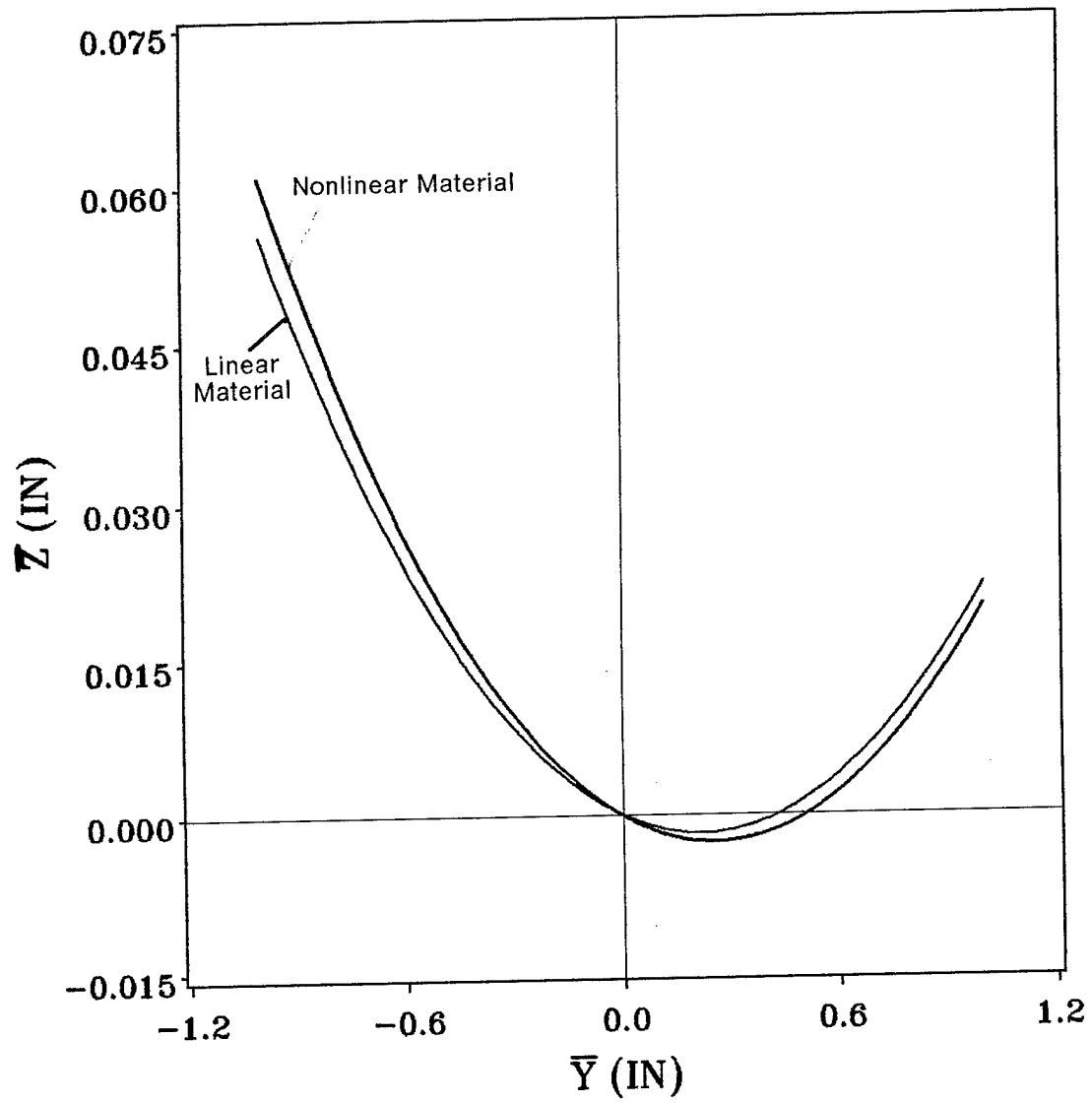


Figure 92. Effect of material nonlinearity on width-wise curvature

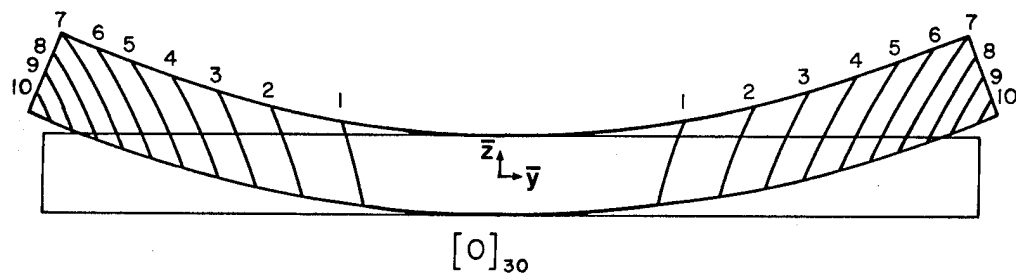
the predicted end displacements was approximately 7.5 inches (18.8 cm). By keeping track of the element local solution for the width-wise degrees of freedom at a given cross section and eliminating the global translation and rotation of that cross section, it was possible to determine what cross sectional warping was present.

The cross section analyzed was at the first beam quarter-point ($x=5$ inches (12.7 cm)). This location was chosen rather than the center of the beam because some of the width-wise degrees of freedom were zero at the beam center. Thus, some aspects of warping would not be present at the center.

The deformed shape of the quarter-point cross section for both laminates is shown in Figure 93. The rectangular figures represent the unwarped cross sections as predicted by standard beam theory. The deformed plots show the displacements in the plane of the cross section (v and w), while the contours show the warping in the cross sections (that is, displacements out of the plane of the cross section).

From this figure, some observations can be made. They are:

1. The cross sectional warping in the $[0]_{30}$ beam is symmetric about the z -axis, while the warping is not symmetric for the $[(30/0/-30)_5]_s$. This is again due to the shear-extension coupling in the $[(30/0/-30)_5]_s$ laminate.
2. The magnitude of the cross sectional warping is much smaller in the $[0]_{30}$ beam than in the $[(30/0/-30)_5]_s$ beam. This is expected, since the width-wise degrees of freedom have much more effect on the response of the $[(30/0/-30)_5]_s$ beam than they do on the $[0]_{30}$ beam (as previously shown).

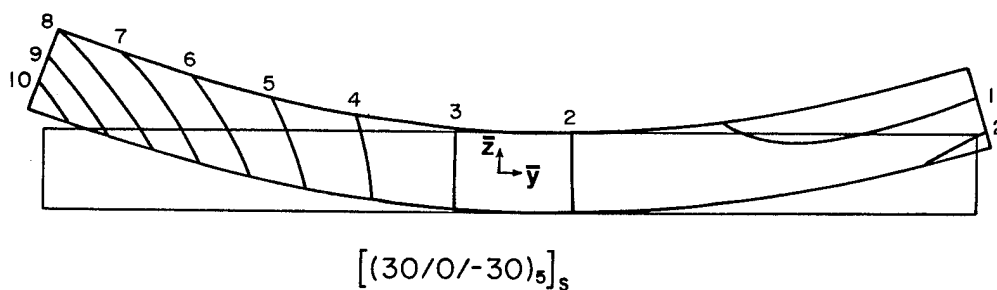


Scale factor for $v, w = 19.1$

Contour values for u

Line 1 = 24.7 μ -in. Line 10 = 247. μ -in. $\Delta = 24.7$ μ -in.

(a) $[0]_{30}$ beam cross section



Scale factor for $v, w = 3.2$

Contour values for u

Line 1 = -424. μ -in. Line 10 = 2150. μ -in. $\Delta = 286$. μ -in.

(b) $[(30/0/-30)_5]_s$ beam cross section

Figure 93. Cross sectional warping in $[0]_{30}$ and $[(30/0/-30)_5]_s$ beams

3. The anticlastic curvature in the $[0]_{30}$ beam is symmetric about the z-axis. However, the anticlastic curvature in the $[(30/0/-30)_s]_s$ beam is not symmetric. This phenomenon is discussed in the previous section.

7.5 Failure Analysis

Using the finite element results obtained earlier in this chapter, a failure analysis was performed. Four existing failure criteria were applied to the beam problem to determine which, if any, adequately predicted laminate failures.

7.5.1 Obtaining Finite Element Results

The finite element model was used to provide the data necessary for the failure analysis. Load was applied to the model until the predicted end displacement equaled the experimental end displacement at failure (or 14 inches (35.6 cm) for the beams which did not fail experimentally) for each laminate. The predicted material principal strains for each ply in each element were used to obtain the material principal stresses ($\sigma_1, \sigma_2, \sigma_{12}$). This was accomplished by integrating the moduli-strain polynomials shown in Appendix F with respect to strain to derive equations for secant moduli as functions of material principal strains. Using these secant moduli, the plane stress stiffness matrices were formed. Multiplying these matrices by the material principal strain vectors yielded the material principal stresses for each ply in each element.

7.5.2 Failure Criteria and Strengths

Four failure criteria were investigated using the computed material principal stresses and strains. They were:

1. Maximum stress (tensile fiber, compressive fiber, tensile matrix, compressive matrix, inplane shear), (Jones, 1975)
2. Maximum strain (tensile fiber, compressive fiber, tensile matrix, compressive matrix, inplane shear), (Jones, 1975)
3. Hashin (tensile fiber, compressive fiber, tensile matrix, compressive matrix), (1980)
4. Tsai-Wu tensor polynomial (Jones, 1975)

To use these criteria, five failure stresses and four failure strains were needed. These are:

X_t = Tensile fiber-direction strength

X_c = Compressive fiber-direction strength

Y_t = Tensile transverse strength

Y_c = Compressive transverse strength

S = Inplane shear strength

ϵ_{1t}^u = Tensile fiber-direction strain to failure

ϵ_{1c}^u = Compressive fiber-direction strain to failure

ϵ_{2t}^u = Tensile transverse strain to failure

ϵ_{2c}^u = Compressive transverse strain to failure

γ_{12}^u = Inplane shear strain to failure

The failure results from the material characterization tests described in Chapter 4 were used for these values. However, the fiber-direction strengths and failure strains were exceptions. Derian and Hyer (1986) observed that failure in the $[0]_{30}$ beams were simultaneous fiber failures on the tensile and compressive sides. The longitudinal surface strains at experimental failure were over twice the magnitude of the failure strains obtained from material characterization. Thus, if material characterization results were used to predict failure, the results would be too conservative. Therefore, the experimental strains at failure for the $[0]_{30}$ beam were used as the failure strains in the various criteria. The fiber-direction strengths were calculated from these strains using the same procedure with which material principal stresses were calculated from material principal strains.

The final strength and failure strains used in the analysis were:

$$X_t = 340.0 \text{ ksi}$$

$$X_c = -250.0 \text{ ksi}$$

$$Y_t = 7.46 \text{ ksi}$$

$$Y_c = -32.3 \text{ ksi}$$

$$S = 12.5 \text{ ksi}$$

$$\epsilon_{1t}^u = 0.015$$

$$\epsilon_{1c}^u = -0.016$$

$$\epsilon_{2t}^u = 0.0055$$

$$\epsilon_{2c}^u = -0.029$$

$$\gamma_{12}^u = 0.025$$

7.5.3 Results

Substituting the strengths and failure strains into the various criteria, the failure functions, $F(\sigma)$ and $F(\epsilon)$, were found for each ply in each element. The maximum value for each criterion was determined for each laminate. The results for all the shear, matrix, and Tsai-Wu criteria all predicted that matrix failures occurred well before final failure of the laminates. This corresponds to the observations by Derian and Hyer (1986) that matrix failures occurred first on the off-axis surface plies, followed by tensile fiber failures on the 0° ply closest to the tensile surface. The failure analysis results for the various tensile fiber failure criteria proved reasonably effective at predicting this first major failure event. Specifically, Hashin's (1980) tensile fiber failure criterion predicted this failure mode more consistently than did either the maximum stress or maximum strain tensile fiber failure criteria. For the laminates which did not suffer tensile fiber failures experimentally, the various criteria generally did not predict failure.

The failure function, F , and values for the various tensile fiber failure criteria for each laminate are shown in Figure 94. The equations used to obtain these results are:

$$\text{Maximum stress: } F(\sigma_1) = \frac{\sigma_1}{X_t}$$

$$\text{Maximum strain: } F(\epsilon_1) = \frac{\epsilon_1}{\epsilon_{1t}^u}$$

$$\text{Hashin: } F(\sigma) = \left(\frac{\sigma_1}{X_t} \right)^2 + \left(\frac{\sigma_{12}}{S} \right)^2$$

For all these criteria, values of F greater than or equal to unity define failure, while values less than unity mean that failure has not occurred.

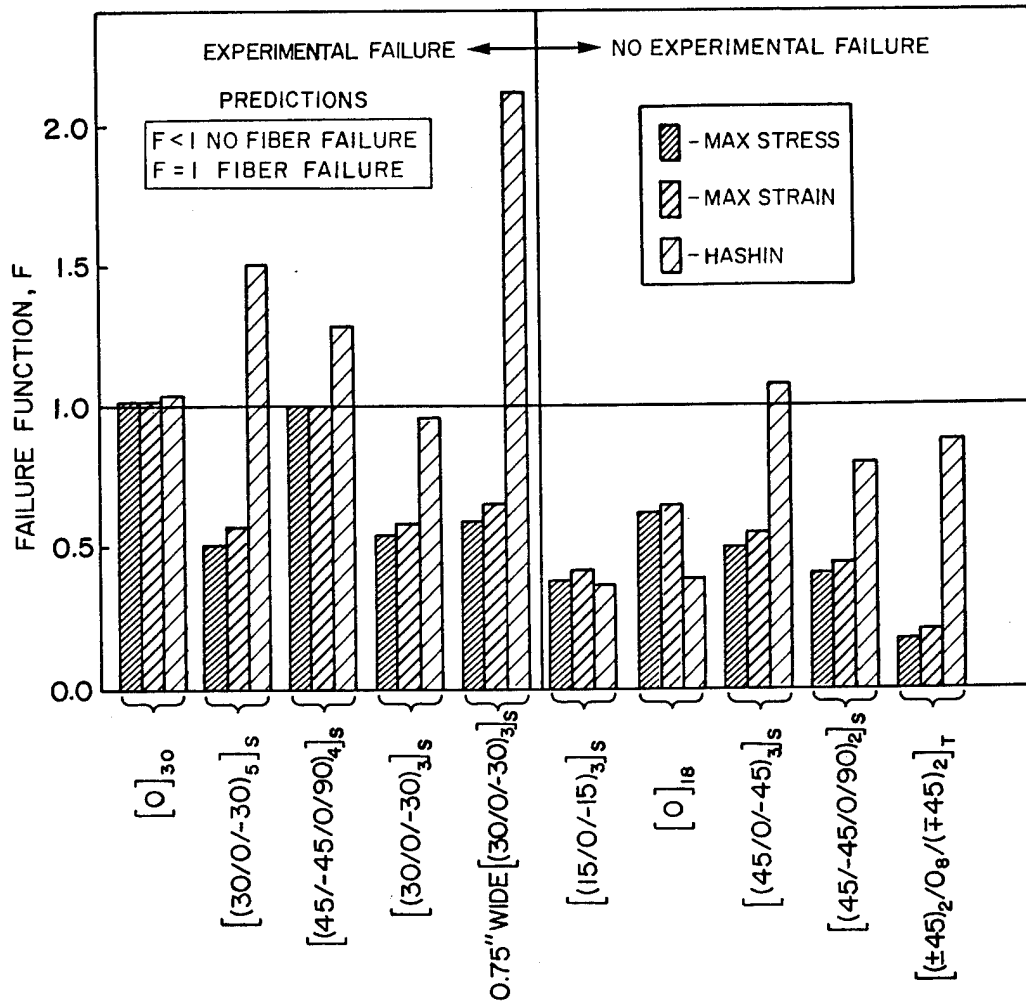


Figure 94. Predicted tensile fiber failure criteria values at experimental failure loads

7.5.4 Observations

From the failure analysis discussed above, some observations were made. They are:

1. The fiber-direction strength and failure strain values obtained from uniaxial material characterization tests predict failure loads that are conservative by a factor of two or more for a unidirectional beam. Using empirical values for these failure stresses and strains that are obtained directly from the flexure tests, three tensile fiber failure criteria are generally consistent at predicting experimental failures for other laminates.

The fact that uniaxial strengths are overly conservative is due in part to the difference between axial and flexural loads. In a uniaxial specimen, all plies of a laminate are subjected to the same strain state. Thus, the probability of failure at a given load is higher than in the flexure case, where only the outermost plies are exposed to the high strains.

The conservative nature of the uniaxial strength data may also be inherent in the test methods. Imperfections in the specimen geometry and loading conditions in the tension and compression tests can result in failures at stress levels lower than the actual material strengths. For the Iosipescu shear test, Pindera, et al (1987) found that "since shear stress concentrations exist at the notch tips... the average shear stress at the instant of initial axial splitting corresponds to an upper lower bound on the shear strength."

2. The Hashin tensile fiber failure criterion generally predicts fiber failure more consistently than do the maximum stress or maximum strain criteria. The latter two criteria are nonconservative in most of the failure cases. However, Hashin's crite-

rion is more conservative. This is because Hashin's criterion accounts for the effect of shear stress (σ_{12}) on the tensile fiber failure mode.

3. Interlaminar stresses and edge effects were not addressed in this analysis. Some beams showed evidence of delamination, although Derian and Hyer (1986) observed that delamination generally occurred subsequent to prior failure(s) and not as the first major failure event. Thus, the effects of interlaminar stresses and edge effects on initial failure events is likely not a major issue for this analysis.

8.0 Conclusions and Recommendations

In this study, the large deformation flexure of rectangular cross-section composite beams was investigated. The study concerned both static and dynamic loading, with particular emphasis on static analysis. The work was an extension of earlier work performed by Derian and Hyer (1986). The overall goals of the current study were to:

1. Revise the drop tower designed by Derian and Hyer (1986) and conduct further impact tests to determine the effects of these revisions. Specifically, it was desired to see if these changes removed spurious noise observed in the data from Derian and Hyer.
2. Conduct static and dynamic tests with a new material batch to determine if the results obtained in the previous study were peculiar to a specific material batch. Specific interest is in the difference in strain magnitudes between the tensile and compressive sides of the beam, as was observed by Derian and Hyer.
3. Investigate the extent and nature of the damage, if any, induced by the high load spikes encountered early in the impact tests.

4. Predict the load-displacement and strain-displacement response, developing a finite element program. Specific interest is in predicting and determining the cause of the observed difference in strain magnitudes.
5. Analytically predict failure of the beams from the finite element results.

8.1 Conclusions

From this study the following conclusions were drawn:

1. The revisions in the drop tower used by Derian and Hyer caused a reduction in the magnitudes of the very high load spikes encountered during the impact tests. The amount of reduction varied between 12 and 34 percent for identical specimens. The probable reason for this reduction was the manner in which the load was measured. In the previous version of the drop tower, the load transducers were mounted directly into the beam support hinges. However, in the current version, the four load transducers are mounted between a load platform and the bottom C-channel fixture support. This setup allows a stationary load measuring platform.
2. The spurious noise observed in the data obtained by Derian and Hyer was also present in the data obtained from tests in the revised drop tower. Particularly, the noise early in the displacement-time curve was still present. It is felt that this was due to unwanted upward motion of the optical transducer wedge.
3. The difference in strain magnitudes between the tensile and compressive sides of the beams was present in the material batch used in the current study at the same magnitude as that observed by Derian and Hyer. Specifically, the compressive side

strain magnitudes were always higher than the tensile side strains. Thus, this phenomenon was not an anomaly of the original material batch.

4. Transverse strain response from some of the dynamic tests indicated that some suppression of anticlastic curvature was present in the thinner beams. However, no transverse strain data was obtained during the static tests, so no conclusion could be made about whether this suppression would be present in the static case.
5. A series of impact alleviation tests was performed, in which some beams were subjected to the initial load spike. The mass car was stopped prior to global laminate failure. The beams were then removed and tested statically to failure, and the results compared with static test data for virgin beams. It was found that only the unidirectional beams suffered significant reduction in stiffness and strength due to the initial load spike. Thicker beams were found to degrade slightly more than thinner beams. Of the thick beams, the specimens with fewer fibers directed longitudinally suffered less damage than the specimens with more fibers directed longitudinally. Peak surface strain data from the impact was more useful in predicting damage than were the peak load data. It was felt that the higher strains encountered by the thick beams as compared to the thin beams was the cause for stiffness and strength degradation. These higher strains likely led to more damage to the plies near the surface of the beam.
6. Uniaxial material characterization tests on the material used in this study showed that the stress-strain responses were indeed nonlinear. The material was found to stiffen in tension in the fiber-direction, while it was found to soften in compression in the fiber-direction, in both tension and compression in the transverse direction, and in inplane shear response.

7. A static finite element model was developed incorporating both geometric nonlinearity and material nonlinearity. The geometric nonlinearity was implemented using a corotational method, while the data from the material characterization tests was used as the material model. The model utilized a Kantrovich method to include displacements across the width of the beam. This model was successful in predicting both the load-displacement and strain-displacement responses encountered in the experiments. Most significantly, the model successfully predicted the magnitude of the differences between the strain magnitudes on the tensile and compressive sides of the beams. It was found that the cause of this strain difference was a combination of material nonlinearity and width-wise effects. The width-wise effects were dependent upon the amount of bend-twist coupling in the laminate.
8. It was shown, using the finite element model described above, that accounting for twist curvature was important to the ability to predict the response of the beams. The amount of the twist was found to be dependent upon bend-twist coupling, stacking sequence, and to a small extent material nonlinearity.
9. A tensile fiber failure criteria developed by Hashin (1980) predicted laminate failure more consistently than did either maximum stress or maximum strain criteria. A tensor polynomial and several matrix failure criteria were found to be too conservative at predicting failure.

8.2 Recommendations

Based on the results of the current study, several recommendations are made for further investigation. These recommendations are:

1. A more intensive study should be undertaken to determine the full extent and effect of damage induced in a beam due to the initial load spike. This testing should include more replicate tests and should also include some type of nondestructive evaluation of the beams both before and after being impacted.
2. The effects of scaling on the dynamic response of beams should also be investigated. In particular, the fact that the thinner beams were less affected by the high load spikes than were the thicker beams leads to uncertainty regarding the scaling of these beams. Morton (1987) found that smaller beam specimens were always stronger than larger beam specimens in scaled dynamic impact-loaded three-point bending. "This was thought to be due to the absolute size of matrix cracks and their effect upon subsequent damage characteristics."
3. From the current study, the two-dimensional aspect of the beam was found to have a strong effect on the longitudinal response (both load and strain). Thus, further static flexure tests should be conducted on beams which are instrumented with strain gage rosettes at various locations along the beam width. This will allow for a thorough characterization of the physical anticlastic curvature exhibited by the beam. Effort should be made to correlate these data with analytical predictions. It may be necessary to perform a two-dimensional nonlinear plate analysis to correctly predict the physical response.
4. The dynamic response of more complicated structural elements should be investigated. In particular, dynamic experiments should be conducted. These tests could reveal important information regarding the application of composite materials to primary aircraft structures.

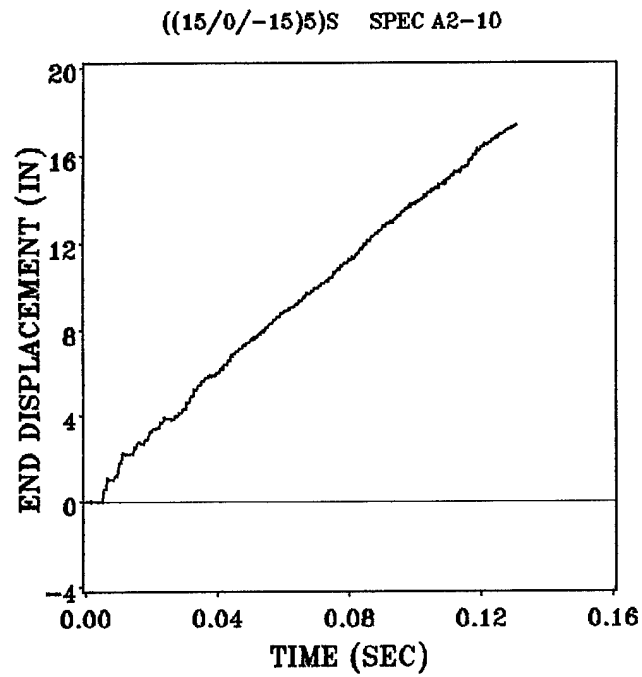
References

- Ashton, J. E., and Whitney, J. M., 1970, *Theory of Laminated Plates*, Technomic Publishing Co., Westport, Conn., pp. 11-16.
- Ashwell, D. G., 1950, "The anticlastic curvature of rectangular beams and plates," *Journal of the Royal Aeronautical Society*, Vol. 54, pp. 708-715.
- Derian, E. J., and Hyer, M. W., 1986, "Large Deformation Dynamic Bending of Composite Beams," NASA Contractor Report 4006.
- Fung, Y. C., 1965, *Foundations of Solid Mechanics*, Prentice-Hall, Inc., Englewood Cliffs, N.J., p. 337.
- Gadala, M. S., Dokainish, M. A., and Oravas, G. AE., 1984, "Formulation Methods of Geometric and Material Nonlinearity Problems," *International Journal for Numerical Methods in Engineering*, Vol. 20, pp. 887-914.
- Hashin, Z., 1980, "Failure Criteria for Unidirectional Fiber Composites," *Journal of Applied Mechanics*, Vol. 47, pp. 329-334.
- Herrmann, G., 1956, "Influence of Large Amplitudes on Flexural Motions of Elastic Plates," *NACA Technical Note 3578*, May 1956.
- Hyer, M. W., and Bhavani, P. C., 1984, "Suppression of Anticlastic Curvature in Isotropic and Composite Plates," *International Journal of Solids and Structures*, Vol. 20, No. 6, pp. 553-570.
- Iosipescu, N., 1967, "New Accurate Procedure for Single Shear Testing of Metals," *Journal of Materials*, Vol. 2, No. 3, p. 537.
- Jones, R. M., 1975, *Mechanics of Composite Materials*, Scripta Book Co., Washington, D. C.
- Jones, R. M., and Morgan, H. S., 1980, "Bending and Extension of Cross-Ply Laminates with Different Moduli in Tension and Compression," *Computers and Structures*, Vol. 11, pp. 181-190.

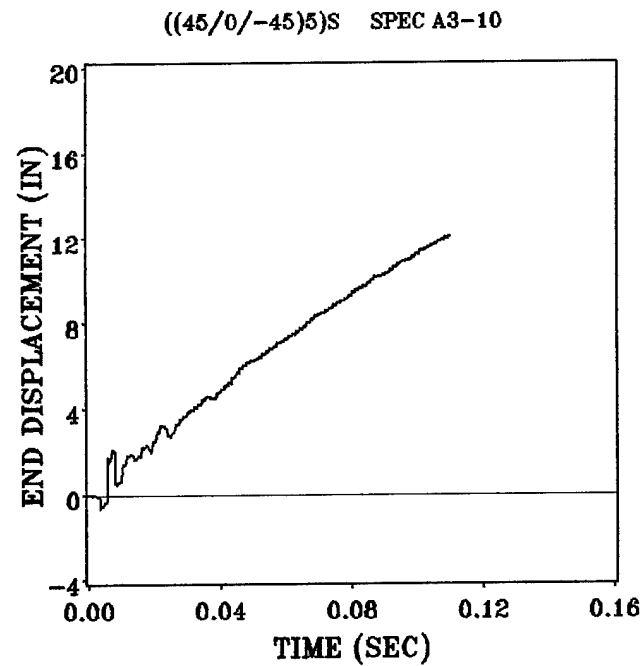
- Kamat, M. P., 1980, "Nonlinear Transient Analysis by Energy Minimization - Theoretical Basis for ACTION Computer Code," NASA Contractor Report 3287, July 1980.
- Kamat, M. P., 1980a, "User's Manual to ACTION Computer Code," NASA Contractor Report 144973, July 1980.
- Mindlin, R. D., 1951, "Influence of Rotary Inertia and Shear on Flexural Motions of Isotropic, Elastic Plates," *Journal of Applied Mechanics*, Vol. 18, pp. 31-38.
- Mondkar, D. P., and Powell, G. H., 1977, "Nonlinear Static and Dynamic Response of Beams and Arches," *International Journal for Numerical Methods in Engineering*, Vol. 11, pp. 499-520.
- Morton, J., 1987, "Scaling of Impact Loaded Carbon Fiber Composites," *Proceedings of the 28th Structures, Structural Dynamics and Materials Conference*, Monterey, California, April 6-8, 1987.
- Pindera, M.-J., Choksi, G., Hidde, J. S., and Herakovich, C. T., 1987, "A Methodology for Accurate Shear Characterization of Unidirectional Composites," *Journal of Composite Materials*, Vol. 21, No. 12, Dec. 1987.
- Reddy, J. N., 1980, "A Penalty Plate-Bending Element for the Analysis of Laminated Anisotropic Composite Plates," *International Journal for Numerical Methods in Engineering*, Vol. 15, pp. 1187-1206.
- Reddy, J. N., and Chao, W. C., 1980, "Finite-Element Analysis of Laminated Bimodulus Composite Material Plates," *Computers and Structures*, Vol. 12, pp. 245-251.
- Stinchcomb, W. W., Reifsnider, K. L., Henneke, E. G., and Kress, G. R., 1985, "Fatigue Damage in Notched Composite Laminates under Tension-Tension Cyclic Loads," NASA Grant NAG-1-232, CCMS-85-12, VPI & SU, Blacksburg, Va.
- Turvey, G. J., 1982, "Study of the Nonlinear Elastic Flexure of Bimodular Composite Strips," *Fibre Science and Technology*, Vol. 16, No. 2, pp. 121-147.
- Walker, A. C., and Hall, D. G., 1968, "An analysis of the Large Deformation of Beams Using the Rayleigh-Ritz Finite Element Method," *The Aeronautical Quarterly*, Nov. 1968, pp. 357-367.
- Yang, P. C., Norris, C. H., and Stavsky, Y., 1966, "Elastic Wave Propagation in Heterogeneous Plates," *International Journal of Solids and Structures*, Vol. 2, pp. 665-684.
- Yang, T. Y., 1972, "Finite Displacement Plate Flexure by the Use of Matrix Incremental Procedure," *International Journal for Numerical Methods in Engineering*, Vol. 4, pp. 415-432.

Appendix A. Dynamic End Displacement-Time for Group One Laminates

This appendix presents the end displacement-time response for all of the Group One laminates with the exception of laminate A1.



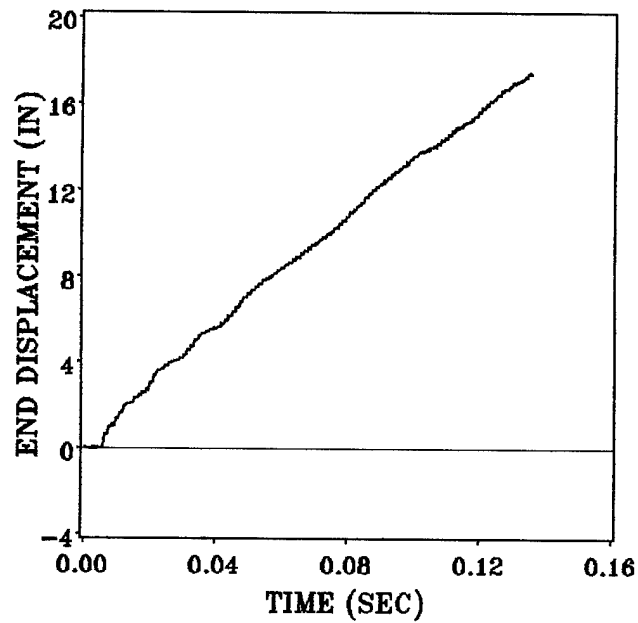
(a) Laminate A2



(b) Laminate A3

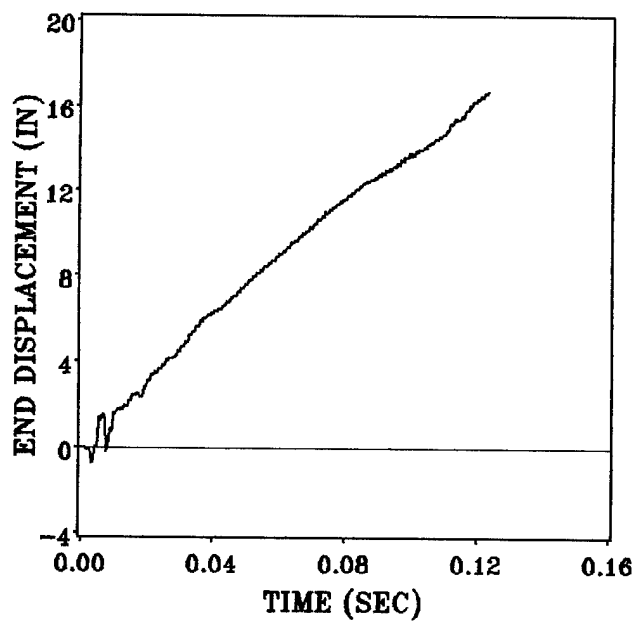
Figure 95. End displacement versus time for laminates A2 and A3

((60/0/-60)5)S SPEC A4-9



(a) Laminate A4

((45/-45/0/90)4)S SPEC A5-8

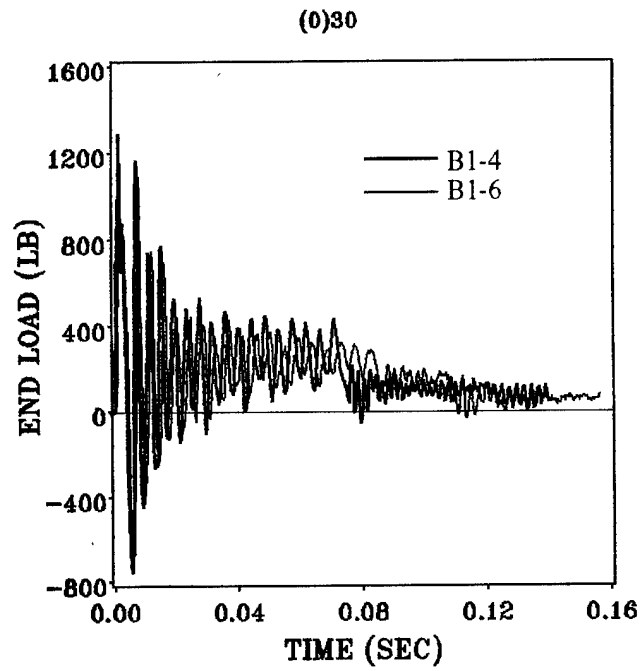


(b) Laminate A5

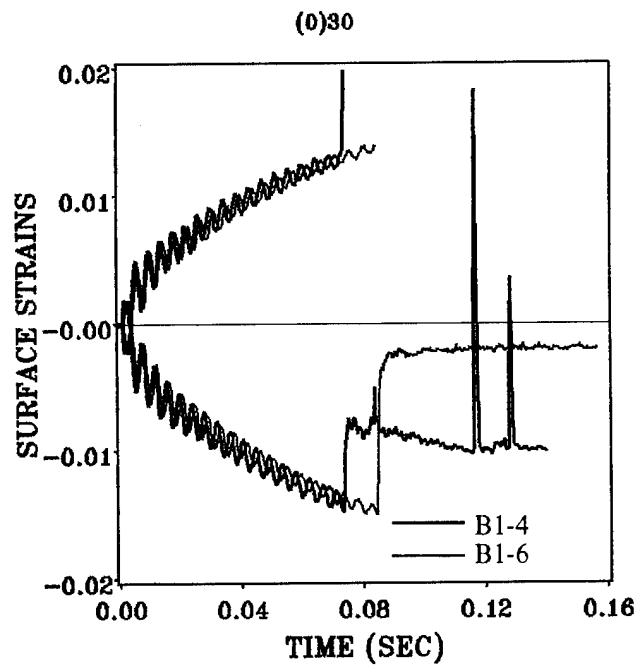
Figure 96. End displacement versus time for laminates A4 and A5

Appendix B. Dynamic Data for Group Two and Group Three Laminates

This appendix presents the load-time and surface strain-time data for all the Group Two and Group Three laminates with the exception of laminate B2. (The data for laminate B2 was presented in Chapter 3). The end displacement-time results for these laminates are also presented in this appendix.

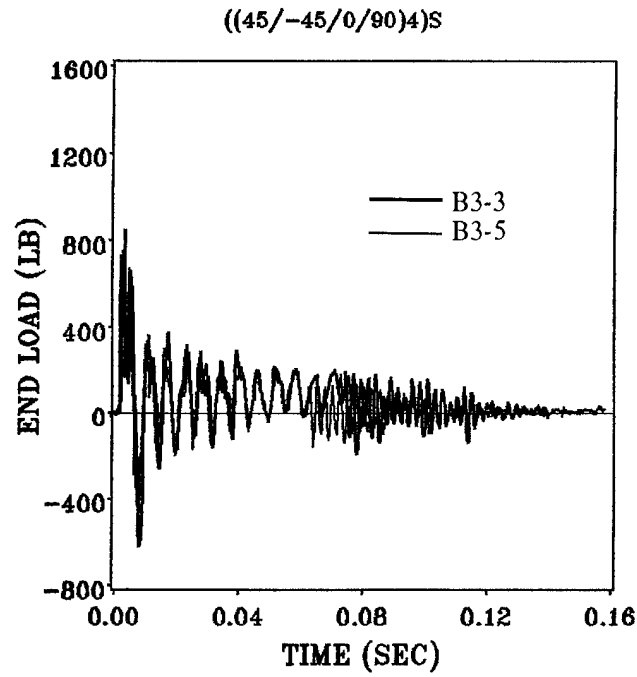


(a) Load versus time

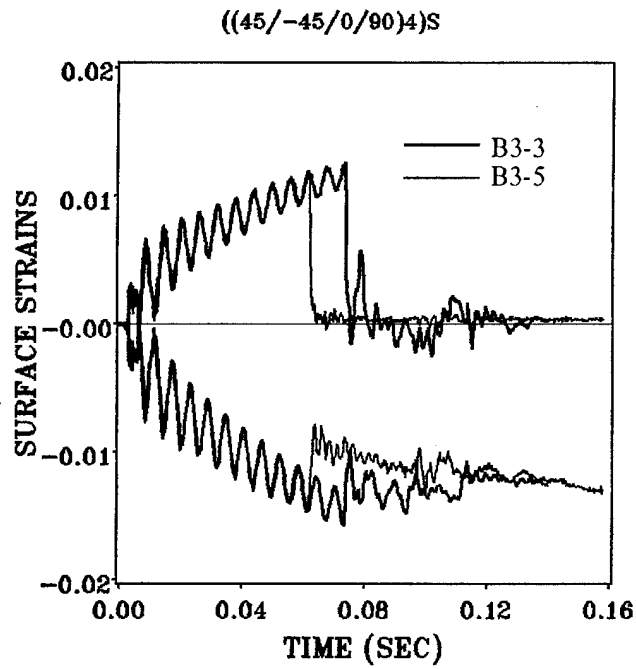


(b) Surface strains at middle versus time

Figure 97. Load and strain versus time for laminate B1

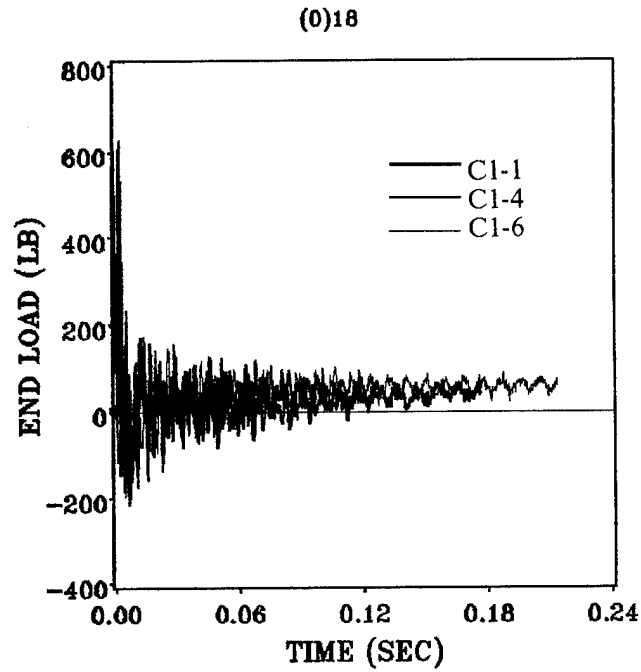


(a) Load versus time

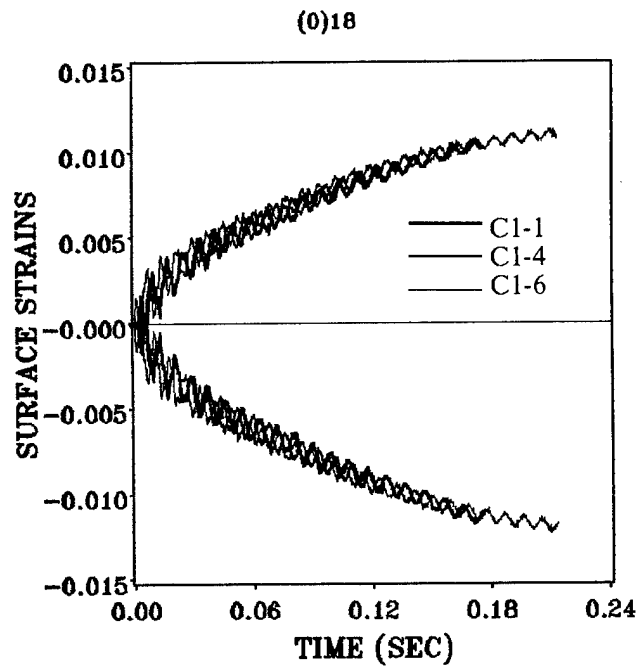


(b) Surface strains at middle versus time

Figure 98. Load and strain versus time for laminate B3

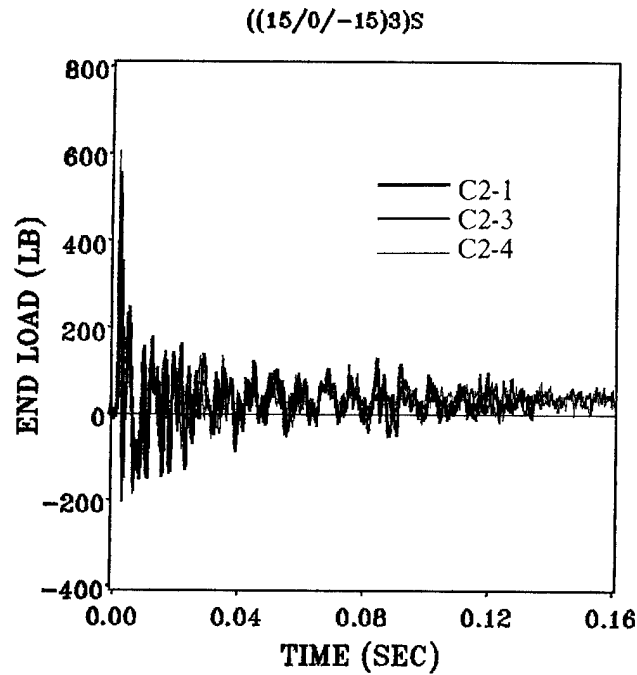


(a) Load versus time

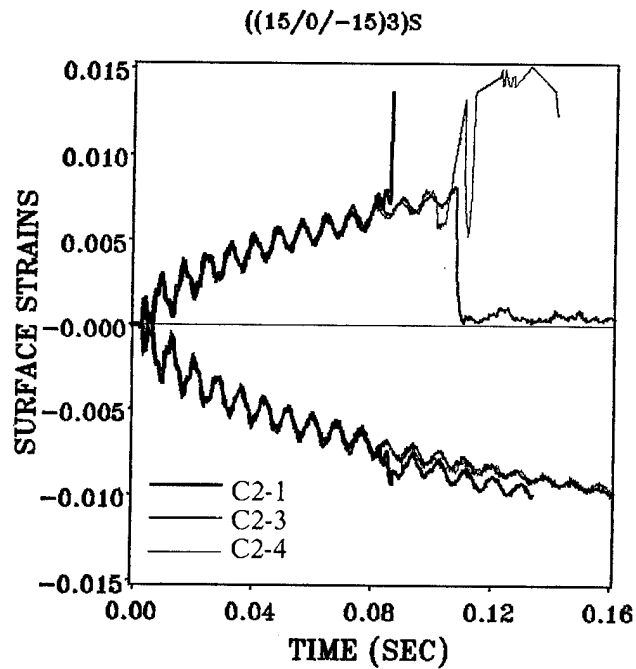


(b) Surface strains at middle versus time

Figure 99. Load and strain versus time for laminate C1

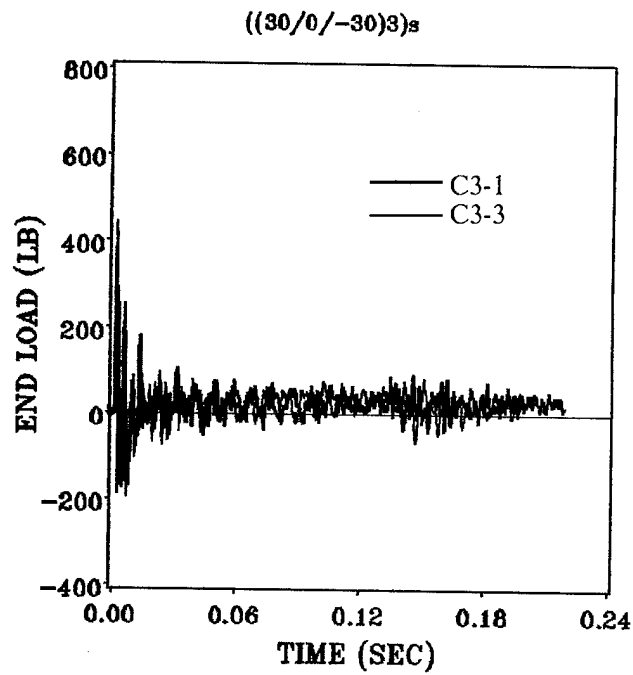


(a) Load versus time

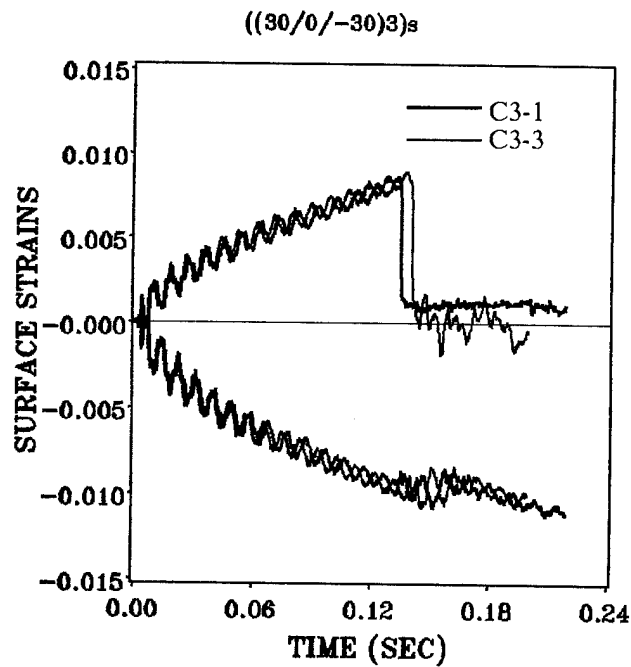


(b) Surface strains at middle versus time

Figure 100. Load and strain versus time for laminate C2

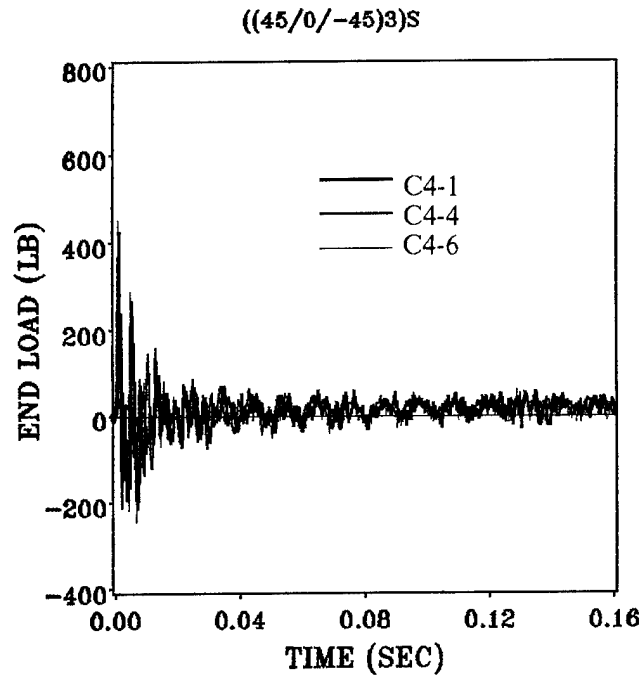


(a) Load versus time

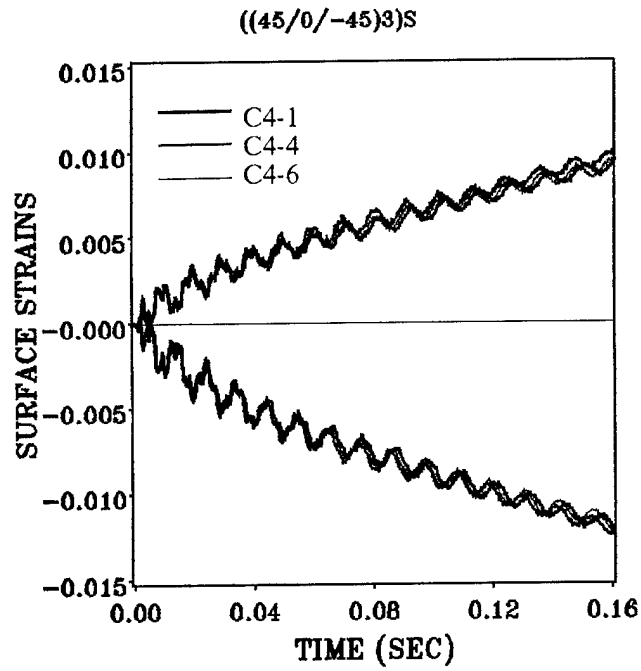


(b) Surface strains at middle versus time

Figure 101. Load and strain versus time for laminate C3

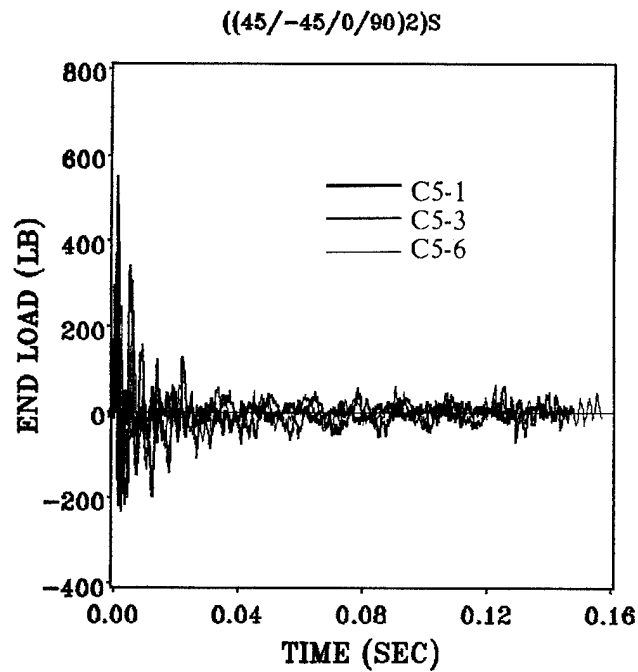


(a) Load versus time

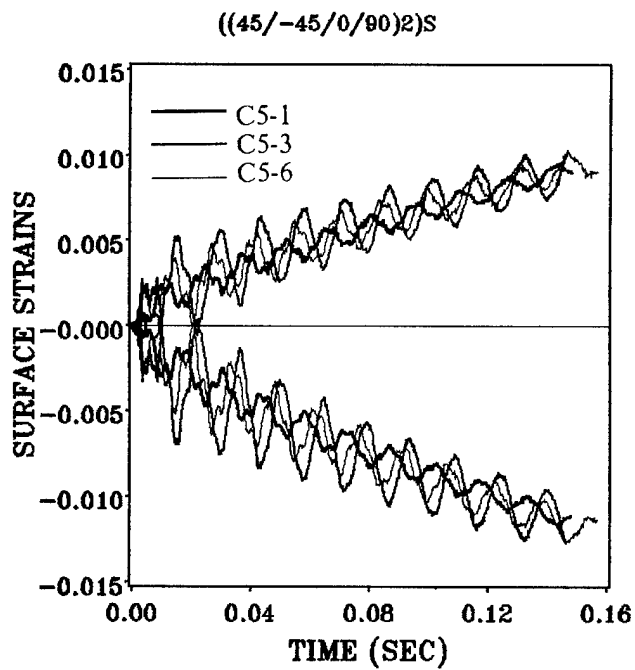


(b) Surface strains at middle versus time

Figure 102. Load and strain versus time for laminate C4

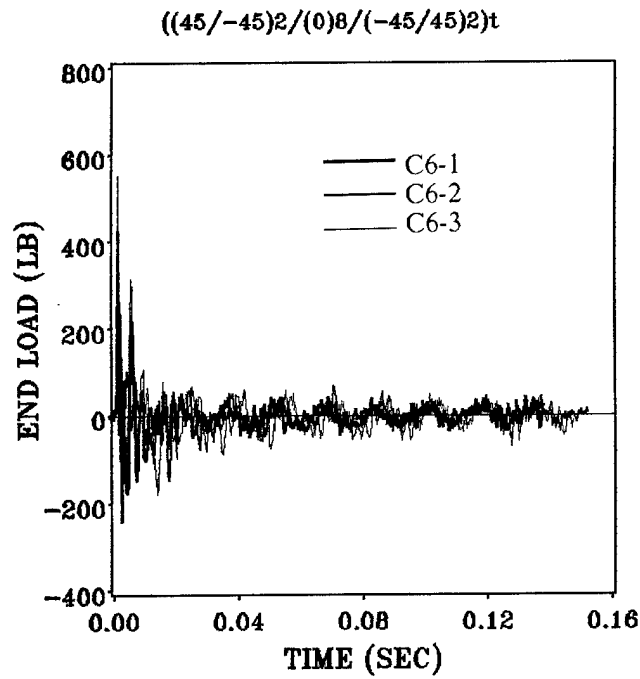


(a) Load versus time

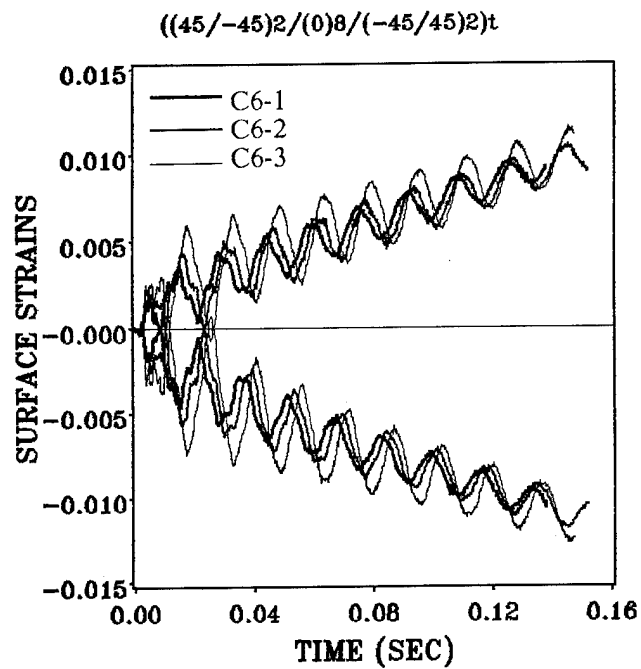


(b) Surface strains at middle versus time

Figure 103. Load and strain versus time for laminate C5

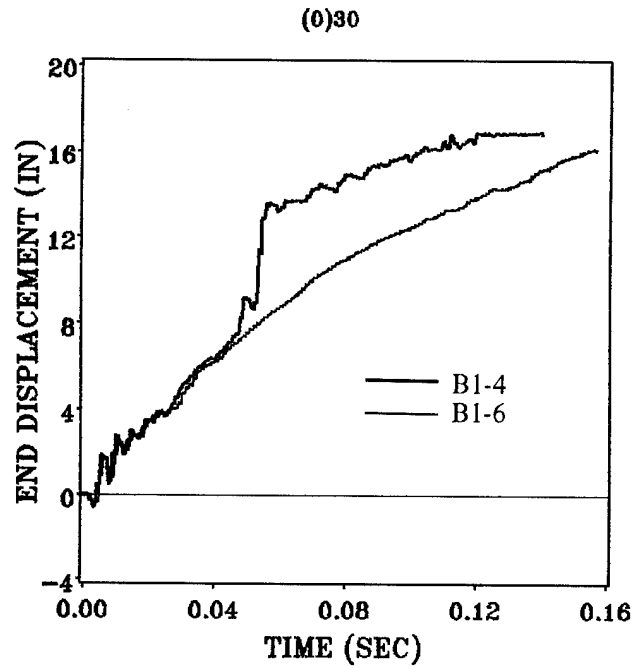


(a) Load versus time

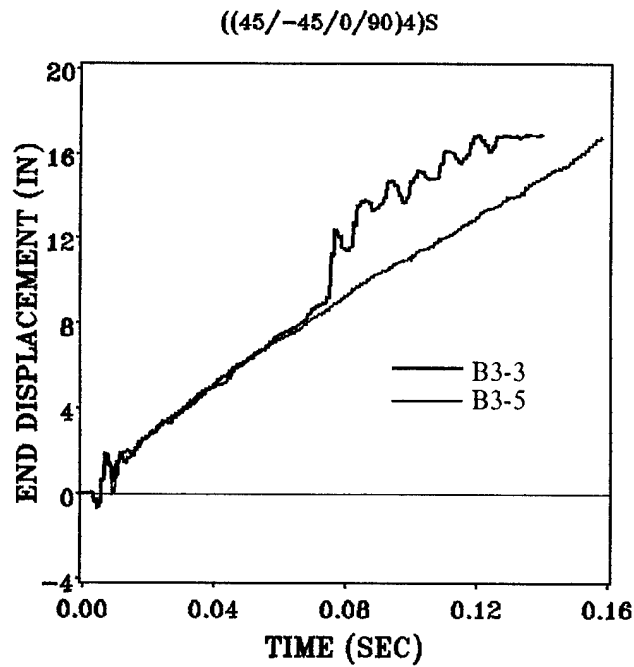


(b) Surface strains at middle versus time

Figure 104. Load and strain versus time for laminate C6

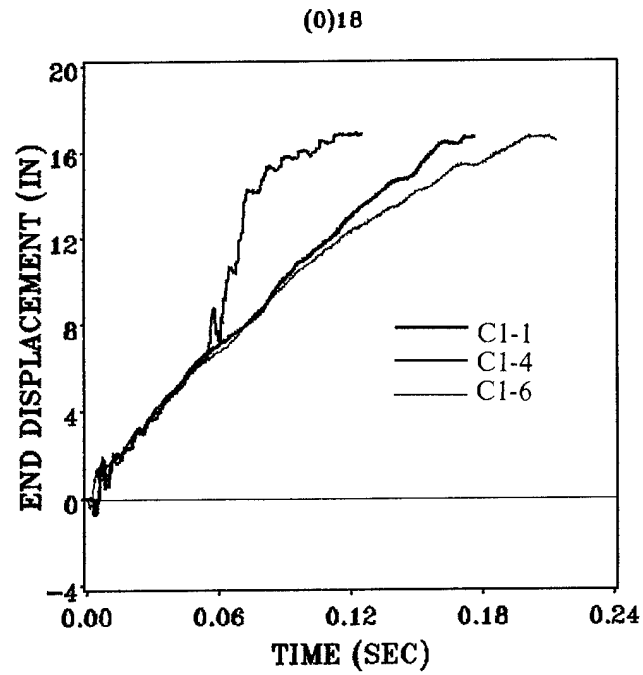


(a) Laminate B1

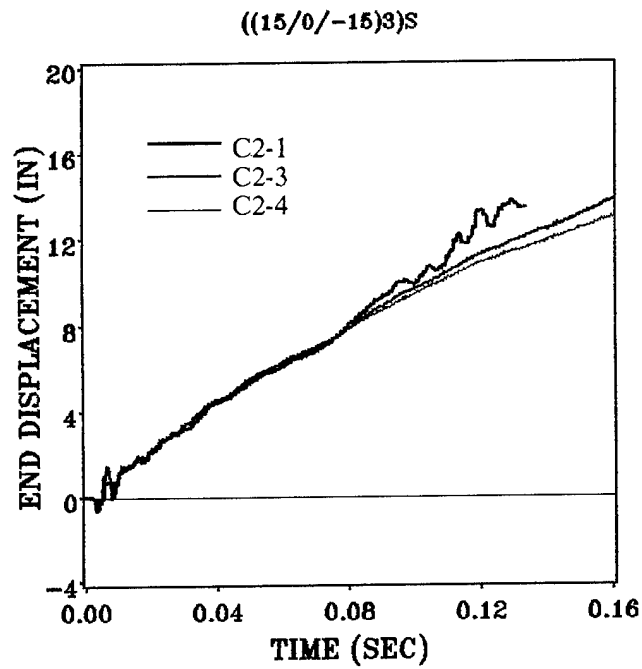


(b) Laminate B3

Figure 105. End displacement versus time for laminates B1 and B3

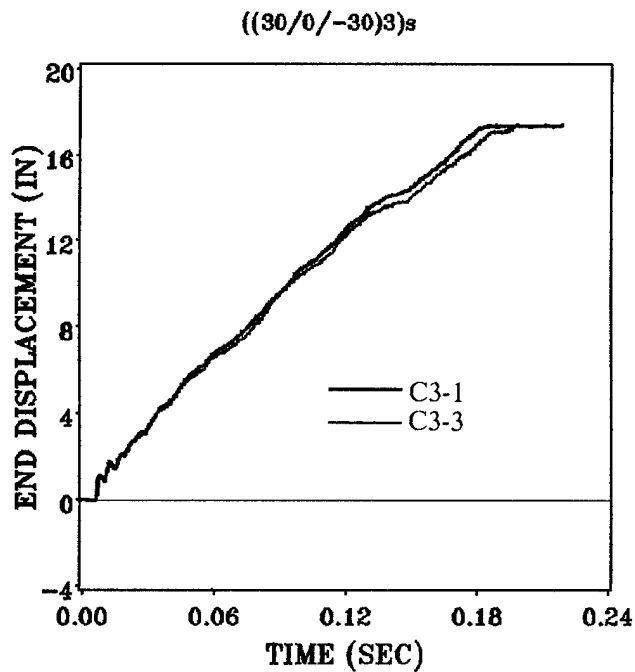


(a) Laminate C1

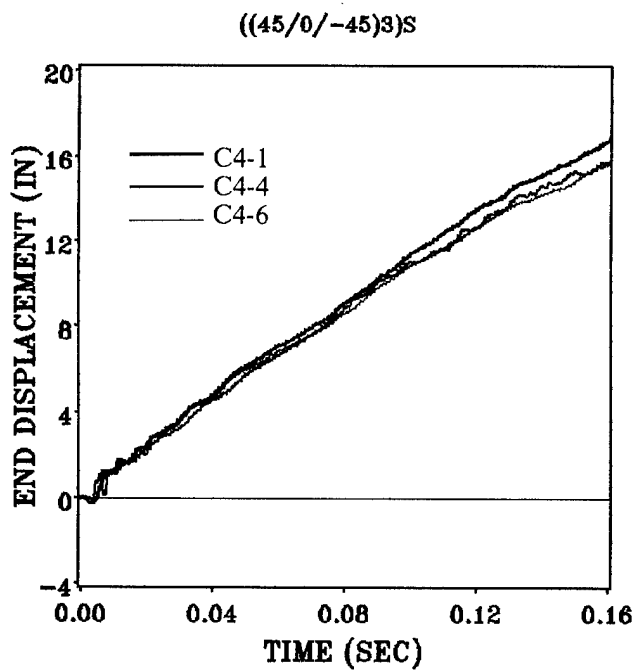


(b) Laminate C2

Figure 106. End displacement versus time for laminates C1 and C2

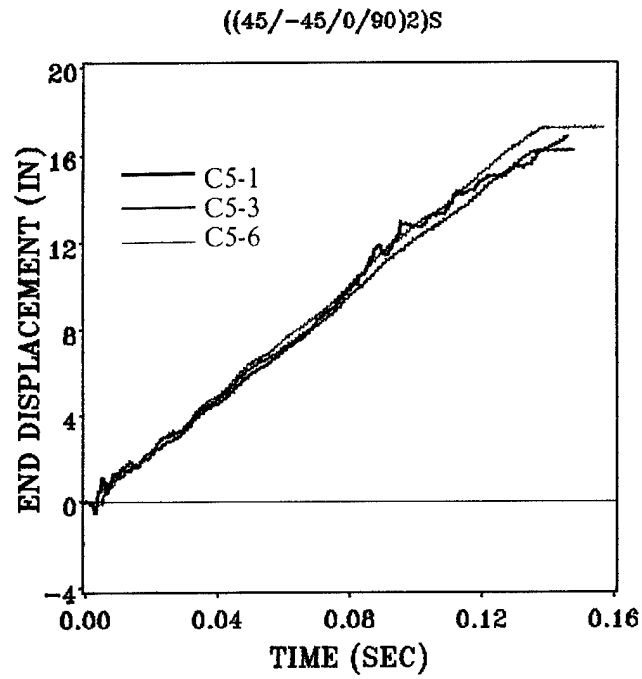


(a) Laminate C3

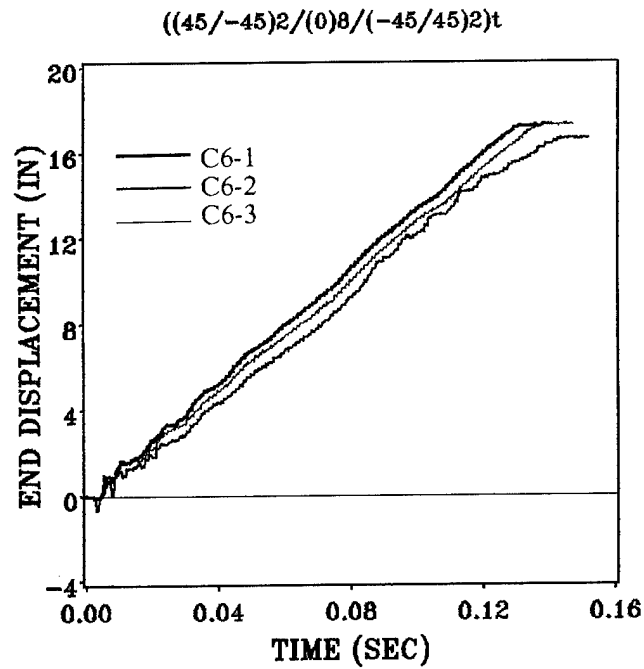


(b) Laminate C4

Figure 107. End displacement versus time for laminates C3 and C4



(a) Laminate C5

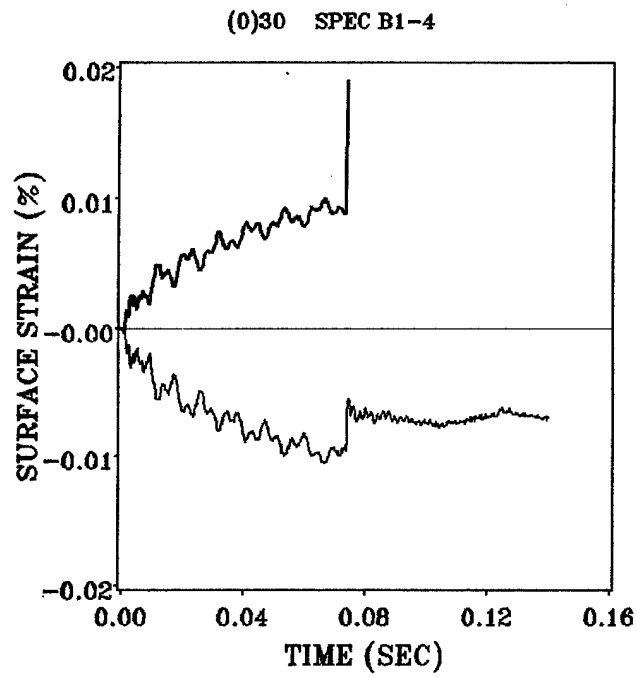


(b) Laminate C6

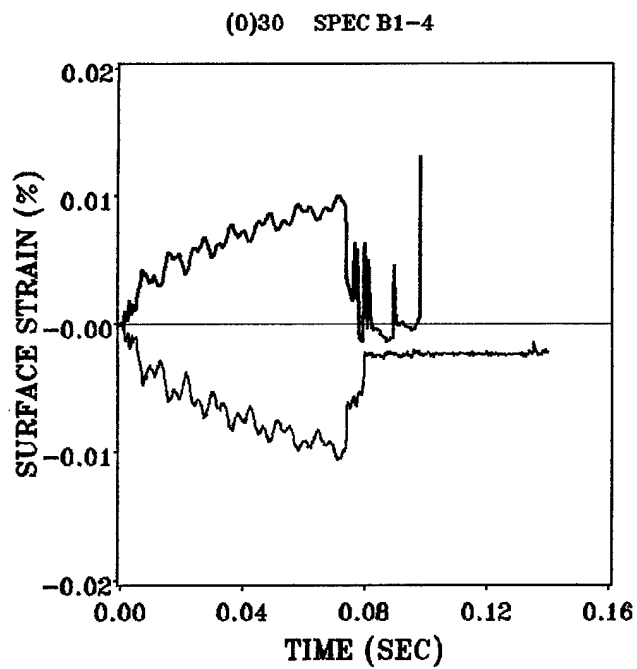
Figure 108. End displacement versus time for laminates C5 and C6

Appendix C. Quarter-Point Dynamic Strain Data

This appendix presents the surface strain-time data for the strain gages which were mounted longitudinally at the beam quarter- points. The data is presented for all laminates from Groups Two and Three except laminates B3 and C3. The data for these two laminates was lost due to strain gage failure.

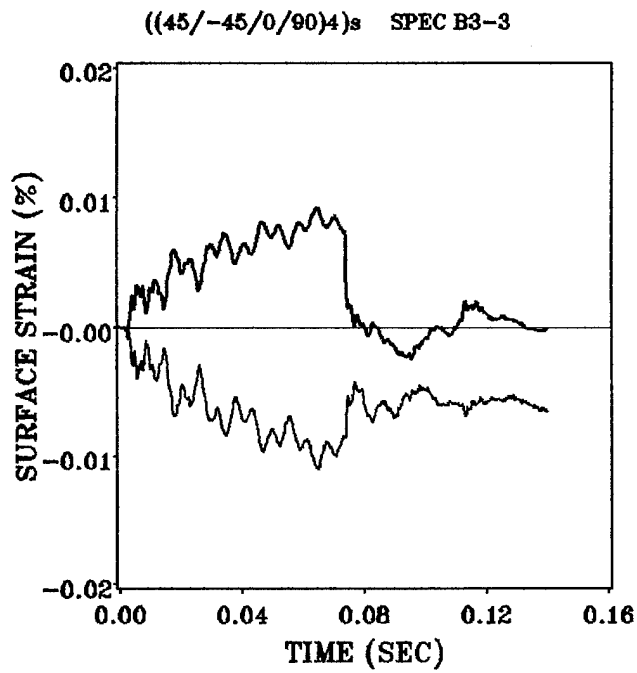


(a) Upper quarter-point

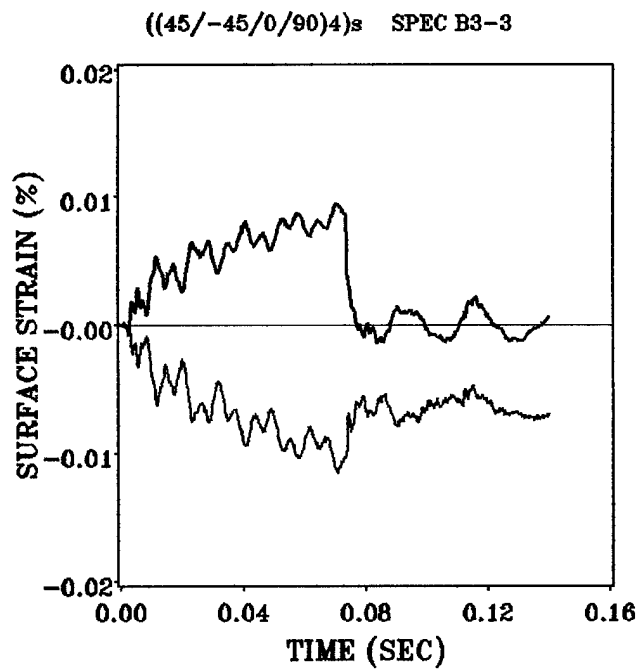


(b) Lower quarter-point

Figure 109. Quarter point strains versus time for laminate B1

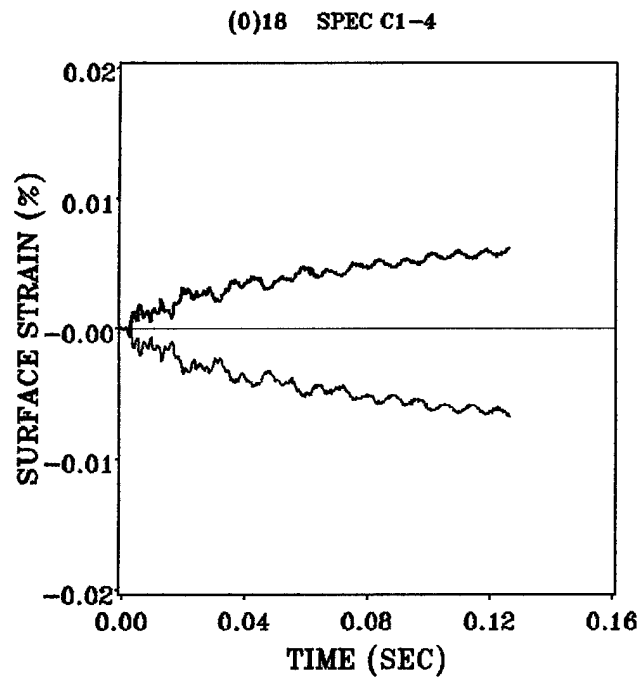


(a) Upper quarter-point

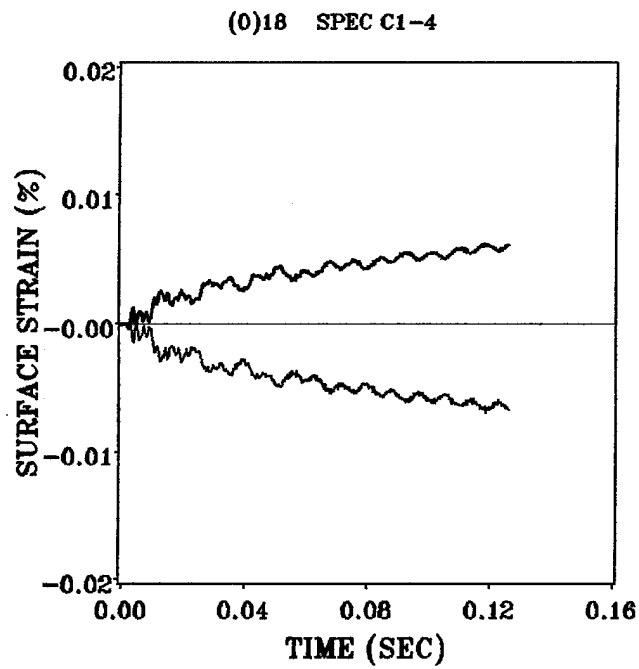


(b) Lower quarter-point

Figure 110. Quarter point strains versus time for laminate B3

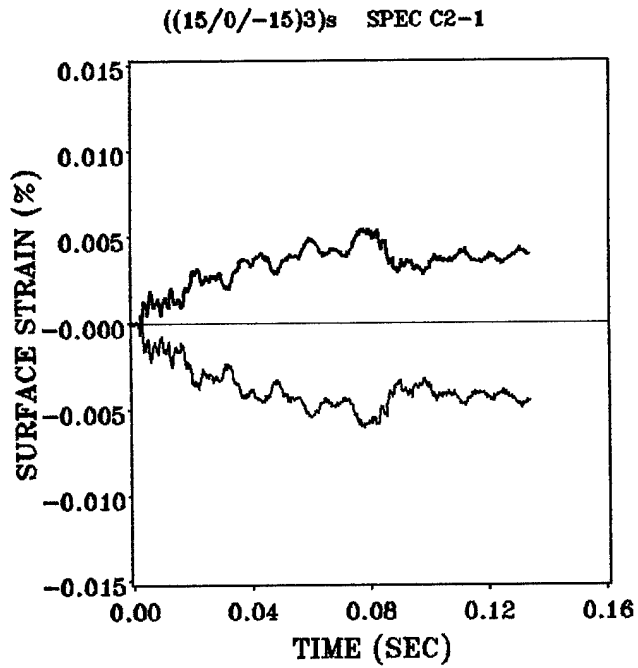


(a) Upper quarter-point

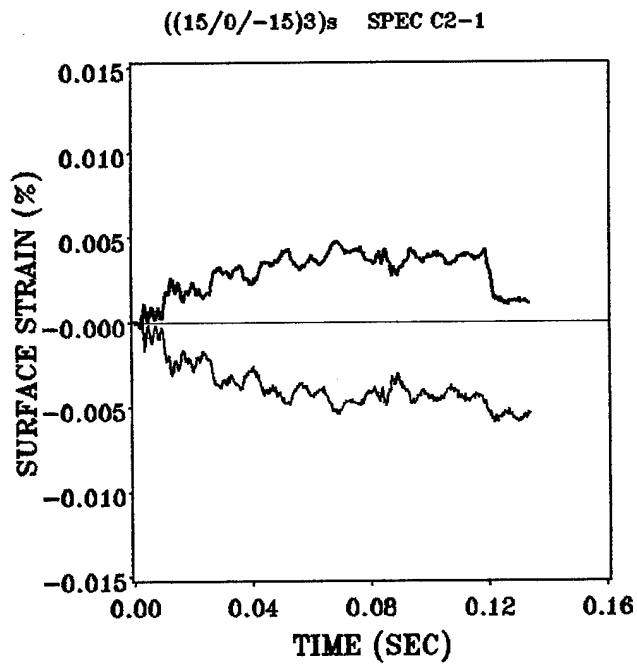


(b) Lower quarter-point

Figure 111. Quarter point strains versus time for laminate C1



(a) Upper quarter-point



(b) Lower quarter-point

Figure 112. Quarter point strains versus time for laminate C2

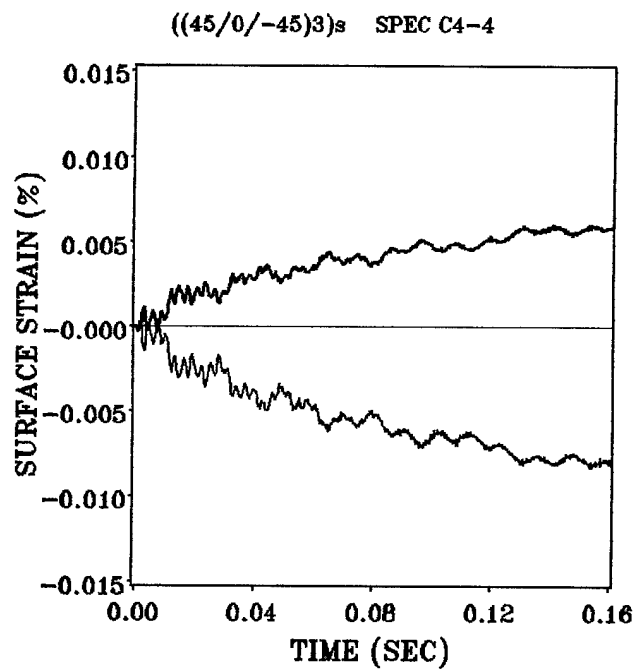
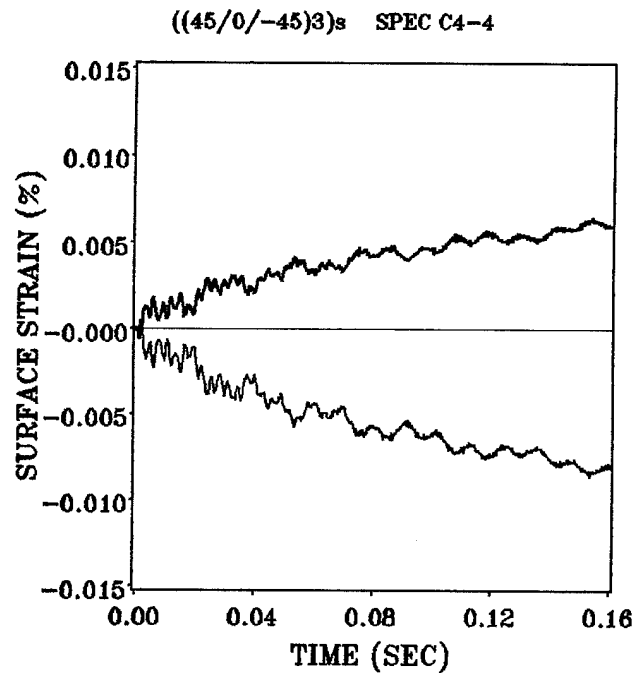


Figure 113. Quarter point strains versus time for laminate C4

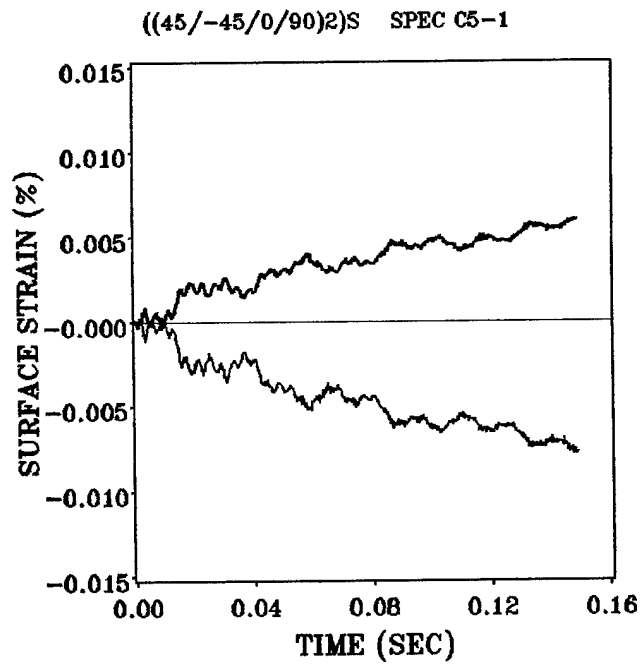
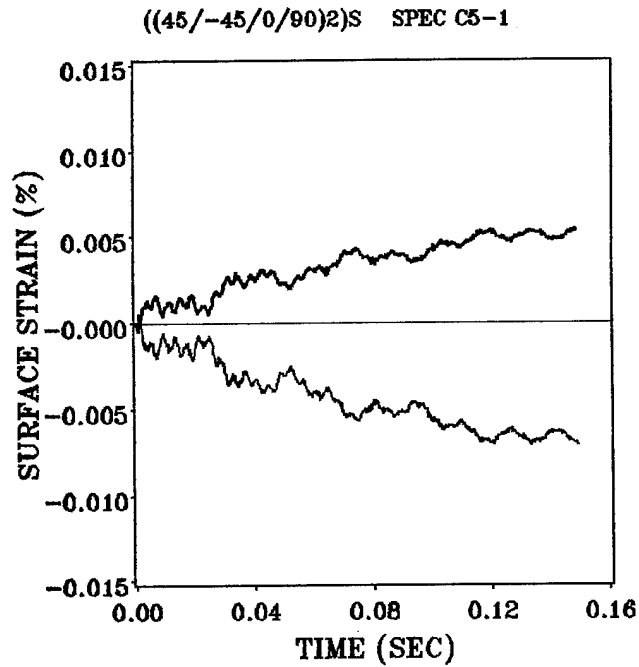
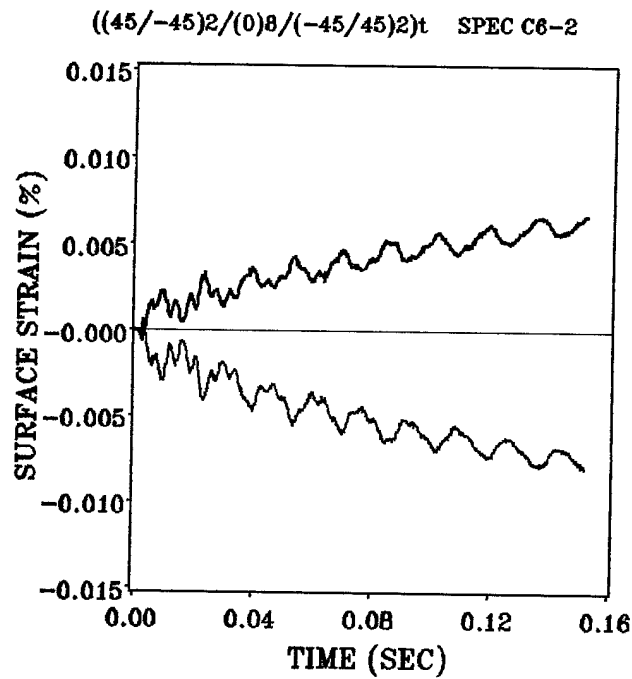
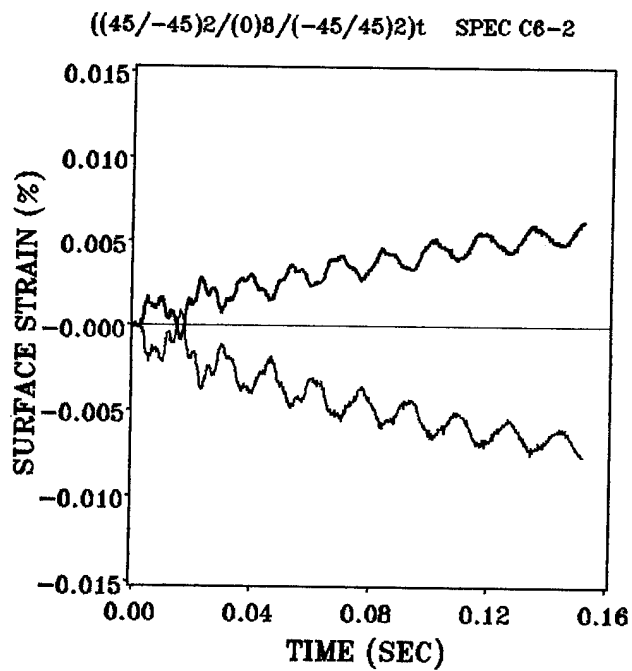


Figure 114. Quarter point strains versus time for laminate C5



(a) Upper quarter-point

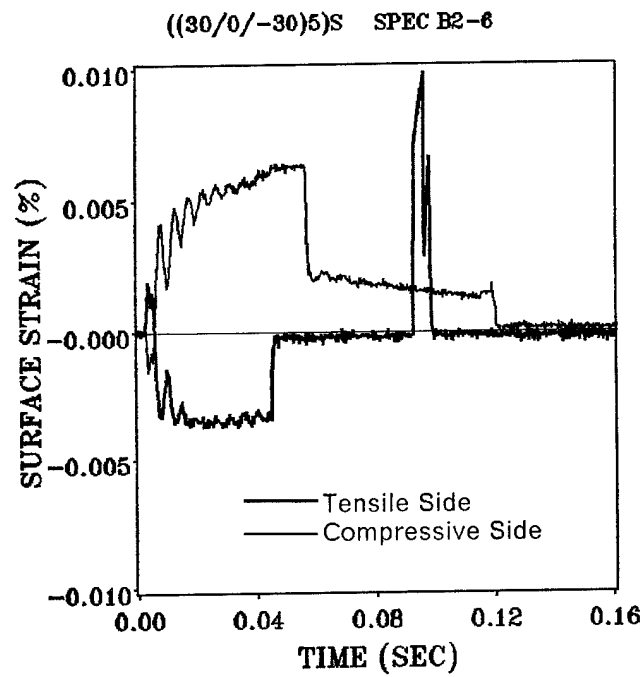


(b) Lower quarter-point

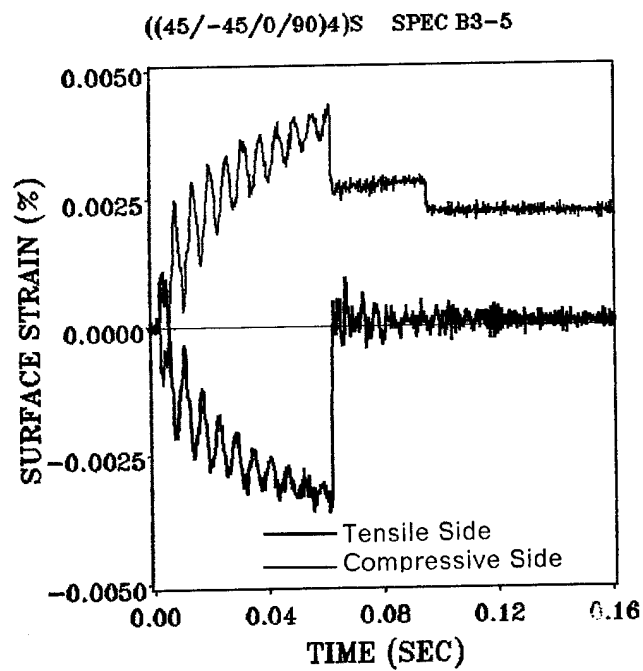
Figure 115. Quarter point strains versus time for laminate C6

Appendix D. Transverse Dynamic Strain Data

This appendix presents the transverse strain-time response for all laminates in Groups Two and Three with the exception of laminate B1. This was the $[0]_{30}$ laminate, which suffered longitudinal cracks almost immediately after impact. These cracks caused the transverse strain gages to debond from the laminate surface.

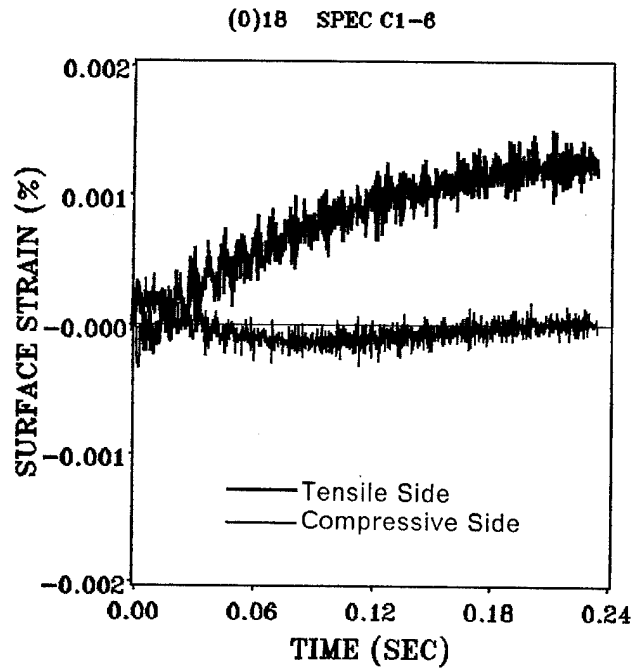


(a) Laminate B2

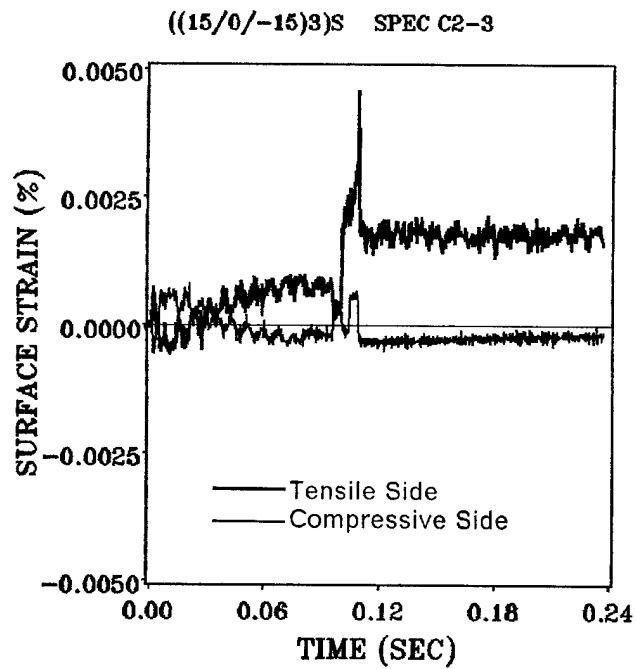


(b) Laminate B3

Figure 116. Transverse strains versus time for laminates B2 and B3



(a) Laminate C1



(b) Laminate C2

Figure 117. Transverse strains versus time for laminates C1 and C2

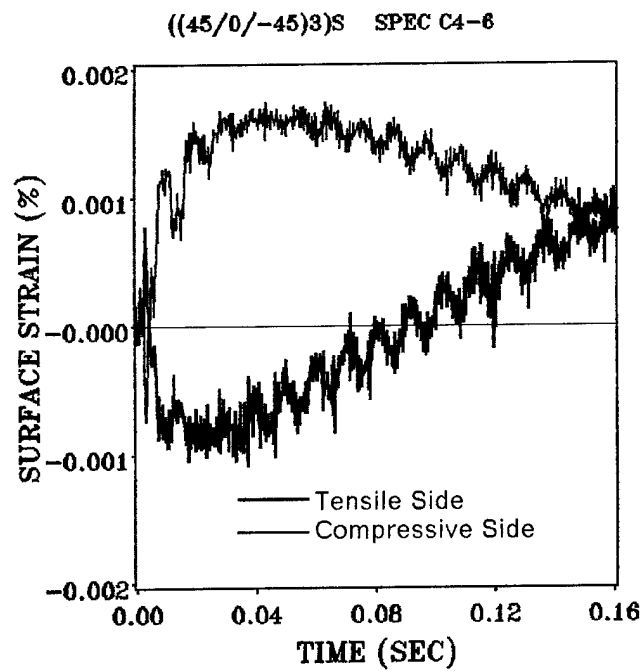
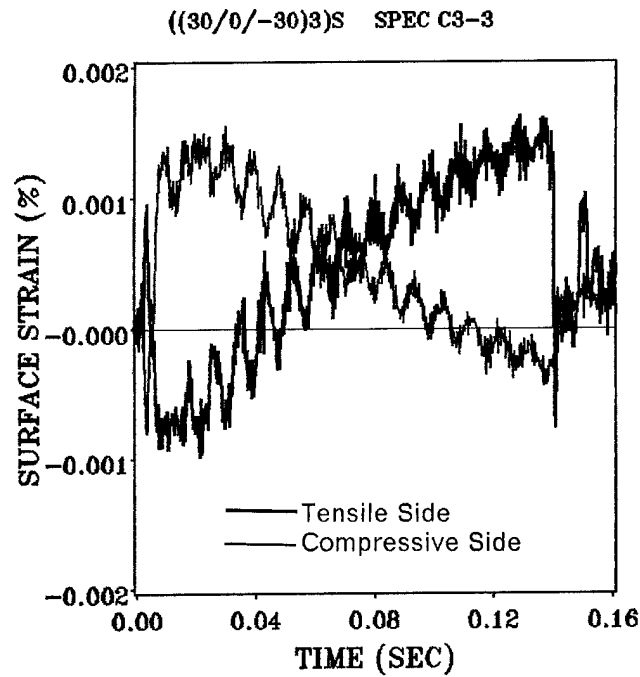


Figure 118. Transverse strains versus time for laminates C3 and C4

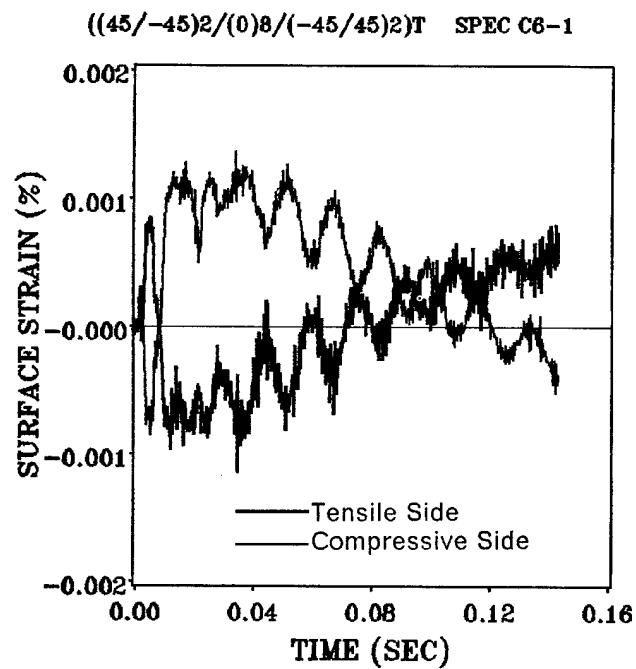
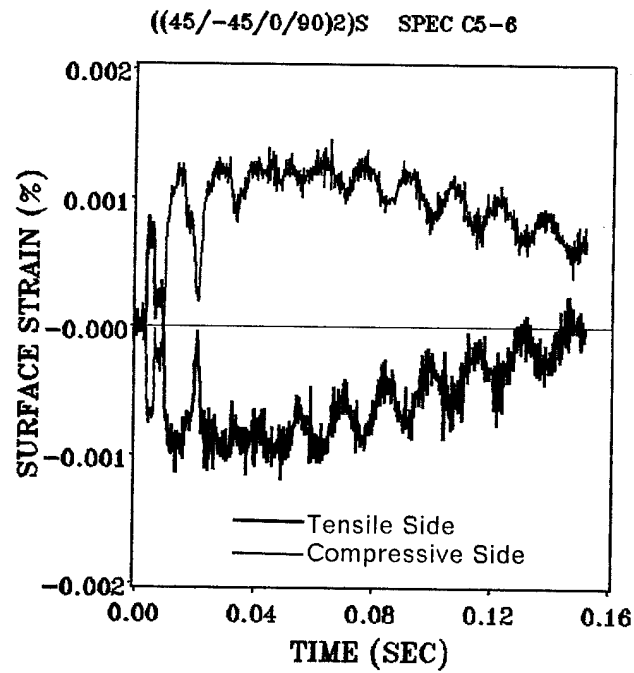


Figure 119. Transverse strains versus time for laminates C5 and C6

Appendix E. Finite Element Equations

The form of the finite element equations was shown in Equation (5.21). The element stiffness matrix is comprised of 64 submatrices. Also, the displacement and force vectors are comprised of eight subvectors. The explicit forms of these submatrices and subvectors are shown here in terms of the laminate stiffnesses A, B, and D, and the width of the beam, $\beta = 2b$.

$$[k^{11}] = A_{11} [S^3]$$

$$[k^{12}] = [k^{21}]^T = \frac{A_{11}\beta^2}{12} [S^3]$$

$$[k^{13}] = [k^{31}]^T = A_{16} [S^2]^T$$

$$[k^{14}] = [k^{41}]^T = A_{16} [S^3]$$

$$[k^{15}] = [k^{51}]^T = A_{12} [S^2]^T$$

$$[k^{16}] = [k^{61}]^T = -B_{11} [S^9]$$

$$[k^{17}] = [k^{71}]^T = -\frac{B_{11}\beta^2}{12} [S^9] - 2B_{12} [S^7]$$

$$[k^{18}] = [k^{81}]^T = -2B_{16} [S^8]$$

$$[k^{22}] = \frac{A_{11}\beta^4}{80} [S^3] + \frac{A_{66}\beta^2}{3} [S^1]$$

$$[k^{23}] = [k^{32}]^T = \frac{A_{16}\beta^2}{12} [S^2]^T + \frac{A_{16}\beta^2}{6} [S^2]$$

$$[k^{24}] = [k^{42}]^T = \frac{A_{16}\beta^2}{12} [S^3]$$

$$[k^{25}] = [k^{52}]^T = \frac{A_{12}\beta^2}{12} [S^2]^T + \frac{A_{66}\beta^2}{6} [S^2]$$

$$[k^{26}] = [k^{62}]^T = -\frac{B_{11}\beta^2}{12} [S^9]$$

$$[k^{27}] = [k^{72}]^T = -\frac{B_{11}\beta^4}{80} [S^9] - \frac{B_{12}\beta^2}{6} [S^7] - \frac{2B_{66}\beta^2}{3} [S^5]$$

$$[k^{28}] = [k^{82}]^T = -\frac{B_{16}\beta^2}{6} [S^8] - \frac{B_{16}\beta^2}{6} [S^6]$$

$$[k^{33}] = \frac{A_{11}\beta^2}{12} [S^3] + A_{66} [S^1]$$

$$[k^{34}] = [k^{43}]^T = A_{66} [S^2]$$

$$[k^{35}] = [k^{53}]^T = \frac{A_{16}\beta^2}{12} [S^3] + A_{26} [S^1]$$

$$[k^{36}] = [k^{63}]^T = -B_{16} [S^6]$$

$$[k^{37}] = [k^{73}]^T = -\frac{B_{16}\beta^2}{3} [S^8] - \frac{B_{16}\beta^2}{12} [S^6] - 2B_{26} [S^4]$$

$$[k^{38}] = [k^{83}]^T = -\frac{B_{11}\beta^2}{12}[S^9] - 2B_{66}[S^5]$$

$$[k^{44}] = A_{66}[S^3]$$

$$[k^{45}] = [k^{54}]^T = A_{26}[S^2]^T$$

$$[k^{46}] = [k^{64}]^T = -B_{16}[S^9]$$

$$[k^{47}] = [k^{74}]^T = -\frac{B_{16}\beta^2}{12}[S^9] - 2B_{26}[S^7]$$

$$[k^{48}] = [k^{84}]^T = -2B_{66}[S^8]$$

$$[k^{55}] = A_{22}[S^1] + \frac{A_{66}\beta^2}{12}[S^3]$$

$$[k^{56}] = [k^{65}]^T = -B_{12}[S^6]$$

$$[k^{57}] = [k^{75}]^T = -\frac{B_{12}\beta^2}{12}[S^6] - 2B_{22}[S^4] - \frac{B_{66}\beta^2}{3}[S^8]$$

$$[k^{58}] = [k^{85}]^T = -2B_{26}[S^5] - \frac{B_{16}\beta^2}{12}[S^9]$$

$$[k^{66}] = D_{11}[S^{15}] + P[S^{13}]$$

$$[k^{67}] = [k^{76}]^T = \frac{D_{11}\beta^2}{12}[S^{15}] + 2D_{12}[S^{12}]^T + \frac{P\beta^2}{12}[S^{13}]$$

$$[k^{68}] = [k^{86}]^T = 2D_{16} [S^{14}]^T$$

$$[k^{77}] = \frac{D_{11}\beta^4}{80} [S^{15}] + \frac{D_{12}\beta^2}{6} \{ [S^{12}] + [S^{12}]^T \} + 4D_{22} [S^{10}]$$

$$+ \frac{4D_{66}\beta^2}{3} [S^{13}] + \frac{P\beta^4}{80} [S^{13}]$$

$$[k^{78}] = [k^{87}]^T = \frac{D_{16}\beta^2}{6} [S^{14}]^T + \frac{D_{16}\beta^2}{3} [S^{14}] + 4D_{26} [S^{11}]$$

$$[k^{88}] = \frac{D_{11}\beta^2}{12} [S^{15}] + 4D_{66} [S^{13}] + \frac{P\beta^2}{12} [S^{13}]$$

$$\{U\} = \begin{Bmatrix} U_1 \\ U_2 \end{Bmatrix}$$

$$\{\alpha\} = \begin{Bmatrix} \alpha_1 \\ \alpha_2 \end{Bmatrix}$$

$$\{\eta\} = \begin{Bmatrix} \eta_1 \\ \eta_2 \end{Bmatrix}$$

$$\{V\} = \begin{Bmatrix} V_1 \\ V_2 \end{Bmatrix}$$

$$\{\omega\} = \begin{Bmatrix} \omega_1 \\ \omega_2 \end{Bmatrix}$$

$$\{W\} = \begin{Bmatrix} W_1 \\ -W'_1 \\ W_2 \\ -W'_2 \end{Bmatrix}$$

$$\{g\} = \begin{Bmatrix} g_1 \\ -g'_1 \\ g_2 \\ -g'_2 \end{Bmatrix}$$

$$\{\Theta\} = \begin{Bmatrix} \Theta_1 \\ -\Theta'_1 \\ \Theta_2 \\ -\Theta'_2 \end{Bmatrix}$$

$$\{F^1\} = \begin{Bmatrix} \bar{N}_{x1} \\ \bar{N}_{x2} \end{Bmatrix}$$

$$\{F^2\} = \frac{\beta^2}{12} \{F^1\}$$

$$\{F^3\} = \begin{Bmatrix} 0 \\ 0 \end{Bmatrix}$$

$$\{F^4\} = \begin{Bmatrix} \bar{N}_{y1} \\ \bar{N}_{y2} \end{Bmatrix}$$

$$\{F^5\} = \begin{Bmatrix} 0 \\ 0 \end{Bmatrix}$$

$$\{F^6\} = \begin{Bmatrix} \bar{Q}_1 \\ \bar{M}_{x1} \\ \bar{Q}_2 \\ \bar{M}_{x2} \end{Bmatrix}$$

$$\{F^7\} = \frac{\beta^2}{12} \{F^6\}$$

$$\{F^8\} = \begin{Bmatrix} 0 \\ 0 \end{Bmatrix}$$

The matrices $[S^1] - [S^{15}]$ are given by the following expressions.

$$[S^1] = \frac{L}{6} \begin{bmatrix} 2 & 1 \\ 1 & 2 \end{bmatrix}$$

$$[S^2] = \frac{1}{2} \begin{bmatrix} -1 & 1 \\ -1 & 1 \end{bmatrix}$$

$$[S^3] = \frac{1}{L} \begin{bmatrix} 1 & -1 \\ -1 & 1 \end{bmatrix}$$

$$[S^4] = L \begin{bmatrix} \frac{7}{20} & \frac{-L}{20} & \frac{3}{20} & \frac{L}{30} \\ \frac{3}{20} & \frac{-L}{30} & \frac{7}{20} & \frac{L}{20} \end{bmatrix}$$

$$[S^5] = \frac{1}{12} \begin{bmatrix} -6 & -L & 6 & L \\ -6 & L & 6 & -L \end{bmatrix}$$

$$[S^6] = \frac{1}{L} \begin{bmatrix} -1 & L & 1 & 0 \\ 1 & 0 & -1 & -L \end{bmatrix}$$

$$[S^7] = \frac{1}{12} \begin{bmatrix} -6 & L & -6 & -L \\ 6 & -L & 6 & L \end{bmatrix}$$

$$[S^8] = \frac{1}{L} \begin{bmatrix} 1 & 0 & -1 & 0 \\ -1 & 0 & 1 & 0 \end{bmatrix}$$

$$[S^9] = \frac{1}{L} \begin{bmatrix} 0 & -1 & 0 & 1 \\ 0 & 1 & 0 & -1 \end{bmatrix}$$

$$[S^{10}] = \frac{L}{420} \begin{bmatrix} 156 & -22L & 54 & 13L \\ -22L & 4L^2 & -13L & -3L^2 \\ 54 & -13L & 156 & 22L \\ 13L & -3L^2 & 22L & 4L^2 \end{bmatrix}$$

$$[S^{11}] = \frac{1}{60} \begin{bmatrix} -30 & -6L & 30 & 6L \\ 6L & 0 & -6L & -L^2 \\ -30 & 6L & 30 & -6L \\ -6L & L^2 & 6L & 0 \end{bmatrix}$$

$$[S^{12}] = \frac{1}{10L} \begin{bmatrix} -12 & 11L & 12 & L \\ L & \frac{-4L^2}{3} & -L & \frac{L^2}{3} \\ 12 & -L & -12 & -11L \\ L & \frac{L^2}{3} & -L & \frac{-4L^2}{3} \end{bmatrix}$$

$$[S^{13}] = \frac{1}{10L} \begin{bmatrix} 12 & -L & -12 & -L \\ -L & \frac{4L^2}{3} & L & \frac{-L^2}{3} \\ -12 & L & 12 & L \\ -L & \frac{-L^2}{3} & L & \frac{4L^2}{3} \end{bmatrix}$$

$$[S^{14}] = \frac{1}{L^2} \begin{bmatrix} 0 & -L & 0 & L \\ L & \frac{-L^2}{2} & -L & \frac{-L^2}{2} \\ 0 & L & 0 & -L \\ -L & \frac{L^2}{2} & L & \frac{L^2}{2} \end{bmatrix}$$

$$[S^{15}] = \frac{2}{L^3} \begin{bmatrix} 6 & -3L & -6 & -3L \\ -3L & 2L^2 & 3L & L^2 \\ -6 & 3L & 6 & 3L \\ -3L & L^2 & 3L & 2L^2 \end{bmatrix}$$

Appendix F. Stress-Strain Curve Approximation

Polynomials

As discussed in Chapter 5, the stress-strain relations obtained from the material characterization tests were approximated using polynomial algebraic expressions. Those expressions are summarized in this Appendix.

Since the finite element model required expressions for moduli as functions of principal strains, the polynomials were derived in that form. Cubic polynomials were chosen and were found to adequately describe the material characterization results. To determine the coefficients of the four cubic terms (constant, ϵ , ϵ^2 , and ϵ^3), the tangent modulus was determined at the initial, final, and two intermediate load points. These moduli were obtained graphically. Substituting these values into the cubic modulus equation yielded four linear equations which were solved for the four coefficients. The modulus expressions obtained by this method were then integrated to obtain the corresponding stress-strain polynomials (which were of fourth-order). These stress-strain functions were plotted with the experimental stress-strain relations and found to correlate well.

The resulting polynomial expressions are summarized here. If strain values were encountered in the model which exceeded the maximum strain encountered in the material characterization tests, the value of the moduli at the highest test strain was used.

F.1 Longitudinal Tension

The expression for tensile fiber-direction modulus, E_{1t} as a function of fiber-direction strain is:

For $0 \leq \epsilon_1 < 0.009$:

$$E_{1t} = E_{10} + A\epsilon_1 + B\epsilon_1^2 + C\epsilon_1^3 \text{ Msi}$$

where:

$$E_{10} = 1.985 \times 10^1$$

$$A = 3.569092 \times 10^2$$

$$B = -3.6704341 \times 10^4$$

$$C = 6.216131926 \times 10^6$$

For $\epsilon_1 \geq 0.009$:

$$E_{1t} = 24.62 \text{ Msi}$$

F.2 Longitudinal Compression

The expression for compressive fiber-direction modulus, E_{1c} as a function of fiber-direction strain is:

For $-0.007 < \epsilon_1 < 0$:

$$E_{1c} = E_{10} + A\epsilon_1 + B\epsilon_1^2 + C\epsilon_1^3 \text{ Msi}$$

where:

$$E_{10} = 1.940 \times 10^1$$

$$A = 3.196797 \times 10^2$$

$$B = 5.2707297 \times 10^4$$

$$C = 1.512244282 \times 10^7$$

For $\epsilon_1 \leq -0.007$:

$$E_{1c} = 14.56 \text{ Msi}$$

F.3 Transverse Tension

The expression for tensile transverse modulus, E_{2t} as a function of transverse strain is:

For $0 \leq \epsilon_2 < 0.0055$:

$$E_{2t} = E_{20} + A\epsilon_2 + B\epsilon_2^2 + C\epsilon_2^3 \text{ Msi}$$

where:

$$E_{20} = 1.430$$

$$A = -1.493939 \times 10^1$$

$$B = 8.6323087 \times 10^3$$

$$C = -2.368620666 \times 10^6$$

For $\epsilon_2 \geq 0.0055$:

$$E_{2t} = 1.21 \text{ Msi}$$

F.4 Transverse Compression

The expression for compressive transverse modulus, E_{2c} as a function of transverse strain is:

For $-0.029 < \epsilon_2 < 0$:

$$E_{2c} = E_{20} + A\epsilon_2 + B\epsilon_2^2 + C\epsilon_2^3 \text{ Msi}$$

where:

$$E_{20} = 1.480$$

$$A = 1.424104 \times 10^1$$

$$B = - 2.5009442 \times 10^2$$

$$C = 4.080186036 \times 10^3$$

For $\varepsilon_2 \leq -0.029$:

$$E_{2c} = 0.76 \text{ Msi}$$

F.5 Inplane Shear

The expression for inplane shear modulus, G_{12} as a function of inplane shear strain is:

For $|\gamma_{12}| < 0.025$:

$$G_{12} = G_{120} + A |\gamma_{12}| + B |\gamma_{12}|^2 + C |\gamma_{12}|^3 \text{ Msi}$$

where:

$$G_{120} = 8.160 \times 10^{-1}$$

$$A = - 6.61714$$

$$B = - 2.551476 \times 10^3$$

$$C = 7.5705187 \times 10^4$$

For $|\gamma_{12}| \geq 0.025$:

$$G_{12} = 0.24 \text{ Msi}$$

F.6 Poisson's Ratio

Since the Poisson's ratio was found to be fairly constant in the longitudinal tension test and the Poisson response data in longitudinal compression was questionable, a constant value was used for principal Poisson's ratio.

$$\nu_{12} = 0.29$$

Report Documentation Page

1. Report No. NASA CR-4118		2. Government Accession No.		3. Recipient's Catalog No.	
4. Title and Subtitle Static and Dynamic Large Deflection Flexural Response of Graphite-Epoxy Beams				5. Report Date March 1988	
				6. Performing Organization Code	
7. Author(s) Mark D. Sensmeier, O. Hayden Griffin, Jr., and Eric R. Johnson				8. Performing Organization Report No. VPI-E-87-7	
				10. Work Unit No. 505-63-01-11	
9. Performing Organization Name and Address Virginia Polytechnic Institute and State University Dept. of Engineering Science and Mechanics 106 Norris Hall Blacksburg, VA 24061				11. Contract or Grant No. NAG1-343	
				13. Type of Report and Period Covered Contractor Report	
12. Sponsoring Agency Name and Address NASA Langley Research Center Hampton, VA 23665-5225				14. Sponsoring Agency Code	
15. Supplementary Notes Langley Technical Monitor: Huey D. Carden					
16. Abstract An experimental and analytical study of the large deflection flexural response of graphite-epoxy beams subjected to eccentric axial compression was conducted. The beam specimens were subjected to axial impact and to static axial loads, in order to assess the damage caused by impact. A one-dimensional geometrically and materially nonlinear finite element model was developed to predict static beam response. The model incorporated width-wise effects by assuming specific forms of the displacements across the width, with length-wise variation introduced as a degree of freedom. The resulting 22° of freedom element accurately predicted the load deflection and strain-deflection responses of the static test specimens.					
17. Key Words (Suggested by Author(s)) Crashworthiness Beam Theory Composite Materials Graphite/Epoxy Impact Loading Nonlinear Response				18. Distribution Statement Unclassified - Unlimited Subject Category 39	
19. Security Classif. (of this report) Unclassified		20. Security Classif. (of this page) Unclassified		21. No. of pages 250	
				22. Price A11	